Investigation of the Structure and Phase Transitions in the Novel A-site Substituted Perovskite Series $(Na_{1-x}K_x)_{0.5}Bi_{0.5}TiO_3$.

by

Glyn Owen Jones B.Sc.(Hons.), M.Sc.

A thesis submitted to the University of Warwick in partial fulfilment of the requirement for the degree of Doctor of Philosophy

Department of Physics

March 2001

Contents

List of Figures

List of Tables

List of Abbreviations

NBT	Sodium Bismuth Titanate, $Na_{0.5}Bi_{0.5}TiO_3$
ICSD	Inorganic Crystal Structure Database
KBT	Potassium Bismuth Titanate, $K_{0.5}Bi_{0.5}TiO_3$
NKBT	Sodium Potassium Bismuth Titanate, $(Na_{1-x}K_x)_{0.5}Bi_{0.5}TiO_3$
SHG	Second Harmonic Generation
XRPD	X-ray Powder Diffraction
EDX	Energy Dispersive X-ray Analysis
SEM	Scanning Electron Microscope
CCD	Charge-Coupled Device
FWHM	Full-Width Half Maximum
GSAS	General Structural Analysis System
PZT	Lead Zirconium Titanate, $Pb(Zr_xTi_{1-x})O_3$
SMART	Siemens Molecular Analytical Research Tool
IP	Image Plate
TEM	Transmission Electron Microscopy
MPB	Morphotropic Phase Boundary

Acknowledgements

I would like thank Dr. P. A. Thomas for her exceptional supervision, guidance and encouragement throughout this study. I would also like to thank the Department of Physics for providing the facilities that made this work possible and acknowledge the Engineering and Physical Sciences Research Council (EPSRC) for funding this research.

I would like to thank Prof. A. M. Glazer, Dr. J. Kreisel, M. A Geday from the Clarendon Laboratory, University of Oxford and Dr. K. Roleder from the Institute of Physics, University of Silesia, Poland, for their collaboration on this project. I wish also to thank Mick Cooper, Keith Briggs and Dave Hammond for technical advice.

I would also like to acknowledge a number of friends and colleagues, including Martin Womersley, Stephen Ison, Ian Gee, Tina Latham, Jonathan Roderick, Vincent Jennings, Thomas Lyford and Adam Duddridge. I would also like to express my gratitude to Scott Jones for useful discussions and suggestions. Finally, on a personal note, I must also thank my parents, family and close friends for their continual support throughout my studies.

Glyn Owen Jones

Declaration

The work for this thesis was carried out in the Department of Physics at the University of Warwick, the Clarendon Laboratory at the University of Oxford, the Synchrotron radiation source at CCLRC Laboratory and the Institut Laue-Langevin (ILL), France. The work was completed during the period from October 1997 to September 2000 and, except where specifically acknowledged in the text, is the result of my own independent research and has not been previously submitted at the University of Warwick, or any other academic institution, in respect of a higher degree. Parts of this thesis have been published or submitted for publication with the following references:

1. *Investigation of the structure and phase transitions in the ferroelctric crystal* $Na_{0.5}Bi_{0.5}TiO_3$. **G. O. Jones** and P. A. Thomas. (1999). Acta Cryst. Supp. A55, 493.

2. *The tetragonal phase of* $Na_{0.5}Bi_{0.5}TiO_3$ *– a new variant of the perovskite structure.* **G. O. Jones** and P. A. Thomas. (2000). Acta Cryst. B56, 426.

3. *An x-ray diffraction and Raman spectroscopy investigation of A-site substituted perovskite compounds: the* $(Na_{1-x}K_x)_{0.5}Bi_{0.5}TiO_3$ $(0 \leq x \leq 1)$ *solid solution.* J. Kreisel, A. M. Glazer, **G. O. Jones**, P. A. Thomas, L. Abello and G. Lucazeau. (2000). J. Phys.: Condens. Matter. 12, 3267.

4. *An investigation of the structure and phase transitions in the A-site substituted perovskite compound* $Na_{0.5}Bi_{0.5}TiO_3$. **G. O. Jones** and P. A. Thomas. (2001). Acta Cryst. B, in press.

5. *A new high-pressure phase of the A-substituted perovskite Sodium Bismuth Titanate.* **G. O. Jones**, P. A. Thomas and M. I. McMahon. (2001). Acta Cryst. B, in press.

It is anticipated that further parts of this thesis will be published in due course.

March 2001 *G. O. Jones*

Abstract

An extensive study of the crystal structure and phase transitions in $Na_{0.5}Bi_{0.5}TiO_3$ has been carried out using neutron/x-ray powder, and single-crystal x-ray, diffraction techniques. This has been complemented with optical and Raman studies. The sequence of phase transitions from the high-temperature prototypic cubic structure (above 813 K), to one of tetragonal (673-773 K) and then rhombohedral structure (5-528 K) has been established in $Na_{0.5}Bi_{0.5}TiO_3$. Coexisting tetragonal/cubic (773-813 K) and rhombohedral/tetragonal (528-673 K) phases have also been observed. Rietveld refinements have revealed the rhombohedral phase, space group R3c, exhibits an antiphase, $a^-a^-a^-$ oxygen octahedra tilt system, with parallel cation displacements. The tetragonal phase, space group P4bm, possesses an unusual combination of in-phase, $a^0a^0c^+$ oxygen octahedra tilts and antiparallel cation displacements along the polar axis. This structure type is unprecedented amongst the perovskites. A high-pressure study using synchrotron and neutron diffraction has revealed the ambient pressure rhombohedral structure undergoes a phase transition to an orthorhombic structure with Pnma symmetry and the $a^-b^+a^-$ oxygen octahedra tilt system together with antiparallel A-cation ordering along [010]. The pure rhombohedral structure persists up to 8 kbar; between 10-19.4 kbar a rhombohedral/orthorhombic coexistence region was observed and above 26.2 kbar the purely orthorhombic phase was seen.

Structural variations as a function of temperature, pressure and doping across the $(Na_{1-x}K_x)_{0.5}Bi_{0.5}TiO_3$ series are also presented. With increasing potassium doping across this series, phase transitions from the rhombohedral structure with octahedral tilting to a non-tilted rhombohedral structure (space group, R3m) and then to a tetragonal structure (space group P4mm) was observed. A basic phase diagram for this series has been assembled outlining phase boundaries across the series and as a function of temperature.

In this study, the optimum conditions used for the fabrication of powders, ceramics and single crystals of the perovskite compound $Na_{0.5}Bi_{0.5}TiO_3$ and the solid solution across the $(Na_{1-x}K_x)_{0.5}Bi_{0.5}TiO_3$ series have been established. A detailed analysis of this A-site substituted distorted perovskite compound is made with structural variations, cation displacements and octahedral distortions for the different phases being reported. The A-site substituted compounds are thoroughly discussed in the context of modern perovskite science.

Chapter 1

An Introduction to the Perovskite Structure

1.1 The Perovskite Structure

Sodium Bismuth Titanate, $Na_{0.5}Bi_{0.5}TiO_3$ (NBT) and its analogues, belong to the class of crystals known as perovskites, many of which are ferroelectric. Perovskites are of considerable interest from both an academic point of view and because of the large array of possible structures, which lead to a diverse range of physical properties and technologically useful applications. In this chapter, the perovskite structure will be examined and the link with ferroelectricity discussed.

The ideal perovskite structure, shown in Figure 1.01, has a general formula ABX_3 where A and B are cations and X the anion and belongs to the cubic space group $Pm\bar{3}m$. It is characterised by a three-dimensional framework of BX_6 octahedra sharing corners with the vacancies between them occupied by A-cations. The A-cation is a monovalent or divalent metal and the B-cation a tetravalent or pentavalent one. The X anion is generally an oxygen atom, although it may be another Group VI element or a Halogen.

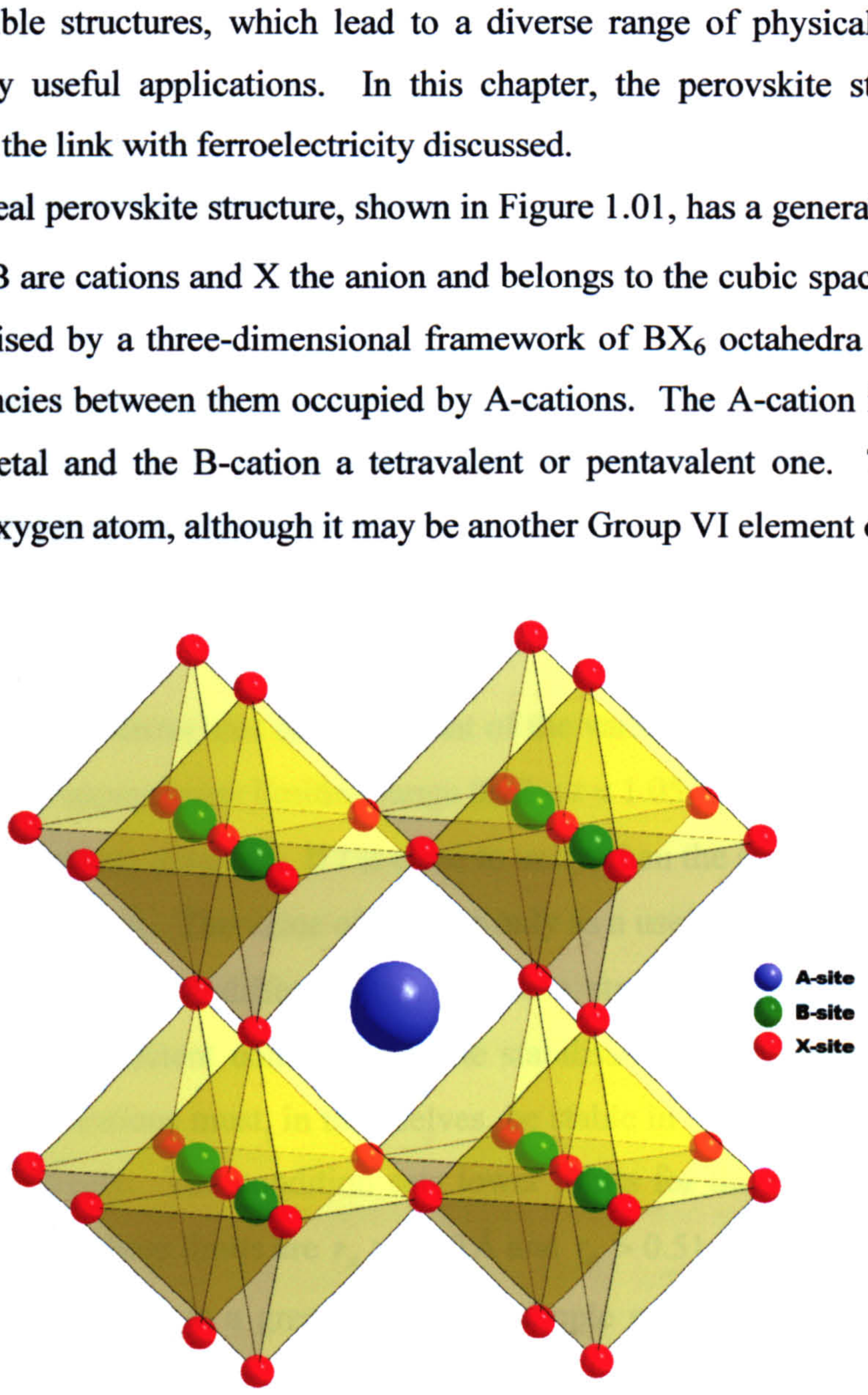

Figure 1.01. The ideal cubic perovskite structure (origin at the B-site).

The perovskite structure is not exclusively restricted to those compounds in which A ions are divalent and B ions tetravalent. Any pair of ions in the structure is compatible provided that they have radii appropriate to the co-ordination (co-ordination numbers of B and X ions being 6, and A ions 12), and an aggregate valency of +6 to confer electrical neutrality on the structure as a whole.

In the early investigations of ABX_3 compounds[1-2] the realisation that the perovskite type structure depended mainly on the ratio of radii of the component ions was reached. To a good approximation the ions may be regarded as spheres whose size is characterised by the ionic radius. In the idealised structure, where the ions are just touching one another, the B-X distance is equal to $a/2$, whereas the A-X distance is $\sqrt{2}(a/2)$ (where a is the cubic unit cell length). In order to have contact between the ions the following condition must be satisfied:

$$r_A + r_X = \sqrt{2}(r_B + r_X) \tag{1.01}$$

where r_A, r_B and r_X are the radii of the A, B and X ions respectively. In practice this condition does not have to be rigorously fulfilled and the structure will be stable whenever the following condition holds[3]:

$$r_A + r_X = t\sqrt{2}(r_B + r_X) \tag{1.02}$$

where t is a tolerance factor that takes account of the variable nature of ionic radii. This may lie within the approximate limiting range $0.78 < t < 1.05$[4]: if t lies outside this range other structure types are obtained. If t is close to unity, then the structure is *usually* cubic with a cell edge of ≈ 4 Å. The value of t serves only as a useful structural guide and does not give a precise rule for differentiating between structures. The above geometric relations are not a sufficient condition for the stabilisation of the perovskite structure, since the A- and B-cations must, in themselves, be stable in twelve-fold and six-fold co-ordination respectively. The condition sets lower limits for the cation radii. In oxide systems for example these limits are $r_A > 0.90$ Å and $r_B > 0.51$ Å.

Even though there is a great number of simple perovskites, ABX_3, many more compounds are possible when multiple ions are substituted for one or more of the original ions thus forming complex perovskites. The vast majority of complex perovskites are formed through the substitution of more than one type of atomic species, either with the same or with different valence states, at the B-cation site and are

represented by the general formula $A(B'_xB''_{1-x})X_3$[5]. Complex perovskites also exist where substitution at the A cation site $(A'_xA''_{1-x})BX_3$ has occurred. When such substitutions are made the ions can occupy the original cation site of the simple structure either randomly or in an ordered manner. For complex perovskites, the average radius of the ions on each site is used for r_B and r_A respectively in equation 1.02.

The A-site position in the structure is most frequently filled by alkaline, alkaline earth or rare earth ions, although other cations may have a suitable size for occupation of these sites. In general a transition metal is the most usual B-site component in perovskite oxides.

1.1.1 Distorted Perovskites

Although many materials possess the ideal $Pm\bar{3}m$ cubic structure, structural variations can take place to produce distorted perovskites. It is well known, for example, that compounds are strongly distorted as a consequence of ion choice. There are many more distorted perovskites (simple and complex), than there are cubic perovskites; even the mineral perovskite itself, $CaTiO_3$, is orthorhombic[6] (at room temperature). These structural distortions can have a significant influence on the physical properties of the materials. The modified structures result from geometrical constraints imposed upon the compound and take place via mechanisms, which include combinations of the following:

(i) displacements of cations from the centre of their co-ordination polyhedra, either in a parallel (ferroelectric structure) or antiparallel (antiferroelectric structure) manner;
(ii) distortion of the polyhedra co-ordinating A and B cations;
(iii) tilting of the anion octahedra, BX_6 about various axes;
(iv) cation ordering (in certain complex perovskites).

Even though the obvious structural differences between many perovskites may not always be clear, the physical properties arising from these subtle variations can differ extensively, especially when external conditions such as temperature, pressure or electric field are altered. This results in the huge number of possible structures, many of which possess properties such as ferroelectricity and piezoelectricity.

Many investigators have studied distortions in the perovskite structure, Thomas[7-8] for example has devised a system for classifying perovskites based on the

polyhedral volumes of the A and B cations, Megaw and Darlington[9] produced a detailed study of the effects of octahedral tilting and deformations in rhombohedral perovskites. However the most influential work on distorted perovskites was produced by Glazer[10-11].

1.1.2 Perovskite Simple Tilt Systems

As previously mentioned when the octahedra are tilted (or the cations are displaced) different types of distortions from the ideal cubic structure are produced. In all, there are 23 possible simple tilt systems describing how octahedra can be tilted. A model for this description and classification has been proposed by Glazer[10-11].

Using the Glazer notation, a tilt system is described by resolving the rotations of the octahedra about each of the three pseudocubic axes. In the classification any tilt system is expressed by the notation $a^i b^j c^k$, where a, b and c specify the magnitude of the rotation about that axis relative to the magnitude of the rotations about other pseudocubic axes. Equality of tilt magnitudes is represented by repetition of the letters appropriate to the particular axes. For example, in the $a^+a^+a^+$ system the rotation angle is the same about each of the three axes, whereas in the $a^+a^+c^+$ tilt system the rotation angle about the *c*-axis is different from the rotation angle about the *a* and *b* axes. The superscripts i, j and, k indicate whether the rotations in adjacent layers are in the same or opposite directions. A negative (-) superscript indicates that the rotations of two neighbouring octahedra, along the tilt axis are in the opposite directions i.e. antiphase tilts, while a positive (+) superscript is used when they tilt in the same direction i.e. in-phase tilts. A zero (0) superscript is used when octahedra are not rotated about any particular axis. Tilt signs are important for establishing the lattice type and unit-cell angles. Any two in-phase tilts, or one in-phase and one antiphase tilt, mean that the relevant axes are normal to each other; any two antiphase tilts mean that the relevant cell axes are inclined to each other. An example of this is the tilt system $a^-b^+c^+$, it has three axes of unequal length normal to each other, whereas $a^-a^-c^+$ has two equal axis inclined to each other but which are both normal to the remaining axis. In some materials the tilting system can be of a much more complicated nature. Table 1.01 lists the 23 possible simple tilt systems.

A further example of how the Glazer notation describes tilted perovskite structures is a comparison of the two one-tilt systems, $a^0a^0c^-$ and $a^0a^0c^+$. The octahedra in both systems are rotated only about the c-axis. Figure 1.02 shows a view of these tilt systems down the c-axis. The rotation of one octahedron forces four of the neighbouring

six octahedra to rotate in an opposite sense. This in turn forces all the octahedra in that plane to be rotated with the same angle as the first octahedron. The other two neighbouring octahedra connected along the *c*-axis are not coupled in the same way and can rotate independently. If these final two octahedra rotate in opposite directions as in Figure 1.02 (a) the tilt system $a^0a^0c^-$ results. However if they rotate in the same direction as in Figure 1.02 (b), the tilt system $a^0a^0c^+$ results.

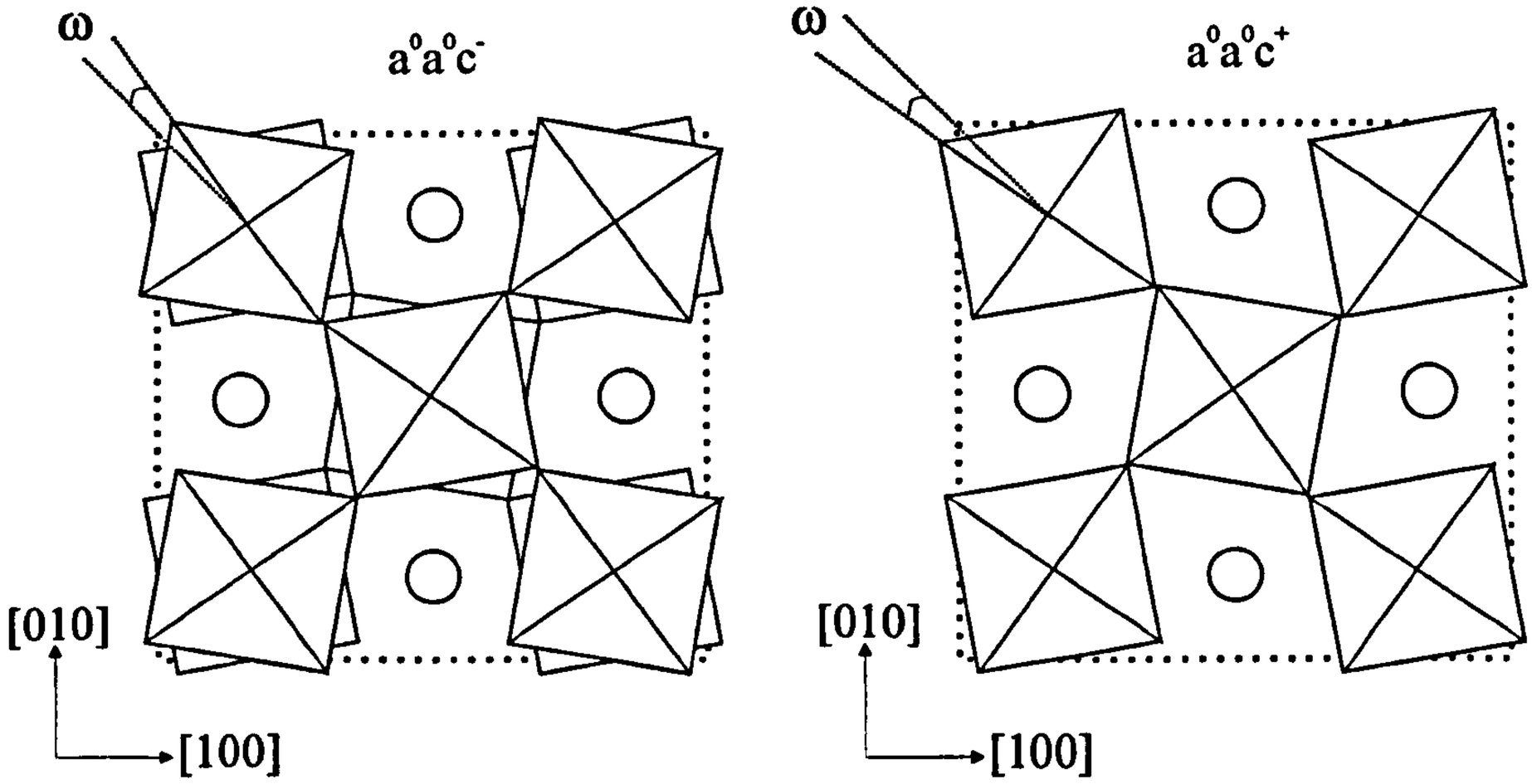

Figure 1.02. *View down the c-axis of two adjacent layers of octahedra for; (a) the $a^0a^0c^-$ tilt system and (b) the $a^0a^0c^+$ tilt system.*

Tilt system number	Tilt system symbol	Relative pseudocubic subcell parameters	Space group
Three-tilt systems			
(1)	$a^+b^+c^+$	$a_p \neq b_p \neq c_p$	Immm (71)
(2)	$a^+b^+b^+$	$a_p \neq b_p = c_p$	Immm (71)
(3)	$a^+a^+a^+$	$a_p = b_p = c_p$	$Im\bar{3}$ (204)
(4)	$a^+b^+c^-$	$a_p \neq b_p \neq c_p$	Pmmm (59)
(5)	$a^+a^+c^-$	$a_p = b_p \neq c_p$	Pmmm (59)
(6)	$a^+b^+b^-$	$a_p = b_p = c_p$	Pmmm (59)
(7)	$a^+a^+a^-$	$a_p \neq b_p = c_p$	Pmmm (59)
(8)	$a^+b^-c^-$	$a_p \neq b_p \neq c_p$, $\alpha \neq 90°$	$A2_1/m11$ (11)
(9)	$a^+a^-c^-$	$a_p = b_p \neq c_p$, $\alpha \neq 90°$	$A2_1/m11$ (11)
(10)	$a^+b^-b^-$	$a_p \neq b_p = c_p$, $\alpha \neq 90°$	Pmnb (62)
(11)	$a^+a^-a^-$	$a_p = b_p = c_p$, $\alpha \neq 90°$	Pmnb (62)
(12)	$a^-b^-c^-$	$a_p \neq b_p \neq c_p$, $\alpha \neq \beta \neq \gamma \neq 90°$	$F\bar{1}$ (71)
(13)	$a^-b^-b^-$	$a_p \neq b_p = c_p$, $\alpha \neq \beta \neq \gamma \neq 90°$	I2/a (15)
(14)	$a^-a^-a^-$	$a_p = b_p = c_p$, $\alpha = \beta = \gamma \neq 90°$	$R\bar{3}c$ (167)
Two-tilt systems			
(15)	$a^0b^+c^+$	$a_p < b_p \neq c_p$	Immm (71)
(16)	$a^0b^+b^+$	$a_p < b_p = c_p$	I4/mmm (139)
(17)	$a^0b^+c^-$	$a_p < b_p \neq c_p$	Bmmb (63)
(18)	$a^0b^+b^-$	$a_p < b_p = c_p$	Bmmb (63)
(19)	$a^0b^-c^-$	$a_p < b_p \neq c_p$, $\alpha \neq 90°$	F2/m11 (12)
(20)	$a^0b^-b^-$	$a_p < b_p = c_p$, $\alpha \neq 90°$	Imcm (71)
One-tilt systems			
(21)	$a^0a^0c^+$	$a_p = b_p < c_p$	C4/mmb (127)
(22)	$a^0a^0c^-$	$a_p = b_p < c_p$	F4/mmc (140)
Zero-tilt systems			
(23)	$a^0a^0a^0$	$a_p = b_p = c_p$	$Pm\bar{3}m$ (221)

Table 1.01. List of possible simple tilt systems (from Glazer[10]).

1.1.2.1 Difference Reflections and Cation Displacements

As tilting of the oxygen octahedra causes a doubling of the unit cell axis (Figure 1.03), extra reflections positioned on half-integral reciprocal lattice planes are produced by the extra periodicity. With reference to a doubled unit cell, these reflections can be indexed with some indices odd, whilst the ordinary main reflections have all indices even. As mentioned earlier there are two types of tilts: in-phase and antiphase tilts. These result in two distinct groups of difference reflections. In-phase tilts will give rise to odd-odd-even reflections, whilst antiphase tilts produce odd-odd-odd reflections. From this the following rules, devised by Glazer[11] are obtained (Table 1.02):

Tilt	Reflection produced	Conditions	Example
a^+	even-odd-odd	$k \neq l$	013, 031,
b^+	odd-even-odd	$h \neq l$	103, 301
c^+	odd-odd-even	$h \neq k$	130, 310
a^-	odd-odd-odd	$k \neq l$	131, 113
b^-	odd-odd-odd	$h \neq l$	113, 311
c^-	odd-odd-odd	$h \neq k$	131, 311

Table 1.02. In-phase and antiphase tilt reflections and conditions.

There are cases when half-integral difference reflections (odd indices on the doubled pseudocubic cell) occur which do not conform to the tilt reflections. These result from antiparallel cation displacements, as when displacements are parallel no difference reflections are observed.

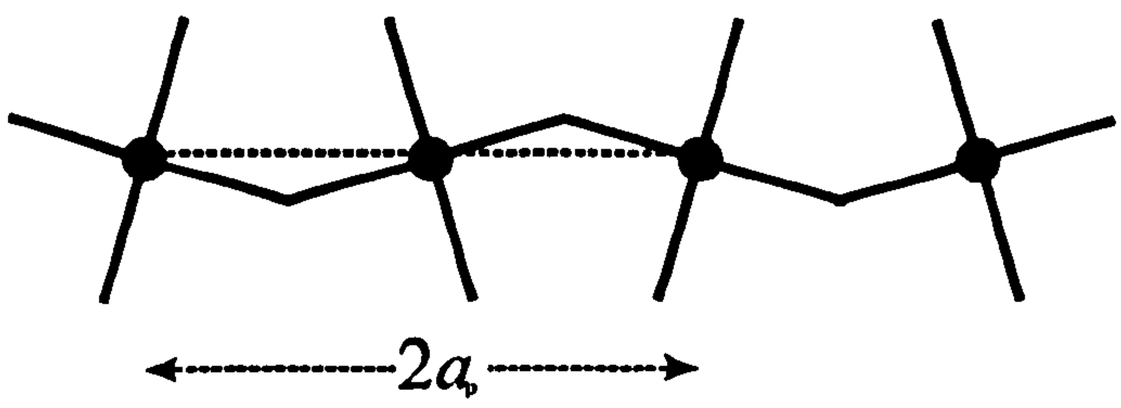

Figure 1.03. Schematic diagram of tilting octahedra, resulting in a doubled cell axis.

An example of a perovskite that possesses, cation displacements and octahedral tilting is the room temperature $CaTiO_3$ structure[6]. The orthorhombic structure (space group, Pnma) possesses the $a^-b^+a^-$ tilt system with antiparallel cation displacements along $[1\bar{1}0]$. The structure is depicted in Figure 1.04.

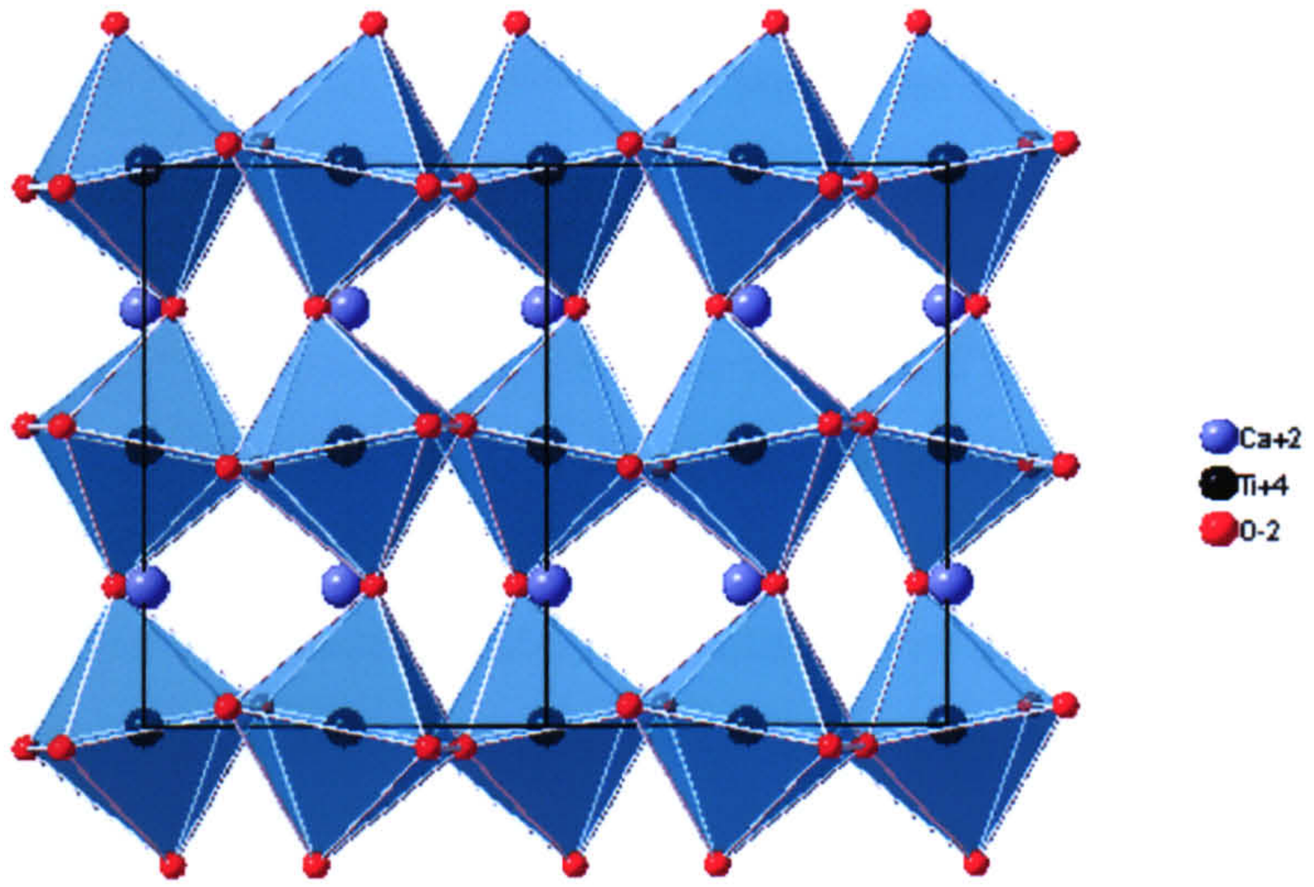

(a)

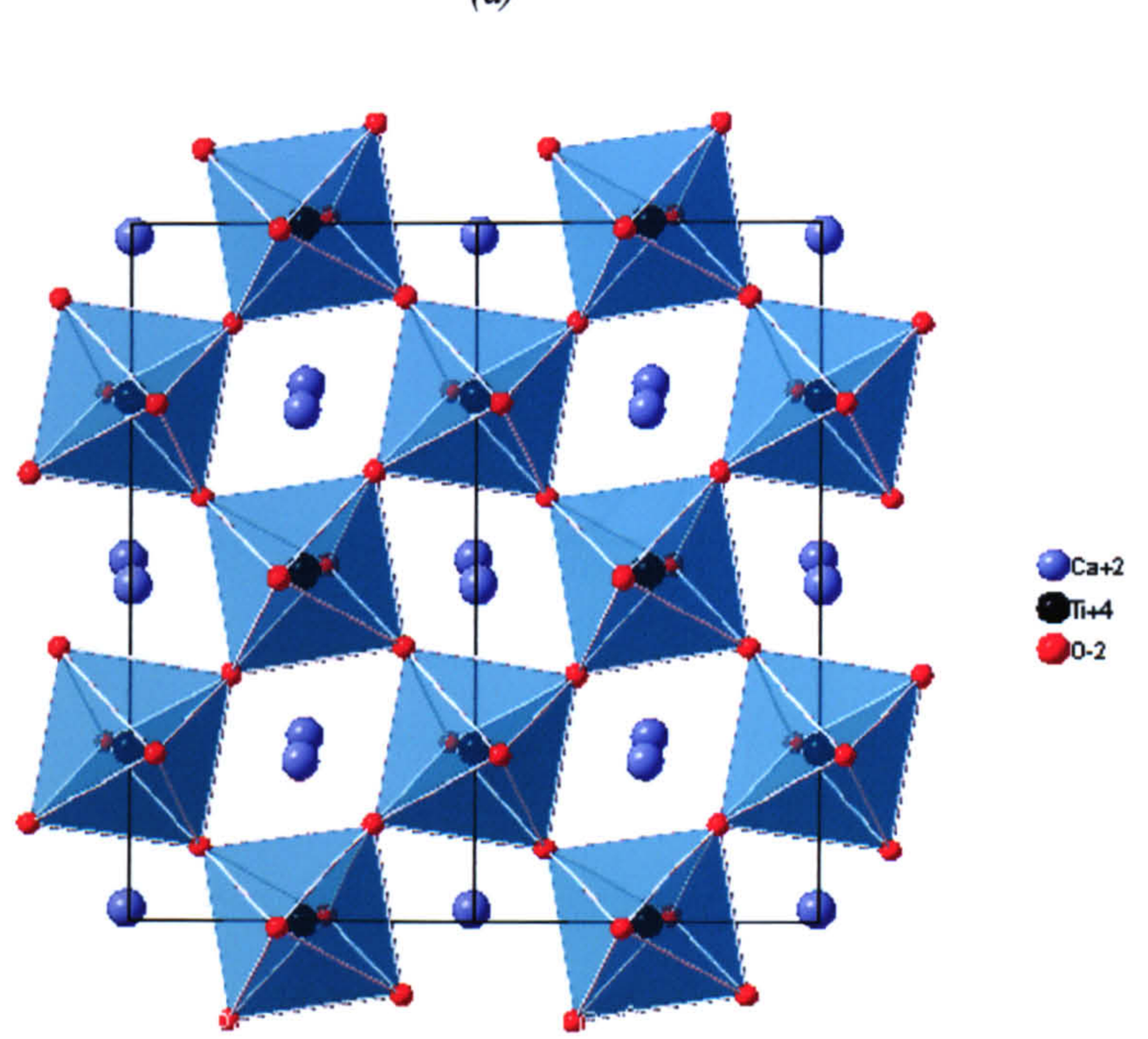

(b)

Figure 1.04. *The structure of the distorted perovskite $CaTiO_3$ (a) view along [010], (b) view down [001].*

1.2 Ferroelectricity and Crystal Structure

Some perovskites form part of the important group of crystals known as ferroelectrics[12]. A ferroelectric crystal can show a spontaneous electric polarisation, P_s, (measured in terms of dipole moment per unit volume), the direction of which may be reversed by the application of a suitable electric field. They also show a hysteresis effect in the relation between electric displacement and electric field.

If we consider a crystal initially composed of an equal number of positive and negative domains (i.e. regions of uniform polarisation oriented in opposite directions), the overall polarisation, P_s, of the crystal is equal to zero. If a small electric field E, is applied in the positive direction, for example, there will be only a linear relationship between P_s and E because the field is not large enough to switch any of the domains and the crystal will behave like a normal dielectric. In the plot of P_s verses E shown schematically in Figure 1.05, we obtain the portion OA of the curve. If the electric field strength is increased, a number of negative domains will switch over in the positive direction and the polarisation will increase rapidly (portion AB), until a state where all domains are aligned in the positive direction is reached. This is a state of saturation (portion BC) and the crystal consists now of a single domain.

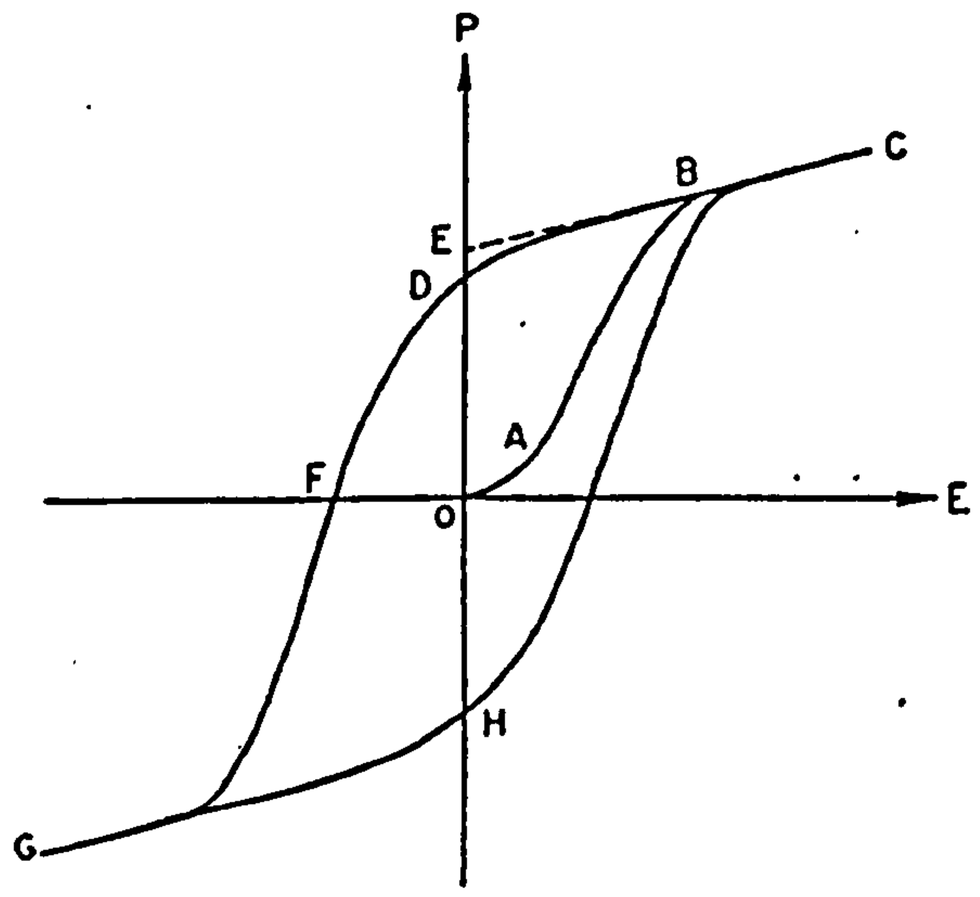

Figure 1.05. Schematic diagram of a ferroelectric hysteresis loop.

If the field strength is decreased, the polarisation will generally not return to zero, but follow the path CD of Figure 1.05. When the field is reduced to zero, some of the domains will remain aligned in the positive direction and the crystal will exhibit a

remnant polarisation P_r (OD). The extrapolation of the linear portion BC of the curve back to the polarisation axis represents the value of the spontaneous polarisation P_s (OE).

In order to annihilate the overall polarisation of the crystal, it is necessary to apply an electric field in the opposite (negative) direction. The value of the field required to reduce P_s to zero (OF) is called the coercive field E_c. Increasing the field further in the negative direction will cause complete alignment of the dipoles in the direction FG, and the cycle can be completed by reversing the field direction once again (GHC). It should be noted that the resulting states for each orientation (positive and negative) are energetically and symmetrically equivalent in the zero external electric field. The relation between P_s and E is thus represented by a hysteresis loop (CDGHC). The essential feature of a ferroelectric is thus not the fact that it has a spontaneous polarisation, but the fact that this polarisation can be reversed by means of an electric field. The hysteresis loop of P_s versus E is qualitatively similar to the loop of dielectric displacement D verses E since:

$$D = E + 4\pi P \tag{1.03}$$

Crystals having a spontaneous polarisation are termed pyroelectric and the direction of the spontaneous polarisation is called the polar axis (however a pyroelectric crystal is not necessarily also a ferroelectric).

Ferroelectric behaviour is mostly observed in certain temperature regions delimited by a transition point above which the crystal is no longer ferroelectric and shows normal dielectric behaviour. The temperature at which the transition from a ferroelectric into a paraelectric state occurs is referred to as the Curie temperature (or Curie point), T_c. The properties of many ferroelectrics show significant changes with temperature near T_c, particularly those represented by the dielectric or piezoelectric coefficients. Most ferroelectrics have a characteristic value of T_c. However, some materials melt or decompose before it has been reached.

One of the key properties of a ferroelectric is the high dielectric constant ε, particularly close to T_c. The dielectric constant of $BaTiO_3$ for example increases in value with temperature from about 1000 to 10000 in a 10 K interval below T_c. Above the transition it decreases according to the Curie-Weiss law:

$$\varepsilon - 1 = \frac{C}{T - T_o} \tag{1.04}$$

where C is the Curie constant (with dimensions of temperature) and T_o the Curie-Weiss temperature. The dielectric susceptibility, χ (which equals ε-1) is defined for an isotropic material by:

$$P = \chi \varepsilon_o E \qquad (1.05)$$

where P is the polarisation, E the electric field and ε_o the permittivity of free space. The susceptibility is another physical property that shows anomalous behaviour at the transition temperature.

1.2.1 Phase Transitions in Ferroelectric Perovskites

It is the off-centre displacements of the cations from their oxygen/anion cation polyhedra that give rise to the polarisation P_s, of a ferroelectric crystal. The movement of cations from their high-symmetry positions in different directions result in polar, ferroelectric or antipolar, antiferroelectric materials being formed.

Atomic arrangements in all ferroelectric crystals are such that small ion displacements result in an equally stable state but with a re-oriented P_s. A structural phase transition in a ferroelectric perovskite is marked either by the appearance of P_s or by the change of its direction. An example of a sequence of ferroelectric phase transitions can be seen in the perovskite $BaTiO_3$. Above its Curie point of 393 K, the unit cell is cubic with ions arranged as in Figure 1.01. Below this temperature it transforms to a distorted tetragonal structure in which the Ti^{4+} and Ba^{2+} ions are displaced by different amounts along [001] with respect to the oxygen framework. The resulting displacements give rise to the spontaneous polarisation along *c*. On lowering the temperature further to around 273 K, the displacements switch to the [110] direction (face diagonal) and the crystal system becomes orthorhombic. Below 193 K the lowest temperature phase of $BaTiO_3$ is obtained where the displacements are along [111] (body diagonal) and the crystal system is now rhombohedral. These transformations are illustrated in Figure 1.06, and the corresponding changes in the values of the lattice parameters are shown in Figure 1.07 (a).

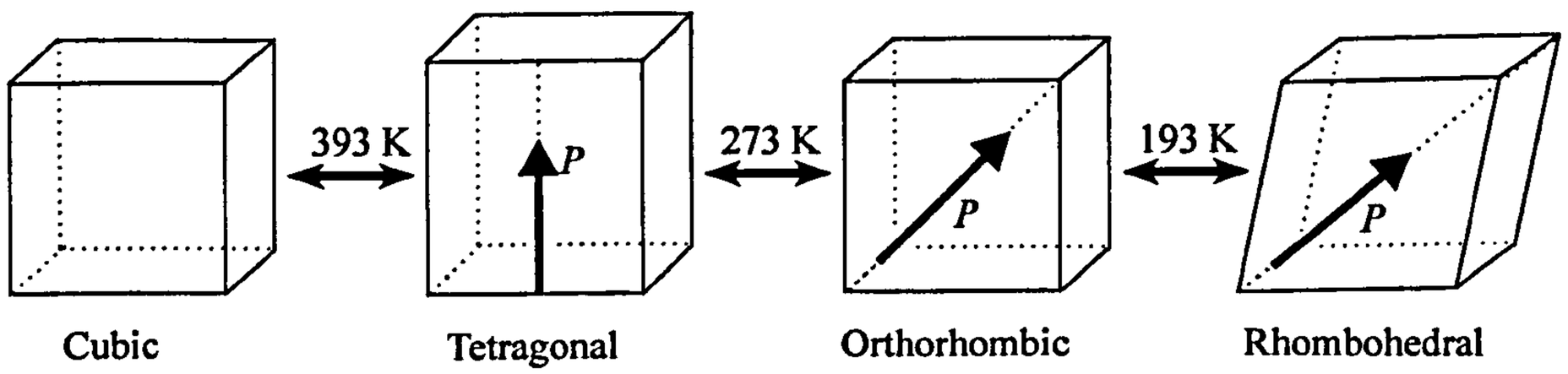

Figure 1.06. Sequence of phase transitions in the simple perovskite $BaTiO_3$.

Figure 1.07 (b) shows the variation of P_s with temperature for $BaTiO_3$. The step down in P_s on cooling as the structure transforms from tetragonal to orthorhombic, at around 273 K, corresponds to the factor $1/\sqrt{2}$, as the change in P_s is in direction only (electrodes being applied on (001)). Similarly, the step down at 193 K corresponds to the factor $\sqrt{2}/\sqrt{3}$ as the change in direction of P_s is from [110] to [111]. The relative permittivity, shown in Figure 1.07 (c) is another physical property that shows anomalous behaviour at the phase transitions.

Within the perovskite family there are many differing types of ferrioc phases including ferroelectrics and antiferroelectrics. Using the perovskite structural tolerance factor t given in equation 1.02, a distribution of ferroelectrics and antiferroelectrics in the perovskite family has been determined[13]. The antiferroelectrics are found to have a limited distribution $0.78 \leq t \leq 1.00$, while the ferroelectrics cover the whole perovskite range $0.78 \leq t \leq 1.05$[4].

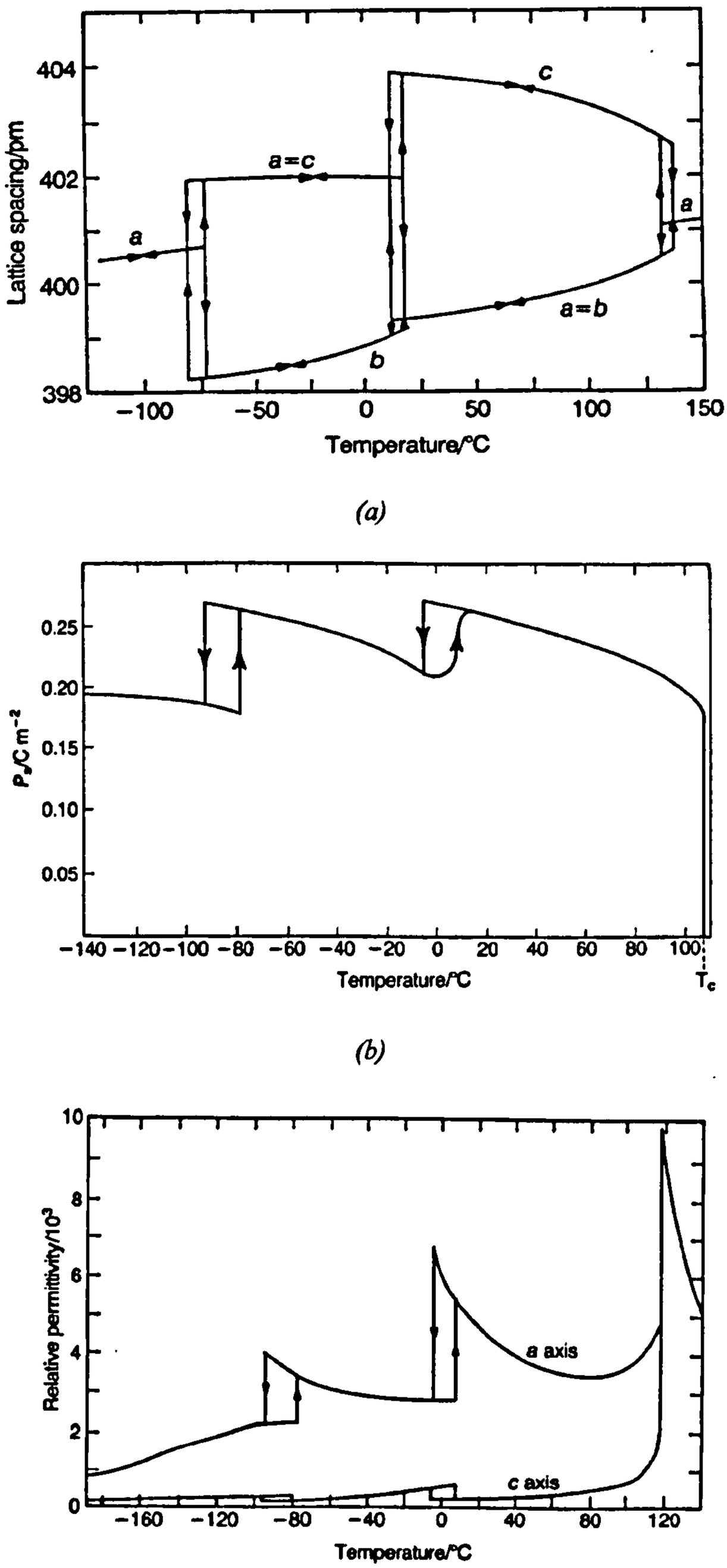

Figure 1.07. *Properties of $BaTiO_3$; (a) Lattice parameters as a function of temperature, (b) spontaneous polarisation verses temperature, (c) relative permittivites measured in the a and c directions verses temperature (from Electroceramics - Materials, Properties and Applications[14]).*

1.2.2 Crystallographic Considerations and Physical Properties

Crystals can be classified into one of the 32 crystal classes according to their symmetry. Eleven of these classes are centrosymmetric i.e. have a centre of symmetry, and possess no polar properties. If for example a uniform stress is applied to such a crystal, a small displacement of the charges within the lattice will be observed but the existence of a centre of symmetry will compensate for these relative displacements. The remaining 21 crystal classes are non-centrosymmetric, and it is possible for these crystals to have one or more polar axes. With one exception (the cubic 432 class which, although without a centre of symmetry, has other symmetry elements that combine to exclude a piezoelectric effect), all classes devoid of a centre of symmetry exhibit the piezoelectric effect. All ferroelectric crystals are simultaneously pyroelectric and piezoelectric as well, however the converse is not necessarily true.

1.2.2.1 The Piezoelectric Effect

The piezoelectric effect can be observed in two forms, the direct and converse effect. The direct piezoelectric effect is the change in the electric dipole moment under the application of mechanical stress and, conversely the occurrence of a strain (mechanical deformation) under the application of an electric field. The change in polarisation, P_i is related to the applied stress, σ_{jk} by a third rank tensor d_{ijk}, the piezoelectric tensor, of which there are twenty-seven components, d_{ijk} as described by:

$$P_i = d_{ijk}\sigma_{jk} \tag{1.06}$$

The strain and electric field relationship in the converse piezoelectric effect is linear, in that a reversal of direction of the variable causes the effect to be opposite. If the direction of the electric field is reversed the material will be compressed rather than stretched. The stain ε_{jk} is related to the field E_i by the same piezoelectric coefficients as in the direct effect:

$$\varepsilon_{jk} = d_{ijk}E_i \tag{1.07}$$

The piezoelectric effect is utilised in filters for telecommunication purposes and for accurate frequency generators in many electrical circuits. The converse piezoelectric effect, where an applied field gives rise to a mechanical strain, is used in many ultrasonic transducer applications.

1.2.2.2 The Pyroelectric Effect

In the pyroelectric effect a change in temperature causes a change in the spontaneous polarisation. This is only exhibited in structures that have a unique polar axis (a unique direction which is unrelated by symmetry to any other direction). Of the thirty-two crystallographic point groups, ten possess a polar axis. Ferroelectric crystals belong to the pyroelectric family and may be described as pyroelectric crystals with reversible polarisation.

The magnitude of the induced polarisation is determined by the pyroelectric coefficients π_i defined by:

$$\Delta P_i = \pi_i \Delta T \tag{1.08}$$

The pyroelectric effect has been utilised in a number of materials for use in sensitive infrared detectors.

1.3 A-site Substituted Complex Perovskites

A-site substituted complex perovskites, have not been as widely investigated in comparison to their B-site substituted counterparts. Examples include $Ba_{0.5}Sr_{0.5}TiO_3$[15], the rare-earth manganites typified by $La_{0.5}Sr_{0.5}MnO_3$[16] and their solid solutions between $A'_{1-x}A''_x$. These materials have chemically different but isovalent atomic species situated at the A-site. Infrequently a feature shown by some perovskites is the formation of ***compounds*** through substitution at the A-site. The small number of examples include $Na_{0.5}Bi_{0.5}TiO_3$[17] and its analogues $Ag_{0.5}Bi_{0.5}TiO_3$[18], $K_{0.5}Bi_{0.5}TiO_3$[17] and $Ag_{0.5}Nd_{0.5}TiO_3$[19]. In the case of $Na_{0.5}Bi_{0.5}TiO_3$ for example, A-site positions are equally occupied by the two non-equivalent valency cations Na^{1+} and Bi^{3+} in a fixed stoichometric ratio 0.5:0.5. Because of valency restrictions no solid solutions of the type $A'_{1-x}A''_x$ are formed. It should also be pointed out that NBT itself is unusual, even when compared to other A-site substituted perovskites in that electronically it possesses, very different ions (Na^{1+} having 10 electrons whereas Bi^{3+} has 80) sharing the A-sites. The property of compound formation means that there must be an energetic stability associated with these particular substitutions. This feature offers an entirely new area of study in the field of perovskite structural science.

1.3.1 Sodium Bismuth Titanate, $Na_{0.5}Bi_{0.5}TiO_3$ (NBT)

Sodium Bismuth Titanate, $Na_{0.5}Bi_{0.5}TiO_3$ (NBT) is an A-site substituted distorted complex perovskite compound. It was first discovered by Smolenskii and Agranovskaya in 1959[17]. Starting from general considerations involving the crystal structure (tolerance factor), electrical neutrality and the tendency of ions to a given co-ordination, they predicted and produced various complex perovskite polycrystalline samples, which included NBT. In a follow up paper[20], x-ray diffraction studies confirmed the perovskite structure of this compound and assuming cubic symmetry, a lattice parameter of 3.88 Å was found.

Since the initial discovery of NBT, structural phase transitions in this compound have been widely studied. Suchanicz & Kwapulinsk[21], carried out an x-ray powder diffraction study of NBT as a function of temperature between 473-893 K on cooling. The fundamental sequence of phase transitions from the high-temperature cubic structure (above 813 K), to a tetragonal phase (773 K) and then, a rhombohedral phase below a temperature of approximately 533 K was established. Cubic/tetragonal and tetragonal/rhombohedral coexistence regions were found between 823-773 and 693-533 K respectively. The symmetries associated with these phases were not reported. Zvirgzds *et al.*[22] studied the temperature dependence of the lattice parameters in NBT single crystals using x-ray diffraction. On cooling, two structural phase transitions in the temperature range 293-920 K, the cubic-to-tetragonal at 793 K and the tetragonal-to-rhombohedral at 533 K, were found. For the cubic, tetragonal and rhombohedral phases the space groups $Pm\bar{3}m$, P4mm and R3m respectively, were assigned. The tetragonal/rhombohedral coexistence phases existed over ≈ 55 K, in contrast to 160 K reported by Suchanicz & Kwapulinsk[21]. There has also been a report of a low temperature phase: Suchanicz *et al.*[23] carried out low-temperature thermal and dielectric studies on NBT. From sound velocity, elastic stiffness moduli and dielectric losses results, they concluded that the presence of a new phase transition in NBT at a temperature of ≈ 5 K was indicated. However no further evidence of this low-temperature phase has been reported elsewhere.

Within the literature, all phases in NBT are discussed controversially, even the room temperature crystal structure given in the Inorganic Crystal Structure Database (ICSD collection code 207886) is incorrect, and there was a hypothesis[24] that the rhombohedral phase is, in fact, triclinic in symmetry. Opinions concerning the properties

between the tetragonal and rhombohedral phases are varied. Some authors contend that antiferroelectric order occurs[25-26], as indicated by dielectric measurements. However the results of neutron, x-ray diffraction and Raman scattering[27] do not prove this hypothesis. From neutron scattering experiments carried out by Vakhrushev *et al.*[28] (and in agreement with x-ray work already discussed), coexistence of rhombohedral/tetragonal phases is evident. Other investigations have taken place[25,29-31], however, conclusive results remained far from clear.

The A-site cations, sodium and bismuth can be distributed either randomly or in a certain order. Cation ordering in B-site substituted perovskites is driven by factors such as ion size and electrostatic forces. Most experimental studies on NBT, have disclosed no long-range ordering of sodium and bismuth ions[22,26,32] in any phase. However Park *et al.*[33] conducting single-crystal rotation camera experiments, found a low degree of ordering (identified from very faint superlattice spots of the type $(h + ½, k + ½, l + ½)$ in the rotation photographs of the high temperature cubic phase. They conclude the high-temperature cubic phase of NBT is not a primitive one, but an ordered face-centred structure with symmetry $Fm\bar{3}m$. There have also been suggestions of the existence of short-range order in NBT. In a neutron diffraction study[34], the authors noted that the background in the diffraction pattern does not vary monotonically, but has a number of broad diffuse peaks (shown by the red curves in Figure 1.08). They attributed these to the presence of short-range order in the sodium and bismuth configurations.

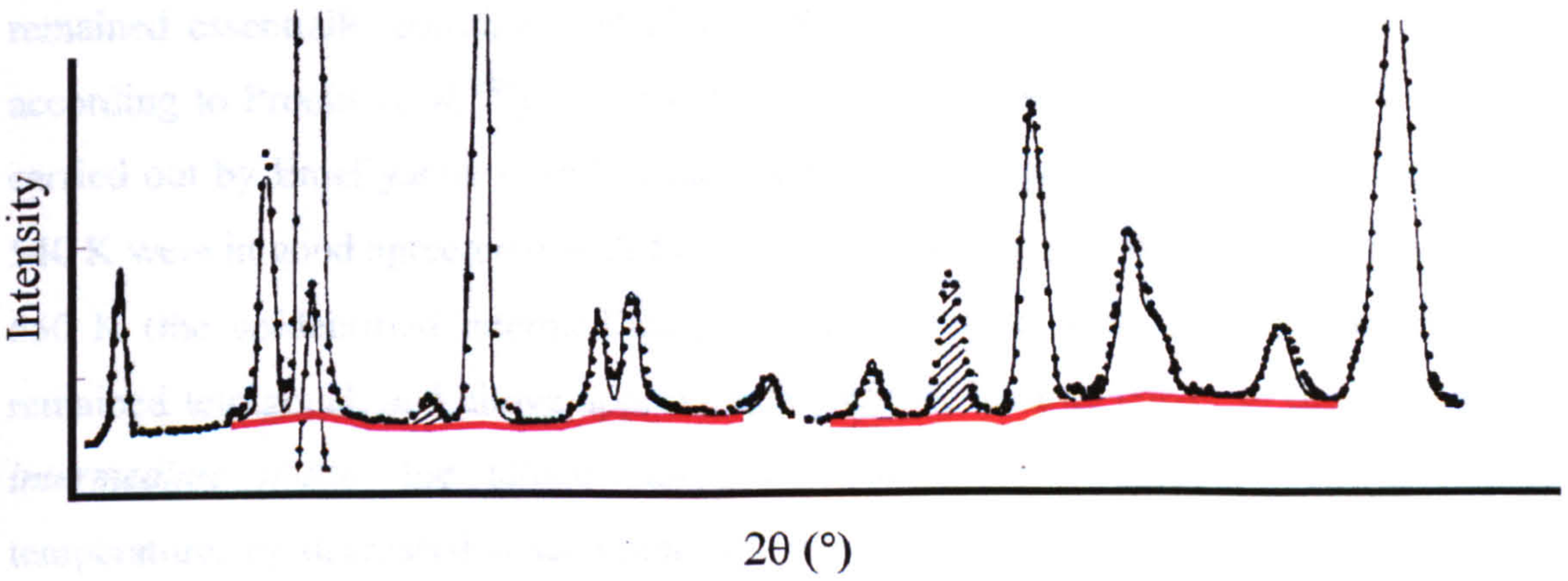

Figure 1.08. *Observed (points) and calculated (continuous curves) neutron pattern for NBT. The shaded peaks are due to scattering by the container material. The red curves show a number of broad diffuse peaks, from*[34].

At the outset of this study, there still remained controversy concerning phase transition temperatures, the development of regions of coexistence of rhombohedral-

tetragonal and tetragonal-cubic phases and their electric order. The actual symmetry and structure of the phases had also not been unambiguously established. It is evident from the state of knowledge prior to this study, that the overall picture relating to structural phases, phase transition behaviour and physical properties was inconsistent and in need of resolving.

1.3.2 Potassium Bismuth Titanate, $K_{0.5}Bi_{0.5}TiO_3$ (KBT)

Potassium Bismuth Titanate, $K_{0.5}Bi_{0.5}TiO_3$ (KBT) is also an A-site substituted distorted complex perovskite compound. KBT was discovered at the same time as NBT and established as a ferroelectric[17]. X-ray diffraction studies on KBT[20] confirmed the perovskite structure of this compound and assuming cubic symmetry, a lattice parameter of 3.94 Å was found.

Very little work relating to this compound can be found in the literature. Ivanova *et al.*[35], conducted x-ray powder diffraction studies as a function of temperature. From their investigations, they established that between room temperature to approximately 543 K (or at approximately 575 K according to other authors[36-37]), the symmetry of the compound remained tetragonal. In the vicinity of 543 K a phase transition was observed. The authors point out that they were unable to ascertain the character of this phase due to the smallness of the distortion and the sample quality (the lines in the pattern were very diffuse). They reported that in the tetragonal region, c_T decreased and a_T increased with increasing temperature. In the temperature range from 543-683 K the lattice parameters remained essentially constant, and above 683 K the symmetry became cubic (655 K according to Pronin *et al.*[38]). An x-ray powder diffraction analysis on KBT was also carried out by Emel'yanov *et al.*[37], the results and changes in lattice parameters up to 540 K were in good agreement with the data reported by Ivanova *et al.*[35]. Between 540-650 K (the unidentified intermediate phase according to some authors), the unit cell remained tetragonal, and above approximately 650 K became cubic. In the *unidentified intermediate phase*, the lattice parameters showed anomalies. With decreasing temperature, c_T decreased discontinuously then increased at around 520 K, while a_T decreased until around 520 K, increased slightly, then fell again. From electrical measurements the authors showed that the intermediate phase was stable and ferroelectric[37,39]. There seems no clear agreement however, about the nature of the *unidentified intermediate phase*, as other authors regard it as antiferroelectric[36,38].

All measurements in the quoted studies were carried out on polycrystalline samples, as crystals of this compound have not been grown. The doubts about the nature of the phase transitions and the absence of published information on KBT make this compound (like NBT) desirable to investigate.

1.3.3 The $(Na_{1-x}K_x)_{0.5}Bi_{0.5}TiO_3$ (NKBT) Solid Solution

As with the case of KBT, only a very limited number of studies[38,40-42] have been conducted on the $(Na_{1-x}K_x)_{0.5}Bi_{0.5}TiO_3$, NKBT solid solution series. The results from these studies show major discrepancies in relation to the nature of the NBT to KBT phase transition across the series. The published works on NKBT all report a room temperature phase boundary at approximately $x = 0.2$. Figure 1.09 shows the phase boundary limits from the published literature.

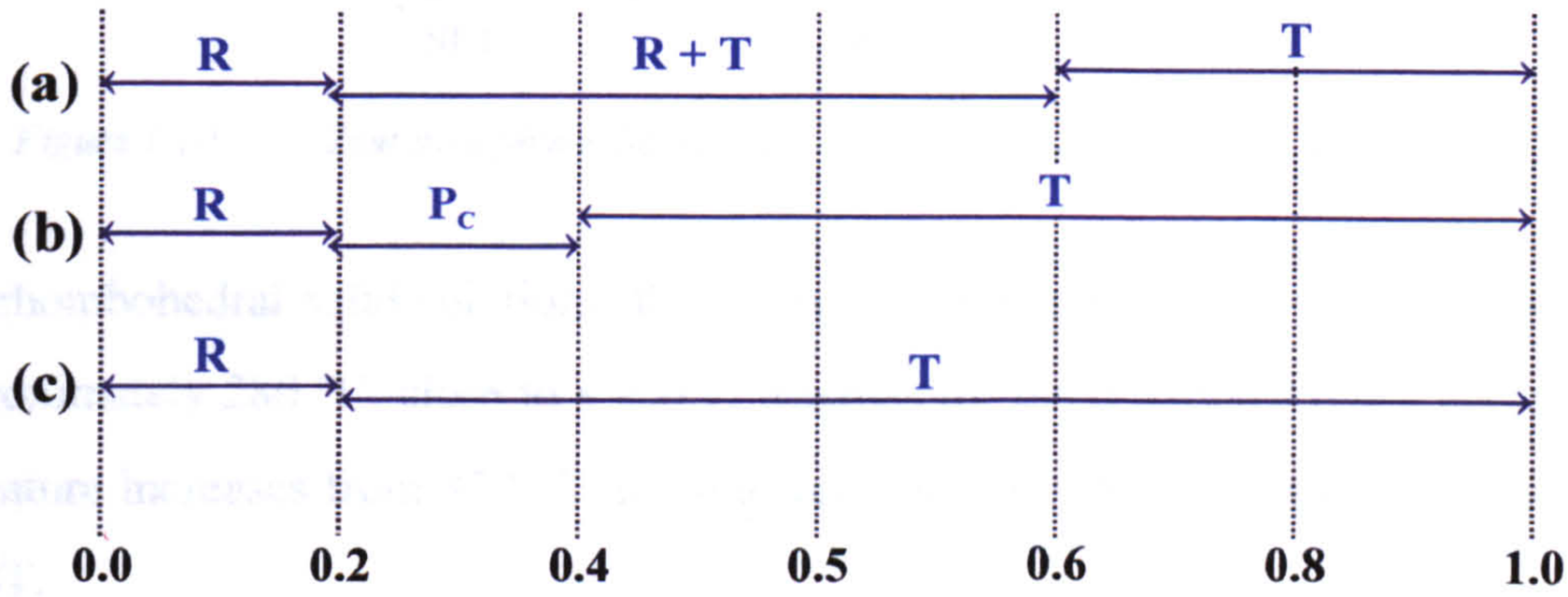

Figure 1.09. *$(Na_{1-x}K_x)_{0.5}Bi_{0.5}TiO_3$ crystal structures (R: Rhombohedral, T: Tetragonal, P_c: Pseudo-cubic phase) as reported in the literature; (a) [40], (b) [38] and (c) [41].*

There is basic agreement between most authors on the room temperature phases of the end members, NBT and KBT possessing rhombohedral and tetragonal symmetries, respectively. However, alternative descriptions of the phase boundary between $0.2 < x < 0.6$ are reported.

Elkechai and Mercurio[40] (Figure 1.09 (a)), carried out a study of NKBT using x-ray diffraction and dielectric measurements on polycrystalline samples. X-ray diffraction data showed two NKBT solid solution ranges, rhombohedral on the sodium-rich side and tetragonal on the potassium-rich side, separated by a coexistence region for $\approx 0.18 < x < 0.6$. The authors also performed x-ray diffraction experiments as a function of temperature for certain compositions in the range. Their results for NBT (and other compounds on the sodium-rich side) *unexpectedly,* do not show any tetragonal

intermediate phase between the rhombohedral and high-temperature cubic phases; this is reflected in their tentative phase diagram for the NKBT system (Figure 1.10).

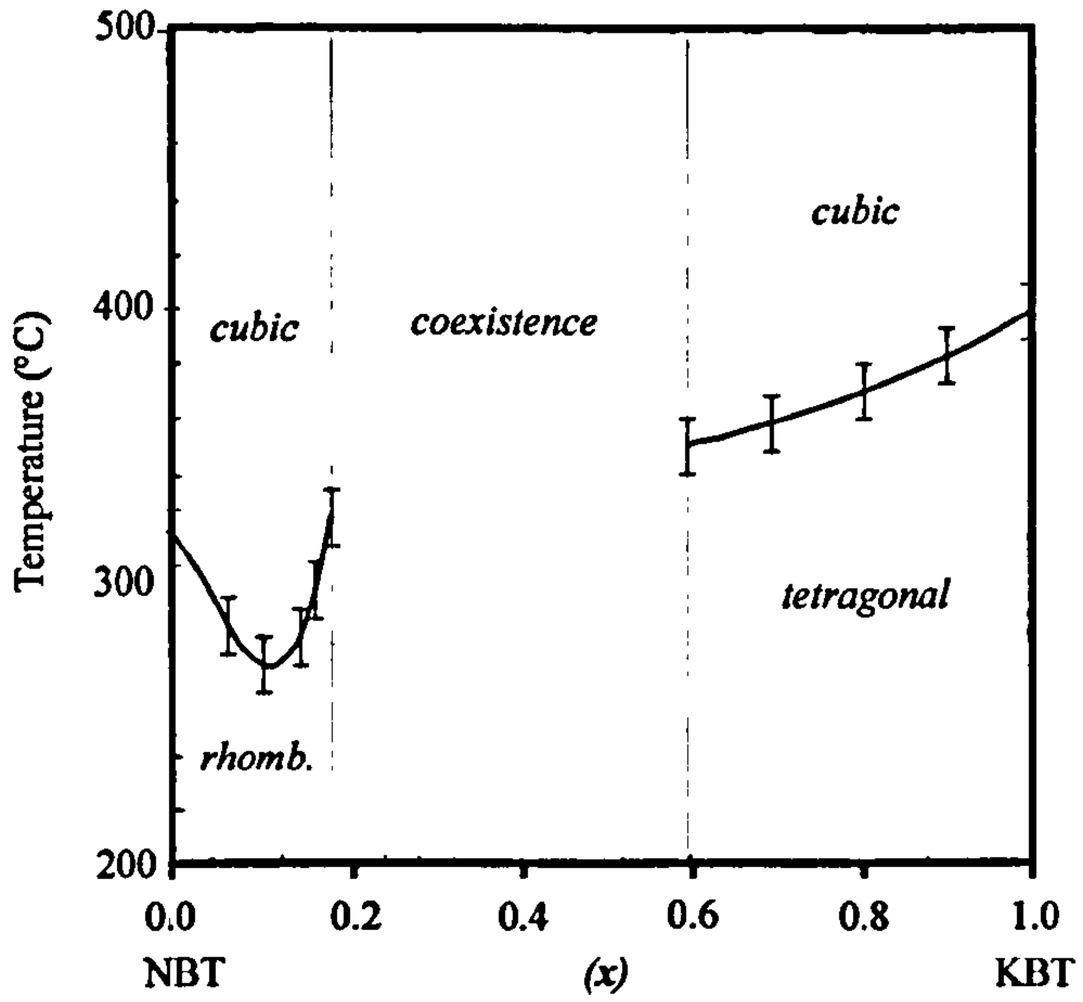

Figure 1.10. Tentative phase diagram for $(Na_{1-x}K_x)_{0.5}Bi_{0.5}TiO_3$ system, taken from[40].

In the rhombohedral solid solutions, the transition temperature goes through a minimum at approximately 280 °C, close to x = 0.1, whereas for the tetragonal ones, the transition temperature increases from 350 °C at the lower solubility limit to approximately 400 °C for KBT.

Pronin *et al.*[38] (Figure 1.09 (b)), also carried out x-ray structural analysis on the NKBT solid solution range using polycrystalline samples. In the interval $0.17 < x < 0.40$ a pseudo-cubic ferroelectric phase was found. They report that at the phase boundary for x = 0.17, there is a discontinuous change in the lattice parameter and in the unit cell volume, whereas at the phase boundary at x = 0.4, the discontinuity becomes very small.

Yamada *et al.*[41] (Figure 1.09 (c)), on the other hand, found the tetragonal phase boundary extended to approximately x = 0.2, with the rhombohedral phase being observed between $0.0 < x < 0.2$.

As with KBT (and NBT), the limited published data concerning the NKBT solid solution series in relation to structural phases, phase transition behaviour and physical properties across the series (and as a function of temperature) reveal major discrepancies that need investigating.

1.4 The aim of the present work

The study of perovskites is of great interest because of the large number of possible structures that can be formed, leading to materials with a wide range of properties and applications[42]. The formation of A-site substituted perovskite compounds offers the opportunity to investigate the structural influence of the A-site as the primary determiner of the resulting crystal structures and phase transitions, and not simply as a spacer required for filling the framework and to charge balance. They therefore present a different perspective on the perovskite structure.

The main scope of this work is to prepare samples of NBT, KBT and the solid solution range between these end members and to undertake a comprehensive study of the crystal structure and successive temperature-driven phase transitions occurring in these compounds. Phase transitions, induced by pressure and variations in composition are also studied. This study thereby aims to resolve any existing disputes relating to the crystal structure and symmetry of these compounds. A prime objective of this work is to establish and to characterise the role of the A-site cations in the resulting structures. A detailed survey of these A-site substituted distorted perovskite compounds is made with structural variations, cation displacements and octahedral distortions for all the different phases being calculated. Finally, results from many different experimental techniques are drawn together and discussed to provide an overview of the structures and properties of members in this unusual series.

References

[1] Goldsmidt, V. M., Barth, T. & Lunde, G. (1945). J. Mat. Naturv. Klasse. 7, 21.

[2] Hoffman, A. (1935). Phys. Chem. B28, 65.

[3] Megaw, H. D. (1946). Proc. Phys. Soc. 58, 133.

[4] Randall, C. A., Bhalla, A. S., Shrout, T. R. & Cross, L. E. (1990). J. Mater. Res. 5, 829.

[5] Galasso, F. S. (1969). Structure, Properties and Preparation of Perovskite-type Compounds, Pergamon Press, Oxford.

[6] Sasaki, S., Prewitt, C. T., Bass, J. D. & Schulze, W. A. (1987). Acta Cryst. C34, 1668.

[7] Thomas, N.W. (1989). Acta Cryst. B45, 337.

[8] Thomas, N.W. (1996). Acta Cryst. B52, 16.

[9] Megaw, H. D. & Darlington, C. N. (1974). Acta Cryst. A31, 161.

[10] Glazer, A. M. (1972). Acta Cryst. B28, 3384.

[11] Glazer, A. M. (1975). Acta Cryst. A31, 756.

[12] Valasek, J. (1921). Phys. Rev. 17, 475.

[13] Ven'skev, Y. N. & Zhdanov, G. S. (1956). Acad. Sci. USSR20, 161.

[14] Moulson, A. J. & Herbert, J. M. (1990). Electroceramics – Materials, properties & Applications. Chapman and Hall.

[15] Vendik, O. G. & Zubko, S. P. (2000). J. Appl. Phys. 88 (9), 5343.

[16] Woodward, P. M., Vogt, T., Cox, D. E., Arulraj, A., Rao, C. N. R., Karen, P. & Cheetham, A. K. (1998). Chem Mater. 10, 3652.

[17] Smolenskii, G. A. & Agranovskaya, A. I. (1959). Soviet Physics Solid State 1, 1429.

[18] Park, J. H., Woodward, P. M., Parise, J. B., Reeder, R. J., Lubomirsky, I. & Stafsudd, O. (1999). Chem. Mater. 11, 177.

[19] Park, J. H., Woodward, P. M. & Parise, J. B. (1998). Chem. Mater. 10, 3092.

[20] Smolenskii, G. A., Isupov, V. A., Agranovskaya, A. I. & Krainik, N.N. (1960). Soviet Physics Solid State 2 (11), 2651.

[21] Suchanicz, J. & Kwapulinski, J. (1995). Ferroelectrics 165, 249.

[22] Zvirgzds, J. A., Kapostinš, P. P., Zvirgde, J. V. & Kruzina, T. V. (1982). Ferroelectrics 40, 75.

[23] Suchanicz, J., Jezowski, A. & Poprawski, R. (1998). Phys. Stat. Sol. 169, 209.

[24] Isupov, V. A., Pronin, I. P. & Kruzina, T. V. (1984). Ferroelectric Letters 2, 205.

[25] Isupov, V. A. & Kruzina, T. V. (1983). Izv AN SSSR Serily Fiz 47 (3), 616.

[26] Pronin, I. P., Syrnikov, P. P., Isupov, V. A., Egorov, V. M., Zaitseva, N. V. & Ioffe, A. F. (1980). Ferroelectrics 25, 385.

[27] Zang, M-S. & Scott, J. F. (1996). Ferroelectrics Letters 6, 147.

[28] Vakhruskev, S. B., Isupov, V. A., Kvyatkovsky, B. E., Okuneva, N. M., Pronin, I. P., Smolensky, G. A. & Syrnikov, P. P. (1985). Ferroelectrics 63, 153.

[29] Suchanicz, J. & Ptak, W. S. (1990). Ferroelectric Letters 12, 71.

[30] Vakhruskev, S. B., Kvyatkovskii, B. E., Malysheva, R. S., Okuneva, N. M. & Syrnikov, P. P. (1989). Kristallografiya 34, 154.

[31] Tu, C., Siny, I. & Schmidt, V. (1994). Physical Review B 49 (17), 11550.

[32] Sakata, K. & Masuda, Y. (1974). Ferroelectric 7, 347.

[33] Park, S., Chung, S., Kim, I & Hong K. S. (1994). J. Am. Ceram. Soc. 77, 2641.

[34] Vakrushev, S. B., Ivanitskii, B. G., Kvyatkovskii, B. E., Maistrenko, A. N., Malysheva, R. S., Okuneva, N. M. & Parfenova, N. N. (1983). Sov. Phys. Solis State 25 (9), 1504.

[35] Ivanova, V. V., Kapyshev, A. G., Venevtsev, Yu. N. & Zhananov, G. S. (1962). Izv AN SSSR Serily Fiz 26, 358.

[36] Gadzhiev, M. S., Abiev, A. K., Isupov, V. A. & Ismailzade, I. G. (1985). Sov. Phys. Solid State 27 (8), 1502.

[37] Emel'yanov, S. M. Raevskii, I. P., Savenko, F. I., Popov, Yu. M., Zaitsev, S. M. & Mazankina, N. S. (1987). Sov. Phys. Solis State 29 (8), 1446.

[38] Pronin, I. P., Parfenova, N. N., Zaitseva, N. V., Isupov, V. A. & Smolenskii, G. A. (1982). Sov. Phys. Solid State 24 (6), 1060.

[39] Emel'yanov, S. M. Raevskii, I. P. & Prokopalo, O. I. (1983). Sov. Phys. Solid State 25 (5), 889.

[40] Elkechai, O., Mainer, M. & Mercurio, J. P. (1996). Phys. Status Solidi A 157, 499.

[41] Yamada, Y., Akutsu, T., Asada, H., Nozawa, K., Hachachiga, S., Kurosaki, T., Fujiki, H., Hozumi, K., Kawamura, T., Amakawa, T., Hirota, K. & Ikeda, T. (1995). Japan. J. Appl. Phys. 34, 5462.

[42] Takenaka, T., Sakata, K. & Toda, K. (1989). J. Appl. Phys. 28, 59.

Chapter 2

Crystal Growth and Ceramic Production

2.1 Introduction

In this chapter, the techniques used for the production of powders, ceramics and single crystals for the experimental studies in this project are described. It was necessary to produce high-quality, chemically pure materials for accurate crystal structure analysis. Powders samples were required for use in both x-ray and neutron powder diffraction studies. They were also used for Second Harmonic Generation (SHG) and Raman studies. Single crystal samples were necessary in order to carry out single crystal diffraction experiments to supplement structural analysis of the powder data. Single crystals were also used for birefringence measurements, in order to investigate structural phase transitions. The fabrication of both polycrystalline and single-crystal samples allowed a combination of different techniques to be used.

2.2 Polycrystalline and Single Crystal Sample Synthesis

The growth of all polycrystalline and single crystals was carried out in 25/50 ml platinum crucibles with tight-fitting lids, unless otherwise stated. These were chosen as platinum is thermally and mechanically stable at the high temperatures needed, and also is chemically inert to the charges when they are in their molten state. Furnace resistance heating was employed with the crucible always placed in a position deemed to be the optimum place to ensure that a uniform temperature gradient was achieved across it. Before sample synthesis was attempted, a temperature calibration was conducted on the furnace. The actual sample temperature and furnace temperature readings were directly compared to see if any disparity existed. This was achieved with the use of an independent calibrated Comark digital thermometer positioned at the sample position within the furnace. From the resulting calibration curve (Figure 2.01), corrections were applied to temperature settings. The same furnace was used throughout the sample synthesis.

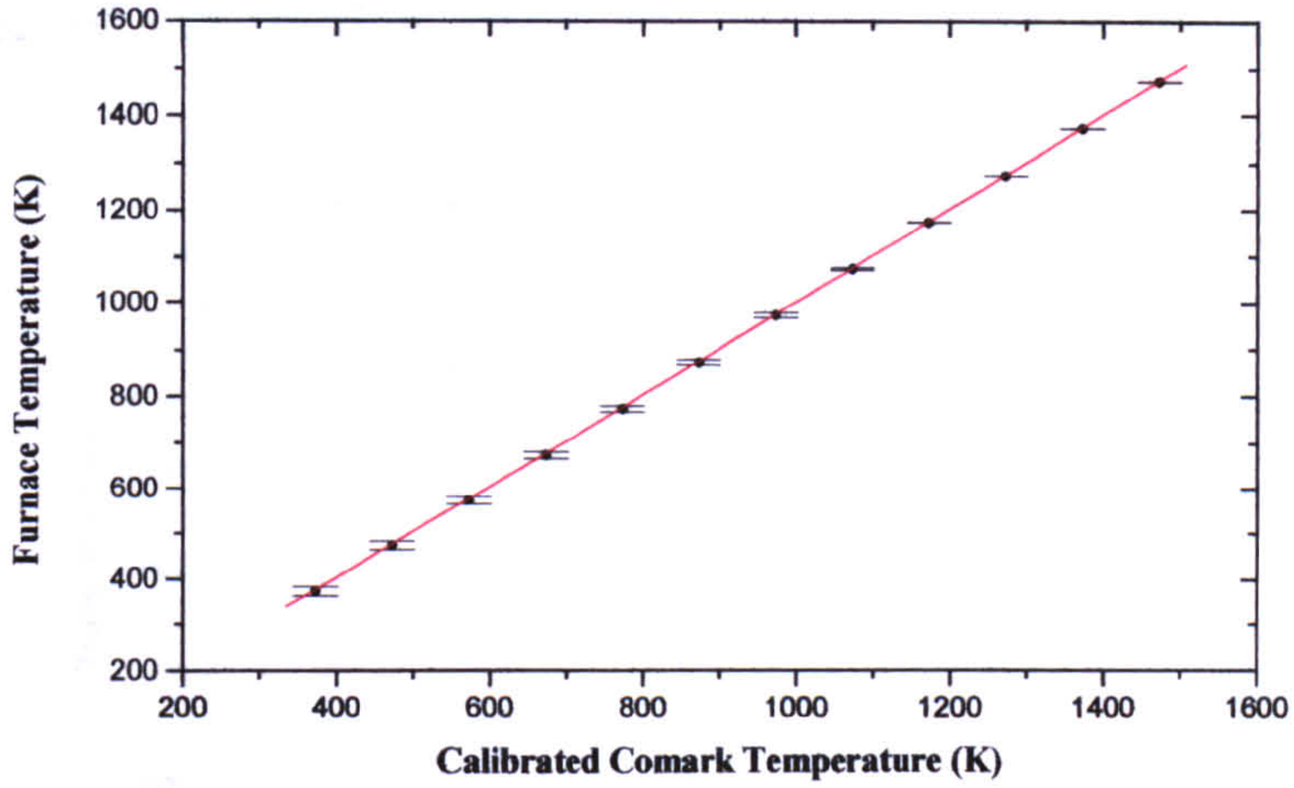

Figure 2.01. Calibration curve for sample temperature and furnace temperature reading.

2.2.1 Polycrystalline Synthesis of NBT

Polycrystalline compounds were prepared by solid state reaction of the starting reagents, Na_2CO_3, Bi_2O_3, and TiO_2, all of analytical reagent grade (99.9 % purity). Following the chemical reaction represented by:

$$Bi_2O_3 + 4TiO_2 + Na_2CO_3 \rightarrow 4Na_{0.5}Bi_{0.5}TiO_3 + CO_2$$

stoichiometric amounts were weighed and mechanically mixed. To achieve a thorough mix and eliminate any aggregates, wet ball-milling was employed. Following standard ceramic mixing methods[1], distilled water (approximately 200 % of the volume of powder) was added to the weighed mixture. In order to achieve an efficient milling action, a ratio of 1:3 of milling media to alumina grinding balls was used. The sample was milled for 18 hours, and oven-dried until all water had evaporated. The sample was ground, sieved to < 38 μm and calcined. Ground powders were calcined in closed platinum crucibles for 6 hours at 1073 K, then reground and calcined under identical conditions to enhance homogeneity.

Following work by Smolenskii *et al.*[2], samples were prepared by mixing as above and firing in air at 1353 K for 6 hours. The furnace cycle is shown in Figure 2.02 (Cycle 1). The resulting material appeared non-crystalline and consisted of small white (presumably Na_2CO_3 & TiO_2) and yellow (Bi_2O_3) regions intermixed in the sample bulk. The sample was therefore reground and re-fired at a higher temperature (1373 K) for the same period and cooled at slower rate. A complete reaction was deemed to have occurred, as the product had an uniform crystalline appearance. Characterisation of the

sample was carried out (section 2.3). The furnace cycle is shown in Figure 2.02 (Cycle 2).

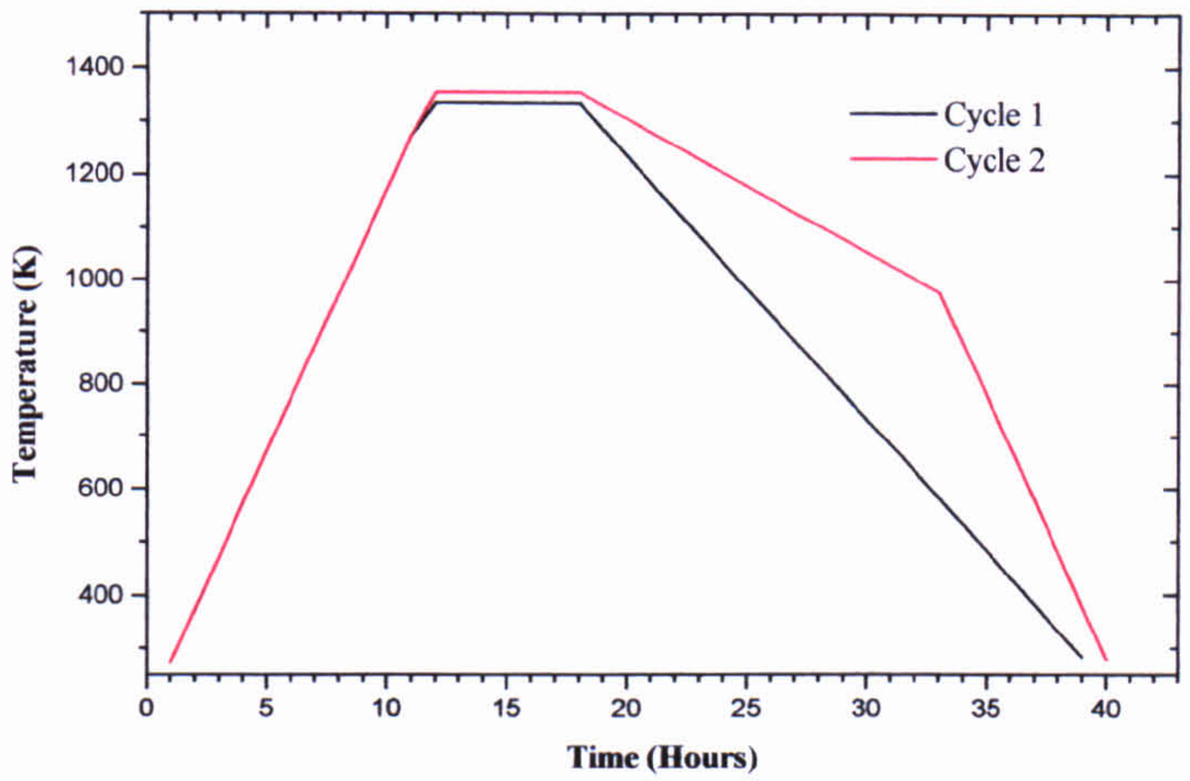

Figure 2.02. Furnace cycles for the fabrication of polycrystalline samples of NBT.

2.2.2 Single Crystal Synthesis of NBT

Two methods of crystal preparation were investigated in order to ascertain the optimum synthesis conditions. Firstly, direct synthesis from oxides and carbonates was tried, and secondly, previously synthesised titanates (section 2.2.1) were utilised. Single crystals of NBT were previously obtained by a flux technique[3] as well as by the Czochralski[4] method. It has been reported[5] that the presence of the various phase transitions in NBT complicates the growth of high-quality crystals by the Czochralski method. So an attempt was made to grow NBT crystals via spontaneous bulk crystallisation, which in many cases enables growing perfect crystals in small dimensions less subject to both thermal shock and the disintegrating action of first-order phase transitions. Different flux methods (*A*-*C*) were investigated in order to produce the best quality crystals.

Flux Method - A

Emel'yanov *et al.*[5] reported the growth of single crystals of NBT from a molten solution in the system $NaF\text{-}NaVO_3\text{-}Na_{0.5}Bi_{0.5}TiO_3$. Their best results were achieved with a charge of the composition $6.5NaF : 2NaVO_3 : 0.5Na_{0.5}Bi_{0.5}TiO_3$ loaded into 50 ml platinum crucibles. The molten solution was soaked between 2-4 hours at 1563-1583 K until complete homogenisation and cooled to 1493 K at the rate of 2 $K.h^{-1}$. After this the mother liquid was decanted off and the crucible with crystals, was furnace-cooled to

room temperature. The method resulted in the production of brown cubic and parallelepiped-shaped crystals up to 3 mm in size.

Using both thoroughly mixed batches of Na_2CO_3, Bi_2O_3 and TiO_2 (of stoichiometric composition relative to NBT) and previously synthesised NBT powders (section 2.2.1), this method was repeated. The furnace cycle chosen for the first run was ramping 200 $K.h^{-1}$ to 1573 K, holding for 3 hours followed by a 2 $K.h^{-1}$ ramp down to 1493 K. The mother liquid was then decanted off, and the remaining solution left to furnace cool. The cooled compound showed very small regions having crystalline form surrounded by the flux matrix. An attempt to separate the extremely small crystallites from the matrix was made by boiling the compound in 20 % nitric acid. This treatment was used as NBT crystals are not soluble in nitric acid[6], but proved unsuccessful.

It was thought that the crystals had not had sufficient time to form and grow, therefore the method was repeated with an extended dwell period and slower cooling rate. The second run cycle was as follows; ramp up at 200 $K.h^{-1}$ to 1583 K dwell for 6 hours, cooling to 1493 K at 1 $K.h^{-1}$. The cooled compound showed a similar appearance as that of the first run and after boiling the compound in 20 % and then 40 % nitric acid, small crystalline regions were again obtained, intermixed with the matrix. Subsequent x-ray analysis on samples from both runs confirmed the (small) presence of a perovskite phase within the mainly non-crystalline sample bulk.

Flux Method - B

Park *et al.*[3] reported the preparation of NBT crystals via the flux technique. A batch of stoichiometric NBT with a 20 % weight excess of Bi_2O_3 and Na_2CO_3 as a self-flux (to compensate for any compositional change) was melted and left at 1473 K for 5 hours followed by a slow cooling rate of 5 $K.h^{-1}$ to 1023 K. Dark brown cuboidal crystals with a maximum size of 4 × 4 × 4 mm were produced. This method was attempted and fired under identical conditions. Very small yellow and brown cubodial crystals were obtained. The surfaces of the crystals possessed traces of the matrix that could not be removed by acid or polishing (due to the small crystal sizes involved). X-ray diffraction patterns showed a multiphase composition.

Flux Method - C

Flux method *B*, although successful, produced extremely small crystals that could not be separated from the flux. It was decided to attempt growth by spontaneous

nucleation, via slow cooling of the melt without any excess components. Tightly sealed platinum crucibles were used in order to minimise any loss of the volatile Bi_2O_3. The thoroughly mixed sample was fired in air at 1573 K for 4 hours. This was followed by a slow cooling rate of 5 $K.h^{-1}$ to 1423 K, held for 2 hours, followed by a further ramping down in temperature of 10 $K.h^{-1}$ to 973 K. A ramping rate of 200 $K.h^{-1}$ to room temperature was then employed. Small well-formed yellow cuboidal (inter-grown) crystals resulted. After initial characterisation (section 2.3) this method was investigated further to find the optimum firing conditions that produced the best quality crystals. Figure 2.03 shows 3 different firing methods used in the growth of crystals via method *C*. The largest crystals with the best optical quality were produced using firing method 3. Yellow crystals were produced with sizes ranging between 0.02-2 mm^3.

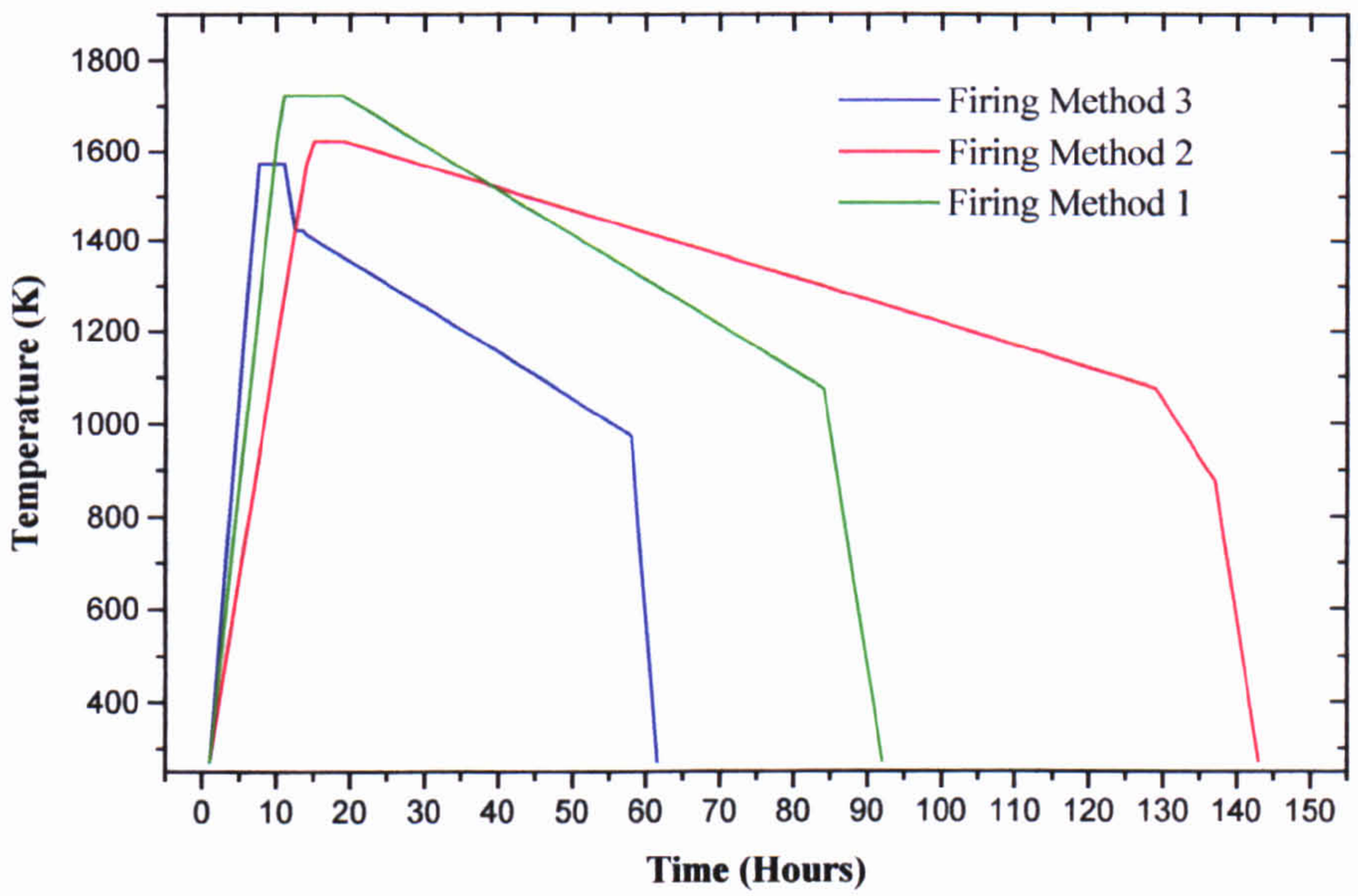

Figure 2.03. Different firing methods used in NBT growth via flux method C.

2.2.3 Polycrystalline and Single Crystal Synthesis of KBT

KBT was prepared using the technique outlined in 2.2.1, incorporating slight modifications to the firing temperatures. Polycrystalline compounds were prepared by solid state reaction of the initial reagents, K_2CO_3, Bi_2O_3, and TiO_2, all of analytical reagent grade. Following the chemical reaction represented by:

$$Bi_2O_3 + 4TiO_2 + K_2CO_3 \rightarrow 4K_{0.5}Bi_{0.5}TiO_3 + CO_2$$

Samples were prepared by firing in air at 1353 K for 6 hours. As with NBT a complete reaction was not realised, as suggested by different coloured regions within the product. The sample was therefore reground and re-fired at a higher temperature (1373 K) for the same period and cooled at slower rate as in section 2.2.1, cycle 2. A complete reaction was deemed to have occurred and characterisation of the sample was carried out (section 2.3).

Within the limited published literature relating to KBT, experiments were only reported on polycrystalline samples. No single crystals of this material had been studied. It was assumed that a similar growth regime to that used for NBT, would result in the successful growth of KBT single crystals. Flux methods *B* and *C* (section 2.2.2) were therefore repeated with KBT constituents as initial products. In flux method *B*, a 20 % weight excess of Bi_2O_3 and K_2CO_3 was used again to compensate for any loss of volatile material. This resulted in a solid mass of material, with no visible crystalline structure. When the solid mass was broken apart, extremely small whisker shaped crystallites where found. All attempts to separate these from the matrix proved unsuccessful. Attempted growth via method *C* resulted in the formation of small embryonic clusters of rectangular shaped crystals embedded at the surface and within the solid matrix mass. These whiskers were very small with an average size of approximately 0.3 × 0.2 × 0.2 mm^3. Energy Dispersive analysis (section 2.3.2) of these crystals identified them as a bismuth titanium oxide.

2.2.4 Polycrystalline and Single Crystal Synthesis of *NKBT*

Polycrystalline samples of the $(Na_{1-x}K_x)_{0.5}Bi_{0.5}TiO_3$, *NKBT*, solid solution range were formed by reacting stoichiometric proportions of Na_2CO_3, K_2CO_3, Bi_2O_3, and TiO_2. Samples were prepared by firing in air at 1373 K for 6 hours as outlined in section 2.2.1. X-ray diffraction studies were carried out on ground powders in order to assess their quality (section 2.3). Single crystals of the series were grown by spontaneous bulk crystallisation via slow cooling of the molten melt. The stoichiometric samples for $x = 0.8, 0.6, 0.5, 0.4$, and 0.2 were thoroughly mixed and fired in air at 1573 K for 4 hours. This was followed by a slow cooling rate of 5 $K.h^{-1}$ to 1423 K, held for 2 hours, followed by a further ramping down in temperature of 10 $K.h^{-1}$ to 973 K. A faster ramping rate of 200 $K.h^{-1}$ to room temperature was then employed. In all cases small well-formed yellow cuboidal crystals resulted.

2.2.5 Isostructural Analogues

The rarity, unusual properties and technological applications of NBT provided the impetus to search for isostructural analogues. Incorporating alternative elements onto the A-site of these materials is restricted by the lack of suitable monovalent and trivalent cations. Following the geometric considerations summarised in section 1.1 and the need for charge-balancing, alternative A-site cation members capable of forming similar perovskite compounds were explored.

The initial approach was first to replace the Na^{1+} with a similar monovalent ion. As silver containing A-site perovskites already exist ($AgNbO_3$ and $AgTaO_3$[7]), and Ag^{1+} has a similar ionic radius to Na^{1+} (Table 2.01), this was considered to be a reasonable replacement. Initially 20 % doping was introduced in replacement of Na^{1+} on the A-site of NBT *i.e.* $(Na_{0.6}Ag_{0.4})_{0.5}Bi_{0.5}TiO_3$. Following the technique outlined in 2.2.1, stoichiometric amounts of the reagents, Ag_2CO_3, Bi_2O_3, and TiO_2, were mixed and fired. The resulting product was a brittle unevenly coloured solid mass. Powder x-ray diffraction analysis revealed a complicated multiphase pattern that could not be indexed. The different firing methods originally carried out for NBT were repeated for this sample. In each case, the sample appeared to have reacted, but it was evident from the x-ray diffraction patterns that no perovskite phase had formed. The procedure was repeated with complete replacement of Ag^{1+} at the Na^{1+} site *i.e.* $Ag_{0.5}Bi_{0.5}TiO_3$ with similar results. This compound has, however, recently be fabricated by Park *et al.*[9], refer to section 2.2.5.1.

The next stage was to try and replace the Bi^{3+} cation with a similar ion. Stoichiometric samples were produced where Sm^{3+} replaced 20 % of the Bi^{3+} *i.e.* $Na_{0.5}(Bi_{0.6}Sm_{0.4})_{0.5}TiO_3$ and where it was replaced fully *i.e.* $Na_{0.5}Sm_{0.5}TiO_3$. Despite many different attempts at varying the firing conditions, the products always appeared non-crystalline and no perovskite phase could be found in subsequent powder x-ray diffraction analysis. The procedure was again repeated with Y^{3+} replacing Bi^{3+}. Again 20 % and 100 % doping was tried, *i.e.* $Na_{0.5}(Bi_{0.6}Y_{0.4})_{0.5}TiO_3$ and $Na_{0.5}Y_{0.5}TiO_3$ respectively. For the 20 % doped sample, following method *C* described in section 2.2.2, small yellow inter-grown cuboidal crystals were obtained. These crystals were of poor optical quality. Powder x-ray diffraction studies on this sample disclosed a orthorhombic perovskite-like phase that could not be indexed. Single crystal diffraction studies were also undertaken on a Brűker SMART diffractometer (section 3.5.1.2) but the x-ray diffraction maxima were split and no unit cell could be found.

Replacing the B-site cation in NBT and KBT was also investigated. Replacement of Ti^{4+} with Zr^{4+} to produce the zirconates $Na_{0.5}Bi_{0.5}ZrO_3$ and $K_{0.5}Bi_{0.5}ZrO_3$ was tried. Different firing conditions and procedures were examined but in each case only resulted in a white solid mass of material. As before, powder x-ray studies showed multiphase patterns in which no perovskite phase was evident and which could not be indexed.

It seems peculiar that NBT and KBT can be formed relatively easily, but incorporating other similar cations into the structure results in unsuccessful formation of these new compounds. As these alternative cations have similar ionic radii and co-ordination geometry they would appear to be reasonable candidates for substitution. From the unsuccessful results, it was concluded that synthesis via a conventional solid-state reaction was not straightforward for formation of these compounds and alternative growth procedures would be needed. Table 2.01 lists the *A*- and *B*-site cations for which substitution was tried. Ionic radii are taken from Shannon[8] and the average radius of the ions on the A-site has been used in the calculation of the tolerance factors.

A-site cation	Ionic Radius (Å)	Compound	Tolerance Factor
Na^{1+}	1.32	NBT	0.85
K^{1+}	1.65	KBT	0.90
Ag^{1+}	1.42	$Ag_{0.5}Bi_{0.5}TiO_3$	0.87
Bi^{3+}	1.31	NBT, KBT	-
Y^{3+}	1.16	$Na_{0.5}Y_{0.5}TiO_3$	0.82
Sm^{3+}	1.22	$Na_{0.5}Sm_{0.5}TiO_3$	0.83
B-site cation			
Ti^{4+}	0.88	NBT, KBT	-
Zr^{4+}	0.98	$Na_{0.5}Bi_{0.5}ZrO_3$	0.81
		$K_{0.5}Bi_{0.5}ZrO_3$	0.86

Table 2.01. Attempted synthesis of various A-site substituted perovskite compounds within this study.

2.2.5.1 High-pressure High-temperature Synthesis

A recently published paper[9] details for the first time the synthesis of the A-site substituted $Ag_{0.5}Bi_{0.5}TiO_3$. This compound was synthesised at 14-14.5 GPa and 1273 K using a uniaxial split-sphere anvil. It is noted in this paper that the poor thermal stability of silver oxides[10] limits the reaction temperatures that can be used and consequently

prevents synthesis via conventional solid-state reaction methods (as attempted in 2.2.5). Using similar techniques the perovskites $(Ca_{0.5}Nd_{0.25}Ag_{0.25})TiO_3$ and $(NdAg)Ti_2O_6$[11], which also both contain Ag^{1+} on the A-site, have been formed.

The realisation of a high-pressure high-temperature synthesis method that allows the addition of cations such as Ag^{1+} into the perovskite structure suggests that this may be an effective route in synthesising other compounds in the A-site substituted series. With this in mind an attempt was made to fabricate the following A-site substituted complex perovskites: Sodium Yttrium Titanate, $Na_{0.5}Y_{0.5}TiO_3$, (NYT); Sodium Samarium Titanate, $Na_{0.5}Sm_{0.5}TiO_3$, (NST); Potassium Bismuth Zirconate, $K_{0.5}Bi_{0.5}ZrO_3$, (KBZ); and Potassium Bismuth Titanate, $K_{0.5}Bi_{0.5}TiO_3$, (KBT). KBT was included in the hope of obtaining single crystals. Synthesis attempts were conducted by T. Nakaya[12] at the department of Geosciences State University of New York, Stony Brook. Compounds were synthesised at 4.4 GPa and 1200 K using a uniaxial split-sphere anvil. NST, KBZ and KBT fabrication attempts resulted in extremely small volume powder samples being produced. Subsequent x-ray analysis showed multiphase patterns and no perovskite phases were clearly evident. NYT fabrication resulted in extremely small crystals being formed. Powder x-ray analysis revealed a multiphase pattern and the presence of a perovskite phase. Single crystal diffraction data were taken but no unit cell could be found. High-pressure high-temperature fabrications undertaken here, were not extremely successful, and due to the extremely small volumes of final products, analysis was made difficult. For future growth attempts, higher pressures (around 14 GPa, as used in the production of $Ag_{0.5}Bi_{0.}5TiO_3$[9]) may be more beneficial (higher pressures were not used due to a problem with the pressure apparatus at that time).

2.3 Sample Characterisation

In order to assess the quality of the synthesised materials different characterisation techniques have been employed. Initially x-ray powder diffraction (XRPD) patterns were collected and analysis performed in order to confirm the correct perovskite phases had been formed. Energy Dispersive X-ray Analysis was also carried out to determine quantitative composition ratios for the different species incorporated in the materials. An optical examination was also conducted on single crystals grown in this study.

2.3.1 X-ray Powder Diffraction Analysis

Polycrystalline samples of each material were finely ground for analysis and XRPD patterns taken. Where single crystals had been produced several were chosen from each batch that showed sharp extinction, these were finely ground and XRPD patterns taken. XRPD data on NBT and KBT were recorded with a Brűker D5005 diffractometer with samples pressed into aluminium holders. NBT was scanned through a 2θ-range of 10-90° and KBT through a 2θ-range of 15-90°. A 0.02° step size and CuK_α radiation was used for both collections. Note the extra peaks in the patterns correspond to aluminium diffraction peaks produced from the sample holder. Figures 2.04 (a) and (b) show the XRPD patterns for NBT (grown via flux method C, section 2.2.2) and KBT respectively. The corresponding patterns given in the Powder Diffraction File[13] for NBT[14] and KBT[15], are also included for comparison. As can be seen, an excellent match is obtained, primarily indicating that fabrication of the compounds was successful.

Concerning the NKBT solid solution range, no powder diffraction patterns appear in the Powder Diffraction File and so unlike NBT and KBT direct comparisons could not be made. However it was assumed that the solid solutions have similar structures to NBT or KBT and therefore give similar patterns. This is based on the assumption that if the sum of the respective ionic radii are reasonably similar, the d-spacing will follow suit and if the relative atomic numbers are similar there will also be similarities between the relative intensities of peaks. Therefore patterns are expected to vary continuously from one end member to the other. XRPD data on NKBT were recorded on a Stöe STADI 2P automatic powder diffractometer working in transmission mode and fitted with a curved position sensitive detector. Each powder (including NBT and KBT for comparison) was scanned through a 2θ-range of 20-80° with a step size of 0.01° using CuK_α radiation. Figure 2.04 (c) shows the diffraction patterns taken for the NKBT solid solution range.

2.3.2 Energy Dispersive X-ray Analysis

Energy Dispersive X-ray Analysis (EDX) was carried out on the successfully fabricated samples in order to determine their elemental compositions. A JEOL JSM-6100 high resolution Scanning Electron Microscope (SEM) with a LINK ISIS[16] analyser system was used. When the electron beam of the SEM impinges the bulk of a sample, characteristic x-rays of the species present are emitted. Detection of these x-rays permits analysis of the material's chemical composition.

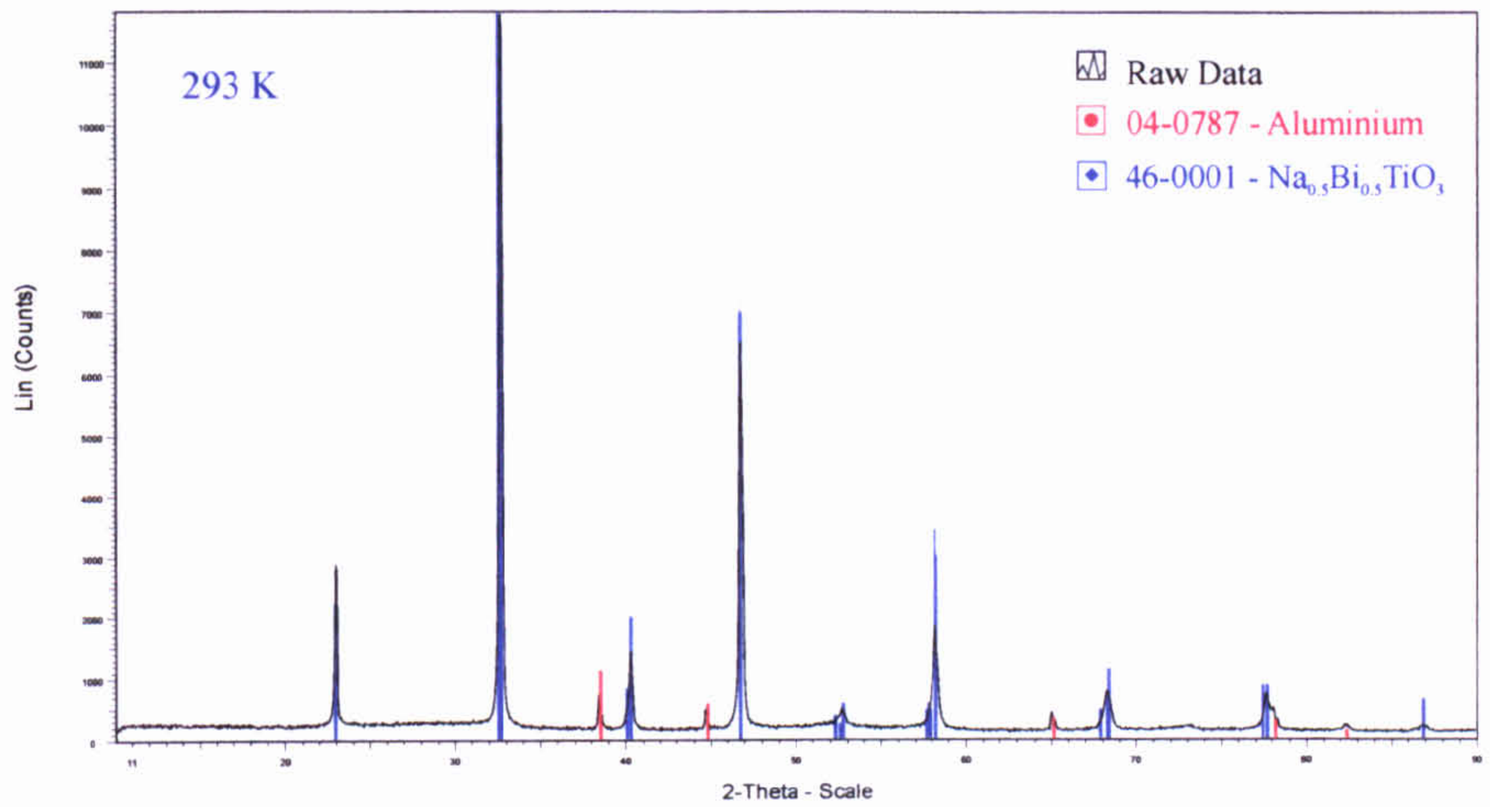

(a)

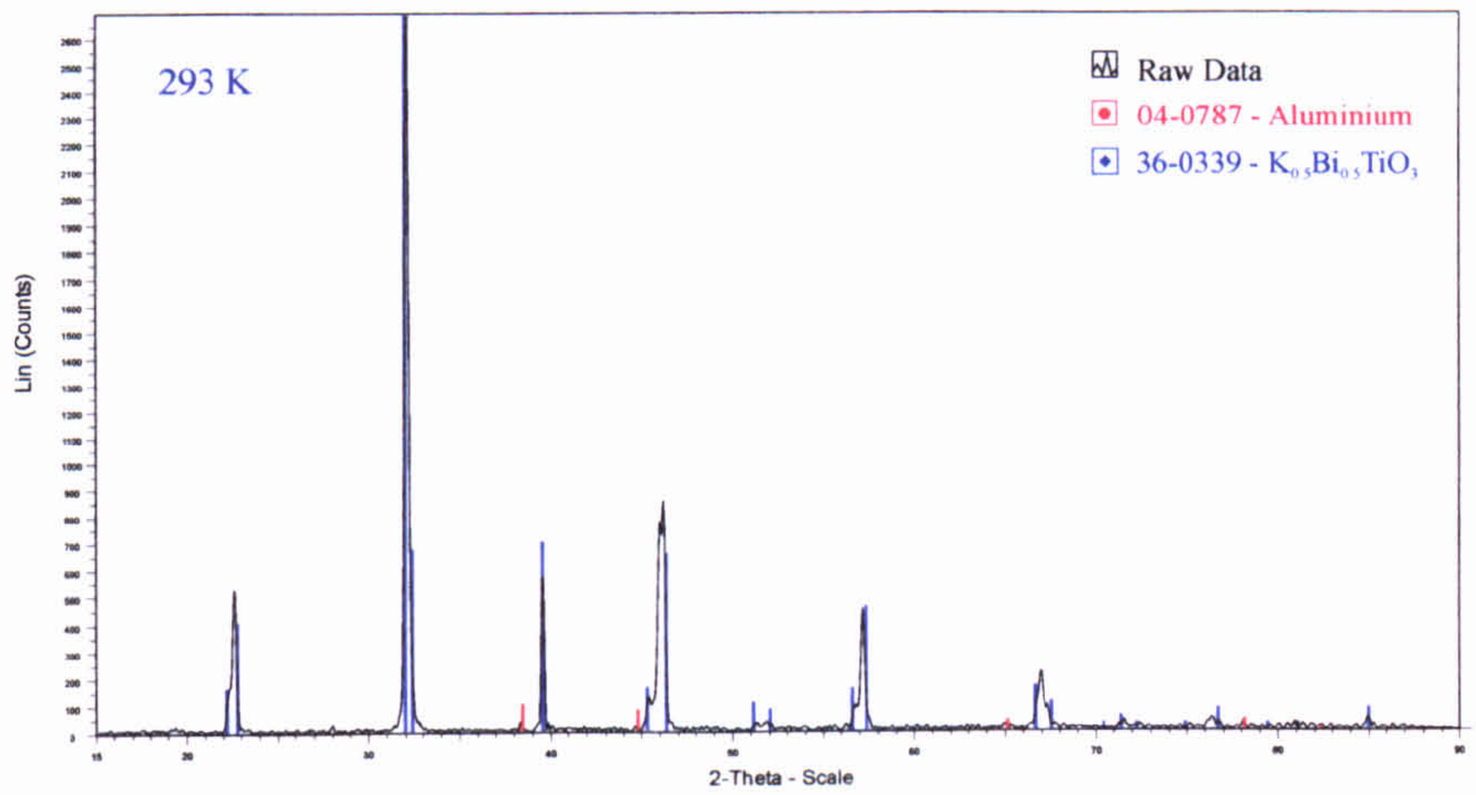

(b)

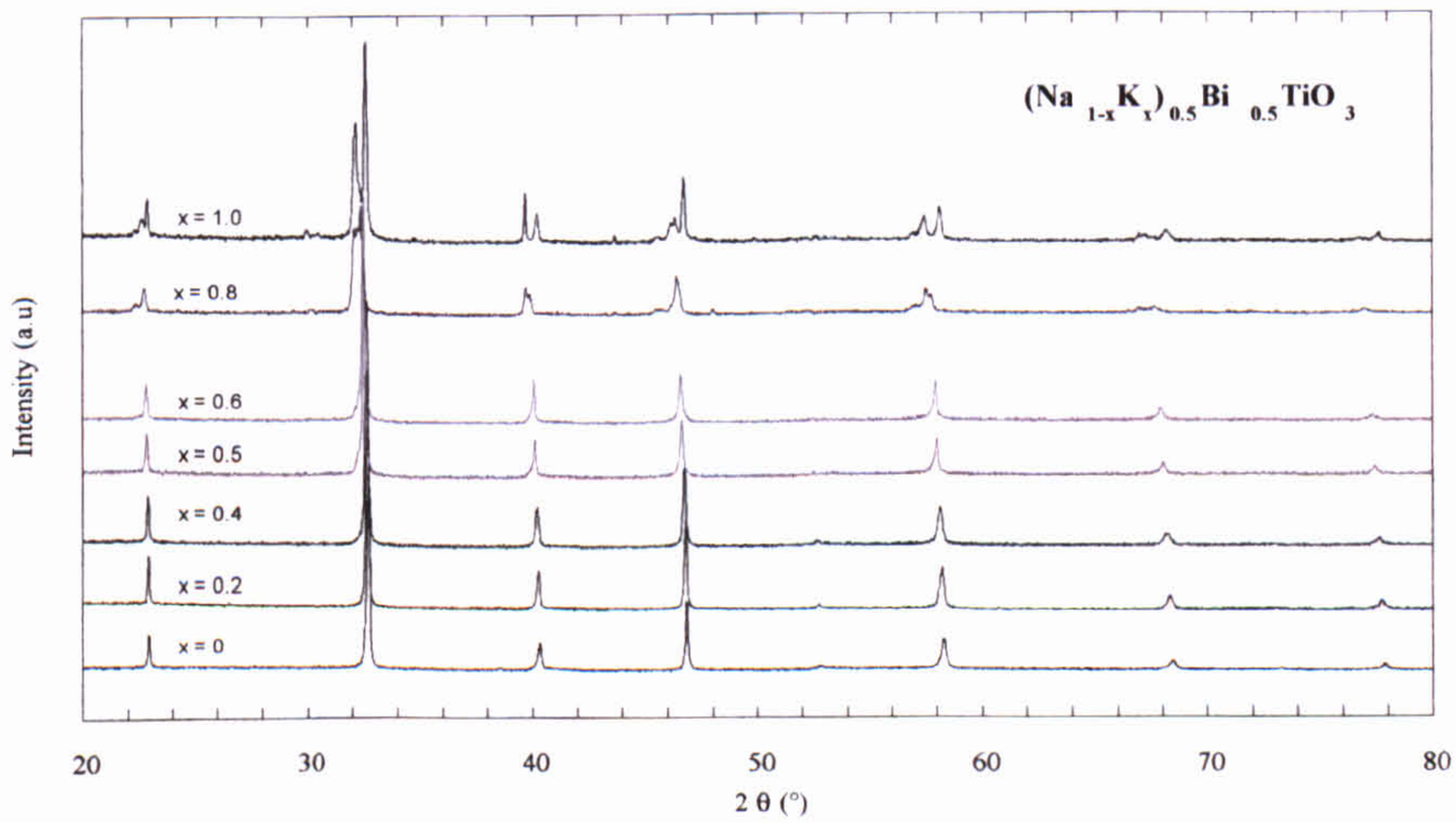

(c)

Figure 2.04. *X-ray diffraction profiles of (a) NBT and (b) KBT, taken on a Brűker D5005 diffractometer. Red lines represent the peak positions of aluminium (PDF Nº 04-0787) and blue lines represent the peak positions for NBT (PDF Nº 46-001) and KBT (PDF Nº 36-0339) taken from Powder Diffraction File. (c) X-ray powder diffraction profiles for* $(Na_{1-x}K_x)_{0.5}Bi_{0.5}TiO_3$.

The x-ray peak positions along the energy scale identify the elements present. With appropriate analysis and processing software carried out using an LINK ISIS quantitative analyser and detector (interfaced with the SEM) and, after the application of appropriate correction factors based on atomic numbers Z, x-ray absorption A, and fluorescence F, (ZAF correction) quantitative analysis can be achieved. The percentage concentrations of each element present can then be obtained.

Crystals that extinguished sharply in each batch were chosen and polished using progressively finer lapping paper to a 1 μm finish. These were mounted on standard aluminium SEM stubs. In the case of KBT, the polycrystalline powder was pressed into a disc to give a uniform surface and also polished to a 1 μm finish. An electron accelerating voltage of 15 kV was used (as the Bi L_α = 10.839 keV) with the sample-emitter working distance set at 16 mm. After calibration using a manganese standard, analysis was undertaken. Six different spot and area measurements (chosen at random) were made across the surface of each sample and average values taken. The EDX spectra for NBT and $(Na_{0.6}K_{0.4})_{0.5}Bi_{0.5}TiO_3$ are shown in Figures 2.05 (a) and (b) respectively. Further experimental details of EDX analysis methods can be found elsewhere[17].

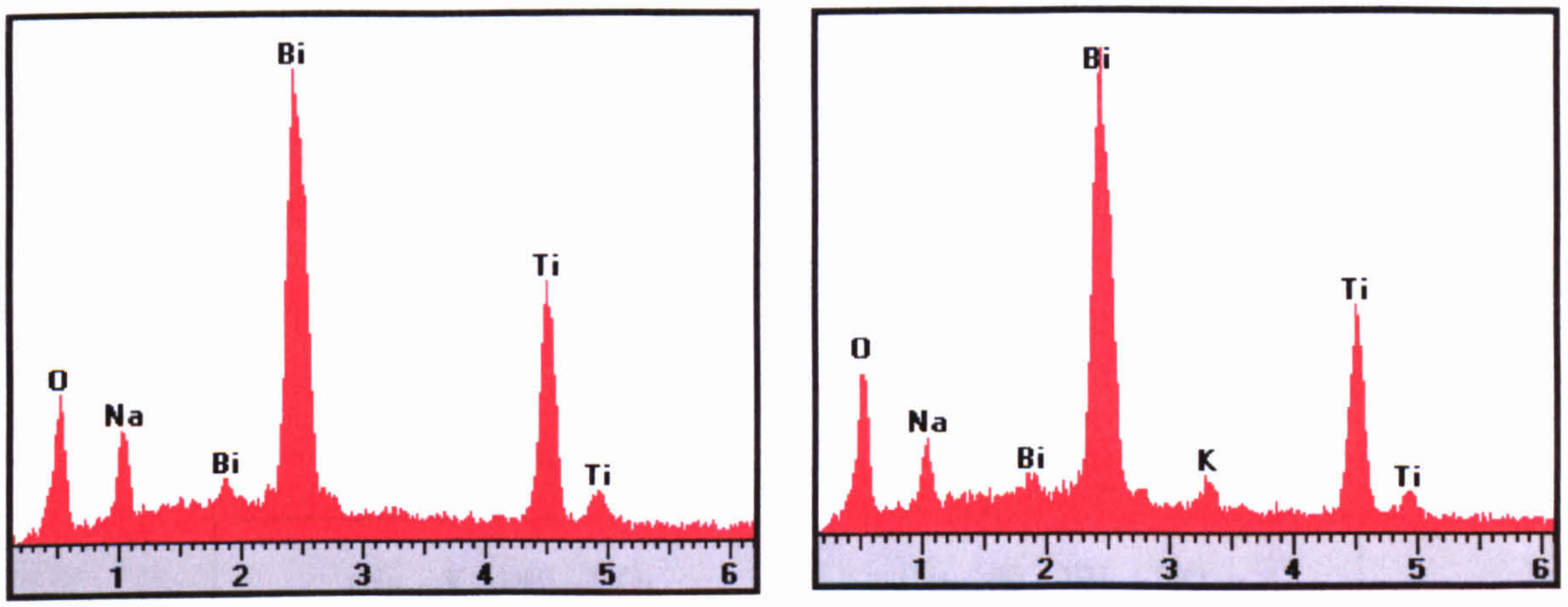

Figure 2.05. EDX spectra for (a) $Na_{0.5}Bi_{0.5}TiO_3$ and (b) $(Na_{0.6}K_{0.4})_{0.5}Bi_{0.5}TiO_3$.

These results are summarised in Table 2.02 for NBT. The derived composition ratios of the constituent elements in the NKBT solid solution range are given in Table 2.03.

NBT Flux Method C – (Section 2.2.2)	Atomic Fraction of Constituent Elements			
	Na	Bi	Ti	O
1	9.29	12.42	21.46	56.83
2	8.91	11.20	19.10	60.79
3	9.24	12.78	21.34	56.64
4	9.31	10.15	14.40	66.14
5	9.24	11.64	21.01	58.11
6	9.83	9.80	20.03	60.34
Mean	**9.3 (3)**	**11 (1)**	**19 (2)**	**59 (3)**

Table2.02. EDX analysis of chemical composition for NBT (figures in brackets represent the standard deviations).

From the Table 2.03 it can be seen that the ratio of elements are in the correct proportion (taking into account a minimum overall error of approximately 5 %). The compositions thus determined can be used to provide the initial starting values for use in structural refinements.

Nominal Ratio in Starting Composition	Averaged EDX Composition
$Na_{0.5}Bi_{0.5}TiO_3$	$Na_{0.47}Bi_{0.57}Ti_{0.98}O_{2.99}$
$(Na_{0.4}K_{0.1})Bi_{0.5}TiO_3$	$(Na_{0.36}K_{0.10})Bi_{0\,65}Ti_{0.99}O_{2.90}$
$(Na_{0.3}K_{0.2})Bi_{0.5}TiO_3$	$(Na_{0.28}K_{0.19})Bi_{0.57}Ti_{0.95}O_{3.10}$
$(Na_{0.25}K_{0.25})Bi_{0.5}TiO_3$	$(Na_{0.24}K_{0.25})Bi_{0.58}TiO_{2.95}$
$(Na_{0.2}K_{0.3})Bi_{0.5}TiO_3$	$(Na_{0.2}K_{0.27})Bi_{0.46}Ti_{0.90}O_{3.20}$
$(Na_{0.1}K_{0.4})Bi_{0.5}TiO_3$	$(Na_{0.08}K_{0.38})Bi_{0.55}Ti_{1.03}O_{2.95}$
$K_{0.5}Bi_{0.5}TiO_3$	$K_{0.46}Bi_{0.54}TiO_3$

Table 2.03 Energy Dispersive X-ray Analysis of Chemical Composition for NKBT.

2.3.3 Optical Examination

An optical examination of all crystals grown was undertaken. Crystals may be grouped, optically, under the headings, isotropic and anisotropic. All crystals belonging to the cubic system, are optically isotropic *i.e.* the refractive index is independent of the direction of the light incident upon it. Non-cubic crystals exhibit a dependence on direction in their interaction with light. Anisotropic crystals are divided into two groups: uniaxial, which have one optically isotropic section and include the tetragonal, hexagonal and trigonal crystal systems, and biaxial, which have two optically isotropic sections and belong to the orthorhombic, monoclinic and triclinic crystal systems.

The optical properties of all crystals were studied using an Olympus SZ-PT polarising microscope. The pale yellow crystals of NBT (section 2.2.2, flux method-C) consisted of individual isolated cuboids and fragments ranging in size between 0.02-2 mm^3. Viewing the specimens firstly in plane polarised light at low magnification, parallelepiped and cuboidal shapes were observed. As these specimens were rotated some fragments showed no noticeable change in appearance, the majority of specimens however showed a marked change in relief (*i.e.* the extent to which they stand out from the background). This change in relief is caused by the variation of the refractive index with vibration direction, and this observation confirms that this material was neither amorphous nor cubic. Viewing NBT specimens between crossed polars, most of the samples showed up light or coloured against the dark background. When the specimens were rotated the majority changed alternately from bright to dark (extinguished). The variation of appearance with sample orientation confirms that all are anisotropic, and therefore crystalline and non-cubic. In smaller crystals/fragments the extinction was sharp but the larger crystals showed a wavy extinction, indicating twinning or strain.

The crystals forming the NKBT solid solution were optically examined with the same method as that used for NBT. All crystals showed similar characteristics and these are summarised in Table 2.04. Figure 2.06 shows digital images taken of the crystals, with the exceptions of $(Na_{0.2}\ K_{0.8})_{0.5}Bi_{0.5}TiO_3$ which were extremely small and KBT (as no single crystals had been successfully produced). Note the dark brown NBT crystal Figure 2.06 (a), was obtained from K. Roleder[18], a collaborator in Poland.

Crystal Composition	Morphology	Colour	Size Range	Transparency
$Na_{0.5}Bi_{0.5}TiO_3$†	Cuboid, parallelepiped Shiny surface	Pale yellow	0.02-2 mm^3	Highly transparent
$Na_{0.5}Bi_{0.5}TiO_3$‡	Cubic parallelepiped Shiny surface	Dark brown	0.5-3 mm^3	Slightly transparent
$(Na_{0.8}K_{0.2})_{0.5}Bi_{0.5}TiO_3$	Cuboid, parallelepiped Shiny surface	Bright yellow	1-3 mm^3	Highly transparent
$(Na_{0.6}K_{0.4})_{0.5}Bi_{0.5}TiO_3$	Cuboid, parallelepiped Shiny surface	yellow/brown	0.02-2 mm^3	Highly transparent
$(Na_{0.5}K_{0.5})_{0.5}Bi_{0.5}TiO_3$	Cuboid, parallelepiped Shiny surface	Light brown	1-2 mm^3	Transparent (milky)
$(Na_{0.4}K_{0.6})_{0.5}Bi_{0.5}TiO_3$	Cuboid, parallelepiped Shiny surface	Golden yellow	0.02-2 mm^3	Transparent (milky)
$(Na_{0.2}K_{0.8})_{0.5}Bi_{0.5}TiO_3$	parallelepiped Shiny surface	Straw-yellow	0.02-0.1 mm^3	Transparent (milky)

Table 2.04. ***Properties of NBT and Solid solution single crystals; NBT† signifies growth via flux method-C (section 2.2.2); NBT‡ signifies crystals grown by Polish group.***

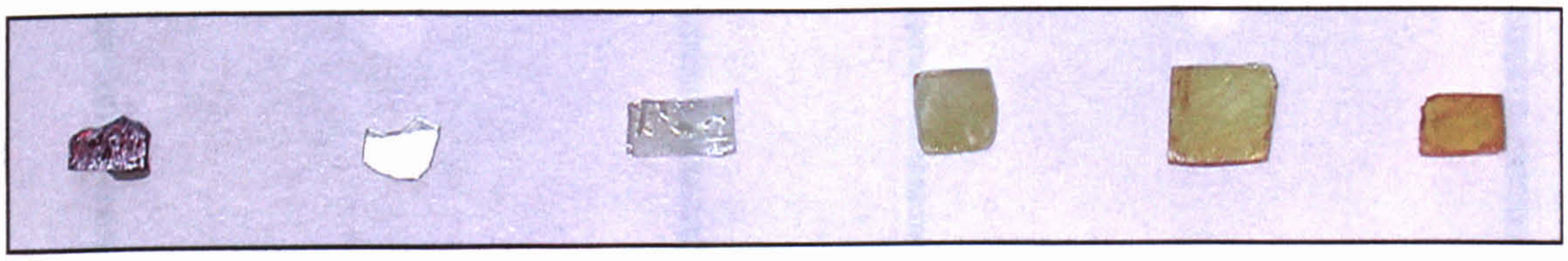

(a) (b) (c) (d) (e) (f)

Figure 2.06. ***Digital images of NKBT (a) $Na_{0.5}Bi_{0.5}TiO_3$ (Polish group[18]), (b) $Na_{0.5}Bi_{0.5}TiO_3$ flux method C section 2.2.2), (c) $(Na_{0.8}K_{0.2})_{0.5}Bi_{0.5}TiO_3$ (d) $(Na_{0.6}K_{0.4})_{0.5}Bi_{0.5}TiO_3$ (e) $(Na_{0.5}K_{0.5})_{0.5}Bi_{0.5}TiO_3$, (f) $(Na_{0.4}K_{0.6})_{0.5}Bi_{0.5}TiO_3$.***

2.3.4 X-ray Diffuse Scattering

X-ray diffuse scattering refers to diffraction from materials that are essentially crystalline but which have structural defects, which destroy the completely regular arrangement of atoms of the perfect crystal. For such crystals, the diffraction pattern will consist of two components; a set of sharp diffraction peaks attributed to the underlying regularity of the crystal lattice, and a weaker diffuse scattering which can be regarded as due to the departures from regularity *i.e.* the disorder. Materials possessing structural disorder will give diffraction patterns showing varying degrees of diffuseness. Diffuse

effects generally occur as planes or rods in reciprocal space producing streaks on x-ray photographs or charge-coupled device (CCD) images. Further information on diffuse x-ray scattering and models of disorder can be found elsewhere[19]. Preliminary x-ray scattering experiments were conducted on NBT to see if diffuse scattering associated with Na/Bi substitutional disorder was present. Figures 2.07 (a) and (b) show Laue photographs taken in reflection and transmission respectively (taken by F. Wondre[20]). Figure 2.07 (c), shows a CCD image of NBT, using MoK_α radiation, which has been enhanced in (d) for greater detail (taken by R. Welberry[21]). The x-ray scattering patterns show areas of diffuse scattering around Bragg peaks and reveal clearly defined streaks. This indicates short-range order is present in NBT. Such short-range order may express the preference of a Na to neighbour another Na, rather than Bi, for example. Some evidence of this was offered by preliminary Transmission Electron Microscopy (TEM) experiments on the same samples.

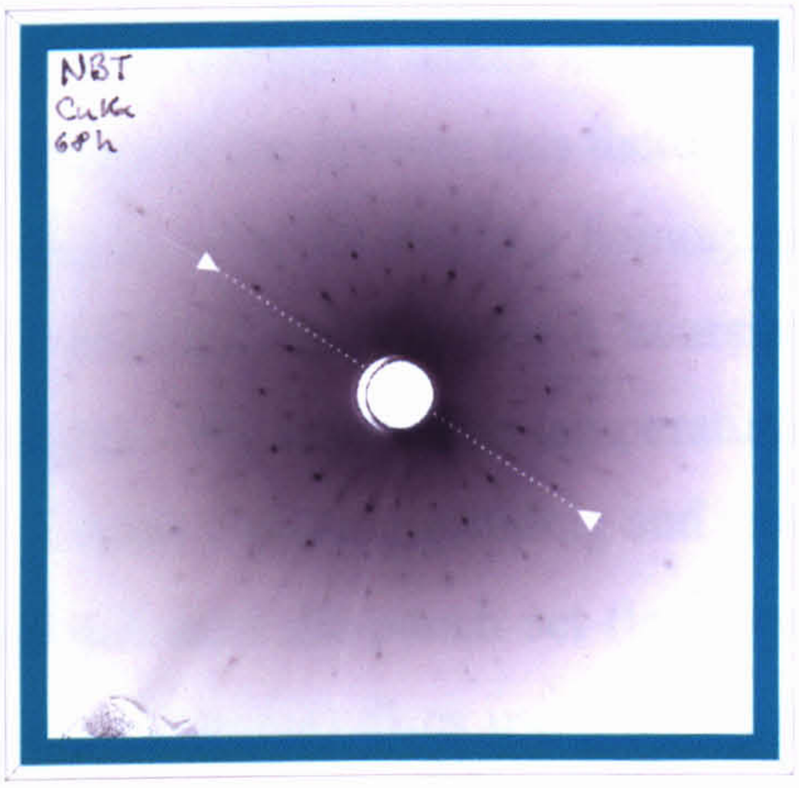

(a)

(b)

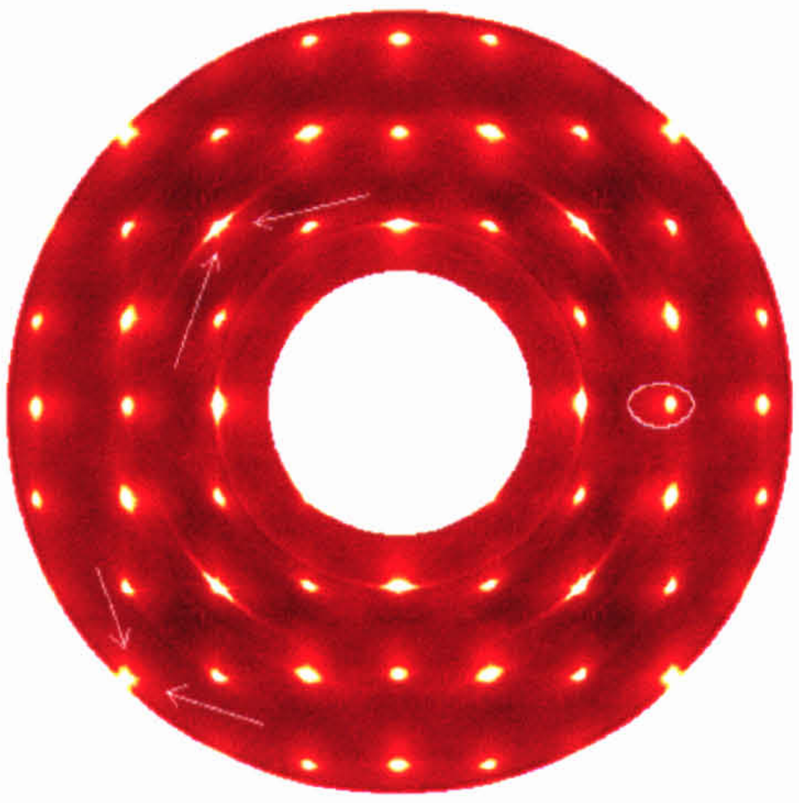

(c)

(d)

Figure 2.07. Laue photographs of NBT in (a) reflection (b) transmission. (c) CCD image of NBT using MoK_α radiation, (d) an enhanced image of (c).

2.4 Ceramic Preparation

Ceramic samples were produced in order to establish a successful fabrication route and to report density measurements on these materials for the first time. Ceramics have the advantage over single crystals that they are relatively easy to produce in any size or shape. It is also relatively simple to change the starting compositions to produce solid solutions in ceramic form, whereas crystal growth may be a more complicated process.

The fabrication process comprises of several stages, which are summed up in Figure 2.08. The starting materials consisted of reagent-grade powders (99.9 % purity) of Na_2CO_3, K_2CO_3, Bi_2O_3 and TiO_2. Stoichiometric amounts were weighed and mechanically mixed. To achieve a thorough mix and eliminate any aggregates, wet ball-milling was employed. The wet-ball milling process has been outlined in section 2.2.1. Samples were milled for 18 hours, and oven-dried until all water had evaporated. Samples were then ground, sieved to < 38 μm and calcined. The calcination process causes the constituent atoms to redistribute themselves in such a way as to minimise the free energy of the system; this thereby limits the redistribution that must occur during the sintering in order to obtain a homogeneous sample. Ground powders were calcined in closed alumina crucibles for 6 hours at 1073 K reground and calcined under identical conditions. The calcination temperature profile is shown in Figure 2.09.

After repeating grinding and sieving stages, powders were uniaxially pressed in a cylindrical steel die/punch set (to a pressure of 3.6×10^7 $N.m^{-2}$) into 16 mm diameter (varying thickness) discs using a 30-ton C-30 hydraulic press. As the discs held shape and had sufficient strength to survive handling, no organic binders were incorporated. There were visible signs of laminated regions within the samples so it was decided to press the discs isostatically. This method can give highly uniform densities, without laminations. Discs were sealed in polythene sheaths and isostatically pressed in water (to a pressure of 1.2×10^9 $N.m^{-2}$) using a Riken Kiki bench press.

The pressed discs were sintered at 1473 K for 4 hours. Sintering is the consolidation of the compacted powder into a denser structure on heating. On sintering, the density increases, with shrinkage occurring as the porosity is reduced. The sintering profile is shown in Figure 2.09. As all samples contained the volatile constituent bismuth oxide, a triple crucible method was used to reduce any loss and retain this oxide at high temperatures. This consisted of placing the disc in a closed alumina crucible surrounded by two upturned larger crucibles. Raw mixed powder containing a 10 % excess of

bismuth oxide was placed in the spaces between crucibles, in effect, creating a sealed environment. The experimental set-up is shown in Figure 2.10. Detailed descriptions of ceramic production methods can be found elsewhere[1,22]. Finally the sintered ceramics were ground and polished using progressively finer lapping papers to a finish of 5 μm.

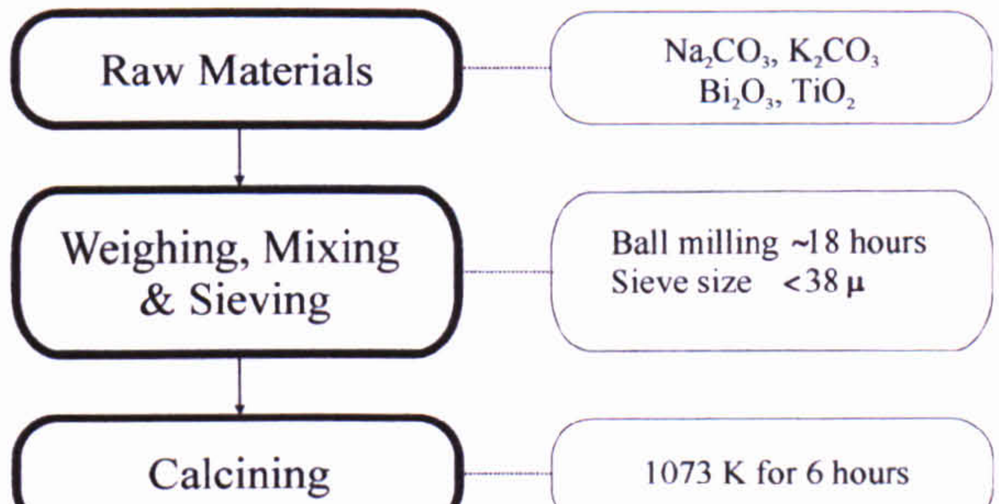

Figure 2.08. Flow chart outlining ceramic preparation and production.

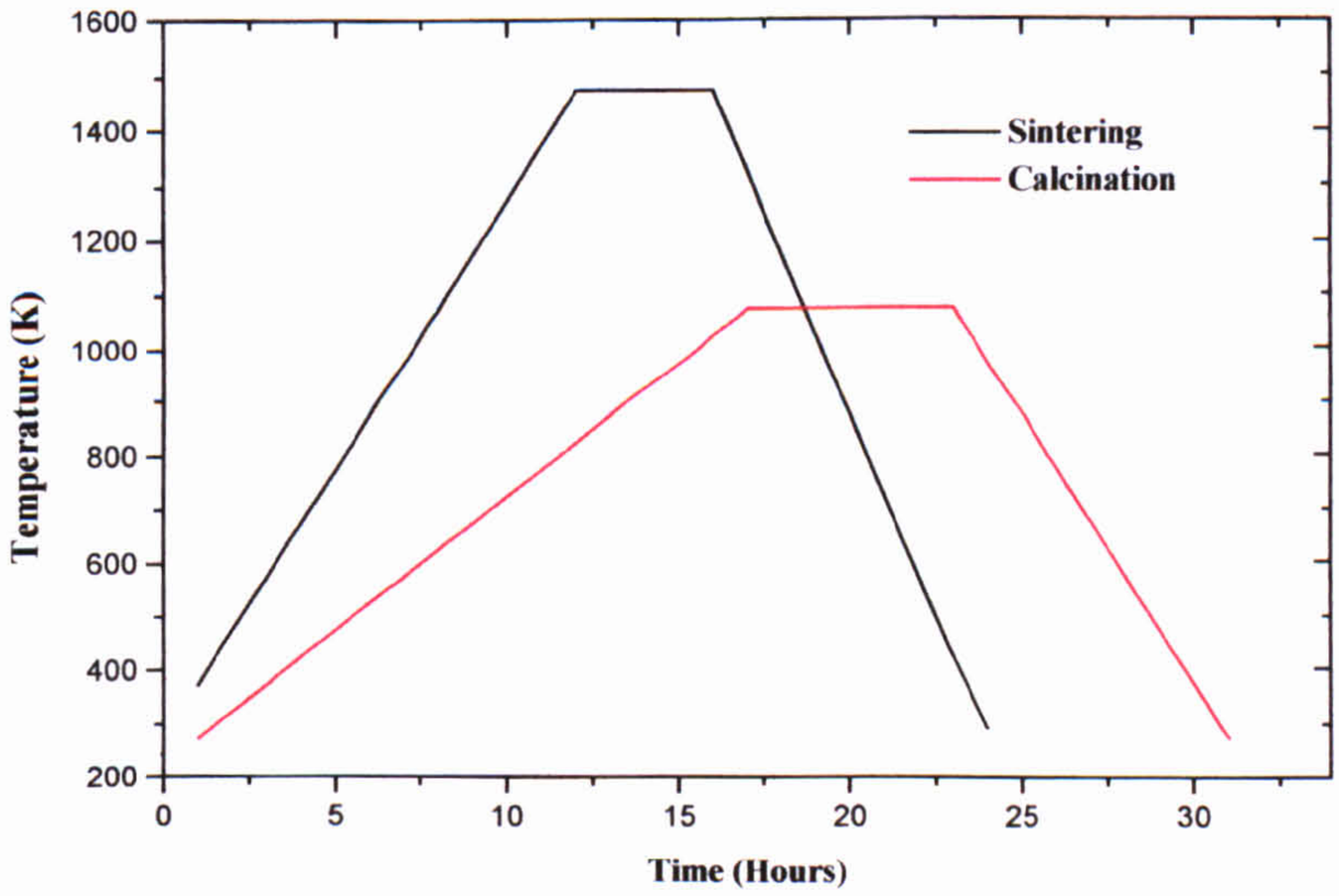

Figure 2.09. Sintering and Calcination profiles for ceramics.

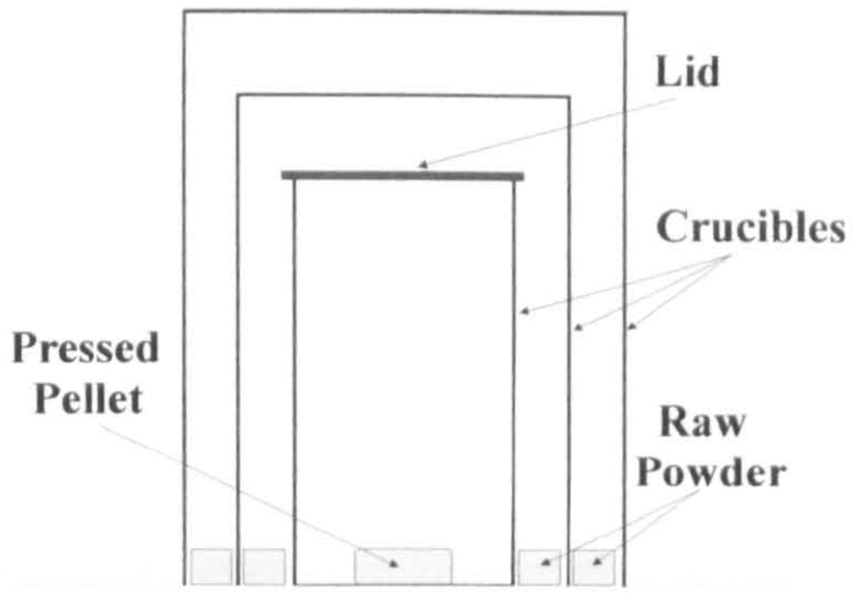

Figure 2.10. Triple crucible method used for sintering of ceramic.

2.4.1 Ceramic Density Measurements

Density measurements of ceramics were made with a digital balance (Precisa 125A), using standard hydrostatic techniques, which was possible because the water absorbed was negligible during immersion for approximately 5 minutes. Samples were weighed first in air and then placed in a pan suspended in distilled water so that their weight on displacement could be found. The temperature was recorded so that a correction could be applied. The density of each sample ρ_s was calculated using the following equation:

$$\rho_s = \frac{W_d \rho_w - W_w \rho_a}{W_d - W_w} \tag{2-1}$$

where ρ_w and ρ_a are the densities of the water and air at the measured temperature respectively (taken from Handbook of Chemistry and Physics[23]), W_d is the dry weight of the sample in air and W_w is the wet weight of the sample immersed in water. For each sample, four measurements were taken and averaged.

NBT ceramics were sintered for the same period at four different temperatures between 1398-1473 K in an air atmosphere. Theoretical densities were calculated directly from room temperature neutron diffraction results (section 3.3.4). This gave a direct measure of the ceramic density and porosity within each sample. Table 2.05 lists the sintering temperatures and density/porosity measurements for NBT. Table 2.06 lists the density/porosity measurements for the $(Na_{1-x}K_x)_{0.5}Bi_{0.5}TiO_3$ ceramics sintered for four hours at 1473 K.

Sintering Temperature (K)	Sintering Time (hrs)	Sintering Loss (%)	Sintered ρ ($g.cm^{-3}$)	Theoretical ρ ($g.cm^{-3}$)	Density (%)	Porosity (%)
1398	4	2.2	5.210	5.992	86.95	13.05
1423	4	3.0	5.330	5.992	88.95	11.05
1448	4	1.4	5.452	5.992	90.99	9.01
1473	4	1.3	5.769	5.992	96.29	3.71

Table 2.05. Density measurements for NBT ceramics at various sintering temperatures.

Ceramic Composition $(Na_{1-x}K_x)_{0.5}Bi_{0.5}TiO_3$ (x)	Sintering Time (hrs)	Sintering Temperature (K)	Sintered ρ ($g.cm^{-3}$)	Theoretical ρ ($g.cm^{-3}$)	Density (%)	Porosity (%)
0.2	4	1473	5.506	6.020	91.46	8.54
0.4	4	1473	5.626	6.034	93.24	6.76
0.5	4	1473	5.800	6.007	96.55	3.45
0.6	4	1473	5.797	6.035	96.06	3.94
0.8	4	1473	5.617	6.071	92.52	7.48
1.0	4	1473	5.496	5.920	92.84	7.16

Table 2.06. Density measurements for $(Na_{1-x}K_x)_{0.5}Bi_{0.5}TiO_3$ ceramics.

References

[1] Moulson, A. J. & Herbert, J. M. (1990). Electroceramics – Materials, properties & Applications. Chapman and Hall.

[2] Smolenskii, G. A. & Agranovskaya, A. I. (1959). Soviet Physics Solid State 1, 1429.

[3] Park, S. & Chung, S. (1996). J. Am. Ceram. Soc. 79 (5), 1290.

[4] Park, S., Chung S., Kim, I. & Hong, K. (1994). J. Am. Ceram. Soc. 77 (10), 2641.

[5] Emel'yanov, S. M., Raevskii, I. P., Smotrakov, V. G. & Savenko, F. I. (1985). Inorganic Materials 21, 727.

[6] Bolko, V. & Myl'nikova, I. E. (1961). Soviet Physics Solid State 2 (11), 2428.

[7] Francombe, M. H. & Lewis, B. (1958). Acta Cryst. 11, 175.

[8] Shannon, R. D. (1976). Acta Cryst. A32, 751.

[9] Park, J. -H., Woodward, P. M., Parise, J. B., Reeder, R. J., Lumbomirsky, I. & Stafsudd, O. (1999). Chem. Materials 11, 177.

[10] CRC Handbook of Chemistry & Physic. (1997). 77th Edition.

[11] Park, J. -H., Woodward, P. M., Parise, J. B. (1998). Chem. Materials 10, 3092.

[12] Nagai, T., Department of Geosciences State University of New York, Stony Brook, 11794-2100, USA.

[13] Powder Diffraction File (2), Database sets 1-47. (1997). International Centre for Diffraction Data.

[14] Zhou, F., Xu, Y. Y., Li, D-y., He, C-f., Gao, M. and Wang, T. B. (1989). Powder Diffraction 4, 223. (Powder Diffraction number 46-0001).

[15] Chang-lin, G., Yu-qin, W. and Tian-Bao, W. (1982). Acta Phys. Sinica, 31, 1119. (Powder Diffraction number 36-0339).

[16] LINK ISIS, Oxford Instruments, Microanalysis Group.

[17] Goodhew, P. J. & Humphrey, F. J. (1988). Electron Microscopy and Analysis. Taylor and Francis, London.

[18] Roleder, K., Institute of Physics, University of Silesia, ul. Uniwersytecka 4, 40-007, Katowice, Poland.

[19] Welberry, T. R. (1985). Rep. Prog. Phys. 48, 1543.

[20] Wondre, F. Physics Department, Clarendon Laboratory, University of Oxford, Parks Road, Oxford. OX1 3PU.

[21] Welberry, R. Research School of Chemistry, Australian National University, PO Box 4, Canberra City 2601, Australia.

[22] Hove, J. E. & Riley, W. C. (1965). Ceramics for Advanced Technologies. New York Pub. Co.

[23] Handbook of Chemistry and Physics. (1967). 47th Edition.

Chapter 3

$Na_{0.5}Bi_{0.5}TiO_3$ - Structural Study as a Function of Temperature

3.1 Introduction

To characterise a crystal structure the positional co-ordinates of the unique atoms in the unit cell, the lattice parameters, space group and thermal displacement parameters are all needed. These parameters can be accurately determined from x-ray and neutron diffraction data. Both single crystal and powder diffraction techniques have been utilised in this study. Each method has particular advantages and disadvantages as discussed in the text. This chapter examines structural studies and techniques, and procedures of data collection and treatment prior to refinement. Refinement procedures are described, structures and structural behaviour as a function of temperature are investigated for NBT and discussed.

3.2 Powder Diffraction

Powder diffraction is a useful tool for structural studies, especially when good-quality single crystals are unobtainable due to factors such as twinning or growth difficulties. An ideal polycrystalline powder can be considered as a collection of a very large number of randomly oriented crystallites. It is a simple matter to obtain a diffraction pattern from a powdered sample as nothing has to be done to align the crystallites and the diffraction pattern is just a function of the scattering angle, all of the reflections for a given angle being superimposed. Provided that overlapping peaks do not cause problems, the intensities measured have certain advantages over single-crystal measurements. In particular, the relative intensities are not affected by absorption in the way that single-crystal measurements are. Powdered samples can suffer from preferred orientation but as this is a function of sample preparation, it can usually be eliminated by finely grinding samples and using experimental strategies such as rapid spinning of the sample holder.

3.2.1 The Rietveld Method

The Rietveld technique[1-2] is a mathematical method for total pattern refinement of a powdered diffraction pattern. The entire diffraction profile is calculated using the

unit cell dimensions to determine the peak positions, the atomic positional and thermal parameters as a model for the peak intensities, a 2θ-dependent analytical function to describe the peak width and shape, and a function to describe the intensity of the background. The method carries out least-squares refinements until the optimum fit is obtained between the whole observed powder diffraction pattern and the entire calculated one.

The experimentally determined diffraction pattern is built up of a numerical intensity value I_o (of one or more peaks) at each increment i, in the pattern. For constant wavelength data (as used for all studies here), the increments are steps in scattering angle 2θ, with the intensity I_o at each step in the pattern being measured directly from the detector. From an initial starting model a comparison of the observed and calculated patterns are made at every step, and by refining the various parameters adjustments are made to the model until the best least-squares fit is obtained. The quantity minimised in the least-squares refinement is the residual M, given by:

$$M = \sum_i w_i |I_o - I_c|^2 \qquad (3.01)$$

where w_i is the weight factor associated with the observation at the i^{th} point (= $1/I_c$), I_o and I_c are the observed and calculated intensity at the i^{th} step respectively and the sum is over all data points.

With the addition of a background contribution and other intensity corrections, the calculated intensity I_c is determined on the assumption that at a specific point its value incorporates the sum of the contributions of all overlapping peaks at that point, i.e.

$$I_c = s\sum_k K_k |F_k|^2 H(\Delta 2\theta_{ik}) + I_b \qquad (3.02)$$

where s is the scale factor, K_k is an additional intensity correction factor for reflection k, F_k is the structure factor for the k^{th} reflection, $\Delta 2\theta_{ik}$ is the difference in 2θ between the reflection position θ_k and the profile point θ_i, $H(\Delta 2\theta_{ik})$ is the peak shape function and I_b the background intensity at the i^{th} step (due mainly to diffuse scattering, fluorescence and detector noise).

The refinement method is based on simultaneously refining parameters. These parameters fall into two categories: those describing the crystal structure and those describing the characteristics of the diffractometer. The first group consists of structural

parameters such as the lattice parameters, the fractional co-ordinates for each atom and temperature factors (isotropic/anisotropic). All of these parameters can be refined within the constraints imposed by the space group setting. The second group consists of the 2θ-zero shift, background profile, wavelength, absorption and peak profile parameters. Absorption corrections can be applied to the data at the refinement stage or alternatively the correction can be applied during data reduction.

The profile function models the effects of both the instrumental features (e.g. peak-profile asymmetry) and features of the specimen (such as strain, particle size or specimen displacement). Of the profile parameters, the peak shape function is used to describe the distribution of intensity in a single peak. Its shape is dependent on several parameters including radiation source, wavelength distribution, beam characteristics (influenced by slit and collimator arrangements), the detector system and the sample. The determination of an accurate peak profile is paramount for a successful refinement. Analytical peak shape functions used to model experimental profiles include Gaussian, Lorentzian, pseudo-Voigt and the Pearson VII functions. Profiles are fitted with respect to the breadth Γ of the peaks measured as full-width half maximum, FWHM (which are not constant across the pattern, because of varying effects of both the diffractometer and sample), modelled for Gaussian[3] and Lorentzian[4] peaks as:

$$\Gamma_G^2 = U\tan^2\theta + V\tan\theta + W \tag{3.03}$$

$$\Gamma_L^2 = X\tan\theta + Y/\cos\theta \tag{3.04}$$

where U, V, W and/or X, Y are the half-width (diffractometer-dependent) refinable parameters. With relation to the specimen features parameters such as *S/L*, *H/L* which are asymmetry terms and *Stec*, *Ptec*, *Sfec* which are anisotropic Lorentzian terms to describe strain broadening, can also used to determine peak shape profiles. For all powder data refinements carried out here, the pseudo-Voigt profile was used. This is a simplification of the Voigt function and results from the linear combination of a Gaussian and Lorentzian profile. The function $F(\Delta\theta)$[4], can model a peak shape from pure Gaussian to pure Lorentzian depending on the mixing factor η:

$$F(\Delta\theta) = \eta L(\Delta\theta, \Gamma_L) + (1-\eta)G(\Delta\theta, \Gamma_G) \tag{3.05}$$

where L is the Lorentzian function with a FWHM of Γ_L and G is the Gaussian function with FWHM of Γ_G. The mixing factor η, is refined as part of the profile function.

The indicators of the quality of the least-squares refinement between the calculated and observed patterns is estimated in the residual R-factors as defined by the following:

R-profile factor:
$$R_p = \frac{\sum |I_o - I_c|}{\sum I_o} \tag{3.06}$$

Weighted R-profile:
$${}_wR_p = \sqrt{\frac{\sum w_i |I_o - I_c|^2}{\sum w_i I_o^2}} \tag{3.07}$$

R-structure factor:
$$R_F = \frac{\sum \left| I_{o(hkl)}^{1/2} - I_{c(hkl)}^{1/2} \right|}{\sum I_{o(hkl)}^{1/2}} \tag{3.08}$$

R-Bragg factor:
$$R_B = \frac{\sum \left| I_{o(hkl)} - I_{c(hkl)} \right|}{\sum I_{o(hkl)}} \tag{3.09}$$

The reduced χ^2 or goodness of fit is defined by the minimisation function as:

Goodness of fit:
$$\chi^2 = \frac{M}{N_{obs} - N_{\text{var}}} \tag{3.10}$$

where N_{obs} and N_{var} are number of observations and refined parameter variables, respectively. The weighted R-factor ${}_wR_p$ and the Goodness of fit χ^2 are the most meaningful in relation to the progress of the refinement, as they incorporate the quantity being minimised, M (equation 3.01), in the least squares in the numerator.

3.2.2 GSAS (General Structural Analysis System)

Diffraction data were refined using the Rietveld refinement software package GSAS[5]. This package consists of a set of programs for processing and analysing powder neutron/x-ray diffraction data and single crystal diffraction data. GSAS allows a number of different functions for peak profile modelling; the pseudo-Voigt function was chosen to model peak shapes for all powder data refined here. As with the peak profile function, the background profile can be modelled within GSAS by different methods.

The function used for all the data here was based on a linear interpolation between points. A maximum of 36 coefficients can be used in GSAS to model the background of a pattern. In all refinements undertaken 8 coefficients were used, as the use of too many can lead to high angle low intensity peaks being fitted as part of the background, resulting in artificially low ${}_wR_p$ values. GSAS can work with multiple data sets simultaneously allowing mixed powders or multiple phases to be refined.

Accurate 2θ reflection positions were obtained using the peak profile analysis program PROFILE[6]. The indexing of these reflections and subsequent unit cell determinations were achieved using the auto-indexing programs DICVOL91[7] or TREOR[8]. The resulting lattice parameters were used in the starting models for Rietveld refinements and subsequently refined to convergence.

3.3 Neutron Powder Diffraction

An alternative to using x-rays as a source of scattering radiation is to use neutrons. As with x-ray powder diffraction, neutron powder diffraction has the obvious advantage that powdered crystalline samples are much easier to obtain than single crystals. Neutron and x-ray diffraction are complementary techniques of crystal structure analysis. The fundamental difference is that neutrons are scattered by the atomic nuclei and not by the electron clouds. This results in neutron scattering factors that vary comparatively little, and are quite irregular with atomic number unlike x-ray scattering factors, which directly increase with the atomic number (as the electron density increases). Hence certain light elements e.g. O, Na, scatter neutrons as effectively as certain heavy elements e.g. Bi, whereas for x-rays light elements consistently scatter least.

This property makes structural determination via neutron powder diffraction beneficial in the NBT family of compounds. Since the x-ray scattering factor of bismuth is much higher than that of oxygen it is difficult to locate accurately the oxygen atom positions from x-ray diffraction data, because of the overwhelming scattering effects of bismuth. For neutrons however, the scattering lengths are of the same order (Table 3.01) and all atoms contribute relatively equally to the final diffraction pattern. The proper determination of the oxygen positions is important as they reveal direct information relating to the oxygen octahedral tilting in the compounds under study. Table 3.01 lists the neutron scattering lengths (used in GSAS) and the corresponding total photon

interaction cross sections (effectively the x-ray scattering ability of an atom) when using CuK_α radiation (taken from International Tables of X-ray Crystallography Vol. C, p193), for the atoms present in compounds in this study.

Atom	Atomic Number	Neutron Scattering Length (10^{-12}cm)	Total photon interaction cross-section (barns/atom) for Cu-K_α
O	8	0.581	3.04×10^2
Na	11	0.350	1.14×10^3
K	19	0.367	9.40×10^3
Ti	22	-0.344	1.59×10^4
Bi	83	0.853	8.43×10^4

Table 3.01. Neutron Scattering Length and Total photon interaction cross-sections.

3.3.1 D2B High-Resolution Diffractometer

D2B[9] is a high-resolution two-axis diffractometer at the Institut Laue-Langevin (ILL), Grenoble, France. The research facility houses a high-flux nuclear reactor, which operates at a thermal power of 58.4 MW using a single fuel-element of U^{235}. The fuel-element sits in the centre of a heavy water filled moderating tank of diameter 2.5 m. Neutron beams are available in the reactor hall from thermal, hot and cold beam ports, technical details of which can be found elsewhere[10].

The diffractometer D2B utilises a continuous supply of thermal neutrons as its source, it is characterised by the high take-off angle (135°) from its Germanium monochromating crystal. The monochromator is 300 mm high and focuses the neutron beam vertically onto approximately 50 mm. The large incident vertical divergence is matched by a detector array of sixty-four 200 mm high ^{3}He counting tubes and collimators spaced at 2.5° intervals. A complete scan between $0 < 2\theta < 160°$ typically takes 30 minutes (one hundred 0.025° step scan in 2θ), a number of these scans are then often repeated and averaged in order to improve the counting statistics. Wavelengths between 1.051-3.152 Å can be selected but the maximum flux is obtained at 1.594 Å. Figure 3.01 shows the schematic layout of the instrument.

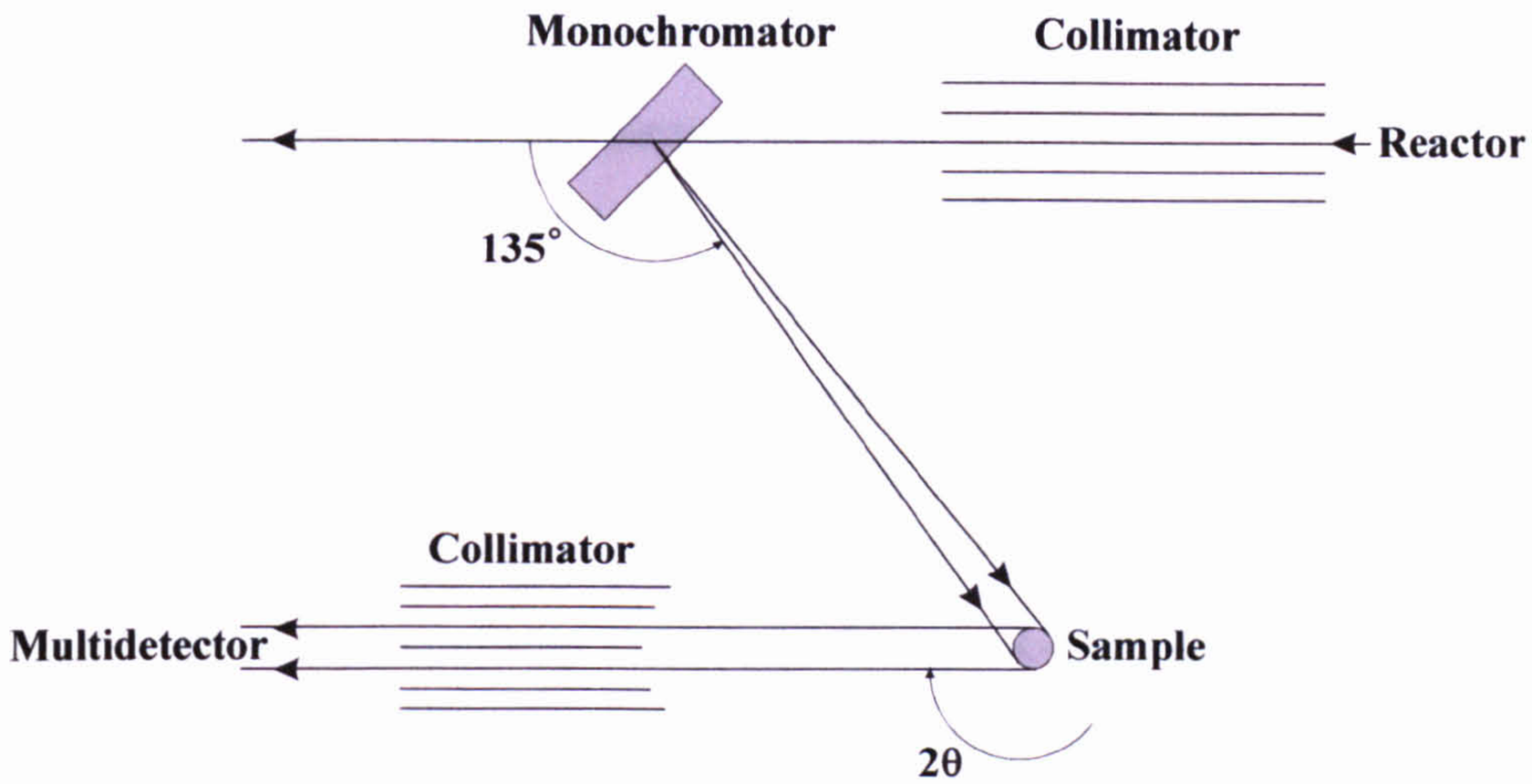

Figure 3.01. Schematic layout of the D2B high-resolution diffractometer.

3.3.2 Sample Preparation

Fragments of flux grown NBT crystals were finely ground into powder. The powder was sieved to obtain particles with approximate diameters < 38 μm and compacted into 60 × 5 mm, thin walled vanadium canisters as shown in Figure 3.02 (a). The canister position was adjusted so that the stainless steel top was clear of the beam and only the lower region lay in the beam path. As an extra precaution a cadmium shield was placed around the top region as shown in Figure 3.02 (b). The sample was aligned on the rotation axis of the diffractometer and the canister was positioned in the beam with the aid of cadmium strips (which contrast as dark shadows due to their high neutron absorption cross-section). Polaroid photographs were taken to confirm the geometry.

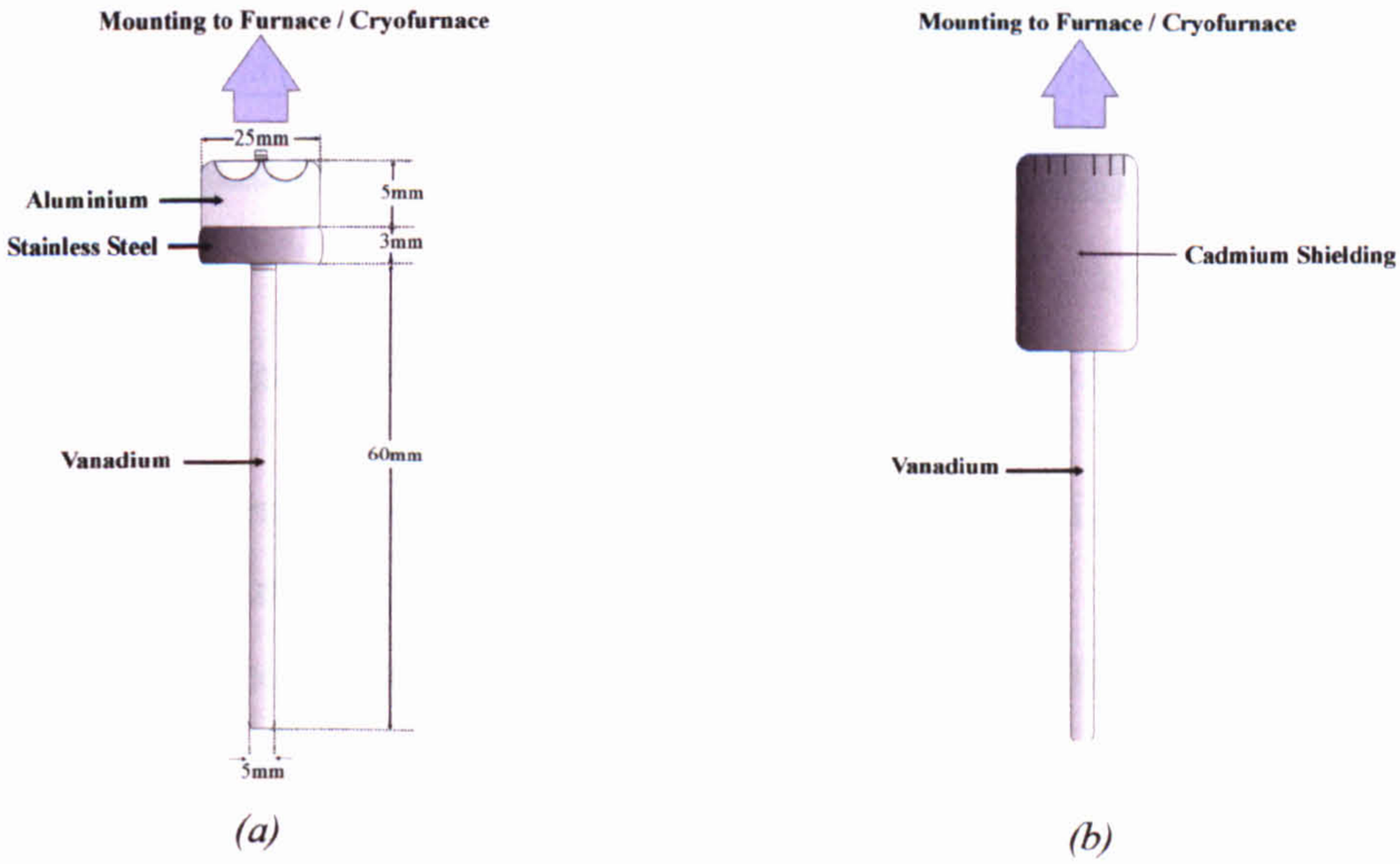

Figure 3.02. (a) Vanadium sample holder canister (b) Canister with cadmium shielding.

3.3.3 Data Collections and Treatment

A high-temperature vacuum furnace (capable of operating between 200-1000 K) was used to collect data from room temperature to 873 K on heating. The furnace is shown schematically in Figure 3.03 (a). Heating was provided by a water-cooled niobium-heating element and was remotely controlled by an Eurotherm controller. Low temperature measurements were carried out in a liquid nitrogen/helium vacuum cryofurnace (capable of operating between 1.5-300 K) between 5-250 K on cooling. The cryofurnace is shown schematically in Figure 3.03 (b). K-type thermocouples were used to measure high and low temperatures. Data sets were collected using a wavelength of 1.594 Å. For all data sets, complete diffraction patterns were made up from sections by counting at each 2θ position until a predetermined number of monitor counts was achieved. The complete angular range between $0 < 2\theta < 160°$ was covered in 50 steps of 0.05°. This procedure was repeated a number of times and the resulting profiles averaged. In all cases four scans were taken and averaged. The individual time per scan varied because of time limitations on the instrument.

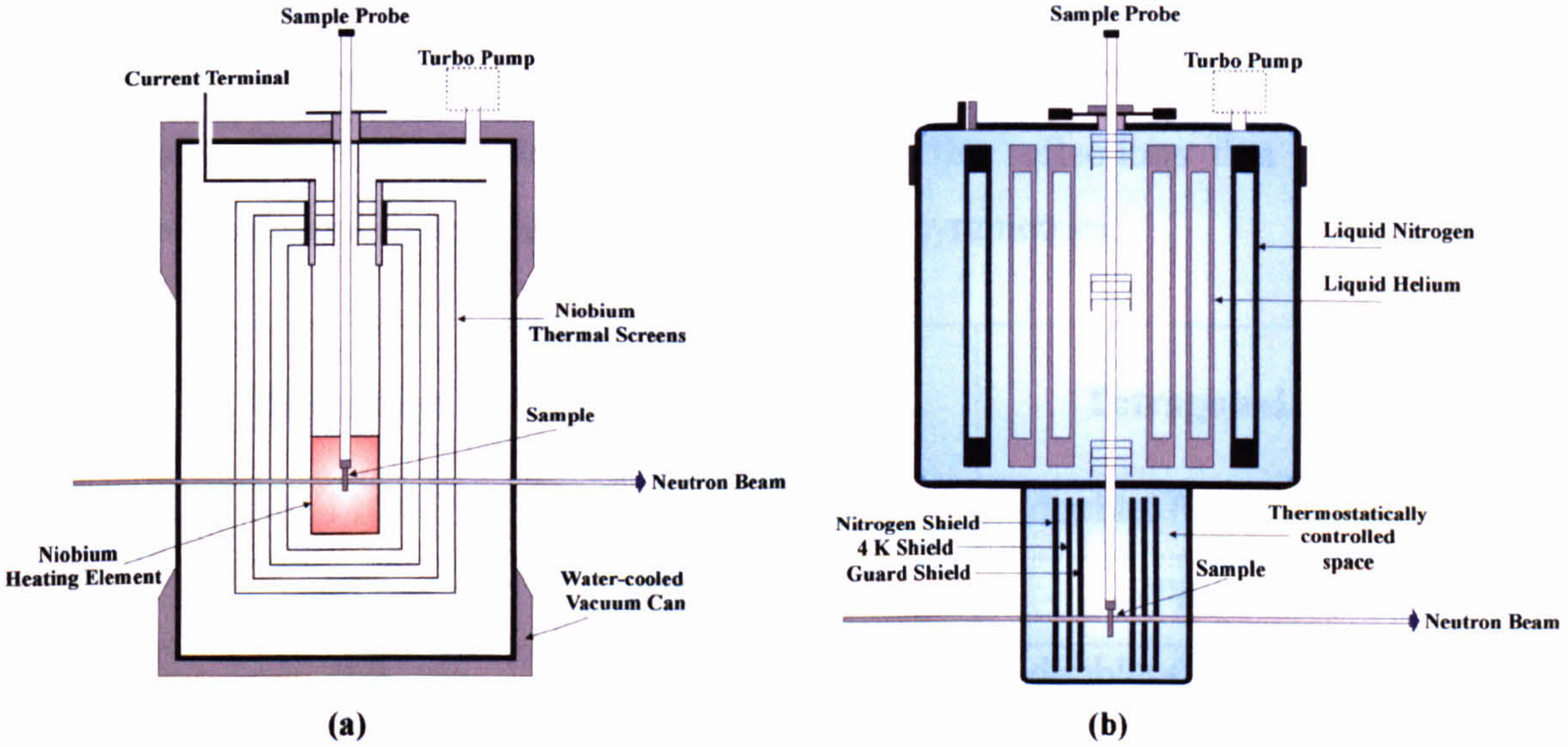

Figure 3.03. (a) High-temperature furnace, (b) Cryofurnace, used on D2B diffractometer.

The method of data collections used allows the calibration of the individual detectors in the array to be carried out. Each peak was scanned by a number of different detectors. Comparison of the subsequent outputs allowed the efficiency differences to be gauged and corrected for. After the scans were corrected in this way and independent runs

merged, the data were converted into a GSAS compatible format. Table 3.02 lists the details of the high and low temperature data collections.

Environment	Temperature (K)	Individual Scans	Total Scan Time (hours)
Furnace	293, 400, 473, 573, 673, 773, 873	Four 60 minute scans averaged	4.0
	528, 593, 698, 723, 793, 813	Four 40 minute scans averaged	2.6
Cryofurnace	5, 50, 100, 150, 200, 250	Four 70 minute scans averaged	4.6

Table 3.02. High and Low neutron data collections on diffractometer D2B.

3.3.4 Rietveld Structural Refinements

Rhombohedral Phase - Refinements by the Rietveld profile fitting method with GSAS were carried out. The refinement of these data sets were based on the rhombohedral unit cell, since splitting/broadening of the h, k, l reflections were $h = k = l$, was directly observed. Table 3.03 lists some of the reflections that were used to determine the present rhombohedral (and tetragonal) symmetries.

Reflection	Rhombohedral	Tetragonal
110	singlet	doublet (011/110)
111	doublet (111/$\bar{1}$11)	singlet
200	singlet	doublet (002/200)
222	doublet (222/$\bar{2}$22)	singlet

Table 3.03. Nature of certain reflections in rhombohedral and tetragonal phases.

Superstructure reflections of the type h odd, k odd, l odd where observed within the temperature range 5-593 K. These were consistent with the $a^-a^-a^-$ tilt system[11] seen in rhombohedral perovskites and arising from oxygen octahedra tilting about the three-fold pseudo-cubic axes. This tilt system is characterised by opposite rotations of adjacent octahedra along each axis, which consequently results in cell doubling of all three

pseudo-cubic axes. The known rhombohedral perovskites are restricted to structures with space groups R3m, $R\bar{3}m$, $R\bar{3}c$, or R3c. The space groups R3c and $R\bar{3}c$ can support tilt systems. R3c has a polar symmetry permitting ferroelectricity, while $R\bar{3}c$ is non-polar and maintains the cations at the centres of inversion. The space group R3m can be immediately disregarded for NBT, because of the presence of superstructure reflections. Initial refinements of this phase were carried out in R3c, and based on the $Pb(Zr_xTi_{1-x})O_3$ (PZT) model proposed by Corker *et al.*[12]. Models for each subsequent temperature were taken from the previous refinement.

As it is standard to describe the rhombohedral system on a rhombohedrally-centred hexagonal lattice projected down the three-fold axis, the rhombohedral structure is referred to hexagonal axes, whose lattice parameters a_H and c_H are specified with relation to the doubled pseudo-cubic cell ($2a_p \times 2b_p \times 2c_p$) by the matrix:

$$\begin{pmatrix} 0.5 & 0 & -0.5 \\ -0.5 & 0.5 & 0 \\ 1 & 1 & 1 \end{pmatrix} \tag{3.11}$$

Consequently the matrix translating the atomic co-ordinates, which is given by the inverse transpose of the lattice parameter matrix is given by:

$$\begin{pmatrix} 2/3 & -2/3 & 1/3 \\ 2/3 & 4/3 & 1/3 \\ -4/3 & -2/3 & 1/3 \end{pmatrix} \tag{3.12}$$

Following the procedure originally developed by Megaw and Darlington[13], this setting allows structural parameters to be readily defined and leads to the set of atomic fractional co-ordinates given in Table 3.04.

Atom Species	Site	x	y	z
Na/Bi	6(a)	0.00	0.00	$s + 0.25$
Ti	6(a)	0.00	0.00	t
O	18(b)	1/6-2e-2d	1/3-4d	1/12

Table 3.04. Fractional co-ordinates for hexagonal setting of R3c, in terms of independent refinable parameters.

where s and t measure the fractional cation displacements along c_H (or $[111]_p$) with respect to an origin chosen to lie midway between opposite faces of an oxygen octahedron. The parameter d describes the way an oxygen octahedron is distorted, keeping three-fold symmetry but making the upper and lower faces with respect to c_H different in size. Parameter e indicates the rotation of an octahedron about c_H, with the angle of tilt, ω, given by $tan\ \omega = 4\sqrt{3}e$.

R3c is characterised by cation displacements along $[111]_p$ combined with antiphase octahedral rotations. The room temperature structure was refined in this space group. The background was based on a linear function and peak shapes described by pseudo-Voigt profiles. After preliminary refinements were made to establish parameters describing diffractometer characteristics and, the scale factor, the structural parameters were refined. As the space group R3c allows an arbitrary choice of origin, in structural refinements the $O_{(Z)}$ position was fixed to 1/12, refer to Table 3.04. Isotropic temperature parameters were initially refined followed by anisotropic parameters. Initially, Na and Bi, each with site occupation factor 0.5, were constrained to be at the same co-ordinates. As a check on the stoichiometry, the occupancies of Na and Bi were refined (given the constraint that the total occupancy should be 1) to values of 0.490 (7) and 0.510 (7), showing that any deviation from the ideal composition was small. The occupancies were subsequently fixed for the remaining refinements. The Na and Bi positions were then allowed to refine separately with the result that Bi became displaced 0.003 (2) Å along the polar axis (+c) with respect to Na. Introducing this freedom had a negligible effect on the profile parameters and no effect on the anisotropic temperature factors. As the displacement of the Bi with respect to the Na was negligible (within errors) their positional parameters were constrained to the same positions for all further refinements. The refinement was stable and converged quickly. It should be noted that an attempt to refine the data in the non-polar space group $R\bar{3}c$ was unstable, as none of the free structural parameters could be refined.

The crystallographic data and the refined profile parameters for the room temperature refinement are summarised in Tables 3.05 and 3.06. The observed, calculated and difference profiles from the final Rietveld refinement in R3c at 293 K are shown in Figure 3.04 (a). Coexistence of rhombohedral and tetragonal phases as indicated by the presence of both types of superstructure reflections (h odd, k odd, l odd and h odd, k odd, l even), were based on the nearest subsequent refinement model and

refined together. From numerical analysis of the diffraction patterns, the contributions to the sample volume of particular phases in the coexistence regions were found. These figures were used as the starting fractions for the coexistence in the refinements. Refinements showed little variation from these calculated fractional volumes. The observed, calculated and difference profiles from the final coexistence Rietveld refinement in R3c and P4bm at 573 K are shown in Figure 3.04 (b).

Tetragonal Phase – Data set refinements were based on the tetragonal unit cell, since tetragonal distortions as shown by the splitting/broadening of certain reflections were clearly evident (Table 3.03). Compared with the pseudo-cubic powder pattern referred to on the $2a \times 2b \times 2c$ ($8 \times 8 \times 8$ Å^3) unit cell, superstructure reflections of the type *h* odd, *k* odd, *l* even were observed within the temperature range 573-793 K. These reflections are consistent with the $a^0a^0c^+$ tilt system and the tetragonal unit cell $\sqrt{2}a \times \sqrt{2}b \times c$. The rotation of the octahedra associated with this system, results in cell doubling in the [100] and [010] directions, but as successive octahedra are rotated in the same direction about [001], there is no doubling in this direction. Following the reported structure of $NaNbO_3$[14], the space group P4/mbm was assigned and the structure (at 698 K) was refined. Initially, Na and Bi, each with site occupation factor 0.5, were constrained to be at the same co-ordinates. The background was based on a linear function and peak shapes, based on earlier refinements of the room temperature structure, were described by pseudo-Voigt profiles. Despite an initially encouraging degree of match between the calculated and observed data with $\chi^2 = 0.3062$, $R_p = 9.14$ % and ${}_wR_p = 13.61$ %, refinement in this space group was impossible as none of the free structural parameters could be refined. Relaxing the mirror plane restriction by choosing polar space group P4bm solved this difficulty. The space group P4bm allows an arbitrary choice of origin, so in structural refinements the $Ti_{(Z)}$ position was fixed at zero. The refinement was stable and converged quickly.

As a further check on the stoichiometry, the occupancies of Na^{1+} and Bi^{3+} refined to values of 0.49 (1) and 0.51 (1). The occupancies were subsequently fixed for the remaining refinements. The Na and Bi positions were then allowed to refine separately with the result that Bi became displaced 0.02 Å along the polar axis (+*c*) with respect to Na. Introducing this freedom had a negligible effect on the profile parameters and no effect on the anisotropic temperature factors. The crystallographic data and the refined profile parameters for the 673 K refinement are summarized in Tables 3.05 and 3.06.

It should be noted that the tetragonal phase of NBT was previously reported in space group P4mm[15]. Refinement of the present data in P4mm (a non-centrosymmetric space group that allows cation displacements), was tried with similar cation displacements to the P4bm model resulting. However, since the superstructure reflections arising from the octahedral tilts are absent in P4mm, this space group can be rejected on these grounds alone. The observed, calculated and difference profiles from the final Rietveld refinement in P4bm at 673 K are shown in Figure 3.05 (a). Coexistence regions of the tetragonal and cubic phases were based on the nearest subsequent refinement models and refined together.

Cubic Phases - The high-temperature, paraelectric cubic form of NBT, space group $Pm\bar{3}m$ possesses no tilts or cation displacements. The refinement was stable and converged quickly, the crystallographic data and the refined profile parameters are summarized in Tables 3.05 and 3.06. The observed, calculated and difference profiles from the final Rietveld refinement at 873 K are shown in Figure 3.05 (b). There is very little apparent difference between the profiles in the coexistence tetragonal/cubic phases and the pure cubic phase, with the tetragonal superstructure reflections being very weak. Starting models for refinement in the coexistence region were based on the nearest subsequent refinement models and refined together.

Figure 3.06 (a) shows the rhombohedral (293 K) structure, from final refinements as viewed down [001]. Figure 3.06 (b) and (c) show the tetragonal (673 K) structure, from final refinements as viewed down [010] and [001] respectively.

Rhombohedral (R3c) Phase (293 K)

Atom	x	y	z	U11	U22	U33	U12	U13	U23
Na	0.0	0.0	0.2627(6)	0.022(3)	0.022(3)	0.036(9)	0.011(2)	0.0	0.0
Bi	0.0	0.0	0.2627(6)	0.036(2)	0.036(2)	0.091(6)	0.018(1)	0.0	0.0
Ti	0.0	0.0	0.0063(6)	0.011(2)	0.011(2)	0.009(3)	0.006(1)	0.0	0.0
O	0.126(1)	0.336(1)	0.0833†	0.031(3)	0.006(1)	0.048(1)	0.014(3)	-0.004(3)	-0.011(1)

†$O_{(z)}$ fixed to deal with floating origin.

Tetragonal (P4bm) Phase (673 K)

Atom	x	y	z	U11	U22	U33	U12	U13	U23
Na	0.0	½	0.545(2)	0.051(6)	0.051(6)	0.039(2)	0.001(1)	0.0	0.0
Bi	0.0	½	0.545(2)	0.071(3)	0.071(3)	0.037(6)	-0.002(4)	0.0	0.0
Ti	0.0	0.0	0.0†	0.014(2)	0.014(2)	0.014(4)	0.0	0.0	0.0
O(I)	0.0	0.0	0.510(3)	0.063(2)	0.063(2)	0.020(3)	0.0	0.0	0.0
O(II)	0.271(1)	0.229(1)	0.015(4)	0.024(1)	0.024(1)	0.056(2)	-0.013(1)	0.001(3)	-0.001(3)

†$Ti_{(z)}$ fixed to deal with floating origin.

Cubic ($Pm\bar{3}m$) Phase (873 K)

Atom	x	y	z	U11	U22	U33	U12	U13	U23
Na	0.0	0.0	0.0	0.077(4)	0.077(4)	0.077(4)	0.0	0.0	0.0
Bi	0.0	0.0	0.0	0.077(2)	0.077(2)	0.077(2)	0.0	0.0	0.0
Ti	½	½	½	0.022(1)	0.022(1)	0.022(1)	0.0	0.0	0.0
O	½	½	0.0	0.062(1)	0.062(1)	0.012(1)	0.0	0.0	0.0

Table 3.05. *Fractional co-ordinates and equivalent anisotropic displacement parameters ($Å^2$) for NBT.*

Chemical formula	$Na_{0.5}Bi_{0.5}TiO_3$
Chemical formula weight	211.88
Specimen Shape	Random powder
Specimen preparation	Crystal growth from flux, Powder prepared from ground crystals
Specimen Pressure	Ambient
Colour	Pale Yellow
Radiation Type	Neutron
Wavelength	1.594 Å

Crystal System	**Rhombohedral**	**Tetragonal**	**Cubic**
Temperature (K)	293	673	873
Space Group	R3c	P4bm	$Pm\bar{3}m$
a_H (Å)	5.4887(2)	-	-
c_H (Å)	13.5048(8)	-	-
a_p (Å)	-	5.5179(2)	3.91368(3)
c_p (Å)	-	3.9073(2)	-
α,β,γ (°)	90,90,120	90,90,90	90,90,90
α_p(°)	89.83	-	-
Volume (Å^3)	352.33(3)	118.96(1)	59.945(5)
Z	6	2	1
D_x (Mg.m^{-3})	5.99	5.91	5.87
s	0.0127(6)	0.035(1)	0.0
t	0.0063(6)	-0.015(4)	0.0
d	-0.0006(3)	-	-
e	0.0209(1)	-	-
Tilt System	$a^-a^-a^-$ (three tilt system, anti-phase)	$a^0a^0c^+$ (one tilt system, in-phase)	$a^0a^0a^0$ (zero-tilt system)
Displacements	Parallel along $[111]_p$	Anti-parallel along [001]	None
ω (°)	8.24(4)	3.06(2)	0.0
$\zeta \times 10^2$	-0.589(8)	-	-
N° of refined parameters	42	43	39
Profile R-factors			
R_p	0.059	0.044	0.045
wR_p	0.078	0.056	0.053
χ^2	0.323	0.786	0.710

Table 3.06. ***Summary of experimental details, data collection and refinement for the three phases of NBT.***

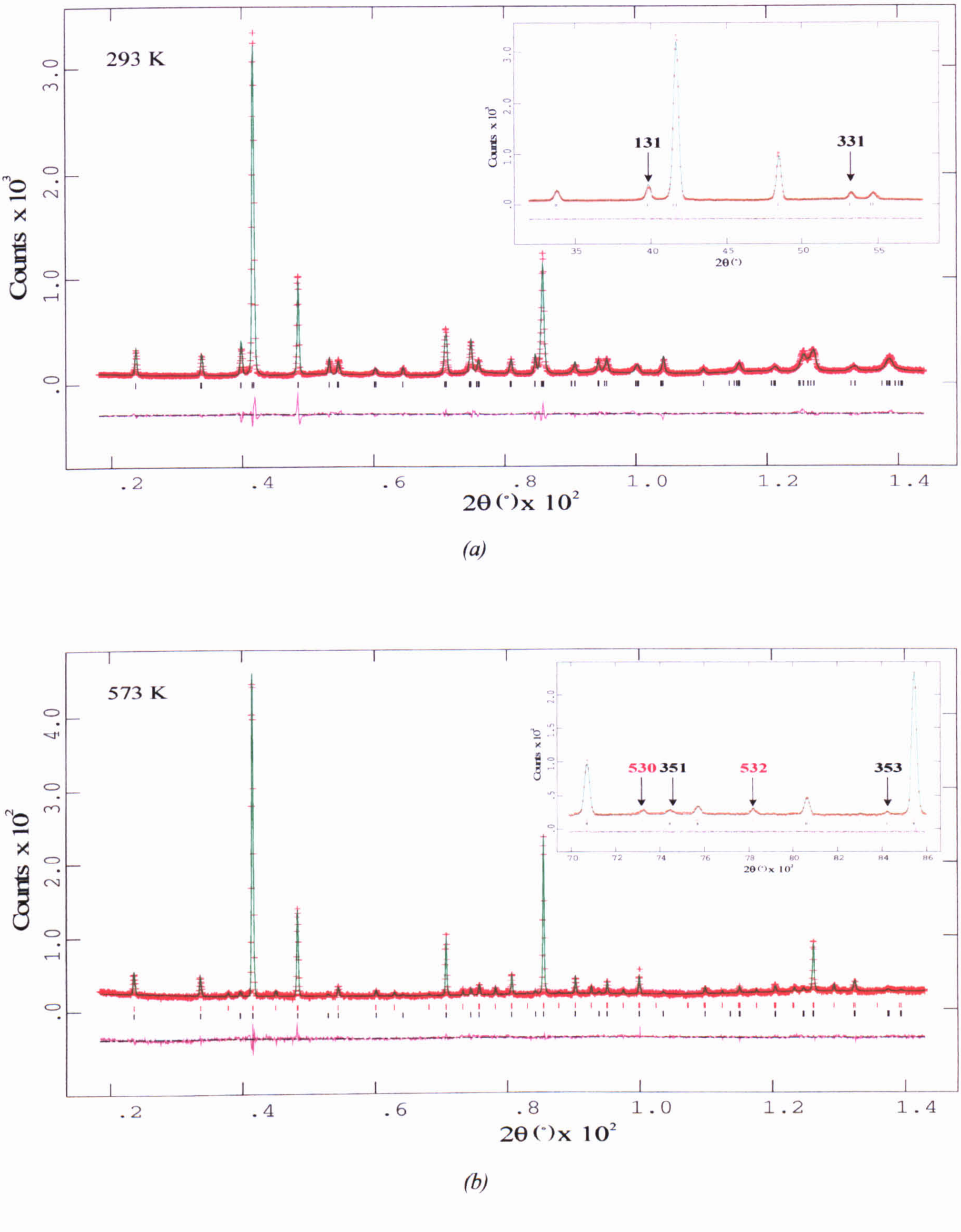

Figure 3.04. *The observed, calculated, and difference curves from the Rietveld refinement of $Na_{0.5}Bi_{0.5}TiO_3$. (a) refinement in R3c, at 293 K, the marks indicate the positions of the reflections. The low angle data ($32 < 2\theta < 58°$), showing the first two superstructure peaks are magnified in the insert. (b) refinement in R3c and P4bm - coexistence region at 773 K, the black and red marks indicate the positions of the rhombohedral and tetragonal reflections respectively. The mid-angle data ($70 < 2\theta < 86°$), showing the positions of rhombohedral (black) and tetragonal (red) superstructure peaks are magnified in the insert.*

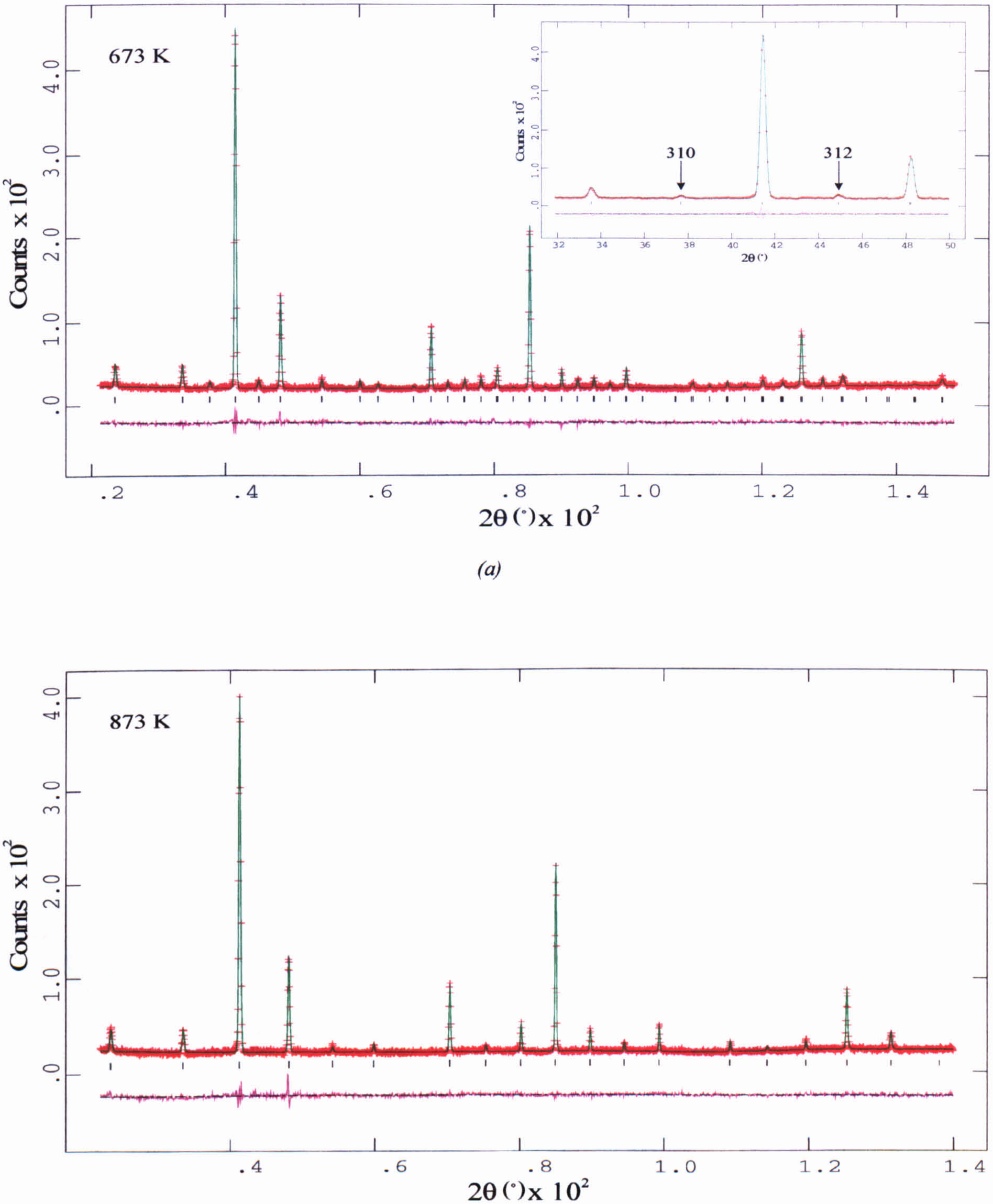

(a)

(b)

Figure 3.05. *The observed, calculated, and difference curves from the Rietveld refinement of $Na_{0.5}Bi_{0.5}TiO_3$. The marks indicate the positions of the reflections. (a) refinement in P4bm, at 673 K, the low angle data ($32 < 2\theta < 50°$), showing the first two superstructure peak are magnified in the insert. (b) refinement in $Pm\bar{3}m$, at 873 K.*

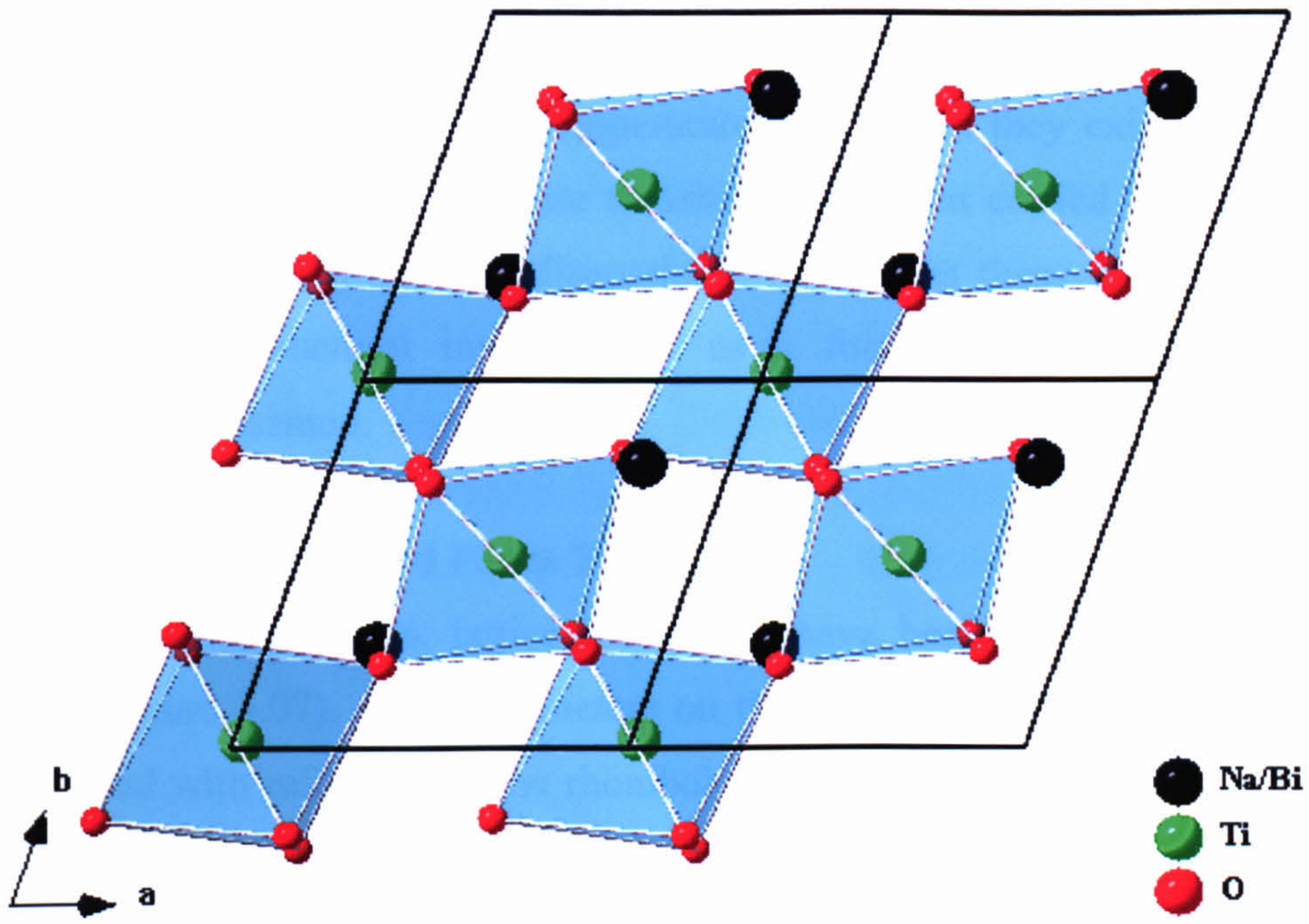

(a)

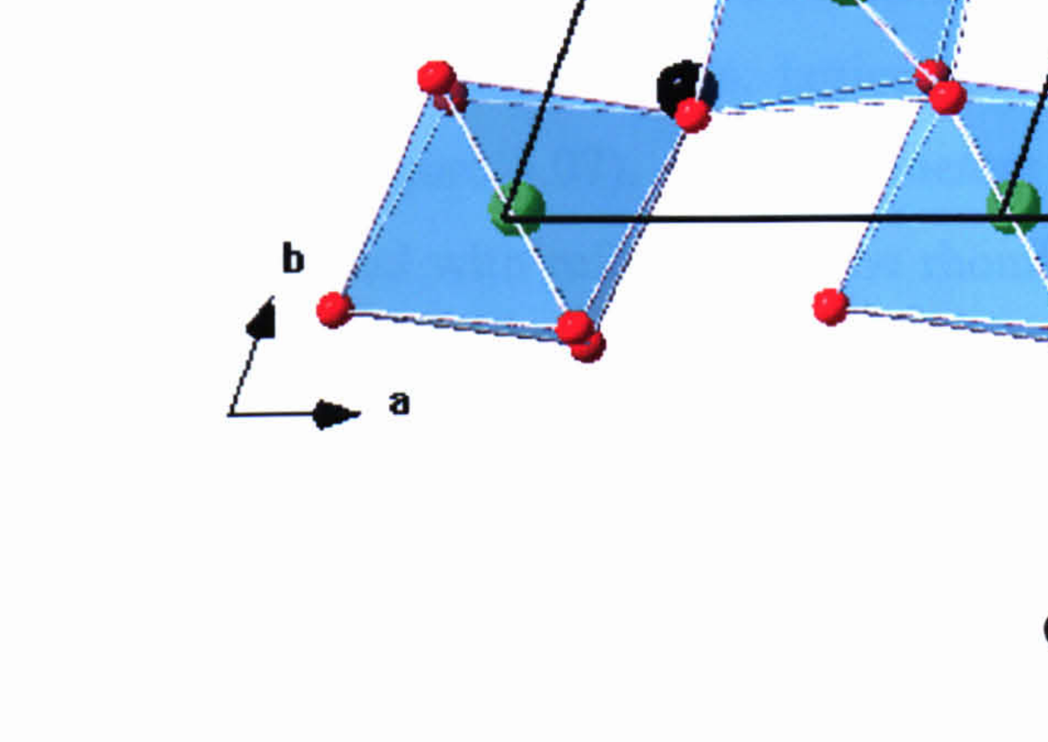

(b)

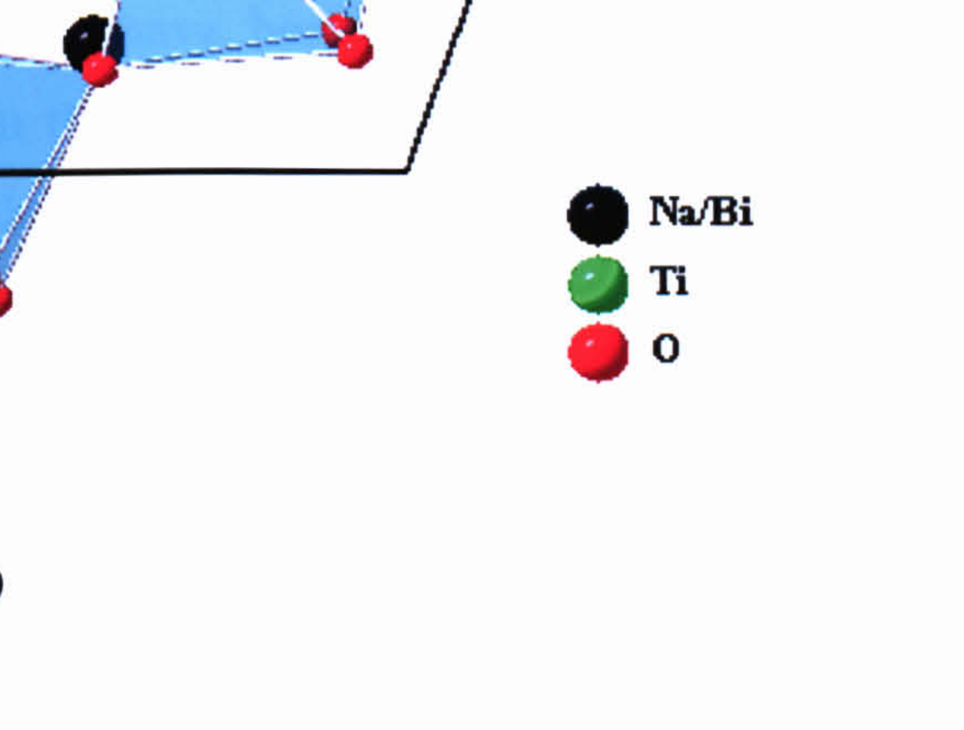

(c)

Figure 3.06. *(a) the rhombohedral (293 K) structure, from final refinements as viewed down [001], (b) the tetragonal (673 K) structure, from final refinements as viewed down [010] and (c) [001].*

3.3.5 Discussion

As pointed out in section 1.3.1, at the outset of this study, despite numerous investigations, there remained significant controversy in relation to the ferroic nature of the different phases in NBT and the temperature over which they exist. An extensive study of the crystal structure and phase transitions has been carried out using neutron powder diffraction. The following discussion will address these controversies and a detailed systematic structural investigation, as a function of temperature for this compound will be presented.

3.3.5.1 Lattice Parameters and Phase Transitions

From final refinements, lattice parameters have been plotted as a function of temperature (Figure 3.07). Cell parameters on the hexagonal setting, shown in Figure 3.08, are plotted with reference to the rhombohedral (a_R) crystallographic axes. Figure 3.07 shows an overall steady increase in lattice parameters as expected with increasing temperature. Figure 3.08 shows the gradual elongation of a_H and contraction of the c_H axes with increasing temperature, (resulting in an overall increase of the unit cell volume). The c_H axis is presumed to respond differently from a_H with increasing temperature because it is the polar axis and highly sensitive to polar cation displacements. On closer inspection there is an irregular progression in the lattice parameters around 400 K. The rate of increase of a_R before 400 K is markedly lower than that after it. This discontinuity may result from a zero error brought about by the use of different experimental environments i.e. cryofurnace/furnace. The lattice parameters at 5 K also show a slight discontinuity, the values are comparable to those seen at 150 K. This could possibly indicate the presence of a phase transition.

The values of the lattice parameters are comparable to those obtained by other authors e.g. Suchanicz & Kwapulinski[16] (slight variations could be attributed to volatilisation of Bi_2O_3 during differing growth methods[17]). Figure 3.09 shows the different symmetry phase volumes as a function of temperature. The pure rhombohedral phase persists from 5-528 K, between 573-593 K a coexistence region can be seen and from 673-773 K the pure tetragonal phase occurs. Due to a limit in the time available for measurements, the regions 528-573 K and 593-673 K could not be investigated more fully. As a result the extent over which the rhombohedral/tetragonal coexistence region lies could not be determined more precisely. The tetragonal/cubic coexistence region lies within 773-813 K, with the pure cubic phase occurring at 813 K. These results are in

close agreement with Suchanicz & Kwapulinski[16] who carried out XRPD measurements between 893-473 K on cooling. As outlined in section 1.3.1, they found the cubic/tetragonal coexistence phase occurs between 823-773 K, and the rhombohedral/tetragonal coexistence region between 693-533 K. There has been much controversy associated with the rhombohedral/tetragonal coexistence of phases in the literature. Some authors[18] suggest an antiferroelectric ordering exists between the rhombohedral/tetragonal phase. However, many investigations, including this one, do not show any evidence to support this. Suchanicz & Kwapulinski[16] found the rhombohedral/tetragonal coexistence range to be 160 K but the results from Zvirgzds *et al.*[19], found the range to be around 55 K. The results from this study suggest an upper limit for this region of 145 K, but it is more likely to be less. The main difference between the results obtained in this study and those conducted by Suchanicz & Kwapulinski[16] are the temperatures at which the pure rhombohedral and tetragonal phases are first seen. Both the values obtained from this study are moderately lower (< 20 K) than their values.

The low-temperature profiles differed from the room-temperature profile only in the positions of the reflections, accounted for by the change of lattice parameters at lower temperature. The relative intensities did not differ appreciably from those at room temperature. All reflections associated with the (R3c) $a^-a^-a^-$ superstructure were observed down to 5 K. There was no sign of a phase transition as previously tentatively reported by Suchanicz *et al.*[20], at 55 K.

3.3.5.2 Cation Ordering

It is known that cation ordering in complex B-site substituted perovskites, is driven by fundamental factors such as ion size and charge[21]. Compounds that possess sufficiently large differences in the size of the B-cations are driven strongly towards ordering by electrostatic forces, whereas materials with closely matched cation sizes are nearly always disordered. Similarly, large variations in the valence between B-cations, results in a powerful tendency towards ordering through electrostatic forces. There are relatively few examples of A-cation ordering, due mainly to the overall limited number of compounds that exist. It would not be unreasonable however, to presume that similar ordering arguments hold for A-site substituted complex perovskites.

Park *et al.*[22], have shown through diffraction studies that a partial ordering of the Nd^{3+}/Ag^{1+} cations occurs in the A-site substituted perovskite $Nd_{0.5}Ag_{0.5}TiO_3$. This

layered A-site ordering is driven by the charge and size difference between Nd^{3+} and Ag^{1+}, were there is a 14 % difference in ionic radii[23]. There have also been reports of long-range cation ordering in NBT. Park *et al.*[17], in single-crystal rotation camera experiments, found a low degree of Na^{1+}/Bi^{3+} ordering and suggested an ordered face-centred structure (space group $Fm\bar{3}m$) for the high temperature cubic phase.

In this study no superstructure peaks associated with cation-ordering were observed in NBT. This is as expected since the ionic radii difference in NBT is close to zero[23] and the $(Na/Bi)O_{12}$ cuboctahedra are approximately the same size. Long-range order is also absent in NBT's analogue $Ag_{0.5}Bi_{0.5}TiO_3$[24], where there is a 8 % difference in ionic radii[23]. The conclusion reached from this study is that Na/Bi cations distribute themselves over the sites randomly and the high temperature (≥ 813 K) structure is therefore a primitive cubic structure with space group $Pm\bar{3}m$.

There has been a previous suggestion of the existence of short-range order in NBT[25] (section 1.3.1). This was based on the observation that the background of a neutron powder diffraction study did not vary linearly, but consisted of a number of diffuse peaks (Figure 1.08). Similar behaviour was not observed in this neutron powder diffraction study. However, the possibility that short-range cation order exists in NBT as suggested by x-ray diffuse scattering experiments (section 2.3.4) remains.

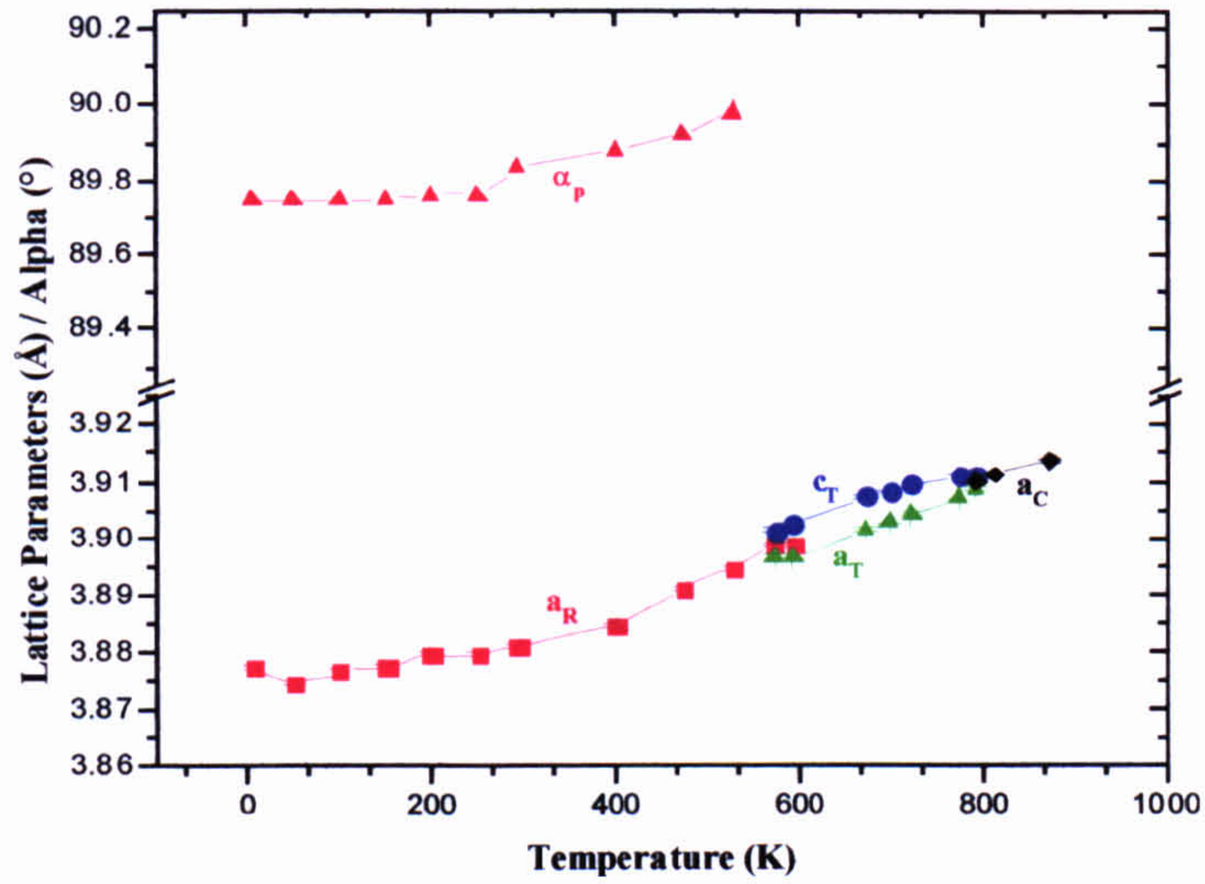

Figure 3.07. *Lattice parameter evolution and α_p as a function of temperature.*

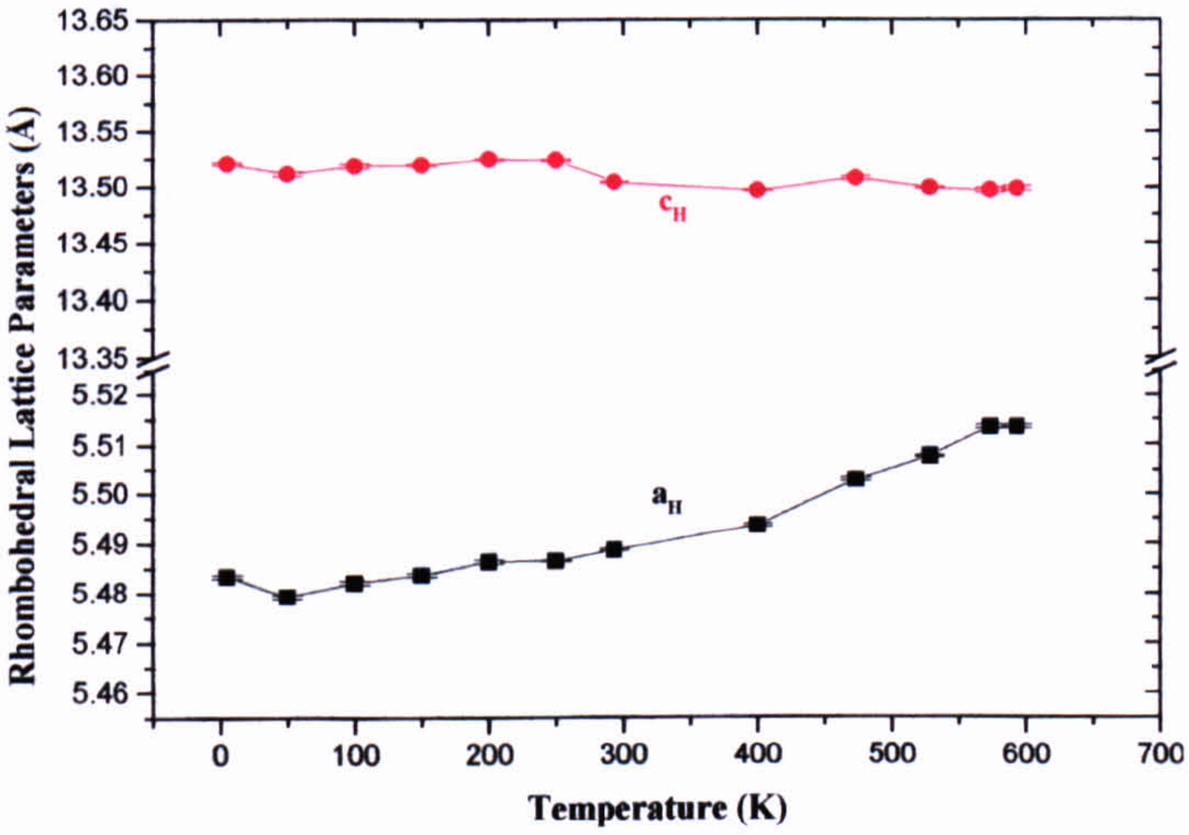

Figure 3.08. *Lattice parameter evolution in rhombohedral phase as a function of temperature.*

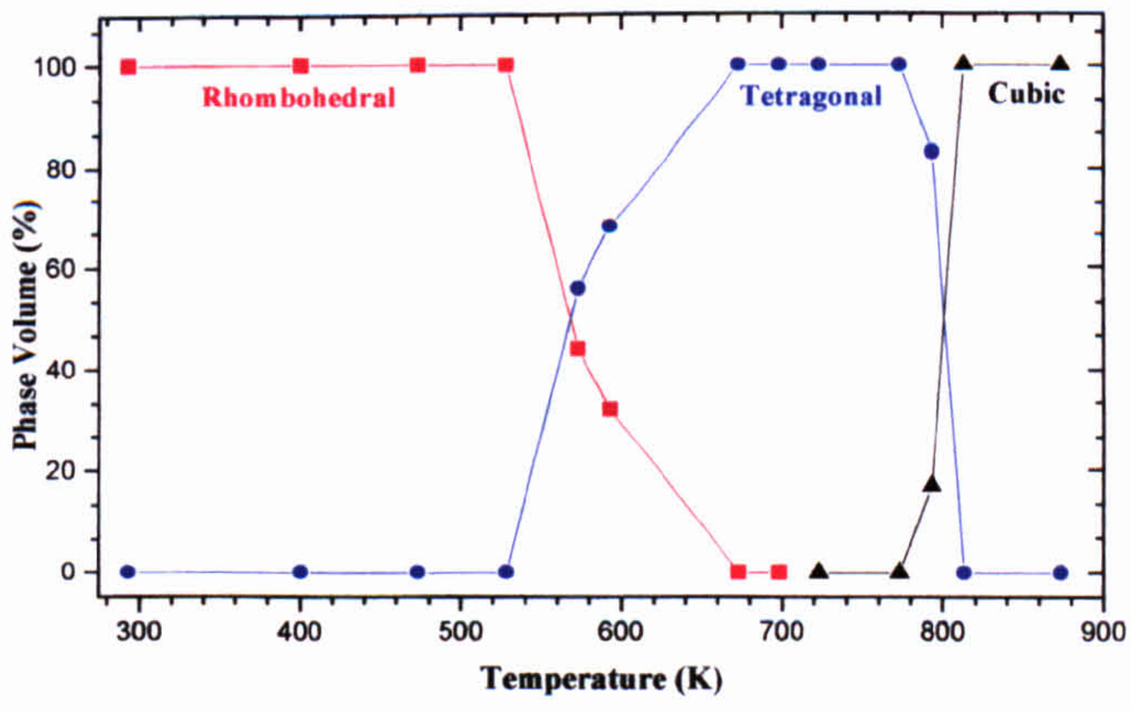

Figure 3.09. *Percentage phase volumes as a function of temperature.*

3.3.5.3 Octahedral Tilting and Cation Displacements

As the temperature is decreased, NBT distorts from the ideal prototypic cubic perovskite structure by octahedral tilting. Tetragonal superstructure reflections are seen to appear, then diminish, with rhombohedral superstructure reflections appearing with further temperature decrease. Figure 3.10 shows the variation in intensity of the $(5\bar{1}\,\bar{3})$ rhombohedral and (532) tetragonal superstructure peaks relative to the main (424) peak. Octahedral tilting is driven by the need to optimize the anion co-ordination about the A-cation. Since Bi^{3+} and Na^{1+} are relatively small cations in the A-site, the presence of octahedral tilts is expected. For example, the $a^-a^-a^-$[13], and $a^0a^0c^+$[14], tilt systems both occur in $NaNbO_3$ and $a^-a^-a^-$[13] is also found in $BiFeO_3$.

The tetragonal structure is distorted from cubic by in-phase rotations of the TiO_6 octahedra about the *c*-axis, combined with antiparallel displacement of the cations along the polar *c*-axis. The $a^0a^0c^+$ tilts in this structure produce an indistinguishable environment for the A-cation when viewed (from the cation), along $+c$ and $-c$. Therefore, from the geometry of the framework alone, there is no incentive for the A-cation to move off-centre. Since A-cation displacements along [001] are not driven by the octahedral tilts, the conclusion that they result from the need to accommodate the stereo-active lone pair on Bi^{3+} is reached. The electronic configuration of Bi^{3+} is the same as that of Pb^{2+} (both having a completed outer 6s shell), which is likewise a lone-pair cation. Thomann[26] noted the tendency of Bi^{3+} to behave similarly to Pb^{2+} in perovskites and identified Bi^{3+} as a cation likely to promote ferroelectric structures. The tetragonal phase of $PbTiO_3$ (space group P4mm) has Pb^{2+} cations displaced 0.47 Å along the *c*-axis[27], although the framework is not tilted as expected for the larger Pb^{2+} ion. This is in contrast with the isostructural material $BaTiO_3$ were the Ba displacement is only 0.07 Å[28]. Within the tilted framework, even though there is no geometric impetus for the cations to move off-centre, the inherent properties of Bi^{3+} promote movement along the polar axis thus generating this unusual structure. Figure 3.11 shows the Na/Bi and Ti refined shifts plotted as a function of temperature for the tetragonal phase of NBT. The overall displacement of cations calculated in the Rietveld refinements are from the centre of their co-ordination polyhedra. A- and B-cation displacements are in opposite directions, both being directed along the polar *c*-axis. A view of the structure down [001] showing the tilt system and in the [010] direction showing relative cation displacements are shown in Figures 3.13 (a) and (b), respectively. Within the tetragonal phase region Na/Bi displacements are seen to follow a gradual rise followed by a quite

rapid drop over a narrow temperature range and then a moderate displacement decrease as a function of increasing temperature. Ti displacements are antiparallel to Na/Bi displacements and show a relatively constant progression with temperature. Figure 3.12 shows the evolution of the octahedral tilt angle ω with temperature. This varies modestly over a wide temperature region then drops to zero when the transition to the cubic phase occurs and the oxygen octahedra are no longer rotated.

The rhombohedral structure of NBT is described by the polar space group R3c, with $a^-a^-a^-$ antiphase rotations of the TiO_6 octahedra about the pseudo-cubic axes. A- and B-cation displacements are parallel to each other, which in turn are parallel to $[111]_p$ (the shifts of the oxygens are also in the same direction). Displacement of the A-site cations along $[111]_p$ results from a need to achieve minimisation of the electrostatic energy associated with the tilting octahedra and also are presumably driven (to a differing extent) by the need to accommodate the steroactive lone pair on Bi^{3+}. Figures 3.14 (a) and (b) show the Na/Bi (*s*) and Ti (*t*) fractional displacements along c_H plotted as a function of temperature for the rhombohedral phase of NBT. A view of the structure down [001] showing the tilt system is shown in Figure 3.15. The overall displacement of cations calculated in the Rietveld refinements are from the centres of their co-ordination polyhedra.

The overall trend in *s* and *t* displacements is a decrease of with increasing temperature. This is expected and is brought about by the contraction of the c_H axes and elongation of the a_H axes with increasing temperature (consequently the *c/a* ratio decreases giving rise to decreases in Na/Bi and Ti shifts relative to their oxygen octahedra). At temperatures lower than ≈ 273 K, the fractional displacement of the Na/Bi cations is approximately twice that of the Ti cations, but at higher temperatures, when the phase is changing to the tetragonal symmetry, these displacements become comparable. The displacement progression with temperature is markedly different for the cation types. The Ti displacements gradually decrease in an approximately linear manner with temperature. Na/Bi displacements decrease fairly constantly until 573 K (coexistence region), when there seems to be a greater relative change, resulting in values comparable with Ti at that temperature. The Na/Bi displacements up to this temperature are approximately twice that of Ti displacements. A similar trend is seen in the B-site substituted perovskite PZT[27], with the shift of the A-cation being 1.5 times that of the B-cation.

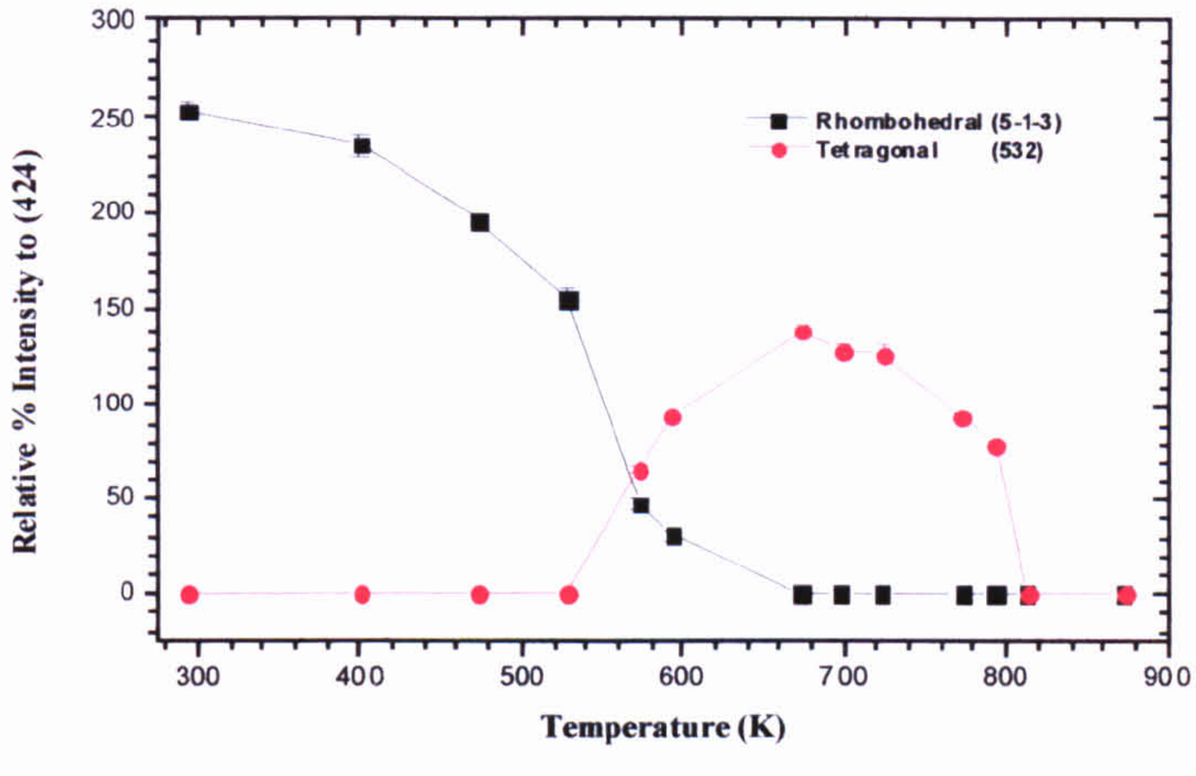

Figure 3.10. *Variation in intensity of (5-1-3) & (532) superstructure peaks relative to (424) main peak.*

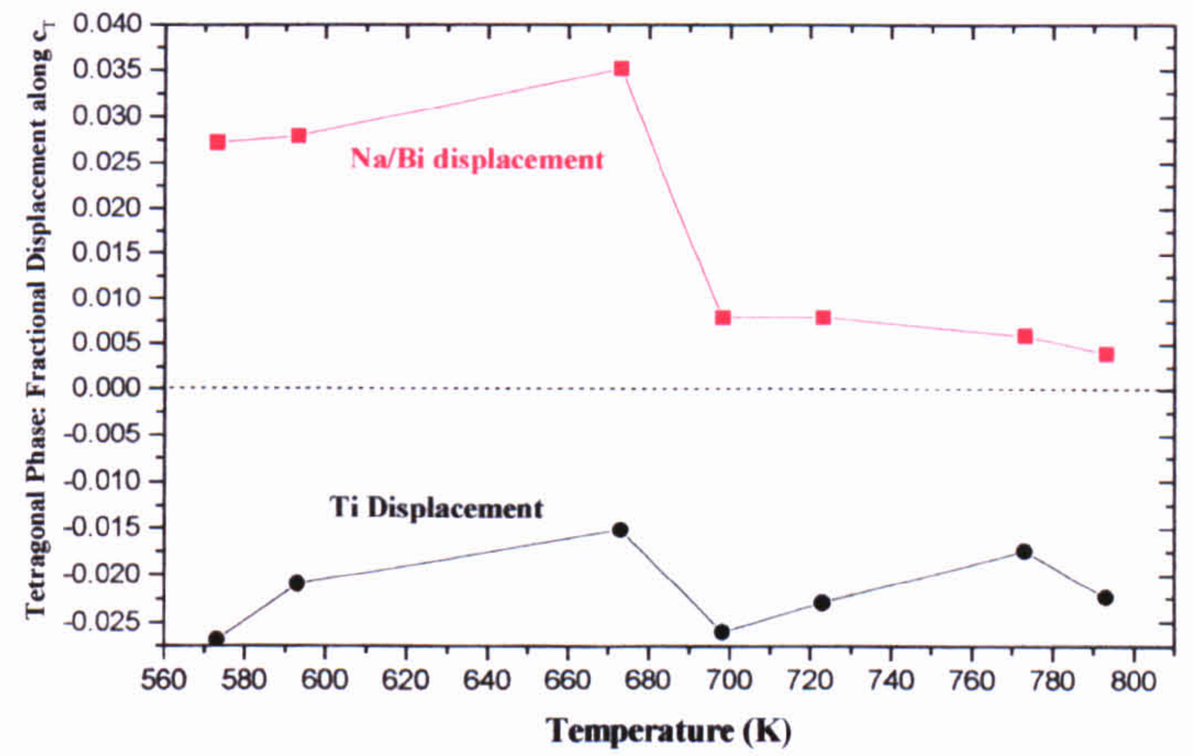

Figure 3.11. *The variation of cation shifts (expressed in fractions of c_T), with temperature.*

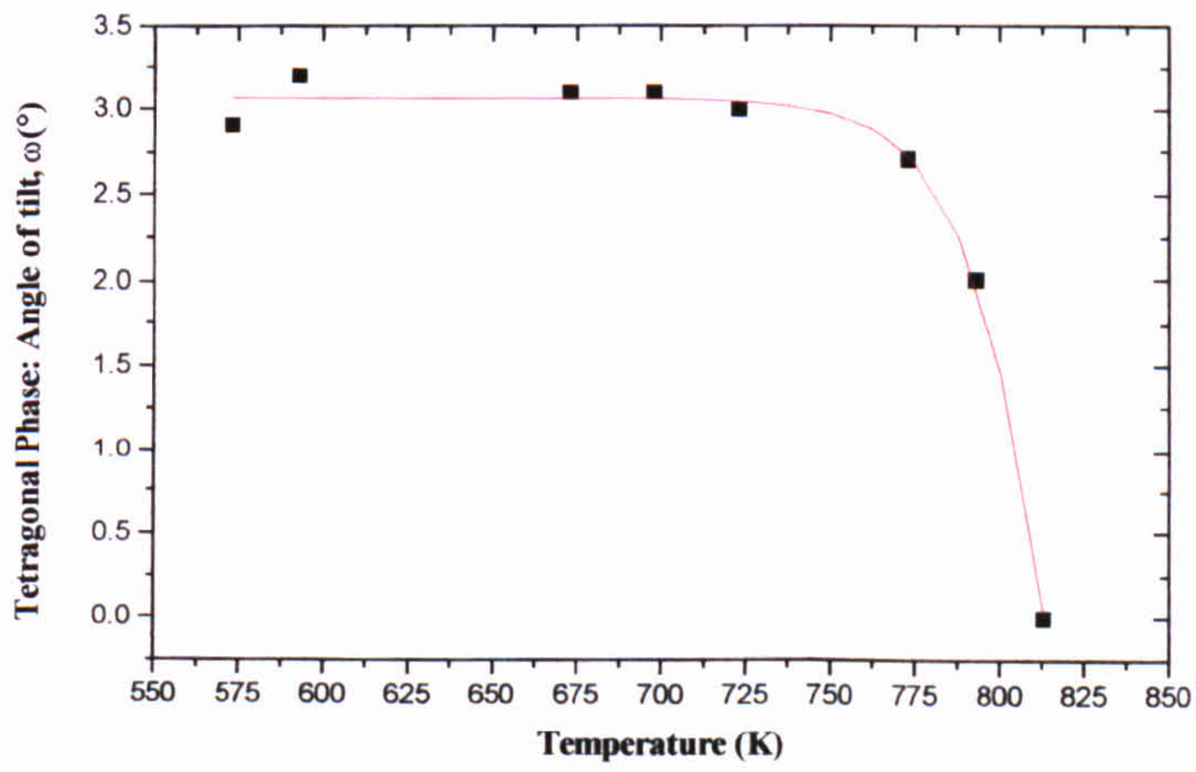

Figure 3.12. *The variation of octahedral tilt angle (ω°) with temperature.*

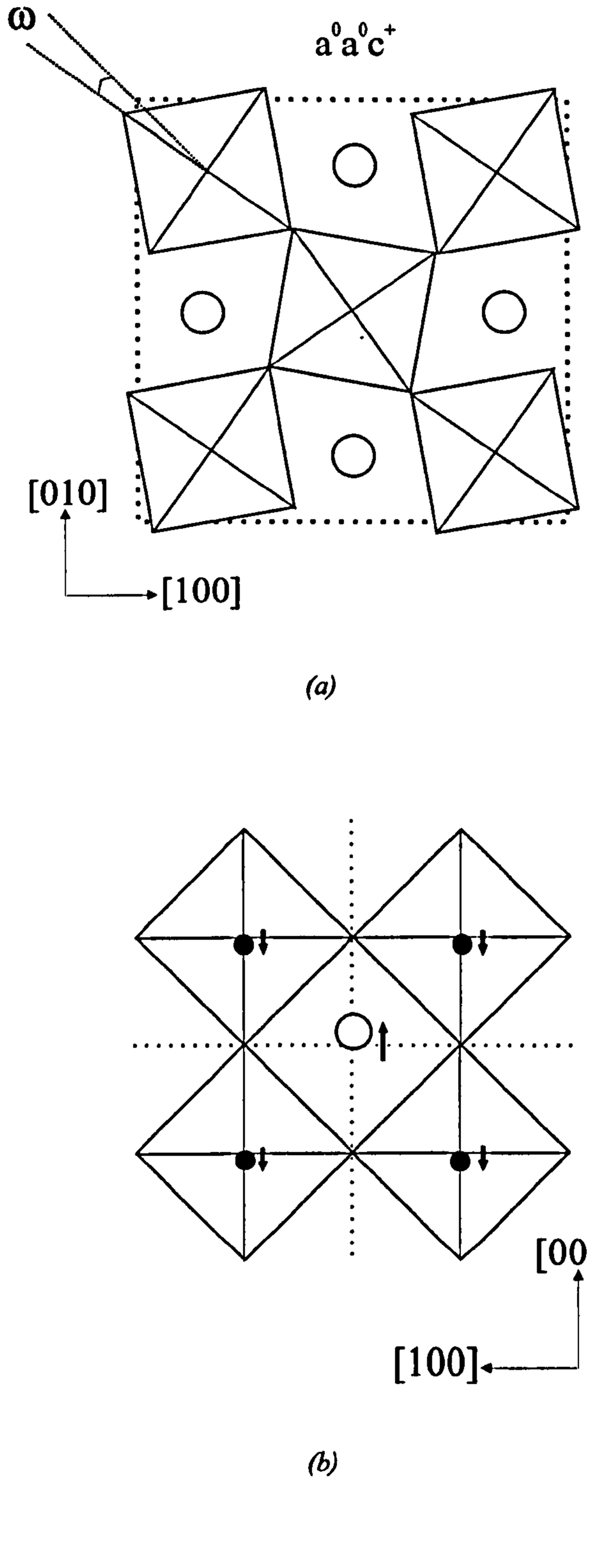

Figure 3.13. *(a). The projection of the tetragonal structure down [001], open circles represent Na/Bi sites. (b) A view of the tetragonal structure along [010], showing the octahedral tilting about the polar c-axis and the relative cation displacements. The open circles represent Na/Bi sites, smaller filled circles represent Ti sites.*

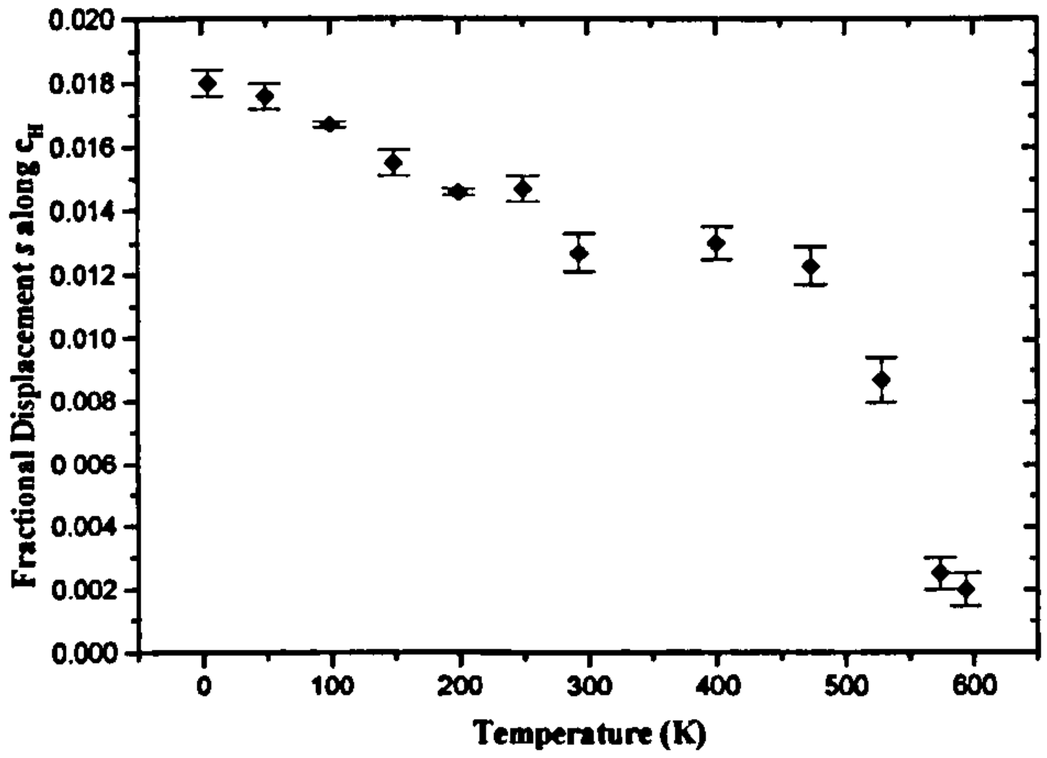

(a)

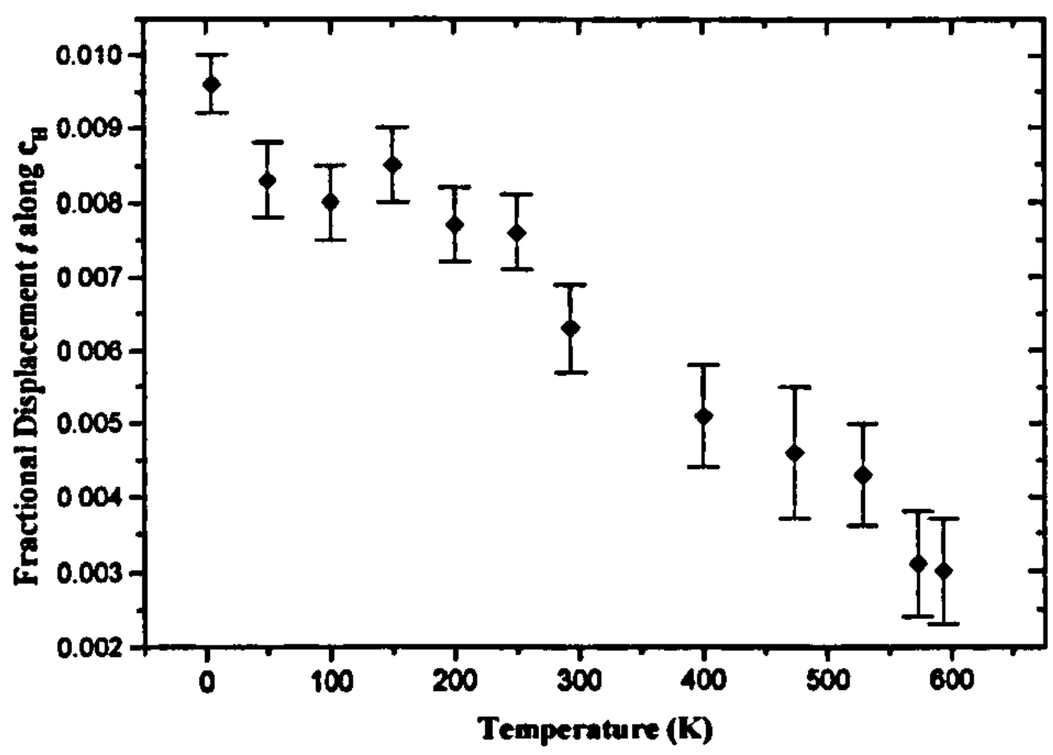

(b)

Figure 3.14. *(a) The variation of Na/Bi cation shifts (expressed in fractions of c_H) with temperature, (b) The variation of Ti cation shifts (expressed in fractions of c_H) with temperature.*

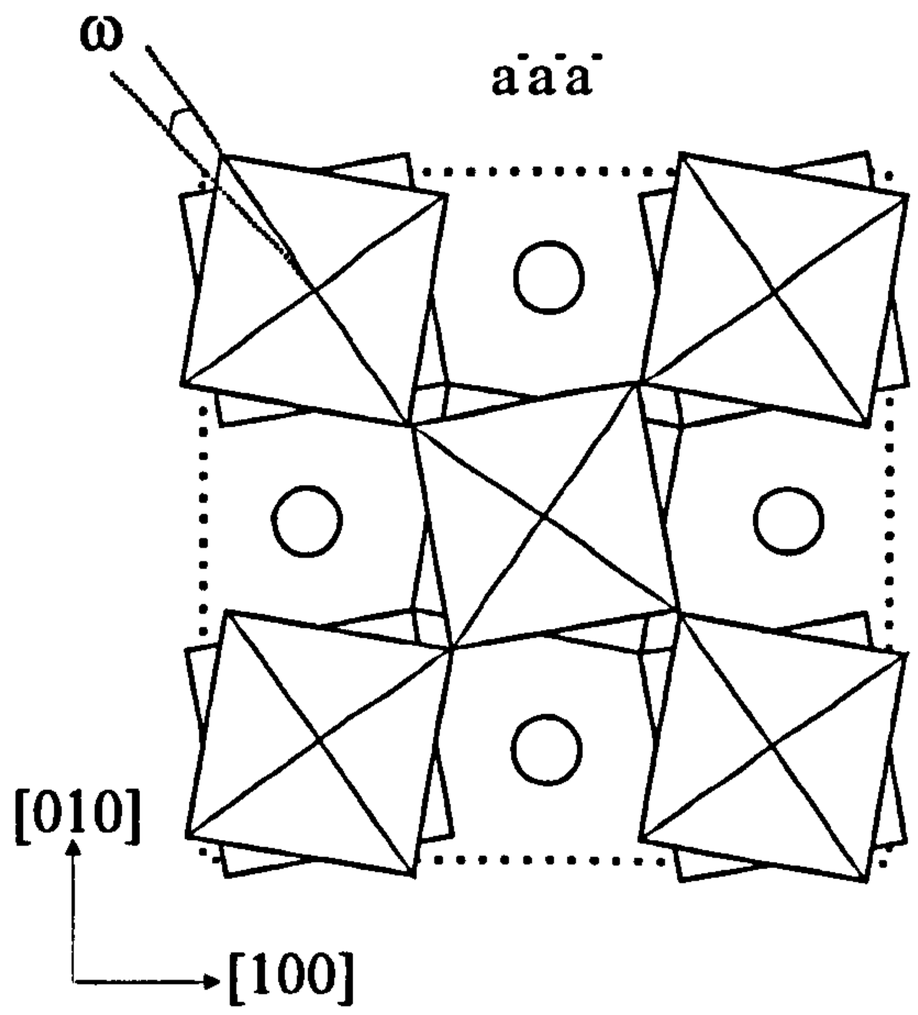

Figure 3.15. *The projection of the rhombohedral structure down [001], open circles represent Na/Bi sites.*

Figure 3.16 (a) shows the thermal evolution of the experimentally-determined tilt angle ω. It clearly shows a continual decrease in the octahedral tilting with increasing temperature. The Na/Bi (*s*) displacement variation with temperature decreases in the same manner. The room-temperature octahedral tilt angle, estimated from oxygen fractional co-ordinates, was found to be 8.24 (4)°. As a comparison, $NaNbO_3$ (at 123 K) $a^-a^-a^-$ tilt system has an octahedral tilting angle equal to 12.1°[13] and $Ag_{0.5}Bi_{0.5}TiO_3$, which shows antiphase rotations about the *c*-axes, tilt system $a^0a^0c^-$ has a similar tilting angle of 8.91 (1)°[24].

The tilt angle and the hexagonal cell parameters are coupled through an additional parameter known as the octahedral strain, ζ. This has been defined by Megaw and Darlington[13], where the factor $1 + \zeta$ is the elongation ($\zeta > 0$) or compression ($\zeta < 0$, $\zeta = 0$ for unstrained octahedra) of the octahedron along c_H. They found that for many of the perovskite-type structures, the octahedral strains are generally negative and decrease when the tilt angle decreases. The evolution of the experimentally determined octahedral strain ζ with temperature, calculated from the unit-cell dimensions, is shown in Figure 3.16 (b). It shows a gradual fall with increasing temperature similar to the tilt angle progression. The sign of the octahedral strain ζ is negative signifying that a flattening of the octahedral units occur. The variation of the octahedron distortion parameter *d*, is not shown, as it remains constant throughout the temperature range to within experimental error (e.g. -0.0006 (3) at 273 K). As the sense of *s* and *t* has already been allocated, the sign of *d* is no longer arbitrary. The distortion remains negative over the temperature range suggesting that the upper face of the octahedron is larger than the lower face. Figure 3.16 (c) shows the relationship between octahedral strain ζ and tilt angle ω, indicating a generally linear relationship.

3.3.5.4 Valency Calculations

A valency deficiency gives rise to a displacement of the cation. The cation moves off centre in order to achieve a valency closer to its ideal value. Bond valence calculations for the room temperature rhombohedral phase were performed using the program VaList[29], with the cations at their refined positions. This gave values for Na^{1+} and Ti^{4+} only 6 % and 2 % different, respectively, from their ideal values. However, the bond valence sum calculated for Bi^{3+} shows a 22 % deficiency from its ideal value of 3.0. In the rhombohedral (R3c) phase of $BiFeO_3$, Bi^{3+} has a valence deficiency of 19 %

despite a displacement along the polar axis, to distort its co-ordination, as large as 0.55 Å. Displacement of Bi^{3+} and valence deficiency was also seen in the orthorhombic phase of $Ag_{0.5}Bi_{0.5}TiO_3$[24] and in the tetragonal phase of NBT[30] with Bi^{3+} showing a 26 % and 32 % deficiency respectively from its ideal value.

Even though Bi^{3+} moves off-centre in order to satisfy its own stereo-chemical preferences, on the A-site of perovskite structures in rhombohedral, tetragonal and orthorhombic polar phases, it seems that it is unable to achieve a perfect match to its valency. It is clear that the character of the bismuth cation plays an important role in determining displacements. The fact that no displacements are present in the analogue $Nd_{0.5}Ag_{0.5}TiO_3$[22], lends support to this idea.

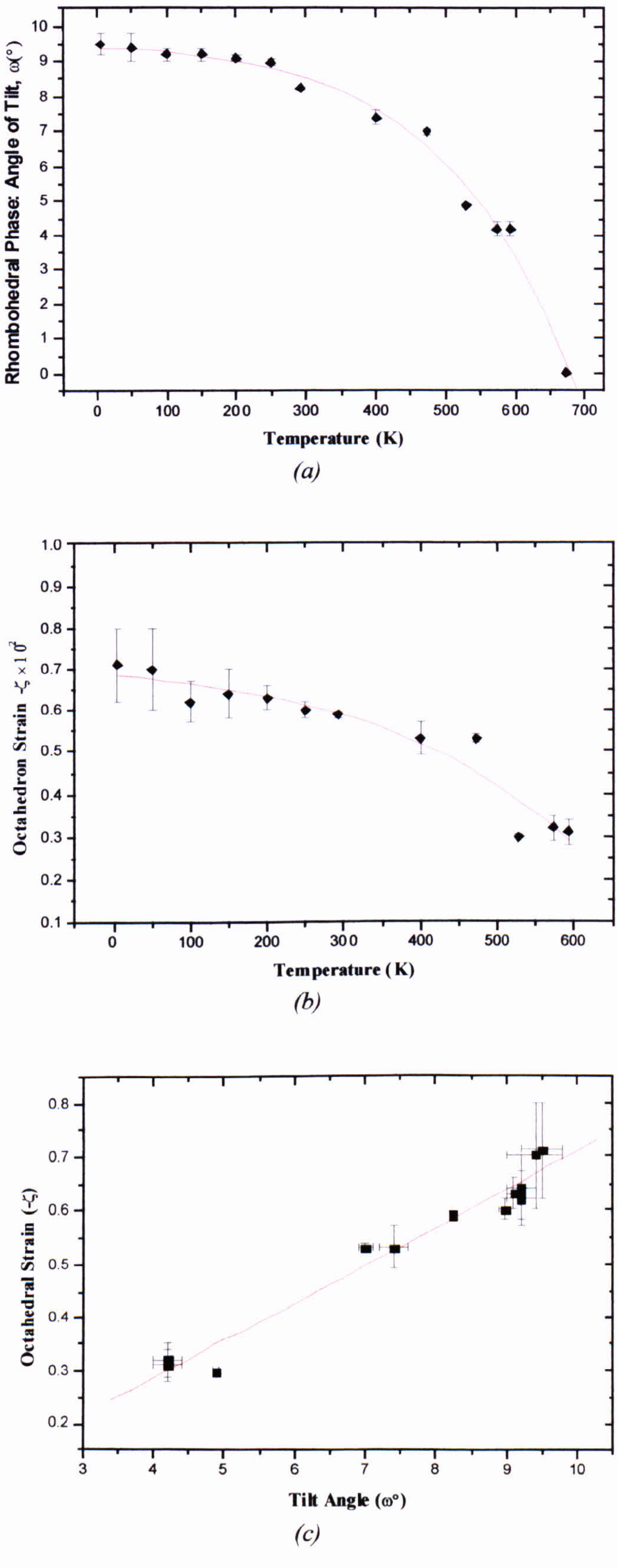

Figure 3.16. *(a) Variation of the octahedron tilt angle, ω with temperature, (b) variation of the octahedral strain, ζ with temperature, (c) variation of octahedral strain, ζ with tilt angle, ω. The lines of best fit to the data act as guides to the eyes only.*

3.4 X-ray Powder Diffraction

X-ray powder diffraction experiments, using a synchrotron radiation source were undertaken as a function of temperature for NBT. Data collections were taken in order to supplement neutron powder diffraction results. This section summarises physical characteristics in each phase and reports structural heating/cooling hysteresis effects observed in NBT.

3.4.1 Synchrotron Radiation Source, Daresbury - Station 9.1

Synchrotron radiation has the advantage over conventional x-ray sources of possessing a much larger photon flux (typically a 1000 × gain). A broad spectral range of radiation is also available and allows the selection of an optimum wavelength to be used, thereby reducing problems associated with wavelength-dependent factors such as absorption and radiation damage. The Synchrotron Radiation Source, CCLRC Laboratory, Daresbury provides an extremely highly collimated x-ray beam with an electron energy of 2 GeV and a beam current of 150-300 mA. XRPD as a function of temperature was carried out on Station 9.1 at Daresbury. The Station houses a 2-circle diffractometer, which operates in the Debye-Scherrer geometry or in flat-plate geometry. The Station receives 2.5 mrads divergence of unfocused beam, which is monochromated by a water-cooled channel-cut Si 111 monochromator crystal. This results in a monochromated beam of around 0.6 mrads divergence being delivered onto the sample with a wavelength range between 0.4-1.5 Å.

3.4.2 Sample Preparation

Fragments of flux grown NBT crystals were finely ground into powder. The powder was sieved to obtain particles with diameters of < 38 μm. NBT is a highly absorbing material for x-rays because of the presence of bismuth so the smallest diameter (0.2 mm) capillaries available were chosen to house the sample. The small diameter of the capillary reduces the quantity of the sample required and increases the transmission of the x-rays to allow better analysis. Powders were dried in an oven to remove any moisture (to facilitate filling of the capillary) and packed as densely as possible into the quartz glass capillaries.

3.4.3 Data Collections and Treatment

A radiative heating high-temperature capillary furnace[31] was used to allow data to be collected from room temperature to 873 K. The furnace and diffraction geometry are shown schematically in Figure 3.17. Heating was provided by a water-cooled RF copper coil and was remotely controlled by an Eurotherm 900 controller. A K-type thermocouple (273-1500 K) was used to measure the temperature, with a thermal stability of ± 1 K.

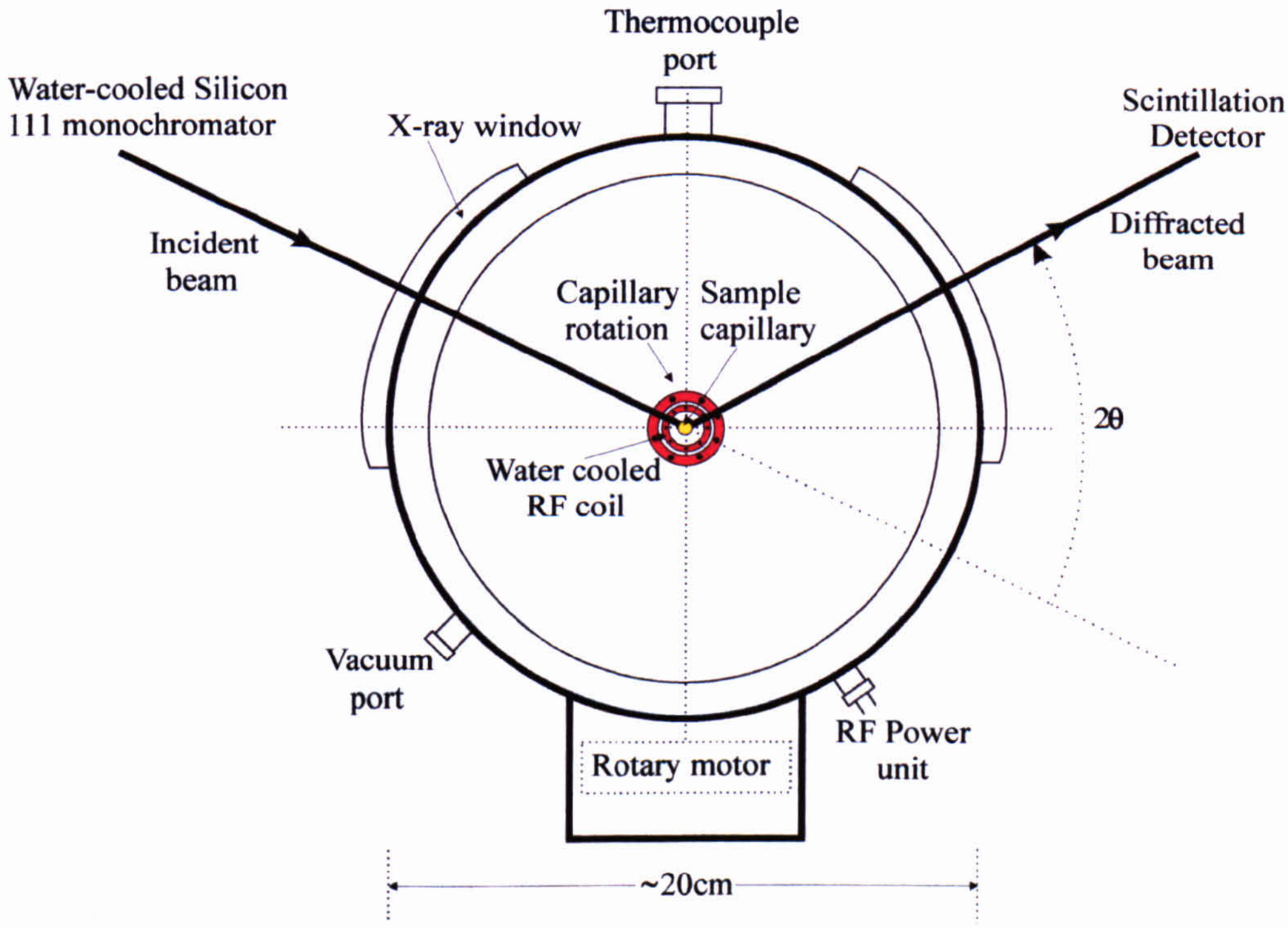

Figure 3.17. Furnace and diffraction geometry of Station 9.1 diffractometer.

Before high-temperature data collections were carried out the furnace controller temperature readings and sample temperatures were calibrated. An independent K-type thermocouple connected to a calibrated Comark digital thermometer was positioned exactly where the beam was incident on the sample. The sample was heated and left to stabilise. At regular intervals, readings from the Comark and controller were compared to see if any disparities existed. In this way, accurate sample temperatures were found. Two controllers were used on separate occasions. Figure 3.18 (a) shows the linear relationship between controller temperature and sample temperature for the runs carried out with a wavelength 0.485Å and Figure 3.18 (b) for runs at 0.551 Å. There is a linearly varying offset between temperatures, with the sample temperature always being lower than the temperature the controller displays. This resulted from the existence of a small

air gap between the furnace and the sample. Temperatures listed for the runs are the actual sample temperatures.

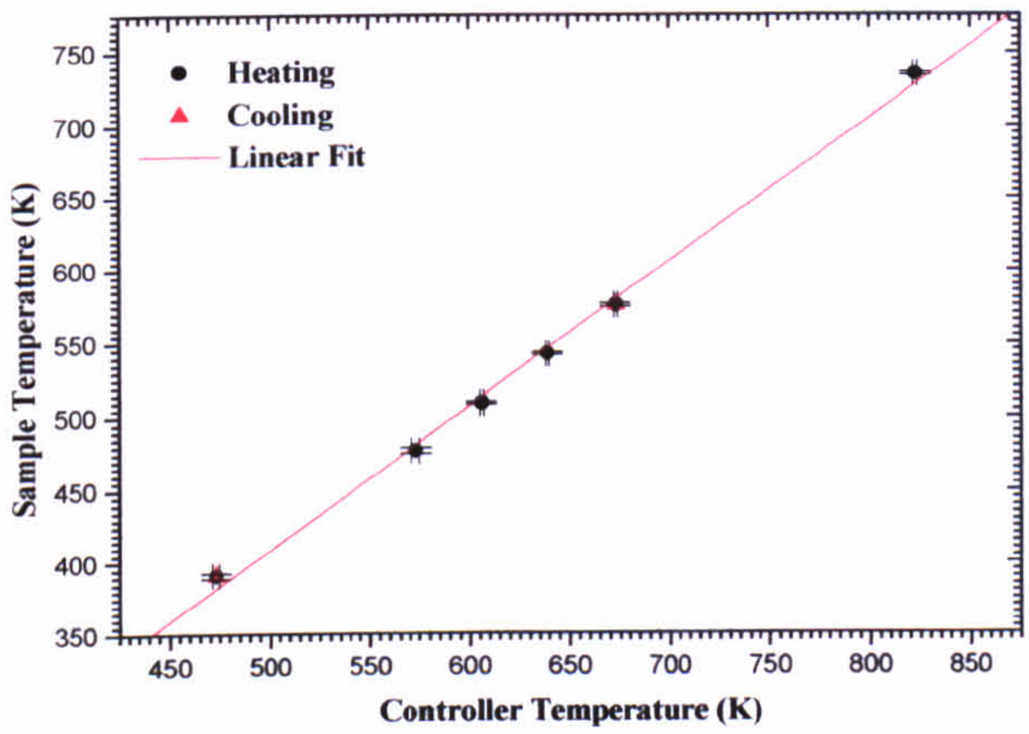

(a)

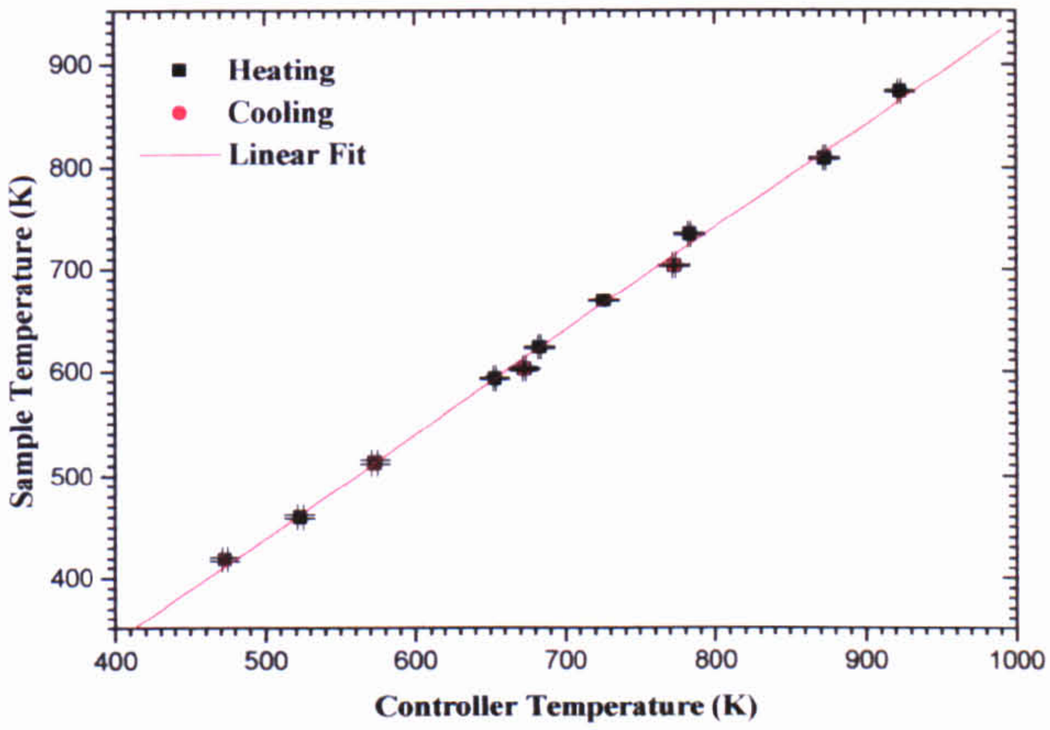

(b)

Figure 3.18. Furnace calibration graphs, (a) runs at 0.485 Å, (b) at 0.551 Å.

Data sets were collected on two separate occasions, the first sets of data were carried out using a wavelength of 0.485 Å. Data sets were collected in sections around the 100, 111, and 222 peaks on heating and cooling, in order to investigate crystal symmetry and lattice parameters as a function of temperature and to plan temperatures at which full scans were to be carried out. The second sets of data were acquired using a wavelength of 0.551 Å. Data sets were collected in sections between ≈ 8-36°. All data collections were performed with the same 2θ-step size of 0.004. The collection of data in sections allows weak high angle reflections to be collected with longer counting times thus improving the counting statistics in that part of the pattern. At the refinement stage it is important to have good quality data for reflection at high angles as they contain information about the thermal vibrations of the atoms as well as precise structural information. The intensities of these reflections were subsequently normalised before refinement. The angular ranges and counting times are given in Table 3.07.

Data collections were performed using synchrotron radiation with a wavelength of 0.485 Å and 0.551 Å. These are above the Bi absorption K-edge, which is at 0.137 Å and were chosen to minimise fluorescence. All data collections were put through a data reduction program prior to refinement. This program, written within the research group, normalised the data with respect to the decay of the synchrotron radiation beam over time and corrected for the absorption of the sample and the quartz capillary. The program utilised mass absorption coefficient data from the International Tables of X-Ray

Crystallography, Volume III[32]. In the calculations for absorption corrections, capillary packing densities were estimated to be 60 %.

Wavelength (Å)	*Temperature (K)*	*Angular Range (°)*	*Time/Step (s)*	*Total Time (Hrs)*
NBT 0.485	293 (heating) 391 (heating/cooling) 575 (heating/cooling) 735 (heating)	6.7-20, 20-31 12.25-12.7, 24.85-25.3 12.22-12.67, 24.85-25.3 6.7-20, 20-31	3, 7 3, 7 3, 7 2.5, 6	8.1 0.3 0.3 6.9
NBT 0.551	293 (heating) 733 (heating) 873 (heating)	8-22.5, 22.5-36 8-22.5, 22.5-35.6 7.96-22.5, 22.5-35.6	2, 4 1.5, 3.5 1.75, 2.75	6.6 5.1 5.1

Table 3.07. Data collection details for the different runs.

3.4.4 Rietveld Structural Refinements

Rhombohedral Phase - The room temperature refinement was carried out based on the starting model obtained from the corresponding neutron refinement. The diffraction pattern shows only slight rhombohedral broadening of lines and only the first superstructure reflection (131) is observed. This peak had one of the highest intensities in the neutron scans but an extremely low intensity here. The minimal intensity of this peak is to be expected as it arises from the tilting of the oxygen octahedra, and as previously stated the overwhelming scattering effects of bismuth makes it difficult for x-rays to determine accurate information about the oxygen atom positions. Structural refinements were carried out (as in neutron refinements) with reference to hexagonal axes, the lattice parameters of which, a_H and c_H, are specified with relation to the double pseudo-cubic cell ($2a_p \times 2b_p \times 2c_p$) by the matrix (3.11). The structure was refined in space group R3c. The background was based on a linear function and peak shapes were described by pseudo-Voigt profiles. Isotropic temperature parameters were initially refined for all atoms and then anisotropic parameters were refined with the exception of the oxygen atoms. The refinement of anisotropic temperature factors for the oxygen atoms resulted in unrealistically large and sometimes negative parameters. Allowing only isotropic refinements for oxygen yielded realistic values. Following the procedure carried out for neutron refinements (section 3.3.4) the occupancies of Na and Bi, initially

constrained at 0.5 were allowed to refine separately, resulting in values of 0.511 (2) and 0.489 (2). Within the errors these values agreed with those refined in the neutron case. The occupancies were subsequently fixed at 0.5 for further refinements. Na and Bi positions were then allowed to refine independently with the result that Bi became displaced 0.004 Å along the polar (+c) axis with respect to Na. The Na and Bi positions were subsequently constrained to occupy the same co-ordinates for all further refinements. The refinement was stable and converged quickly. Crystallographic data and refined profile parameters are summarised in Tables 3.08 and 3.09. The observed, calculated and difference profiles from the final Rietveld refinement in R3c at 293 K are shown in Figure 3.19 (a).

Tetragonal Phase - The diffraction pattern obtained at 773 K shows sharper peak shapes than the room temperature pattern and also the disappearance of the weak superstructure reflection. No tetragonal superstructure peaks could be seen. Refinement was carried out based on the starting model obtained from the corresponding neutron refinement in space group P4bm. Na and Bi each with site occupancies 0.5, were again constrained to be at the same co-ordinates, the background was based on a linear function and peak shapes based on earlier refinements of the room temperature structure, were described by pseudo-Voigt profiles. The refinement was stable and converged quickly. Crystallographic data and refined profile parameters are summarised in Tables 3.08 and 3.09. The observed, calculated and difference profiles from the final Rietveld refinement in P4bm at 773 K are shown in Figure 3.19 (b). As no superstructure peaks were observed, the space group P4mm was also tried. This is a non-centrosymmetric space group that allows cation displacements but does not allow superstructure reflections. The starting model was initially based on the neutron diffraction model at the corresponding temperature. The refinement progressed satisfactorily ($R_p = 0.0532$, ${}_wR_p = 0.0686$ & $\chi^2 = 0.7552$) until the positional parameters were refined. The refinement at this point was unstable and diverged. The refinement was repeated with starting positions given at their ideal sites without any cation displacements. The refinement still was unstable and could not be refined, in contrast to the P4bm model.

Cubic Phase - The diffraction pattern obtained at 873 K shows the sharpest peak profiles. The space group $Pm\bar{3}m$ was used as before. The refinement was stable and converged quickly. Crystallographic data and refined profile parameters are summarised

in Tables 3.08 and 3.09. The observed, calculated and difference profiles from the final Rietveld refinement in $Pm\bar{3}m$ at 873 K are shown in Figure 3.19 (c).

Rhombohedral (R3c) Phase (293 K)

Atom	x	y	z	U11	U22	U33	U12	U13	U23
Na	0.0	0.0	0.2665(1)	0.017(6)	0.017(6)	0.040(2)	0.009(3)	0.0	0.0
Bi	0.0	0.0	0.2665(1)	0.044(1)	0.044(1)	0.072(2)	0.022(1)	0.0	0.0
Ti	0.0	0.0	0.0109(7)	0.025(1)	0.025(1)	0.013(3)	0.012(1)	0.0	0.0
O	0.127(2)	0.341(3)	0.0833†	0.015(2)	Isotropic				

†$O_{(z)}$ fixed to deal with floating origin.

Tetragonal (P4bm) Phase (773 K)

Atom	x	y	z	U11	U22	U33	U12	U13	U23
Na	0.0	½	0.518(4)	0.048(2)	0.048(2)	0.051(3)	0.041(4)	0.0	0.0
Bi	0.0	½	0.518(4)	0.079(2)	0.079(2)	0.10(3)	-0.007(4)	0.0	0.0
Ti	0.0	0.0	0.0†	0.021(2)	0.021(2)	0.037(5)	0.0	0.0	0.0
O(I)	0.0	0.0	0.510(2)	0.035(7)	Isotropic				
O(II)	0.272(2)	0.228(2)	0.033(4)	0.053(3)	Isotropic				

†$Ti_{(z)}$ fixed to deal with floating origin.

Cubic ($Pm\bar{3}m$) Phase (873 K)

Atom	x	y	z	U11	U22	U33	U12	U13	U23
Na	0.0	0.0	0.0	0.046(7)	0.046(7)	0.046(7)	0.0	0.0	0.0
Bi	0.0	0.0	0.0	0.082(1)	0.082(1)	0.082(1)	0.0	0.0	0.0
Ti	½	½	½	0.026(1)	0.026(1)	0.026(1)	0.0	0.0	0.0
O	½	½	0.0	0.042(2)	Isotropic				

Table 3.08. Fractional co-ordinates and equivalent anisotropic displacement parameters ($Å^2$) for NBT.

Chemical formula	$Na_{0.5}Bi_{0.5}TiO_3$		
Chemical formula weight	211.88		
Specimen Shape	Random powder		
Specimen preparation	Crystal growth from flux, Powder prepared from ground crystals		
Specimen Pressure	Ambient		
Radiation Type	Synchrotron		
Wavelength	0.551 Å		
Crystal System	**Rhombohedral**	**Tetragonal**	**Cubic**
Temperature (K)	293	773	873
Space Group	R3c	P4bm	$Pm\bar{3}m$
a_H (Å)	5.4800 (1)	-	-
c_H (Å)	13.4716 (5)	-	-
a_p (Å)	-	5.5097 (1)	3.90719 (5)
c_p (Å)	-	3.9024 (1)	-
α,β,γ (°)	90,90,120	90,90,90	90,90,90
α_p(°)	89.86	-	-
Volume (Å^3)	350.35 (2)	118.464 (5)	59.647 (2)
Z	6	2	1
D_x (Mg.m^{-3})	6.025	5.940	5.874
s	0.016 (1)	0.008 (2)	0.0
t	0.011 (1)	-0.033 (4)	0.0
d	-0.0019 (8)	-	-
e	0.0217 (7)	-	-
Tilt System	$a^-a^-a^-$ (three tilt system, anti-phase)	$a^0a^0c^+$ (one tilt system, in-phase)	$a^0a^0a^0$ (zero-tilt system)
Displacements	Parallel along $[111]_p$	Anti-parallel along [001]	None
ω (°)	8.6 (3)	3.28 (3)	0.0
$\zeta \times 10^2$	-0.77 (8)	-	-
DATA COLLECTION			
Specimen mounting	Quartz capillary	Quartz capillary	Quartz capillary
Scan Time (hours)	6.6	5.1	5.1
$2\theta_{min}$ (°)	8	8	7.96
$2\theta_{max}$ (°)	36	35.6	35.6
REFINEMENTS			
Background / coefficients	linear interpolation / 8	linear interpolation / 8	linear interpolation / 8
Scale	0.1791(5)	0.632(2)	0.33(2)
2θ zero-error	-0.05(3)	0.38(2)	0.45(2)
G(U), G(V), G(W), G(P).	321(3), -66(7), 4(5), 0.1(3)	10.5(7), -0.10(9), 0.25(1)	1.6(5), -1.12(8), 0.28(9), 0.20(1)
L_x, L_y	1.37(5), 6(3)	0.18(1), 10.7(9)	0.07(1), 11.73(9)
S/L, H/L.	0.01281(8), 0	0.0099(4), 0	0.0106(4), 0.00083(4)
Stec, Ptec, Sfec.	9.3(5), 0.61(5), 0	-2.4(2), -0.03(2), 0	-2.9(3), -0.1(5), 0
N$^{\underline{o}}$ of refined parameters	41	42	38
Profile R-factors			
R_p	0.058	0.052	0.053
$_wR_p$	0.073	0.066	0.067
χ^2	0.714	0.755	0.654

Table 3.09. *Summary of experimental details, data collection and refinement for the three phases of NBT.*

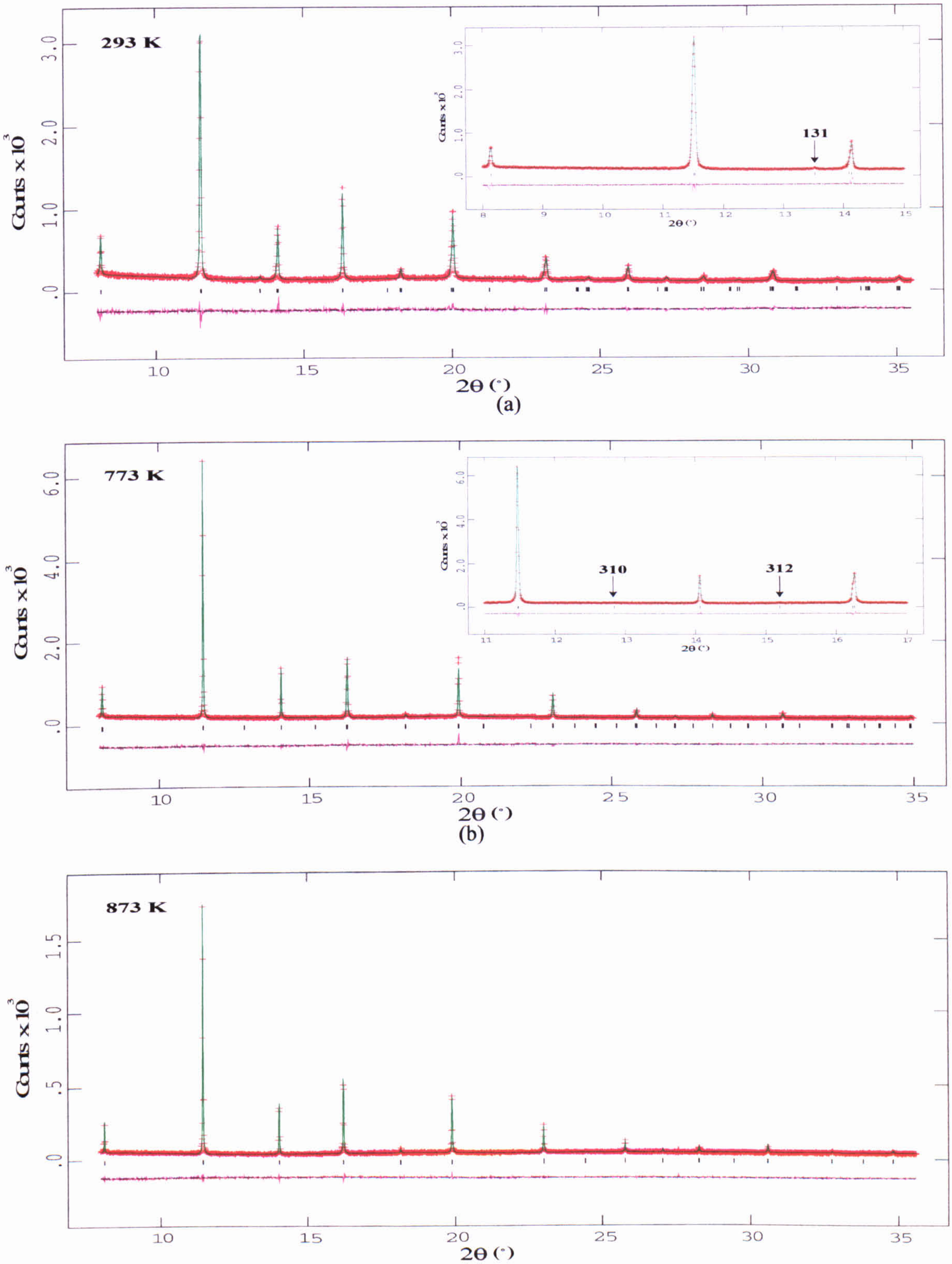

Figure 3.19. *The observed, calculated, and difference curves from the Rietveld refinement of $Na_{0.5}Bi_{0.5}TiO_3$, for $\lambda = 0.551$ Å. The marks indicate the positions of the reflections. (a) refinement in R3c, at 293 K, the low angle data ($8<2\theta<15°$), showing the first superstructure peak is magnified in the insert. (b) refinement in P4bm, at 773 K, the low angle data ($11<2\theta<17°$), showing the positions where the first two superstructure peaks would be, are magnified in the insert. (c) refinement in $Pm\bar{3}m$, at 873 K.*

3.4.5 Discussion

Due to the limited time available only one full scan in each phase could be measured. Regions around certain peaks were obtained in order to observe the variation of lattice parameters with temperature on heating and cooling. Figure 3.20 (a) shows the progression of lattice parameters on heating and cooling. An overall increase in the lattice parameters is observed as expected with increasing temperature. The lattice parameters obtained from the full scans and subsequent refinements, (on heating) are all slightly less but in good agreement with the corresponding values obtained through neutron refinements (Table 3.06 & Figure 3.07). Unfortunately due to the limited number of scans taken, no conclusions can be reached about the phase transition temperatures. There is a thermal hysteresis in the lattice parameters on heating and cooling. Figure 3.20 (b) shows the shift in the 222 reflection at 391 K (rhombohedral phase) and 575 K (tetragonal phase) on heating and cooling. The rhombohedrally broadened 222 peak position at 391 K has a 2θ shift of 0.0469°, corresponding to a lattice parameter change Δa_R = 0.0166 (1) Å. In the 575 K case, the now single peak shows a shift of 0.0177° which corresponds to a lattice parameter change Δa_T = 0.0056 (1) Å. This hysteresis could explain the variation in the structural phase transition temperatures found in this neutron study (section 3.3.5.1), which was performed on heating, and the results obtained from the x-ray study by Suchanicz & Kwapulinski[16], which was performed on cooling.

With relation to octahedral tilting, only a weak intensity 131 superstructure reflection could be observed at room temperature. The room temperature octahedral tilting angle ω, estimated from oxygen fractional co-ordinates was calculated to be 8.6 (3)°, with the associated octahedral strain ($\zeta \times 10^2$), being –0.77 (8), the values being slightly higher than corresponding values found in neutron diffraction studies (section 3.3.5.3). The cation displacements in comparison with the neutron room temperature results are also slightly higher (i.e. Δs = 0.0033 (4), Δt = 0.0047 (4)) and are more comparable to the 50 K results.

The octahedral tilting in the tetragonal phase was found to be 3.28 (3)°, whereas in the neutron case at this temperature a value of 2.7 ° is found. Likewise as in the rhombohedral case, the cation displacements in comparison with the neutron results are also slightly higher (i.e. Δs = 0.002 (3), Δt = 0.016 (4)) and are more comparable to the 573 K results.

In this study no superstructure peaks associated with cation-ordering were observed in NBT. This is consistent with neutron diffraction results (section 3.3.5.2).

Valency calculations on the room temperature structure reveal similar results obtained from neutron data, with values for Na^{1+}, Ti^{4+} being only 9 % and 3 % different, respectively, from their ideal values and Bi^{3+} showing a 21 % deficiency from its ideal value. In the tetragonal phase (773 K) deficiencies of 4 %, 2 % and 41 % are seen for Na^{1+}, Ti^{4+} and Bi^{3+} respectively.

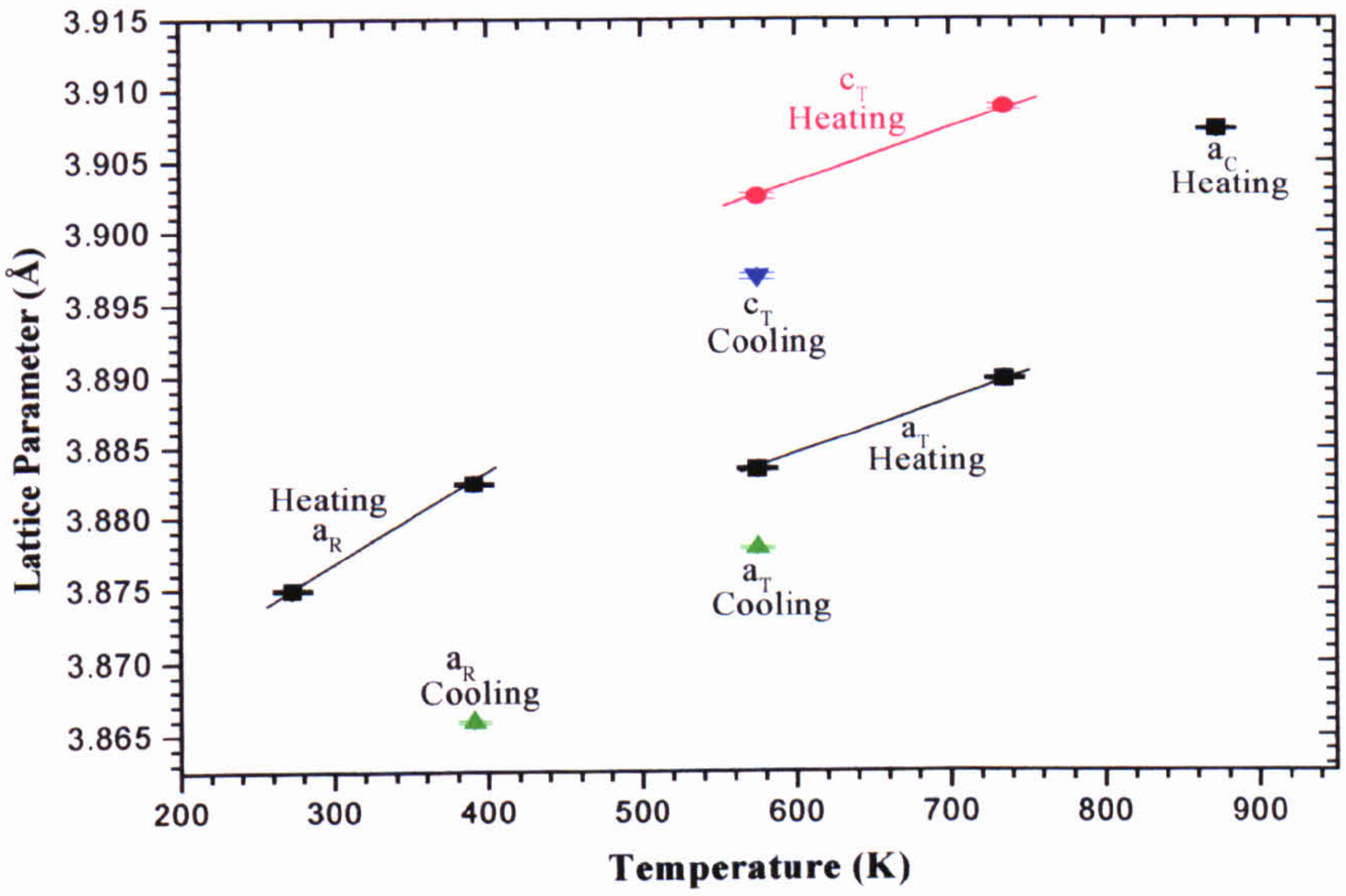

(a)

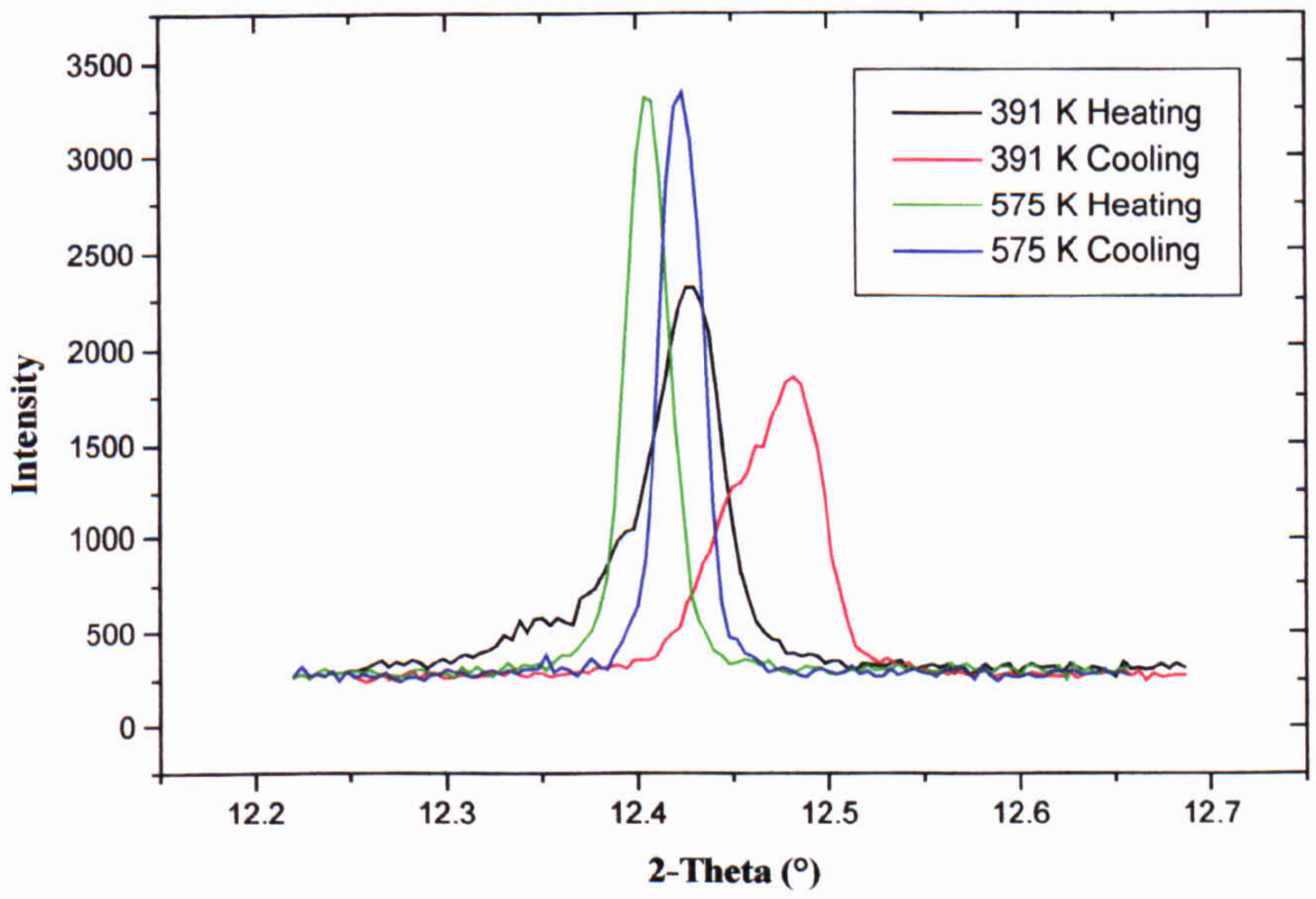

(b)

Figure 3.20. *(a) Lattice parameter evolution as a function of heating and cooling. (b) The 222 reflection (on doubled unit cell) on heating/cooling for $\lambda = 0.485$ Å.*

3.5 Single Crystal X-ray Diffraction

Single crystal x-ray diffraction experiments were carried out in order to supplement characterisation work on powdered samples of NBT. In this way, it was hoped that the use of different techniques might reveal new information on this compound.

In order to calculate the relative structure factor amplitudes (F_H) used in solving crystal structures, the observed intensities measured on a single crystal diffractometer must be amended by the application of suitable correction factors. The procedure followed in order to extract this information from raw integrated intensities is termed data reduction. In this process, the various reflection-dependent factors present are taken into account. The integrated relative intensity I_H of a reflection is given by[33]:

$$I_H = k_1 k_2 I_o LPTE|F_H|^2 \qquad (3.13)$$

where k_1, k_2 are scaling factors, I_o is the intensity of the incident beam, L, P, T, are the Lorentz, polarisation and transmission factors respectively, and E is the extinction coefficient.

The Lorentz correction[34] expresses the relative time for which a given set of planes is in the reflecting position. The reciprocal lattice nodes are not infinitesimal points but have a finite size. They therefore spend a finite time passing through the surface of the sphere of reflection. This is not normally the same for all points. If a reciprocal lattice point is in the diffracting position for a longer time the intensity of the corresponding reflection will be proportionally higher. The Lorentz correction takes this factor into account normalising all intensities.

The polarisation correction[35,36] depends on the state of polarisation of the incident x-ray beam and on the scattering angle of the resulting diffracted beam. The crystal does not diffract waves vibrating in all directions with equal efficiency. This results in the reflected beam being partially polarised. This reduces the intensity of the diffracted beam by a factor of $(1+\cos^2 2\theta)/2$. The greatest intensity reduction occurs at $2\theta = 90°$, the least at $2\theta = 0°$or $2\theta = 180°$, and the intensities of reflections at very low and very high Bragg angles will be enhanced relative to those at intermediate values.

Absorption reduces the intensity of a x-ray beam travelling through matter (through interactions with the electron clouds of the atoms it encounters) by an amount

that depends on the material itself and the path length transversed. The reduction in intensity is given by:

$$I = I_o e^{-\mu x} \tag{3.14}$$

where I_o is the initial intensity of the beam, I is the reduced intensity after travelling a distance x through the absorbing medium and μ is the linear absorption coefficient of the medium for radiation of the relevant wavelength. The linear absorption coefficient for a crystal can be calculated from the mass absorption coefficients[32] μ_m, of the atoms present. The transmission factor T for the whole crystal, is obtained by integrating equation (3.14), over the total crystal volume V:

$$T = \frac{1}{V}\int_v e^{-\mu(p+q)} dv \tag{3.15}$$

where the path length x is replaced with incident beam path p, and the diffracted beam path length q. From the values of μ_m for a selected wavelength, μ can be calculated by the following equation[33]:

$$\mu = \rho \sum_i g_i \mu_m^i \tag{3.16}$$

where g_i is the mass fraction of element i present in the unit cell, μ_m^i, is its mass absorption coefficient and ρ is the crystal density. As μ_m^i is an increasing function of an element's atomic number and the wavelength of the radiation used, its value is smaller for lower atomic numbers and for shorter wavelengths.

The integrated intensity of the diffracted beams may also be affected by extinction[33]. There are two types of extinction, primary and secondary. Secondary extinction is the most significant. It happens when a large proportion of the primary beam is reflected by the initial lattice planes encountered and, as a consequence, deeper planes receive less of the primary radiation. For high intensity reflections at low $\sin\theta/\lambda$ values, the reduction of the diffracted intensity is greatest. Primary extinction is associated with the loss of intensity due to dynamic effects within individual mosaic blocks. At the Bragg angle every incident wave can suffer multiple reflections from different lattice planes this can lead to destructive interference, weakening the intensity for a particular reflection. Primary extinction is only significant if individual mosaic blocks are large. However, as most crystals contain many dislocations and

imperfections, the beam normally reaches a discontinuity before it has been significantly weakened. Reflections affected by extinction can be recognised in the later stages of crystal structural refinements when for some high-intensity reflection $|F_{obs}| < |F_{cal}|$, at which stage an extinction correction can be brought into the refinement to offset the effects.

3.5.1 Single Crystal Diffractometers

Single crystal diffractometers consist of an x-ray source, detector and goniometer which orients the crystal in order that the chosen x-ray diffracted beam can be received by the detector. A computer is also used to control the goniometer and detector movements, it also performs the operations required to position the crystal and detector into the desired orientation. In order to obtain integrated intensities of reflections, the entire volume of the reciprocal lattice point must be swept through the Ewald sphere while the detector records the diffracted photons. Two of the most widely used scan modes are the ω-scan and the ω-2θ-scan, shown schematically in Figures 3.21 (a) and (b) respectively. The detector is left stationary in the ω-scan mode while the crystal and the reciprocal lattice node is made to cross the Ewald sphere by a rotation of $\Delta\omega$ about the main axis. In the ω-2θ-scan the crystal is moved in the same way but the detector follows the ω rotation at twice the angular speed.

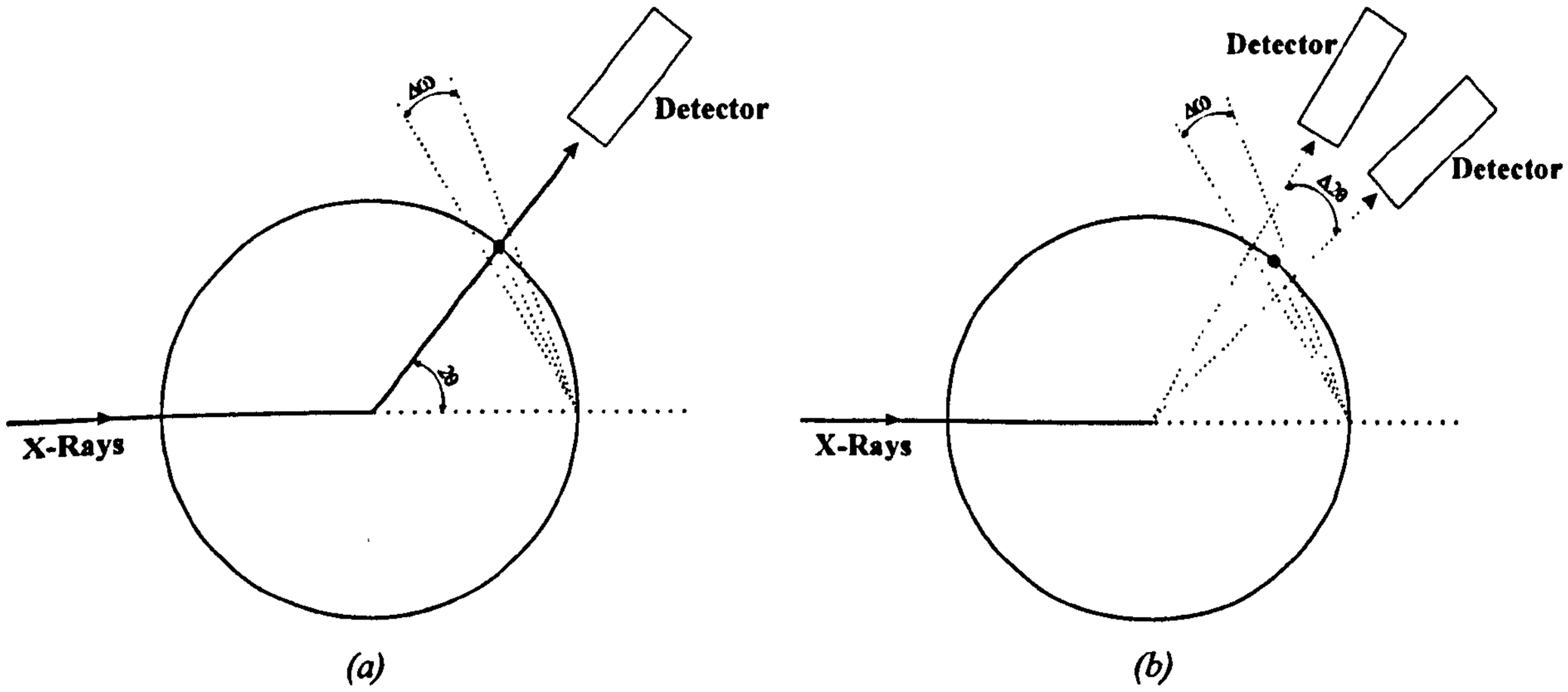

(a) *(b)*

Figure 3.21. Diffractometer scanning modes (a) ω-scan (b) ω-2θ-scan.

Single crystal data collections in this study were performed using a Stöe STADI (4-Circle) diffractometer and a Brűker SMART (3-Circle) diffractometer.

3.5.1.1 Stoë STADI 4-Circle Diffractometer

The Stoë STADI 4 is a 4-Circle Eulerian-cradle diffractometer, it has 4 independent axes of rotation shown schematically in Figure 3.22 (a). The four-circles of the diffractometer consist of the χ, and ϕ -circles about which the crystal can be orientated, the ω-circle defined by the rotation of the Eulerian-cradle, and the 2θ-circle defined by the rotation of the detector about the main axis. The x-ray source used is a molybdenum target, sealed x-ray tube and a scintillation counter is employed as the detector. Before the values of χ, ϕ, ω and 2θ at which diffraction of a specific reflection will be observed, can be calculated, the crystal orientation with respect to the Eulerian-cradle is required. A random search is performed in reciprocal space for reflections to create an orientation matrix. This relates the crystal reciprocal lattice to the co-ordinate frame of the diffractometer. Angles of observed reflections are measured and a list of reflections produced. These reflections are then indexed to provide the unit cell and Bravais lattice type for the crystal.

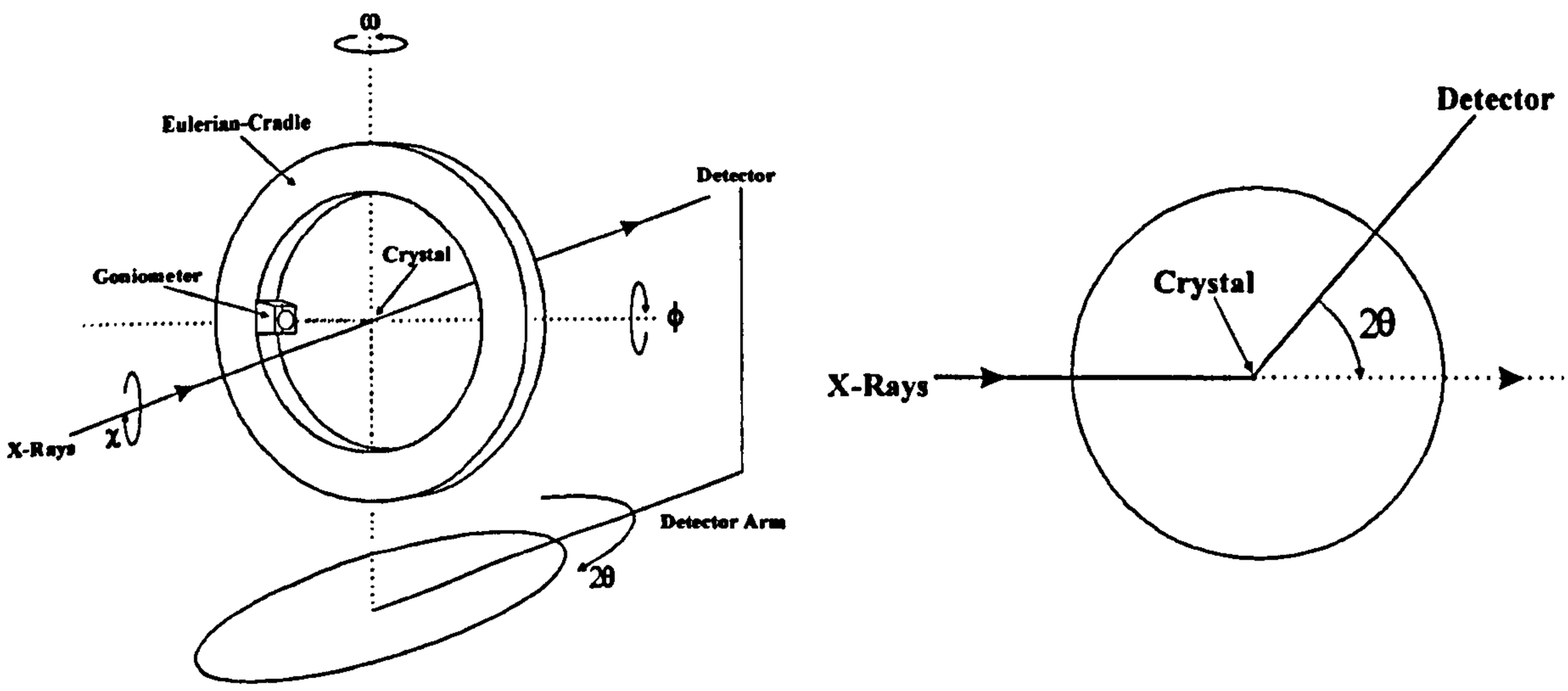

Figure 3.22. (a) 4-circle Eulerian-cradle diffractometer, (b) diffractometer equatorial geometry.

3.5.1.2 Brűker SMART Diffractometer

The Brűker SMART (Siemens Molecular Analytical Research Tool) is a 3-circle diffractometer. Instead of employing an Eulerian-cradle, a κ-goniometer (carrying the crystal) that can rotate about an axis called the κ-axis is used. In this geometry the χ-circle does not exist and the angle χ is fixed at 54.74°. The 2θ-circle is also fixed, so ω and ϕ -circles are used to bring reflections into the diffraction plane. The SMART

system utilises a CCD area detector. This consists of a two-dimensional array of (1024 × 1024) pixels coupled by a fibre-optic taper to a fluorescent phosphor screen positioned behind an x-ray transparent beryllium window. The phosphor screen converts x-rays into optical photons. Diffraction peak intensities are measured by converting and storing these optical photons as electrons. The detector is maintained at 218 K to reduce thermal noise. The area detector allows all reflections within a range of χ to be measured instead of varying χ to bring the reflection coincident with the diffraction plane, as in the case of a scintillation detector. The analogue signal from the CCD is digitised to form frames of data and stored. As with the Stoë STADI 4 diffractometer, an orientation matrix is used to calculate the angular positions of reflections with respect to the diffractometer. The x-ray source used is a molybdenum target, sealed x-ray tube. Advantages of this set-up over a scintillation counter are that scans over a large area of reciprocal space can be recorded simultaneously, so reducing the total data collection times. Also, because of the dynamic range and high sensitivity of the CCD detector, weak reflections are well observed.

3.5.2 Single Crystal Data Refinement - SHELX97

Structural refinements of single crystal diffraction data were carried out using the processing and analysis program SHELXL which forms part of the SHELX97[37] package. SHELXL sorts and merges symmetry-equivalent reflections and eliminates systematic absence violations. By simultaneously refining various parameters, adjustments are made to the model until the best least-squares fit is obtained. An indication of the quality of the least-squares refinement is estimated in the R_{int} factor produced, defined as follows:

$$R_{\text{int}} = \frac{\sum \left| F_o^2 - \overline{F}_o^2 \right|}{\sum [F_o^2]} \tag{3.17}$$

where F_o^2 is proportional to the experimental measurement of the reflection intensity. This factor gives an indication as to the equivalence of the symmetry-related reflections and the effectiveness of any absorption corrections applied. The quantity minimised in the least-squares refinement is the residual M:

$$M = \sum_i w(F_o - F_c)^2 \tag{3.18}$$

The *R*-indices and weights generated are defined as follows:

$$_{w}R_2 = \left\{ \frac{\sum[w(F_o^2 - F_c^2)^2]}{\sum[w(F_o^2)^2]^2} \right\}^{1/2} \tag{3.19}$$

For comparison with refinements based on *F*, a conventional index R_1 based on observed *F* values larger than $4\sigma(F_o)$ is also defined:

$$R_1 = \frac{\sum \| F_o | - | F_c \|}{\sum |F_o|} \tag{3.20}$$

The Goodness of Fit based on F^2 is defined as:

$$S = \left\{ \frac{\sum[w(F_o^2 - F_c^2)^2]}{(n-p)} \right\}^{1/2} \tag{3.21}$$

where *n* is the number of reflections and *p* the total number of parameters refined.

A refined weighting function can also be applied. This is often left at the default value until the refinement is near completion and then can be altered as recommended by the program. When two or less weighting parameters are specified the weighting scheme simplifies to:

$$w = \frac{1}{[\sigma^2(F_o^2) + (aP)^2 + bP]} \tag{3.22}$$

where $P = (2F_c^2 + F_o^2)/3$ and *a*, *b* represent the number of weighting parameters.

SHELXL also allows an extinction parameter *x*, to be refined, where F_c is mulitplied by the following:

$$k[1 + 0.001xF_c^2\lambda^3/\sin(2\theta)]^{-1/4} \tag{3.23}$$

where *k* is the overall scale factor. The expression above (3.23) is empirical and represents a compromise, taking into account both primary and secondary isotropic extinction as outlined by Larson[38].

3.5.3 Sample Preparation and Mounting

NBT crystals that extinguished sharply under polarised light and exhibited no visible signs of twinning were selected for experiments. These irregularly shaped crystals were gently crushed into small fragments and ground until they were spherical.

This was achieved (after a period of a few days) using an Enraf-Nonius air spheruliser, which consists of a cylinder lined with fine abrasive paper and connected to a compressed air supply. Spheres with the best shape (isotropic) that extinguished sharply were glued using epoxy resin (Araldite) onto the end of a fine quartz fibre, which was in turn attached to a brass rod and mounted onto the goniometer head. At the collection stage the goniometer head was secured and the crystal was centred optically in such a way that it was always coincident with the centre of rotation axis of the diffractometer. This ensures it always lies at the centre of the beam.

3.5.4 Data Collections

Room temperature single-crystal data collections were performed on a Stoë STADI-4 and SMART diffractometers. In each case the goniometer head was mounted and the crystal centred optically on the rotation axis of the diffractometer. During preliminary x-ray analysis it was apparent that the large majority of crystals selected for use on both diffractometers were twinned. This was indicated by split peak profiles and unusual cell assignments. After suitable crystals were found, a search for reflections used to determine the orientation matrix and unit cell parameters was carried out. Once a satisfactory number of reflections (with reasonable peak profiles) had been found a preliminary orientation matrix and unit cell were determined.

Data collection on the Stoë STADI-4 diffractometer were taken with a step size of 0.05° and counting time of 1 second per step. Intensities of symmetry related equivalent reflections were checked for consistency. In order to correct for the absorption of the crystal a Ψ-scan was initially conducted. This was then used in the data reduction stage of data performed using the programme X-RED[39].

Data collection on the SMART diffractometer composed of a series of eight scans, collecting for 30 seconds, step size (frame width) 0.3°. A detector to sample distance of 5 cm was used to measure reflections. The total scan time was approximately 40 hours. The interactive graphics program ASTRO[40] (Area detector STRategy Organiser, a supplementary utility program in the SMART[41] package) was used to set up the data collection strategy to collect efficiently the data required for structure determination. The raw data frames from individual runs, when combined with the orientation matrix, were converted to a set of integrated corrected intensities listed by the data processing program SAINT[42] (Siemens Area detector INTegration also supplied as

part of the SMART software). The program SADABS[43] was used to correct for absorption (a spherical crystal model for absorption was used).

3.5.5 Structural Refinements

Structural refinements of single crystal diffraction data collected from both the Stoë STADI-4 and SMART diffractometers were carried out using SHELXL. Refinements were carried out in the space group R3c, with the rhombohedral structure described on hexagonal axes (section 3.3.4). Initially, Na and Bi, each with fixed site occupation factor 0.5, were constrained to be at the same co-ordinates. The Na and Bi positions were then allowed to refine separately with the result that Bi became displaced 0.018 (4) Å (from Stoë STADI-4 data) and 0.042 (2) Å (from SMART data) along the polar axis (+*c*) with respect to Na. This resulted is slightly worse *R*-factors. Introducing this freedom had negligible effect on the temperature parameters. The fractional occupancies were allowed to refine separately. However, in both cases this resulted in unstable refinements, due to the lack of information that can be obtained about Na in the presence of Bi. The Na and Bi positional parameters were constrained to the same positions and the occupancies were fixed for the remaining refinements. Initially, the Na and Bi isotropic temperature factors were refined separately. With the SMART data, this resulted in values, which were similar in magnitude (typically around 0.02 $Å^2$). In the case of the Stoë data, allowing the Na and Bi isotropic temperature factors to be refined separately resulted in a large value (0.0983 (2) $Å^2$) for the Bi atoms. For both sets of data, the Na and Bi atoms were subsequently constrained to be the same and anisotropic parameters were refined for the remaining refinements. The Na and Bi temperature factors were constrained to be the same for the remaining refinements.

In the refinement of the Stoë STADI-4 data the Flack parameter, *x*, refined to 0.54 (7) indicating that this crystal was 50 % inversion twinned. A twinned refinement was carried out using the twin matrix:

$$T = \begin{bmatrix} -1 & 0 & 0 \\ 0 & -1 & 0 \\ 0 & 0 & -1 \end{bmatrix} \tag{3.24}$$

The resulting twin component then refined to 0.52 (8). In the refinement of the SMART data *x*, refined to 0.4 (1). The above twin law and parameter, *x*, were refined in the remaining refinements. The fractional contributions of the twin components refined to

0.49 and 0.46 for the Stoë STADI-4 and SMART data respectively. An extinction parameter was introduced to the refinements but was found to be negligibly small for the SMART data and refined to a value of 0.02 in the Stoë STADI-4 case. As the final step in the refinement process, the default weighting function was altered as recommended by the program. The details of the refinement are shown in Table 3.10. The atomic co-ordinates and thermal parameters from refinements are listed in Table 3.11.

Chemical Formula	**$Na_{0.5}Bi_{0.5}TiO_3$**	
Crystal System	Rhombohedral	
Space Group	R3c	
Temperature (K)	293	
Crystal Shape	Spherical	
Radiation, λ (Å)	X-ray, 0.71073	
Diffractometer	**Stoë Stadi-4**	**SMART**
Crystal Data		
a_H (Å)	5.502 (1)	5.4947 (3)
b_H (Å)	5.502 (1)	5.4947 (3)
c_H (Å)	13.478 (4)	13.479 (1)
α, β, γ (°)	90, 90, 120	90, 90, 120
V (Å^3)	353.34	352.44
D_x (Mg.m^{-3})	5.975	5.990
Z	6	6
s	0.0040 (6)	0.019 (5)
t	0.0075 (7)	0.010 (7)
d	-0.0084 (8)	-0.004 (2)
e	0.0077 (7)	0.019 (2)
ω (°)	3.1 (3)	7.5 (8)
$\zeta \times 10^2$	-0.14 (2)	-0.710 (2)
Crystal diameter (mm)	0.02	0.015
Data Collection		
Scan-type	ω-2θ	ω-scan
$2\theta_{max}$ (°)	56.38	45.67
h, k, l Range	h = ± 7, k = ± 7, l = ± 17	h = ± 6, k = ± 6, l = ± 14
Absorption correction	Spherical	Spherical
Min, Max effective transmission	0.07637 0.28883	0.0817 0.0475
Nº. Reflections measured	1512	1044
Data reduction		
Structure refinement	SHELXL	SHELXL
Weighting scheme *a, b*	0.0059, 25.7506	0.0069, 26.7306
Extinction parameter	0.0155	0.0
Flack parameter, *x*	0.54 (7)	0.4 (1)
$\Delta\rho_{min}$, $\Delta\rho_{max}$ (eÅ^3)	0.90, 0.88	1.77, 1.38
Nº. of refined parameters	27	27
R_{int}	0.0373	0.0700
R_1	0.0509	0.0609
$_wR_2$	0.0948	0.1260
S	1.142	2.400

Table 3.10. X-ray single crystal collection details & structural refinements.

Stoĕ Stadi-4 Diffractometer (293 K)

Atom	x	y	z	U11	U22	U33	U12	U13	U23
Na	0.0	0.0	0.2477(4)	0.079(2)	0.079(2)	0.082(2)	0.0	0.0	0.0394(8)
Bi	0.0	0.0	0.2477(4)	0.079(2)	0.079(2)	0.082(2)	0.0	0.0	0.0394(8)
Ti	0.0	0.0	0.0012(3)	0.022(1)	0.022(1)	0.016(1)	0.0	0.0	0.0110(5)
O	0.168(3)	0.367(3)	0.077(1)	0.049(7)	0.001(4)	0.046(5)	-0.006(4)	0.028(8)	-0.002(6)

SMART Diffractometer (293 K)

Atom	x	y	z	U11	U22	U33	U12	U13	U23
Na	0.0	0.0	0.2503(1)	0.023(2)	0.023(2)	0.043(4)	0.0	0.0	0.012(1)
Bi	0.0	0.0	0.2503(1)	0.023(2)	0.023(2)	0.043(4)	0.0	0.0	0.012(1)
Ti	0.0	0.0	-0.008(2)	0.011(2)	0.011(2)	0.001(1)	0.0	0.0	0.005(1)
O	0.136(5)	0.348(8)	0.065(5)	0.03 (2)	0.02 (1)	0.0	0.004(1)	0.01 (1)	0.01 (2)

Table 3.11. Fractional co-ordinates and equivalent anisotropic displacement parameters ($Å^2$) for NBT.

3.5.6 Discussion

The final ${}_wR_2$-factors for the structures refined from single crystal data were not as good as was hoped for at 9.48 and 12.6 % for data taken on the Stoë Stadi-4 and SMART diffractometers respectively. The final ${}_wR_2$-factors for the Stoë data could be reduced (typically to around 6 %) by allowing the anisotropic temperature parameters for Bi to refine independently of the Na atoms. However this resulted in large and physically questionable values (> 0.09 $Å^2$). It was thought that the large temperature factors pointed to static disorder of Bi, so models with split Bi sites were tried. However, a suitable disordered model was not found. Other reasons for the large ${}_wR_2$-factors can be due to an inadequate absorption correction being applied for this highly absorbing crystal or unresolved twinning within the crystals under study.

The atomic positions, bond lengths and angles have been refined to sensible values. From the two diffractometers, the refined lattice parameters derived were very close with only a 0.1 and 0.007 % differences in a_H and c_H being observed. In comparison with room temperature results obtained via neutron powder diffraction studies (section 3.3.4), there is a good agreement of most parameters. A and B-cation displacements along c_H refined to values of 0.004 (6), 0.0075 (7) and 0.019 (5), 0.010 (7) for data taken on the Stoë Stadi-4 and SMART diffractometers respectively and 0.0127 (6), 0.0063 (6) in the neutron case. The octahedron tilting estimated from the oxygen

fraction co-ordinates, were found to be 3.1 (3), 7.5(8)° for the Stoë Stadi-4 and SMART diffractometers in comparison to 8.24 (4)° in the neutron case.

Bond valence calculations were performed using the program VaList[29], with the cations at their refined positions. This reveals similar results obtained from neutron data, giving deficiencies for Na^{1+}, Ti^{4+}, Bi^{3+} of 4, 5, 30 % and 8, 1, 21 %, for data taken on the Stoë Stadi-4 and SMART diffractometers respectively. A similar conclusion to that outlined in section 3.3.5.4 must be drawn.

A study was also performed on the peak shapes for diffraction data taken on the SMART diffractometer. Bragg peaks for many of the strong reflections showed clear distortions, particularly in the tails. Strong reflections were very extended, in some cases for example some reflections existed over 15 frames (4.5°) from high to low intensity. It was also noted that satellite reflections existed around many of the main reflections. Additional scattering in the diffraction patterns from NBT was also observed, this appeared to occur in streaks over different frames. Figure 3.23 shows one of these streaks, which appears close to the 440 reflection (which appears on the previous frame). The diffuse scattering streaks are evident on many frames but, when examined in sufficient detail, do not appear to correspond to diffraction along specific simple planes. It was often necessary to set the maximum intensity count level displayed by the program to a significantly lower level than the maximum counts of the strong reflections in order to observe these streaks. The streaks of diffuse scattering indicates that there is some short range ordering of the A-site cations (occupational disorder) in support of observations found in section 2.3.4. Alternative NBT crystals also showed this feature.

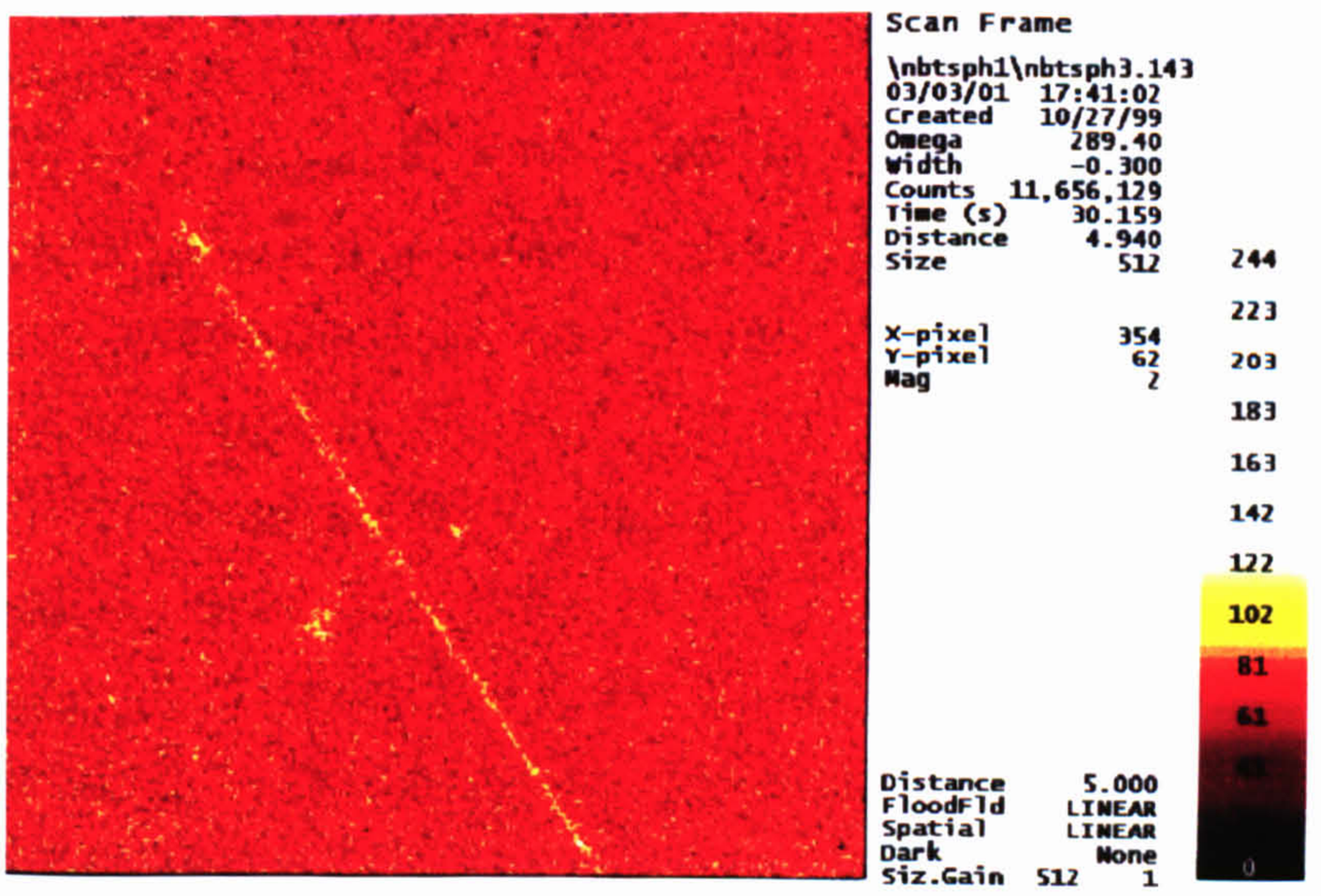

Figure 3.23. Frame of X-ray area detector data showing a diffuse streak.

References

[1] Rietveld, H. M. (1967). Acta Cryst. 20, 508.

[2] Rietveld, H. M. (1969). J. Appl. Cryst. 2, 65.

[3] Caglioti, G., Paoletti, A. & Ricci, F. P. (1958). Nucl. Instrum. Methods 35, 223.

[4] Young, R. A. The Rietveld Method. (1993). IUCr Oxford Uni. Press, 9.

[5] Von Dreele, R. & Larson, A. (1995). University of California.

[6] PROFILE, Version 1.0, Bruker Analytical X-ray Systems.

[7] Boultif, A. & Louër, D. (1991). J. Appl. Cryst. 24, 987.

[8] Werner, P.E, Eriksson, L. & Westdahl, M. J. (1985). J. Appl. Cryst. 18, 367.

[9] Hewat, A. W. (1986). Mat. Sci. Forum. 9, 69.

[10] Ageron, P. (1989). Nucl. Instr. And Meth. A284, 197199.

[11] Glazer, A. M. (1975). Acta Cryst. A31, 756.

[12] Corker, D. L., Glazer, A. M., Whatmore, R. W., Stallard, A. & Fauth, F. (1998). J. Phys. Condens. Matter. 10, 6251.

[13] Megaw, H. D. & Darlington, C. N. (1974). Acta Cryst. A31, 161.

[14] Glazer, A. M. & Megaw, H. D. (1972). Phil. Mag. 25, 1119.

[15] Zvirgzds, J. A., Kapostins, P. P., Zvirgzde J. V. & Kruzina, T. V. (1982). Ferroelectrics 40, 75.

[16] Suchanicz, J. & Kwapulinski, J. (1995). Ferroelectrics 165, 249-253.

[17] Park, S., Chung, S., Kim, I & Hong K. S. (1994). J. Am. Ceram. Soc. 77, 2641.

[18] Kuharuangrong, S. & Schulze, W. (1996). J. Am. Ceram. Soc. 79, 1273.

[19] Zvirgzds, J. A., Kapostins, P. P., Zvirgzde J. V. & Kruzina, T. V. (1982). Ferroelectrics 40, 75.

[20] Suchanicz, J., Jezowski, A. & Poprawski, R. (1998). Phys. Stat. Sol. 169, 209.

[21] Setter, N. & Cross, L. E. (1980). J. Material Science 15, 2478.

[22] Park, J. H., Woodward, P. M. & Parise, J. B. (1998). Chem. Mater. 10, 3092.

[23] Shannon, R. D. (1976). Acta Cryst. A32, 751.

[24] Park, J. H., Woodward, P. M., Parise, J. B., Reeder, R. J., Lubomirsky, I. & Stafsudd, O. (1999). Chem. Mater. 11, 177.

[25] Vakrushev, S. B., Ivanitskii, B. G., Kvyatkovskii, B. E., Maistrenko, A. N., Malysheva, R. S., Okuneva, N. M. & Parfenova, N. N. (1983). Sov. Phys. Solis State 25 (9), 1504.

[26] Thomann, H. (1987). Ferroelectrics 73, 183.

[27] Glazer, A. M., Mabud, S. A. & Clarke, R. (1978). Acta Cryst. B34, 1060.

[28] Shirane, G., Pepinsky, R. & Frazer, B. C. (1955). Phys. Rev. 97, 1179.

[29] Willis, A. S. & Brown, I. D. (1999), VaList, CEA, France.

[30] Jones, G. O. & Thomas, P. A. (2000). Acta Cryst. B56, 426.

[31] Tang, C. C., Bushnell-Wye, G. & Cernik, R. J. (1998). J. Sync. Rad. 5, 929.

[32] International Tables of X-Ray Crystallography Vol 3, (1968).

[33] Giacovazzo, C., Monaco, H. L., Viterbo, D., Scordari, G., Gilli, G., Zanotti, G. & Catti, M. (1992). Fundamentals of Crystallography, IUCr Texts on Crystallography – 2, Oxford University Press.

[34] Lipson, H. (1959). International Tables of X-Ray Crystallography Vol 2, 237.

[35] Harker, D. and Kasper, J. S. (1948). Acta Cryst. A42, 325.

[36] Stout, G. H. & Jensen, L. H. (1989). X-ray Structure Determination, Wiley, New York, 312.

[37] Sheldrick, G. (1990). Acta. Cryst. A46, 467.

[38] Larson, A. C. (1970). Crystallographic Computing, edited by Ahmed, F., Hall, S., & Huber, C., 291.

[39] X-RED Reference Manual, (1999). Stoë CIE Diffraction Systems Ltd.

[40] ASTRO Software Reference Manual, (1998). Bruker AXS Inc, USA.

[41] SMART Software Reference Manual, (1998). Bruker AXS Inc, USA.

[42] SAINT Software Reference Manual, (1998). Bruker AXS Inc, USA.

[43] SADABS Software Reference Manual, (1998). Bruker AXS Inc, USA.

Chapter 4

$Na_{0.5}Bi_{0.5}TiO_3$ – Structural Study as a Function of Pressure

4.1 Introduction

In this chapter, the characterisation of NBT as a function of pressure using powder diffraction methods is described. Powder x-ray diffraction studies have been conducted at ambient pressure and various values up to 97.5 kbar. Neutron powder diffraction studies have also been conducted up to a pressure of 10 kbar. The high-pressure orthorhombic structure of NBT is reported for the first time. The ambient pressure rhombohedral structure is seen to undergo a phase transition to a purely orthorhombic structure at a pressure of 19.4 kbar with the further application of pressure increasing the orthorhombic distortion. The structure has Pnma symmetry with the $a^-b^+a^-$ tilt system of oxygen octahedra and antiparallel A-cation ordering along [010]. The new phase and the structural modifications induced by pressure are discussed.

4.2 X-ray Powder Diffraction at Pressure

In the past there have been certain inherent problems in performing powder x-ray diffraction experiments on samples enclosed in pressure cells, which made accurate structural refinements difficult. The limiting factor is the very small sample volume used (typically $< 5 \times 10^{-4}$ mm^{-3}) which results in weak signals and a poor powder average because of the limited number of crystallites. These problems may be overcome by using an area detector so that the diffracted intensity from a large proportion of the Debye-Scherrer rings is measured, thus greatly improving the powder averaging and total diffracted intensity. Over the last decade, structure determination from high-pressure powder diffraction data using angle-dispersive techniques with area imaging plates has been greatly advanced[1-2], offering a precise method of performing structural studies. Pressure studies can be of great interest as the application of pressure can have dramatic effects on physical properties and induce a diverse range of transitions and structures.

4.2.1 Sample Preparation and Environment

Fragments of flux-grown crystals were finely ground into powder. The powder was sieved to obtain particles with approximate diameters < 38 μm. Samples were

loaded into a Merrill-Bassett type[3] diamond-anvil pressure cell with 4:1 methanol:ethanol as a pressure-transmitting medium[4-5]. The sample and the pressure transmitting fluid are contained in a metal gasket, which is placed between the flat tips of two gem-quality (400 μm culet) diamonds. By the use of a piston-cylinder arrangement, the two diamonds are brought closer together, pressing on the medium, and indirectly on to the sample, thereby transmitting the desired pressure to the sample. The effective sample volume is of the order of 100 μm in diameter and 50 μm thick. A schematic diagram of the pressure cell is shown in Figure 4.01. The pressure cell is mounted on aluminium blocks which are held on a manually adjustable XZ stage (there is no adjustment along Y, parallel to the beam). A high-power telescope, placed between the cell and the image plate (section 4.2.2), is focussed on the sample for accurate sample alignment.

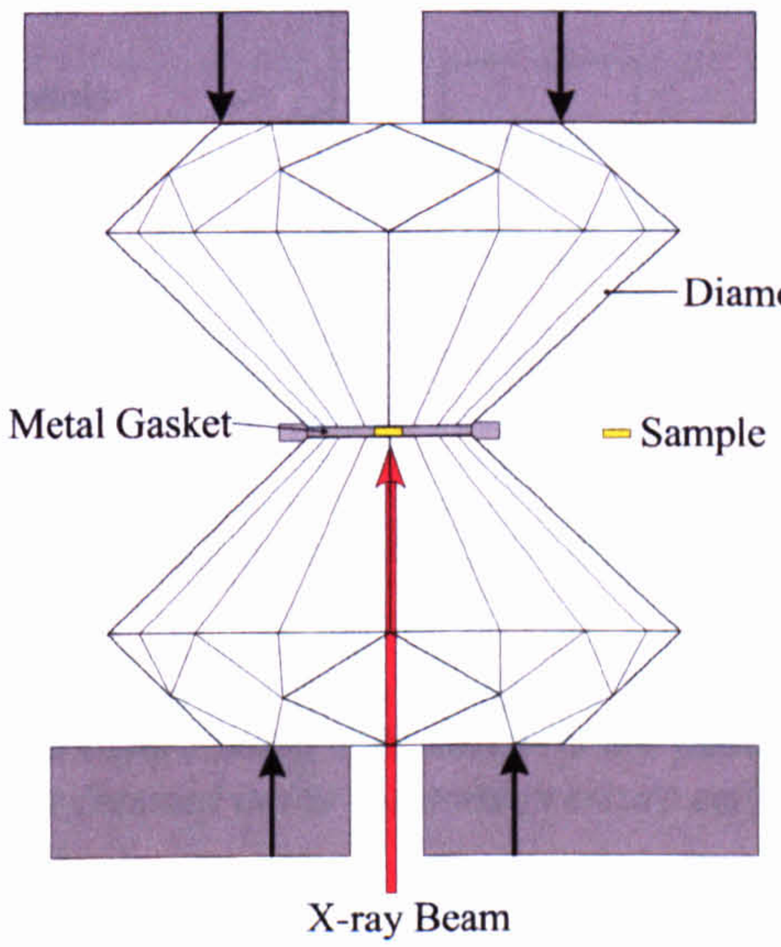

Figure 4.01. Schematic diagram of a Merrill-Bassett type diamond-anvil pressure cell.

4.2.2 Data Collections and Treatment

X-ray powder diffraction studies were performed at room temperature on Station 9.1 at the Synchrotron Radiation Source, CCLRC Laboratory, Daresbury using angle-dispersive diffraction techniques and an image-plate area detector. Operational details relating to Station 9.1 can be found in section 3.4.1. An incident wavelength of 0.4654 Å was used.

The image plate (IP) system, which is illustrated schematically in Figure 4.02, was situated approximately 15 m from the 5 T wiggler magnet. A water-cooled double-bounce channel-cut Si (111) monochromator was used to select the required wavelength

(from the range 0.42-0.75 Å) after which tungsten-carbide slits reduced the monochromatic beam dimensions to 0.5 × 0.5 mm^2. This beam then passed through a lead shield. The IP is highly sensitive to the short (≤ 0.75Å) wavelengths needed to penetrate the pressure cell. To prevent scatter and fluorescence from the incident beam being detected by the IP, further shielding completely enclosed the monochromatic beam until it was finally collimated to a circular beam 50-100 μm in diameter by a pinhole, which was mounted at the end of a tungsten-carbide tube. The pinhole arrangement was mounted on a motorised 3D stage to facilitate alignment of the pinhole with respect to the monochromatic beam.

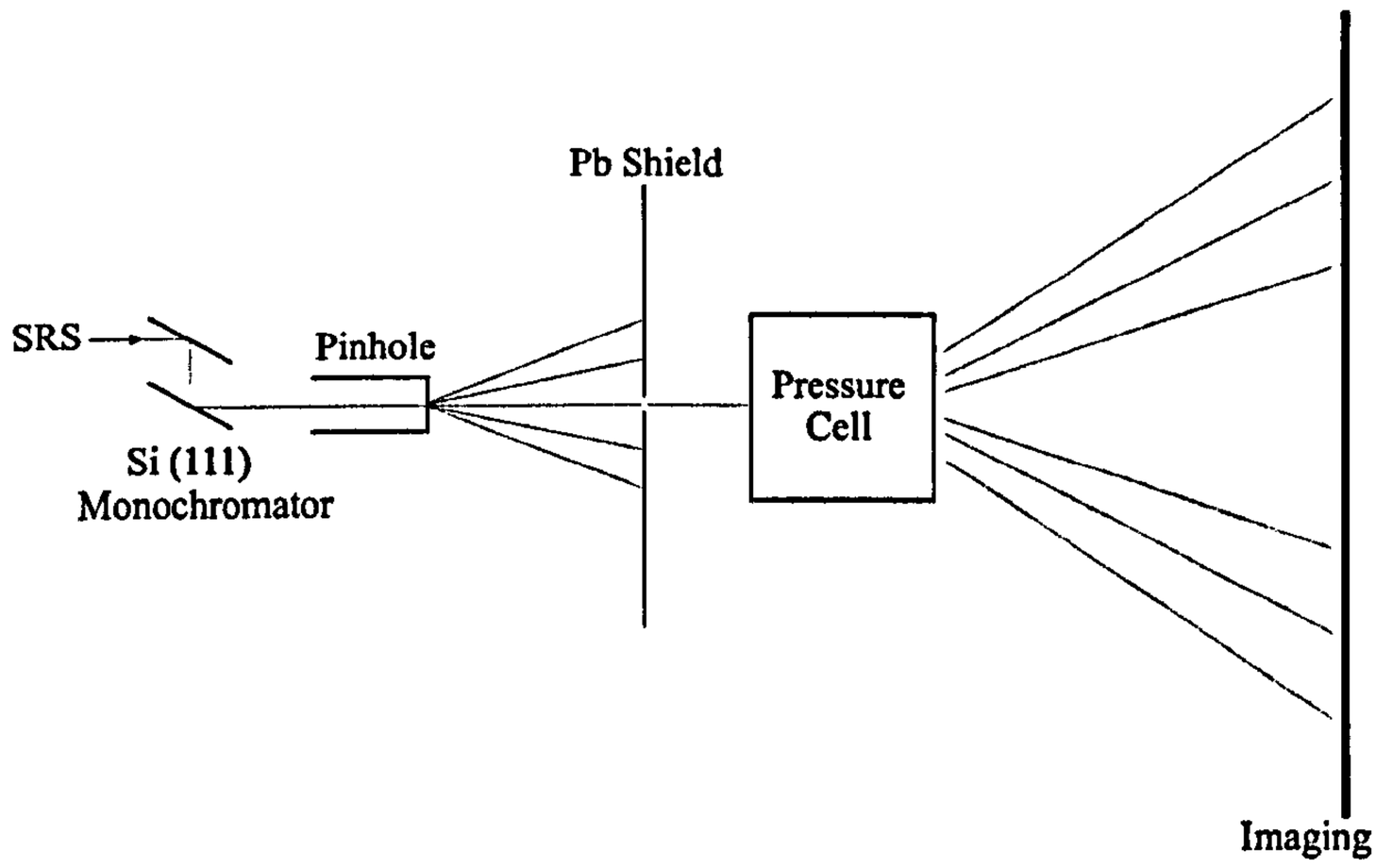

Figure 4.02. *Schematic diagram of the beam set-up on Station 9.1. The incident white beam is monochromated before being collimated by the pinhole system. The diffraction pattern from the sample (housed in the diamond pressure cell) is intercepted at the image plate.*

The IP is a highly sensitive (film-like) radiation image detector of high spatial resolution, which was first developed by Fuji Photo Co., Ltd in Japan. The plate consists of a thin photo-sensitive phosphor layer of Barium fluorobromide containing a trace amount of bivalent europium as a luminescence centre ($BaFBr:Eu^{2+}$) on a supporting polyester film that traps and stores the radiation energy. The stored radiation energy can then be read out with a He-Ne laser. The laser stimulates the phosphor during reading and the emitted light is collected by a photomultiplier tube through a light collection guide and converted to electric signals, which are amplified and digitally processed.

A rectangular Kodak Storage Phosphor imaging plate (20 × 25 cm^2) bonded onto a flat aluminium backing plate was used. The IP was kept in a light-tight holder during x-ray exposure and was only removed at the scanning stage. Scanning was carried out on a Molecular Dynamics 400A PhosphorImager. A schematic diagram of the image plate

scanner is shown in Figure 4.03. The image plate reader has an 86 × 88 μm^2 pixel size, and takes approximately 9 minutes to read a plate and store the digitised image in ≈ 2800 × 2000 pixels.

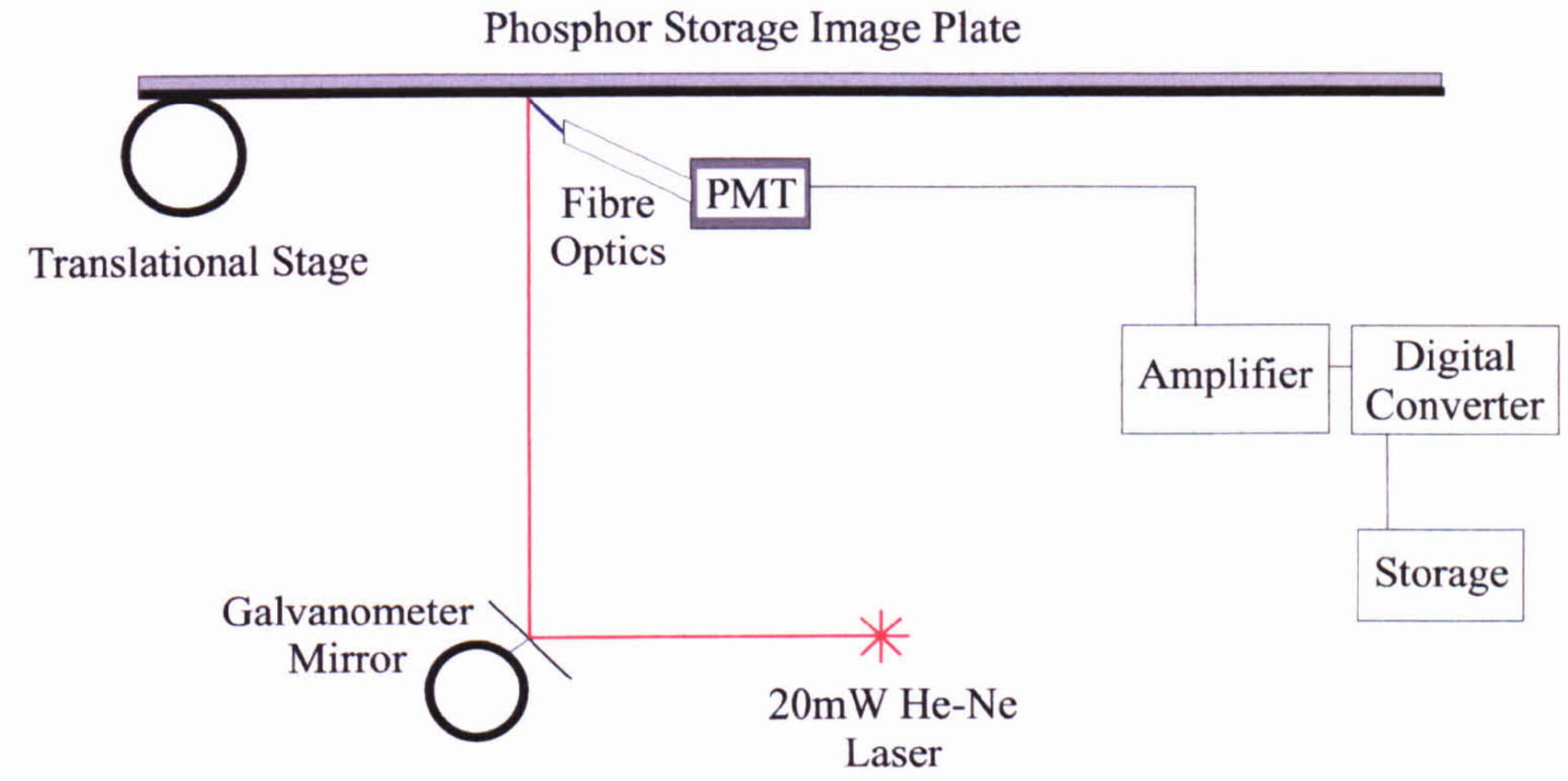

Figure 4.03. *A schematic diagram of the Molecular Dynamics 400A PhosphorImager image plate scanner.*

The two-dimensional digitised images were integrated around the Debye-Scherrer rings to give one-dimensional standard powder profiles using the program suite PLATYPUS[6]. By fitting the image of the direct beam the centre of the diffraction pattern was found. The two-dimensional diffraction pattern was then split into 30 sectors around this centre. Each individual sector is integrated along circular arcs producing 30 one-dimensional profiles and the tilts of the image plate away from being perpendicular to the primary beam (as the IP is flat) were then refined so all the profiles came into register to produce a summed profile. The full two-dimensional image was then recombined taking into account the refined tilts to give a final one-dimensional profile. Data processing techniques can be found in detail elsewhere[6-8]. Diffraction data were collected at ambient pressure, 19.4, 26.2, 33.6, 47.8, 68.9, and 97.5 kbar. The complete angular range between $3 < 2\theta < 30°$ was covered in increments of 0.015°. Typical total scan times were of 30 minutes in duration.

4.2.3 Rietveld Structural Refinements

The Rietveld method (section 3.2.1) was used to refine the crystal structure as a function of pressure. All data sets were analysed with the program GSAS (section 3.2.2). The ambient pressure refinement was carried out based on the starting model obtained from the corresponding synchrotron room temperature model (section 3.4.4). Similarly

to the previous synchrotron diffraction profiles, the ambient pressure pattern only shows a slight rhombohedral broadening of lines and only the first superstructure reflection (131) is faintly observed. As previously pointed out, the very low intensity of this peak is to be expected since it originates purely from the oxygen octahedral tilting. Structural refinements were carried out (as in previous cases) with reference to hexagonal axes. The structure was refined in the space group R3c. The background was based on a linear interpolation function and peak shapes were described by pseudo-Voigt profiles. The $O_{(Z)}$ position was fixed to 1/12 (refer to Table 3.04). Isotropic temperature factors were refined for all atoms. Attempts to refine the anisotropic temperature factors resulted in the non-positive definite ellipsoids for the oxygen atoms; therefore, all values for the oxygen atoms were fixed to isotropic values of 0.01 $Å^2$. Occupancies of Na and Bi were constrained to be 0.5 and the positional parameters of these two atoms were fixed to be identical. The refinement was stable and converged quickly. Crystallographic data and refined profile parameters are summarised in Tables 4.01 (a) and 4.02. The observed, calculated and difference profiles from the final Rietveld refinement in R3c at room temperature, ambient pressure are shown in Figure 4.04 (a).

The room temperature, ambient pressure rhombohedral structure is seen to have undergone a phase transition to an orthorhombic distortion at a pressure of 19.4 kbar. Figure 4.06, shows the 205 ordering peak and the orthorhombic distortion at 33.6 kbar relative to the ambient pressure rhombohedral phase.

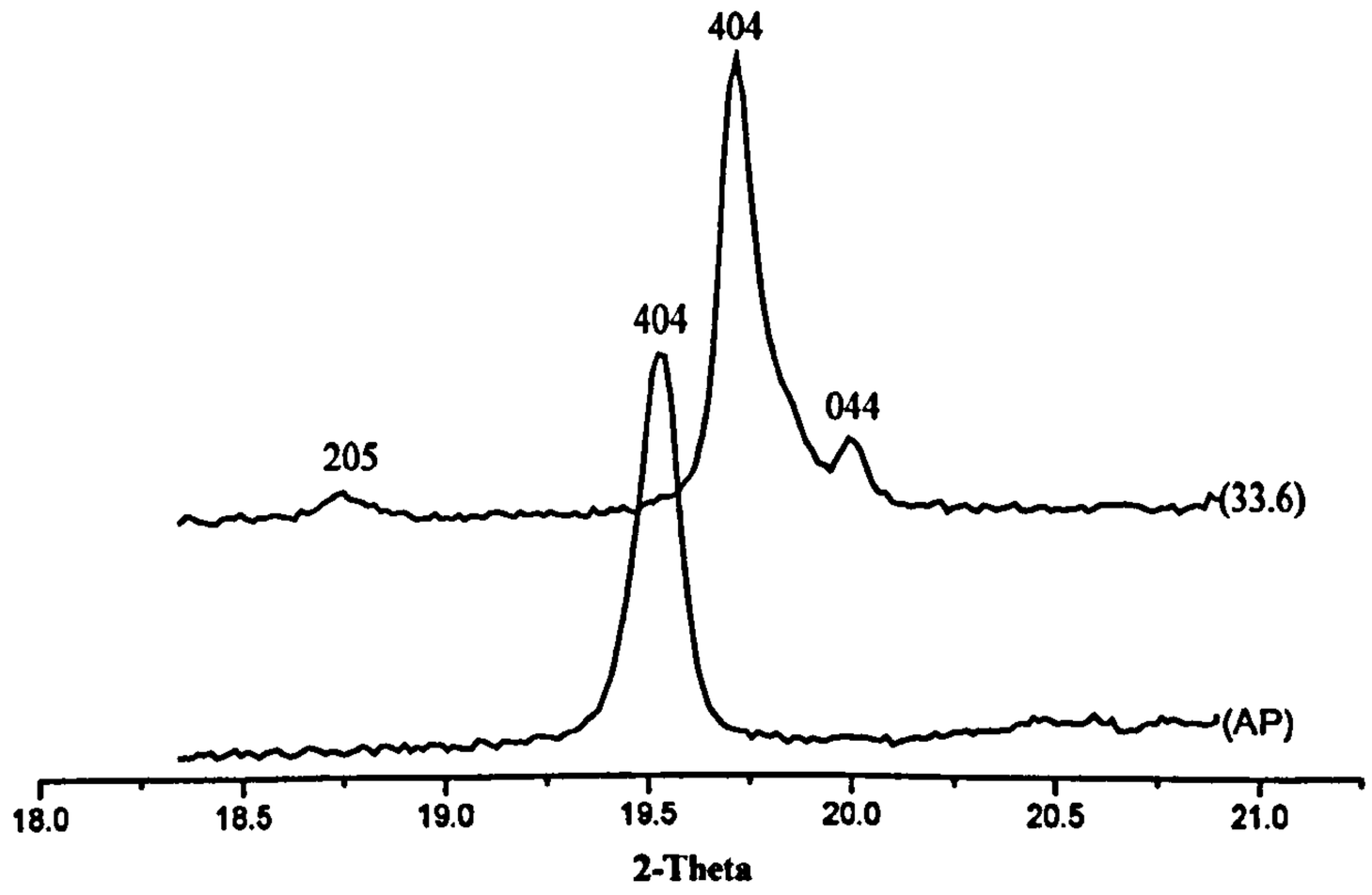

Figure 4.06. *Profile of peak 404 at ambient pressure and 33.6 kbar, indicating the orthorhombic distortion.*

Chemical formula	$Na_{0.5}Bi_{0.5}TiO_3$		
Chemical formula weight	211.88		
Specimen Shape	Random powder		
Radiation Type	Synchrotron		
Wavelength	0.4654 Å		
CRYSTAL SYSTEM	**Rhombohedral**	**Rhombohedral (26 %)**	**Orthorhombic (74 %)**
Space Group	R3c	R3c	Pnma
a (Å)	5.4849 (4)	5.4561 (6)	5.454 (2)
b (Å)	5.4849 (4)	5.4561 (6)	7.733 (2)
c (Å)	13.5000 (2)	13.4081 (8)	5.442 (2)
α,β,γ (°)	90,90,120	90,90,120	90,90,90
α_p (°)	89.82	89.88	-
Volume (Å^3)	351.73 (8)	345.67 (9)	229.5 (2)
Z	6	6	4
D_x (Mg.m^{-3})	6.002	6.107	6.131
Tilt System	$a^-a^-a^-$	$a^-a^-a^-$	$a^-b^+a^-$
Displacements	Parallel along $[111]_p$	Parallel along $[111]_p$	Parallel along [100]
Ordering	-	-	Anti-parallel along [010]
ω (°)	8.47 (8)	7.85 (8)	3.5 anticlockwise about [010] 4.3 clockwise about [100]/[001]
$\zeta \times 10^2$	-0.61 (1)	-0.62 (5)	-
DATA COLLECTION			
Pressure (kbar)	AP	19.4	19.4
Temperature (K)	273	273	273
Specimen environment	Diamond anvil cell	Diamond anvil cell	Diamond anvil cell
Scan Time (hours)	0.5	0.5	0.5
$2\theta_{min}$ (°)	3	3	3
$2\theta_{max}$ (°)	30	30	30
REFINEMENTS			
Background / coefficients	linear interpolation / 8	linear interpolation / 8	linear interpolation / 8
Scale	0.627 (2)	0.862 (4)	0.862 (4)
2θ zero-error	0.36 (9)	1.51 (3)	1.51 (3)
Excluded Regions	-	10.73-10.96	10.73-10.96
Peak Shape parameters:			
G(U), G(V), G(W),	181 (1), -53 (3), 0.1 (1)	210 (2), -58 (4), 5.2 (4)	679 (4), -143 (4), 12.1 (4)
G(P).	8.2 (4)	8.0 (4)	0
L_x, L_y	1.4 (1), 32 (1)	1.5 (1), 4 (1)	3.7 (1), 29 (1)
S/L, H/L.	0, 0	0, 0	0, 0
Stec, Ptec, Sfec.	-1.1(1), -0.009 (1), 0	6 (3), 0, 0	0, 0, 0
N^o. of parameters	39	39	32
R_p	0.0301	0.0335	0.0335
$_wR_p$	0.0379	0.0483	0.0483
χ^2	1.706	2.925	2.925

Table 4.01. (a) *Summary of experimental details, data collection and refinement for $Na_{0.5}Bi_{0.5}TiO_3$.*

Chemical formula	$Na_{0.5}Bi_{0.5}TiO_3$	
Chemical formula weight	211.88	
Specimen Shape	Random powder	
Radiation Type	Synchrotron	
Wavelength	0.4654 Å	
CRYSTAL SYSTEM	**Orthorhombic**	**Orthorhombic**
Space Group	Pnma	Pnma
a (Å)	5.4430 (4)	5.3750 (4)
b (Å)	7.7038 (8)	7.6165 (5)
c (Å)	5.4031 (3)	5.3222 (4)
α,β,γ (°)	90,90,90	90,90,90
Volume (Å^3)	226.56 (5)	217.88 (5)
Z	4	4
D_x (Mg.m^{-3})	6.212	6.459
Tilt System	$a^-b^+a^-$	$a^-b^+a^-$
Displacements	Parallel along [100]	Parallel along [100]
Ordering	Anti-parallel along [010]	Anti-parallel along [010]
ω (°)	3.8 anticlockwise about [010]	5.0 anticlockwise about [010]
	9.6 clockwise about [100]/[001]	16.9 clockwise about [100]/[001]
DATA COLLECTION		
Pressure (kbar)	33.6	97.5
Temperature (K)	273	273
Specimen environment	Diamond anvil cell	Diamond anvil cell
Scan Time (hours)	0.5	0.5
$2\theta_{min}$ (°)	3	3
$2\theta_{max}$ (°)	30	30
REFINEMENTS		
Background / coefficients	linear interpolation / 8	linear interpolation / 8
Scale	0.936 (7)	1.19 (4)
2θ zero-error	0.51 (2)	1.11 (3)
Excluded Regions	11.18-11.45	11.80-12.05
Peak Shape parameters:		
G(U), G(V), G(W),	436 (15), -53.9 (2), 6.6 (1)	741 (21), -45 (2), 6.8 (2)
G(P).	0	0
L_x, L_y	2.12 (6), 15.4 (6)	2.43 (6), 13.8 (7)
S/L, H/L	0, 0	0, 0
Stec, Ptec, Sfec.	0.29 (8), -0.15 (9), 0	6 (1), 0, 0
Nº. of parameters	32	32
R_p	0.0298	0.0284
$_wR_p$	0.0400	0.0371
χ^2	1.685	1.725

Table 4.01. (b) *Summary of experimental details, data collection and refinement for $Na_{0.5}Bi_{0.5}TiO_3$.*

Pressure (kbar) →	Ambient	19.4		33.6	97.5
Phase →	Rhombohedral (R3c)	Rhombohedral (R3c) (26 %)	Orthorhombic (Pnma) (74 %)	Orthorhombic (Pnma)	Orthorhombic (Pnma)
Atomic Positions ↓					
Na					
x	0	0	0.022 (4)	0.0278 (5)	0.0321 (4)
y	0	0	0.250	0.2500	0.2500
z	0.2730 (9)	0.2548 (2)	-0.014 (2)	-0.0077 (5)	-0.0043 (4)
Bi					
x	0	0	0.022 (4)	0.0178 (5)	0.0321 (4)
y	0	0	0.25	0.2500	0.2500
z	0.2730 (9)	0.2548 (2)	-0.014 (2)	-0.0077 (5)	-0.0043 (4)
Ti					
x	0	0	0.5	0.5	0.5
y	0	0	0	0	0
z	0.0065 (2)	0.0012 (1)	0	0	0
O(4)					
x	0.1238 (4)	0.1279 (1)	0.774 (4)	0.783 (3)	0.767 (3)
y	0.3336 (2)	0.3358 (7)	-0.017 (1)	-0.029 (2)	-0.022 (2)
z	0.0833	0.0833	0.306 (2)	0.318 (3)	0.313 (3)
O(5)					
x	-	-	-0.012 (1)	-0.020 (4)	-0.054 (5)
y	-	-	0.25	0.2500	0.2500
z	-	-	0.464 (1)	0.417 (3)	0.351 (3)
Thermal Parameters					
Na	0.033 (4)	0.024 (4)	0.027 (8)	0.019 (8)	0.016 (7)
Bi	0.041 (2)	0.043 (9)	0.058 (3)	0.041 (1)	0.0353 (8)
Ti	0.010 (3)	0.022 (5)	0.012 (1)	0.014 (1)	0.019 (1)
O(4)	0.01	0.01	0.01	0.01	0.01
O(5)	-	-	0.01	0.01	0.01

Table 4.02. ***Fractional co-ordinates and equivalent anisotropic displacement parameters ($Å^2$) for $Na_{0.5}Bi_{0.5}TiO_3$, at various pressures.***

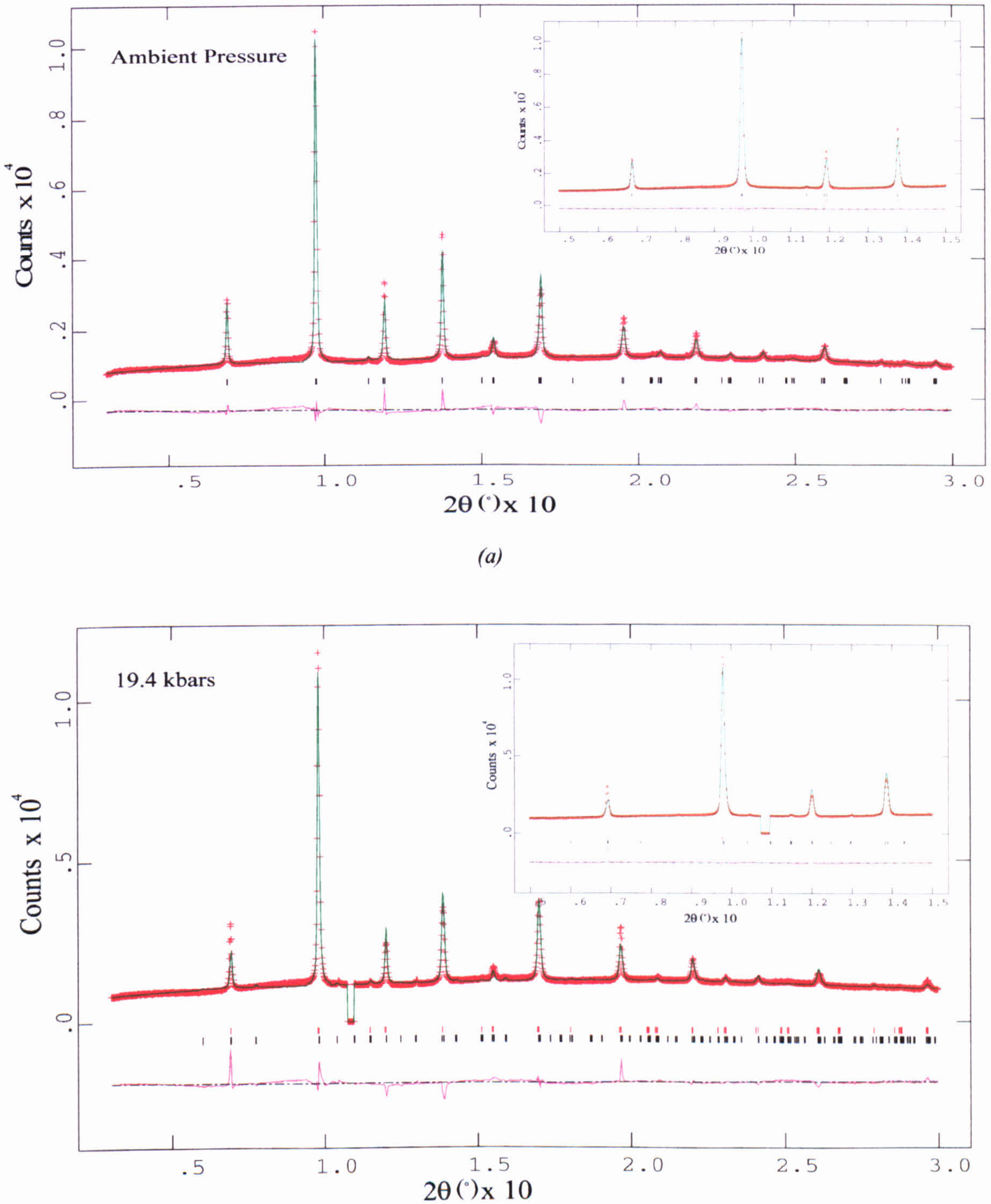

(a)

(b)

Figure 4.04. *The observed, calculated, and difference curves from the Rietveld refinement of $Na_{0.5}Bi_{0.5}TiO_3$. (a) refinement in R3c, at 293 K, ambient pressure, the marks indicate the positions of the reflections. (b) refinement in R3c and Pmna - coexistence region at 19.4 kbar, the red and black marks indicate the positions of the rhombohedral and orthorhombic reflections respectively. The low angle data ($5<2\theta<15°$) is magnified in the insert. A diffraction peak originating from the metal gasket of the pressure cell was evident in the profiles at pressures above 19.4 kbar; this peak was excluded in the refinement process.*

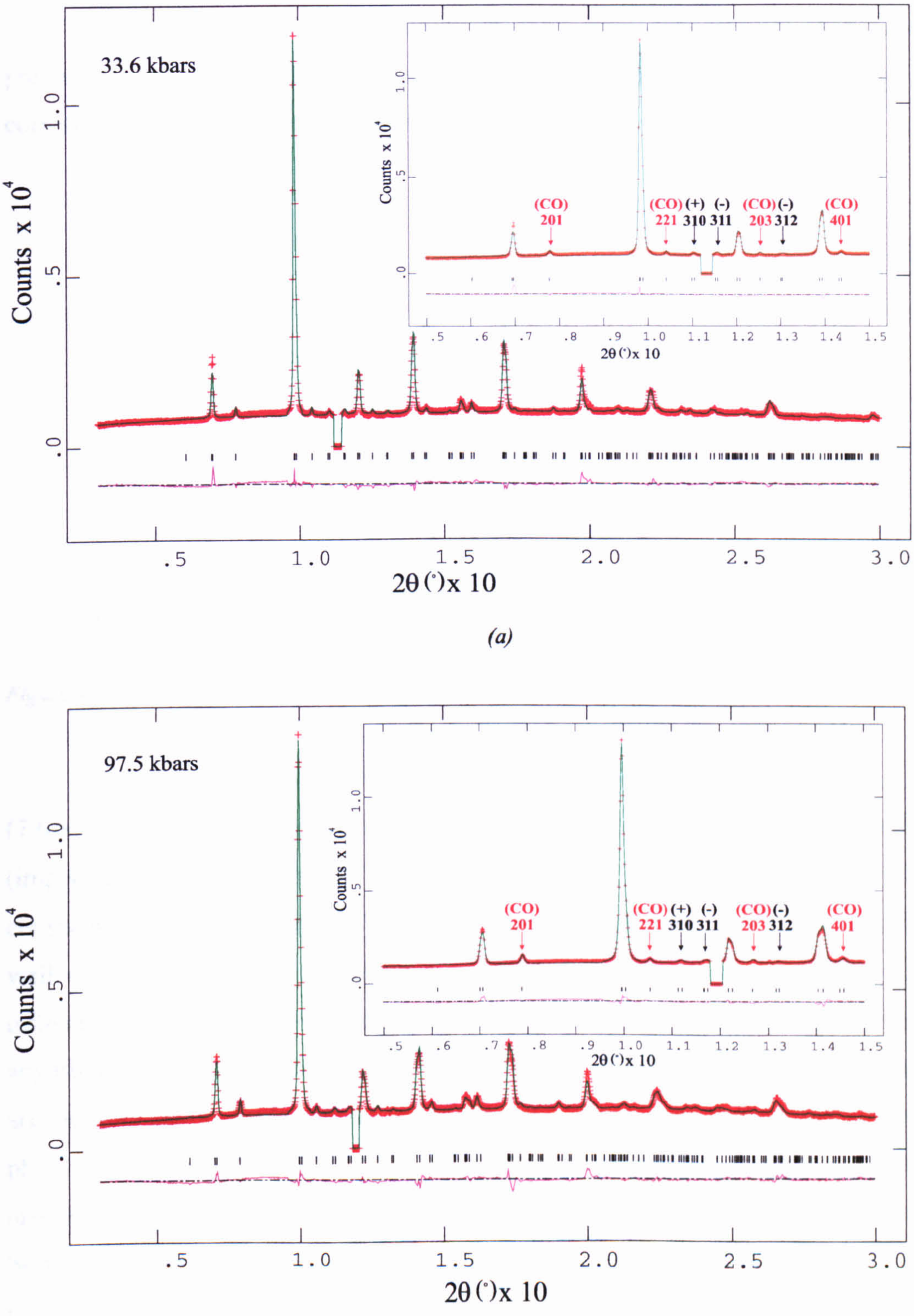

Figure 4.05. *The observed, calculated, and difference curves from the Rietveld refinement of $Na_{0.5}Bi_{0.5}TiO_3$. (a) refinement in Pnma, at 293 K, 33.6 kbar, (b) refinement in Pnma at 97.5 kbar. The marks indicate the positions of the reflections. The low angle data ($5<2\theta<15°$), showing the positions of peaks due to cation ordering (CO) and in-phase (+)/anti-phase (-) tilts are magnified in the insert. A diffraction peak originating from the metal gasket of the pressure cell was evident in the profiles at pressures above 19.4 kbar; this peak was excluded in the refinement process.*

Figure 4.07 shows the evolution of diffraction data profiles as a function of pressure. As the applied pressure is increased, the peak positions are shifted corresponding to a compression of the unit cell.

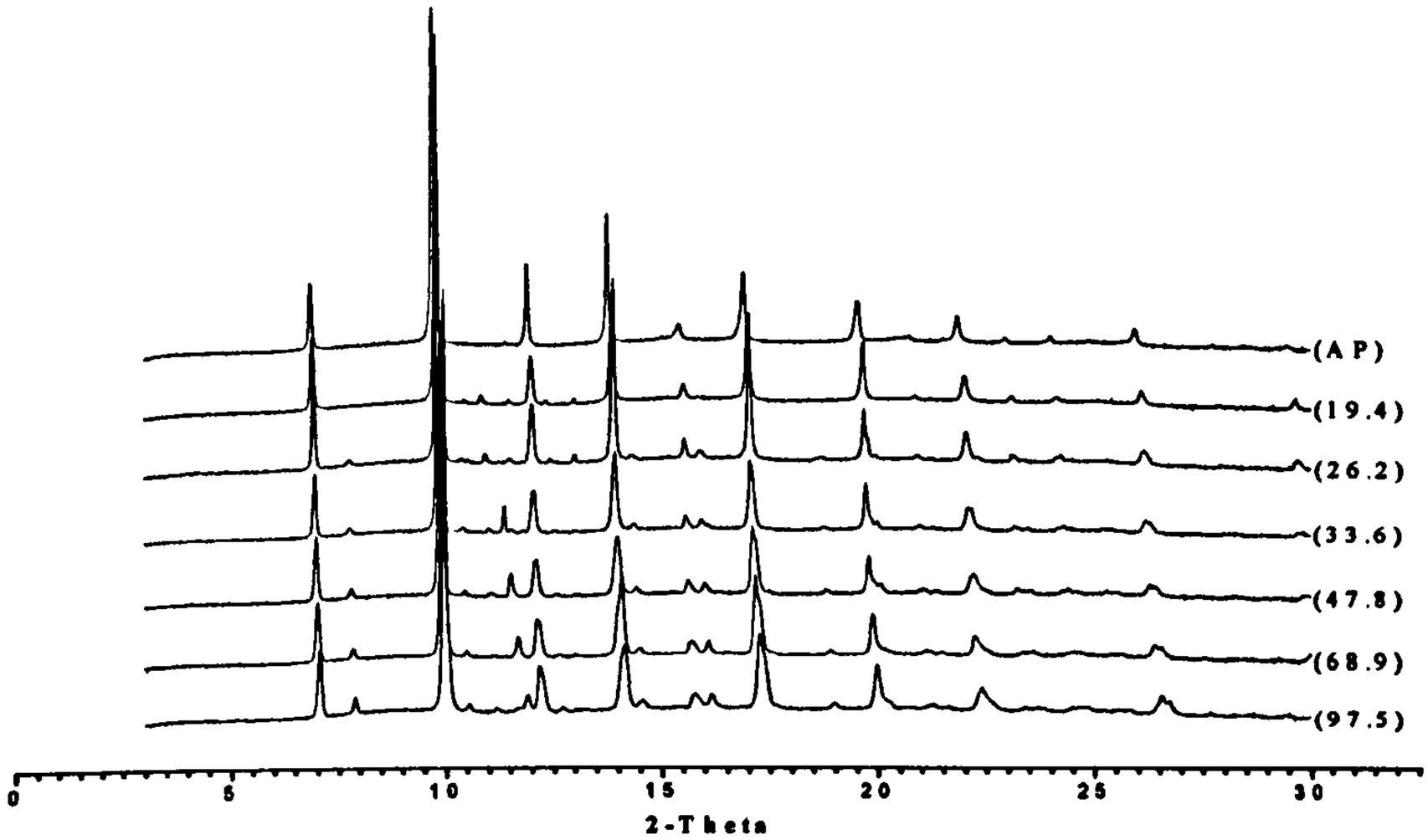

Figure 4.07. Integrated diffraction data profiles, figures in parenthesis indicate pressure in kbar.

Compared with the pseudo-cubic powder pattern referred to on the $2a \times 2b \times 2c$ ($7.6 \times 7.6 \times 7.6$ Å^3) unit cell, superstructure reflections of the type *h* odd, *k* odd, *l* odd (implying b^+ tilt) and, *h* odd, *k* even, *l* odd (implying a^- tilt) were observed. These are consistent with the tilt system $a^-b^+a^-$ and the orthorhombic unit cell $\sqrt{2}a \times 2b \times \sqrt{2}c$. As well as the superstructure reflections resulting from the tilting of oxygen octahedra, reflections of the type *h* even, *k* even, *l* odd were observed. These are not consistent with any tilt system, and therefore must result from cation displacements. The observed peaks arising from cation displacements are of the same type as seen in the orthorhombic Pnma phase of $CaTiO_3$[9]. In this structure Ti^{4+} cations lie on centres of symmetry and are not displaced whereas the Ca^{2+} cations are antiferroelectrically ordered along [010]. Significantly, this structure is also observed in the complex A-site substituted perovskite $Ca_2NdAgTi_4O_{12}$[10] and in some rare-earth manganites[11].

Figure 4.08 shows the near-identical position of peaks in the NBT diffraction data taken at a pressure of 47.8 kbar and that for $CaTiO_3$ (taken from Inorganic Crystal Structure Database[12] ICSD, collection code 42-0423) indicating the similarity of these structures. Following the reported structure of $CaTiO_3$ the space group Pnma was assigned and the structure refined with the initial starting positions of $CaTiO_3$.

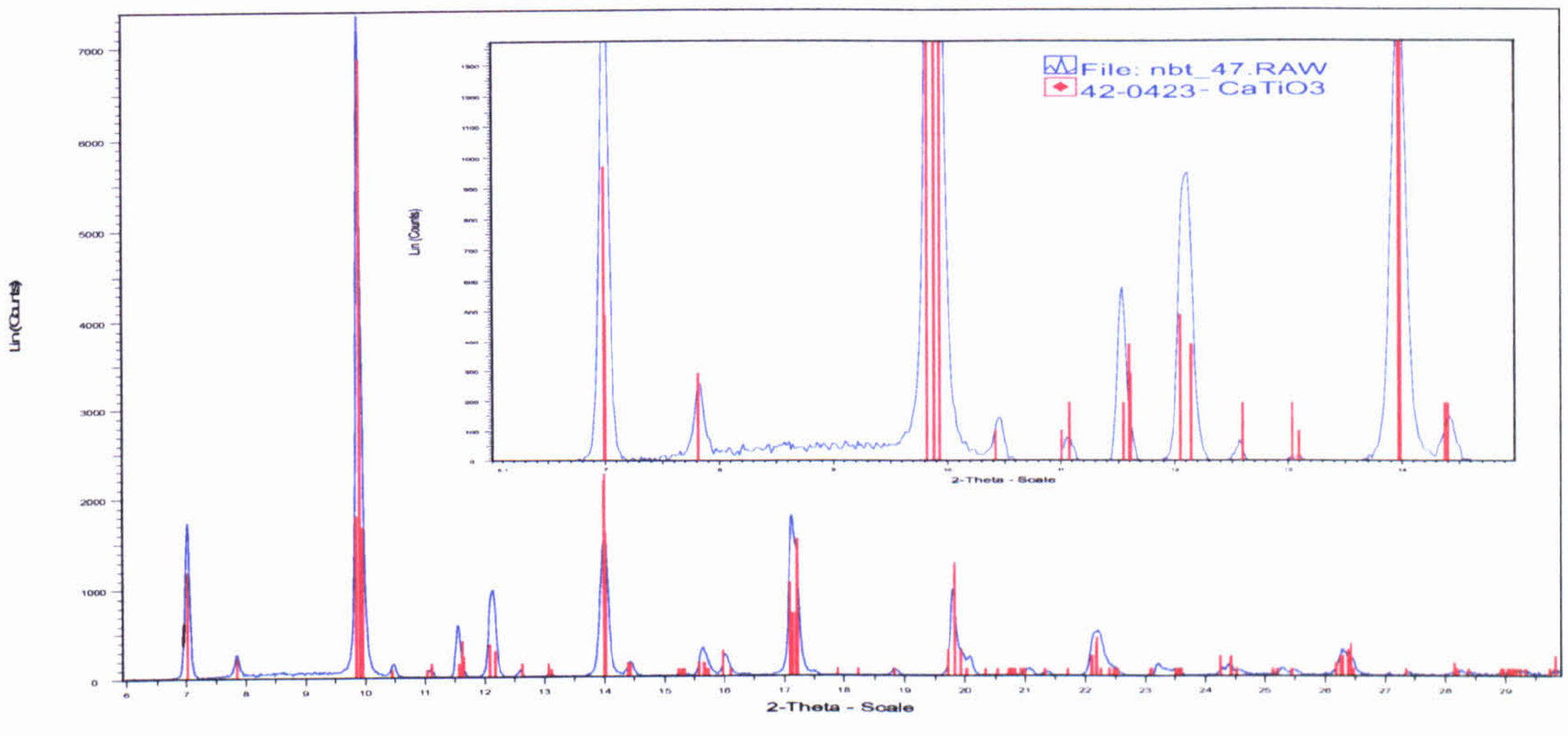

Figure 4.08. *Diffraction data of NBT taken at 47.8 kbar, superimposed (red lines) the peak positions given for the orthorhombic phase (Pnma) of $CaTiO_3$ (ICSD (42-0423)). The low angle data ($5<2\theta<11°$) are magnified in the insert.*

The background was based on a linear function and peak shapes, described by pseudo-Voigt profiles. It was decided to start with the 97.5 kbar pattern, and use the refined values from this for subsequent lower pressure refinements. As with the ambient pressure refinement, isotropic temperature factors were refined with oxygen atoms values being fixed to 0.01 $Å^2$. The Na and Bi atoms, each with site occupation factor 0.5, were constrained to be at the same positions during refinements. A diffraction peak originating from the metal gasket of the pressure cell was evident in the profiles at pressures above 19.4 kbar; this peak was excluded in the refinement process. The refinements were stable and converged quickly. The crystallographic data and the refined profile parameters for the refinements at 19.4, 33.6, and 97.5 kbar are summarised in Tables 4.01 (a), (b) and 4.02. The observed, calculated and difference profiles from the final Rietveld refinements are shown in Figures 4.04 and 4.05.

4.3 Neutron Powder Diffraction at Pressure

As an accompaniment to the x-ray data as a function of pressure, neutron powder diffraction data at various pressures were also taken on the high-resolution diffractometer D1A. As previously pointed out in section 3.3, the structural determination of NBT via neutron diffraction is beneficial over x-rays in locating accurately the oxygen atoms and, therefore for revealing information relating to the tilt systems in the compound. Pressure measurements were taken in a clamped high-pressure cell of maximum load 10 kbar.

Studies at pressures greater than this were not attempted due to a limitation in the pressure cells available for use.

4.3.1 D1A High-Resolution Diffractometer

The high-resolution two-axis diffractometer D1A[13] at the Institut Laue-Langevin (ILL), Grenoble, France was used in diffraction experiments. Details of the research facility can be found in section 3.3.1. The diffractometer utilises a continuous supply of thermal neutrons as its source, it is characterised by the high take-off angle (122°) from its Germanium monochromating crystals, giving high resolution at large scattering angles (up to 160°). A bank of 25 high efficiency collimators and ^{3}He counting tubes (at 5 atm) are employed. Complete scans between $0 < 2\theta < 160°$ typically take between 2-10 hours. A wide choice of wavelengths, from 1.39-2.99 Å can be selected by rotation of the focussing monochromator. Figure 4.09 shows the schematic layout of the instrument.

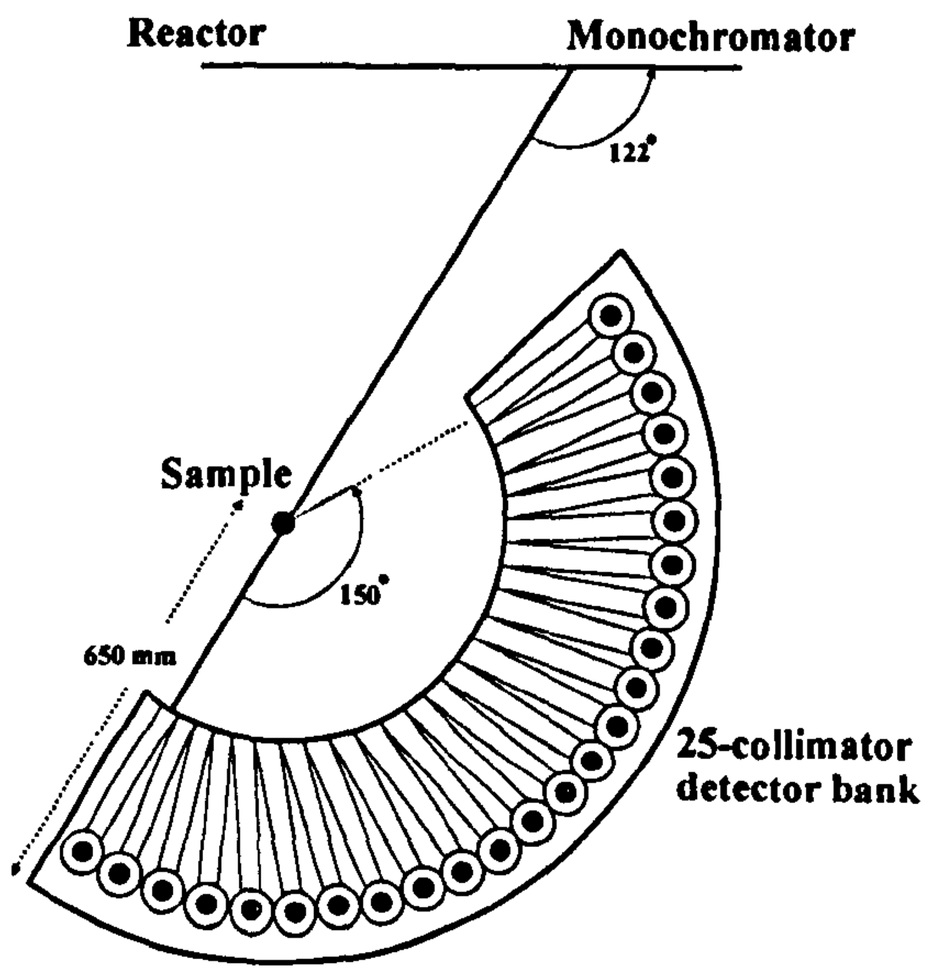

Figure 4.09. *Schematic layout of the D1A high-resolution diffractometer located at Institut Laue Langevin.*

4.3.2 Sample Preparation and Environment

Fragments of flux grown crystals were finely ground into powder. The powder was sieved to obtain particles with approximate diameters < 38 μm and compacted into 20 × 5 mm diameter hole within the pressure cell. A schematic representation of the high-pressure clamped cell is shown in Figure 4.10. The clamped high-pressure cell used was a *zero-matrix* type, the walls of which were made of an alloy of the elements Ti and Zr. If conventional materials such as steel were used, Bragg reflections (possibly of

orders of magnitudes greater than the reflections from the sample) in the data from the cell itself would result. These unwanted reflections would complicate the diffraction pattern and make precise structure refinements difficult. However, since Ti and Zr, have coherent scattering lengths of opposite sign, it is possible to prepare a material whose averaged coherent scattering lengths are equal to zero and so no Bragg reflections from the cell will contribute to the diffraction pattern.

The cell was loaded to the desired pressure in a hydraulic press and then clamped by a locking nut before being transferred into the neutron beam. The maximum pressure attainable using this cell was 10 kbar. The pressure cell position was adjusted so that only the sample region lay in the beam path. A cadmium shield was made and placed around the cell in order to shield all but the sample region. The sample was aligned on the rotation axis of the diffractometer and Polaroid photographs were taken of the direct beam through the sample to confirm the correct geometry had been obtained.

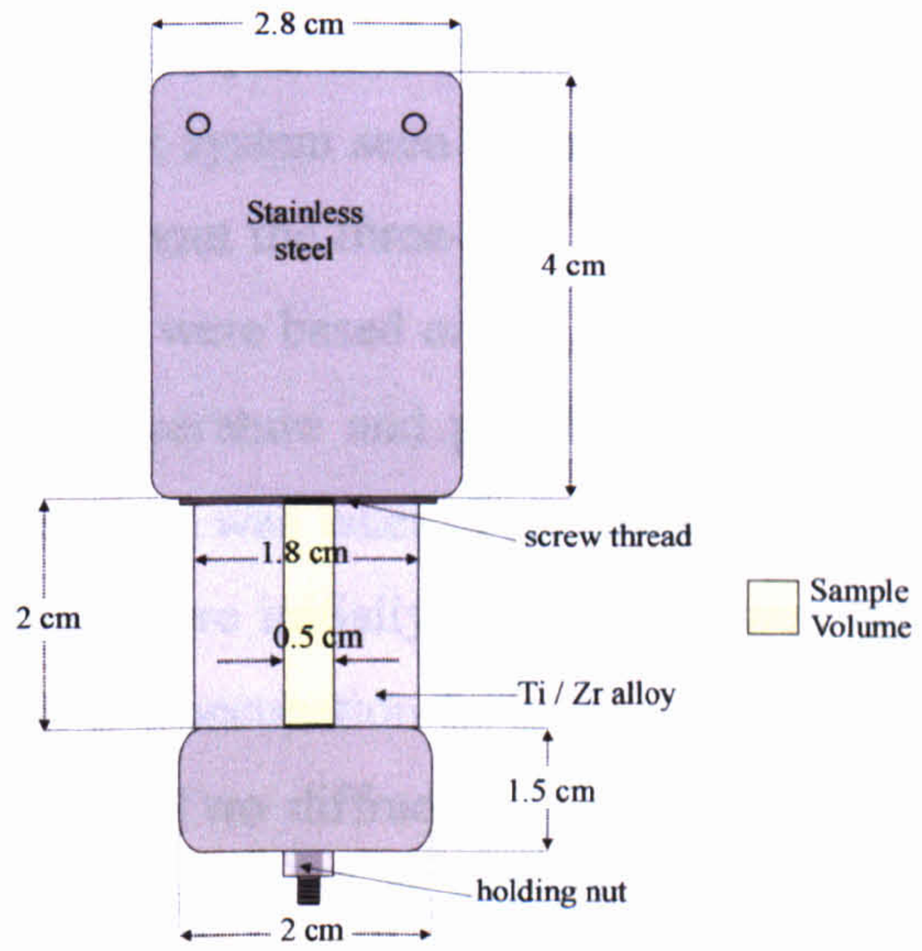

Figure 4.10. *Schematic representation of the zero-matrix high-pressure clamped cell (walls are made of an Ti/Zr alloy) used in neutron powder diffraction experiments on instrument D1A.*

4.3.3 Data Collections and Treatment

Data sets were collected using a wavelength of 1.91 Å. For all data sets, complete diffraction profiles were made up from sections by counting at each 2θ position until a predetermined number of monitor counts was achieved. The complete angular range between $0 < 2\theta < 160°$ was covered in 120 steps of 0.05°. This procedure was repeated eight times and the resulting profiles averaged. In all cases individual data runs were merged and converted into a GSAS compatible format. Table 4.03 lists the details of data collections.

Pressure (kbar)	Individual Scans	Total Scan Time (hours)
Ambient @ 293 K	eight, 2 hour scans	16
8 @ 293 K	eight, 2.5 hour scans	20
10 @ 293 K	eight, 2.5 hour scans	20

Table 4.03. Neutron data collections on D1A in clamped pressure cell.

4.3.4 Rietveld Structural Refinements

The Rietveld method was used to refine the crystallographic structure as a function of pressure. All data sets were analysed with the program GSAS. Superstructure reflections of the type *h* odd, *k* odd, *l* odd were observed for the ambient pressure (as expected) and 8 kbar profiles. As previously discussed (section 3.3.4) these are consistent with the $a^-a^-a^-$ tilt system seen in rhombohedral perovskites and arise from the oxygen octahedra tilting about the three-fold pseudo-cubic axes. Initial refinements for the ambient-pressure phase were based on the final refinements of neutron diffraction data obtained at ambient temperature and pressure as outlined in section 3.3.4. The initial model for the 8 kbar data was taken from the final ambient pressure refinement. Isotropic temperature factors were initially refined followed by anisotropic parameters. Na and Bi atoms each with site occupation factor 0.5 were constrained to be at the same positions during refinements. Two diffraction peaks that originated from the pressure cell housing (identified from a blank sample data collection) were excluded in the refinement process. The refinements were stable and converged quickly.

Data taken at 10 kbar revealed the rhombohedral phase with the corresponding superstructure peaks due to the oxygen octahedra tilts and the presence of an unidentified peak. Using the program CRYSTALLOGRAPHICA[14] a powder pattern simulation was calculated for neutron radiation (1.91 Å) using the data from the 19.4 kbar synchrotron final refinement. The position of the unidentified peak matched (taking into account a small shift in peak position that would occur due to the difference in lattice parameters at the two pressures) the highest intensity peak calculated. From this it was inferred that at 10 kbar pressure a coexistence region of the rhombohedral and orthorhombic phases exist. Refinements of rhombohedral and orthorhombic coexistence phases were based

on the 8 kbar (R3c) neutron and 19.4 kbar (Pnma) synchrotron final refinements respectively. Like previous refinements the background was based on a linear function and peak shapes, described by pseudo-Voigt profiles and the Na and Bi atoms each with site occupation factor 0.5 were constrained to be at the same positions. The refinements were stable and converged quickly. The crystallographic data and the refined profile parameters for all neutron refinements are summarised in Tables 4.04 and 4.05 (a) and (b). The observed, calculated and difference profiles from the final Rietveld refinements are shown in Figures 4.11 (a)-(c).

Rhombohedral (R3c) Phase (293 K) at ambient pressure

Atom	x	y	z	U11	U22	U33	U12	U13	U23
Na	0.0	0.0	0.2651 (5)	0.007 (1)	0.007 (1)	0.021 (4)	0.004 (1)	0.0	0.0
Bi	0.0	0.0	0.2651 (5)	0.043 (4)	0.043 (4)	0.062 (7)	0.021 (1)	0.0	0.0
Ti	0.0	0.0	0.0061 (6)	0.013 (3)	0.013 (3)	-0.057 (3)	0.006 (1)	0.0	0.0
O	0.1264 (4)	0.3355 (9)	0.0833	0.011 (4)	0.019 (3)	0.029 (2)	-0.021(5)	0.018 (4)	-0.016(2)

Rhombohedral (R3c) Phase (293 K) at 8 kbar

Atom	x	y	z	U11	U22	U33	U12	U13	U23
Na	0.0	0.0	0.2618 (5)	0.018 (6)	0.018 (6)	0.04 (1)	0.009 (3)	0.0	0.0
Bi	0.0	0.0	0.2618 (5)	0.036 (3)	0.036 (3)	0.030 (5)	0.018 (2)	0.0	0.0
Ti	0.0	0.0	0.0021 (8)	0.017 (3)	0.017 (3)	-0.036 (4)	0.009 (1)	0.0	0.0
O	0.1289 (9)	0.339 (1)	0.0833	0.017 (3)	0.008 (2)	0.038 (2)	-0.021(5)	0.016 (4)	-0.016(2)

Rhombohedral (R3c) Phase (293 K) at 10 kbar

Atom	x	y	z	U11	U22	U33	U12	U13	U23
Na	0.0	0.0	0.2551(5)	0.016(3)	0.016(3)	0.038(9)	0.008(2)	0.0	0.0
Bi	0.0	0.0	0.2551(5)	0.034(2)	0.034(2)	0.035(6)	0.017(2)	0.0	0.0
Ti	0.0	0.0	0.0020(3)	0.027(2)	0.027(2)	-0.041(2)	0.013(3)	0.0	0.0
O	0.1219(2)	0.3361(2)	0.0833	0.006(4)	0.010(6)	0.034(5)	-0.006(3)	0.014(5)	-0.015(4)

Orthorhombic (Pnma) Phase (293 K) at 10 kbar

Atom	x	y	z	U11	U22	U33	U12	U13	U23
Na	0.028(5)	0.25	-0.007(2)	0.034(9)	0.034(9)	-0.036(1)	0.0	0.040(6)	0.0
Bi	0.028(5)	0.25	-0.007(2)	0.060(3)	0.038(6)	-0.061(7)	0.0	0.039(6)	0.0
Ti	½	0.0	0.0	0.046(9)	0.048(9)	0.025(8)	0.039(2)	0.038(2)	0.011(3)
O(I)	0.795(6)	-0.036(9)	0.350(8)	0.040(7)	0.080(8)	0.021(4)	-0.048(9)	0.023(5)	0.043(5)
O(II)	-0.412(3)	¼	0.292(1)	0.022(9)	0.023(8)	0.040(6)	0.0	0.040(8)	0.0

Table 4.04. Fractional co-ordinates and equivalent anisotropic displacement parameters ($Å^2$) for NBT.

Chemical formula	$Na_{0.5}Bi_{0.5}TiO_3$	
Chemical formula weight	211.88	
Specimen Shape	Random powder	
Radiation Type	Neutron	
Wavelength	1.91 Å	
CRYSTAL SYSTEM	**Rhombohedral**	**Rhombohedral**
Space Group	R3c	R3c
a (Å)	5.4872 (2)	5.4772 (3)
b (Å)	5.4872 (2)	5.4772 (3)
c (Å)	13.4901 (6)	13.4680 (8)
α,β,γ (°)	90,90,120	90,90,120
α_p (°)	89.86	89.85
Volume (Å^3)	351.76 (2)	349.91 (6)
Z	6	6
D_x (Mg.m^{-3})	6.002	6.094
Tilt System	$a^-a^-a^-$	$a^-a^-a^-$
Displacements	Parallel along $[111]_p$	Parallel along $[111]_p$
ω (°)	8.12 (4)	8.0 (2)
$\zeta \times 10^2$	-0.64 (1)	-0.59 (5)
DATA COLLECTION		
Pressure (kbar)	AP	8
Temperature (K)	273	273
Specimen environment	Clamped zero-matrix cell	Clamped zero-matrix cell
Scan Time (hours)	16	20
$2\theta_{min}$ (°)	26.01	26.01
$2\theta_{max}$ (°)	128.01	114.51
REFINEMENTS		
Background / coefficients	linear interpolation / 8	linear interpolation / 8
Scale	1475 (6)	2499 (8)
2θ zero-error	-0.3 (2)	-0.58 (5)
Excluded Regions	54.41-57.08	54.33-57.03
	82.60-84.37	82.74-85.10
Peak Shape parameters:		
G(U), G(V), G(W),	324 (5), -318 (9), 207 (4)	67 (5), -34 (9), 136 (3)
G(P).	0	0
L_x, L_y	5 (2), 1.5 (6)	2.4 (4), 18.8 (7)
asym	2.8 (8)	29 (1)
Nº. of parameters	42	42
R_p	0.0263	0.0220
$_wR_p$	0.0360	0.0298
χ^2	0.076	0.0914

Table 4.05. (a) Summary of experimental details, data collection and refinement for $Na_{0.5}Bi_{0.5}TiO_3$.

Chemical formula	**$Na_{0.5}Bi_{0.5}TiO_3$**	
Chemical formula weight	211.88	
Specimen Shape	Random powder	
Radiation Type	Neutron	
Wavelength	1.91 Å	
CRYSTAL SYSTEM	**Rhombohedral (83 %)**	**Orthorhmbic (17 %)**
Space Group	R3c	Pnma
a (Å)	5.4601 (1)	5.535 (2)
b (Å)	5.4601 (1)	7.735 (2)
c (Å)	13.4261(7)	5.356 (1)
α,β,γ (°)	90,90,120	90,90,90
α_p (°)	89.85	-
Volume (Å^3)	346.64 (1)	229.30 (9)
Z	6	4
D_x (Mg.m^{-3})	6.029	6.138
Tilt System	$a^-a^-a^-$	$a^-b^+a^-$
Displacements	Parallel along $[111]_p$	Parallel along [100]
Ordering	-	Anti-parallel along [010]
ω (°)	7.93 (8)	5.0 anticlockwise about [010] 16.9 clockwise about [100]/[001]
$\zeta \times 10^2$	-0.0057 (2)	-
DATA COLLECTION		
Pressure (kbar)	10	10
Temperature (K)	273	273
Specimen environment	Clamped zero-matrix cell	Clamped zero-matrix cell
Scan Time (hours)	20	20
$2\theta_{min}$ (°)	27.31	27.31
$2\theta_{max}$ (°)	126.94	126.94
REFINEMENTS		
Background / coefficients	linear interpolation / 8	linear interpolation / 8
Scale	2101 (9)	2101 (9)
2θ zero-error	0.10 (1)	0.10 (1)
Excluded Regions	54.56-57.48 82.43-84.46	54.56-57.48 82.43-84.46
Peak Shape parameters:		
G(U), G(V), G(W),	44 (7), -37 (6), 133 (4)	58 (1), -62 (6), 122 (1)
G(P).	0	0
L_x, L_y	1.3 (3), 19.8 (4)	1.12 (2), 12.35 (4)
asym	28.6 (5)	6.01 (2)
Nº. of parameters	42	50
R_p	0.0338	0.0338
$_wR_p$	0.0465	0.0465
χ^2	0.1501	0.1501

Table 4.05. (b) Summary of experimental details, data collection and refinement for $Na_{0.5}Bi_{0.5}TiO_3$.

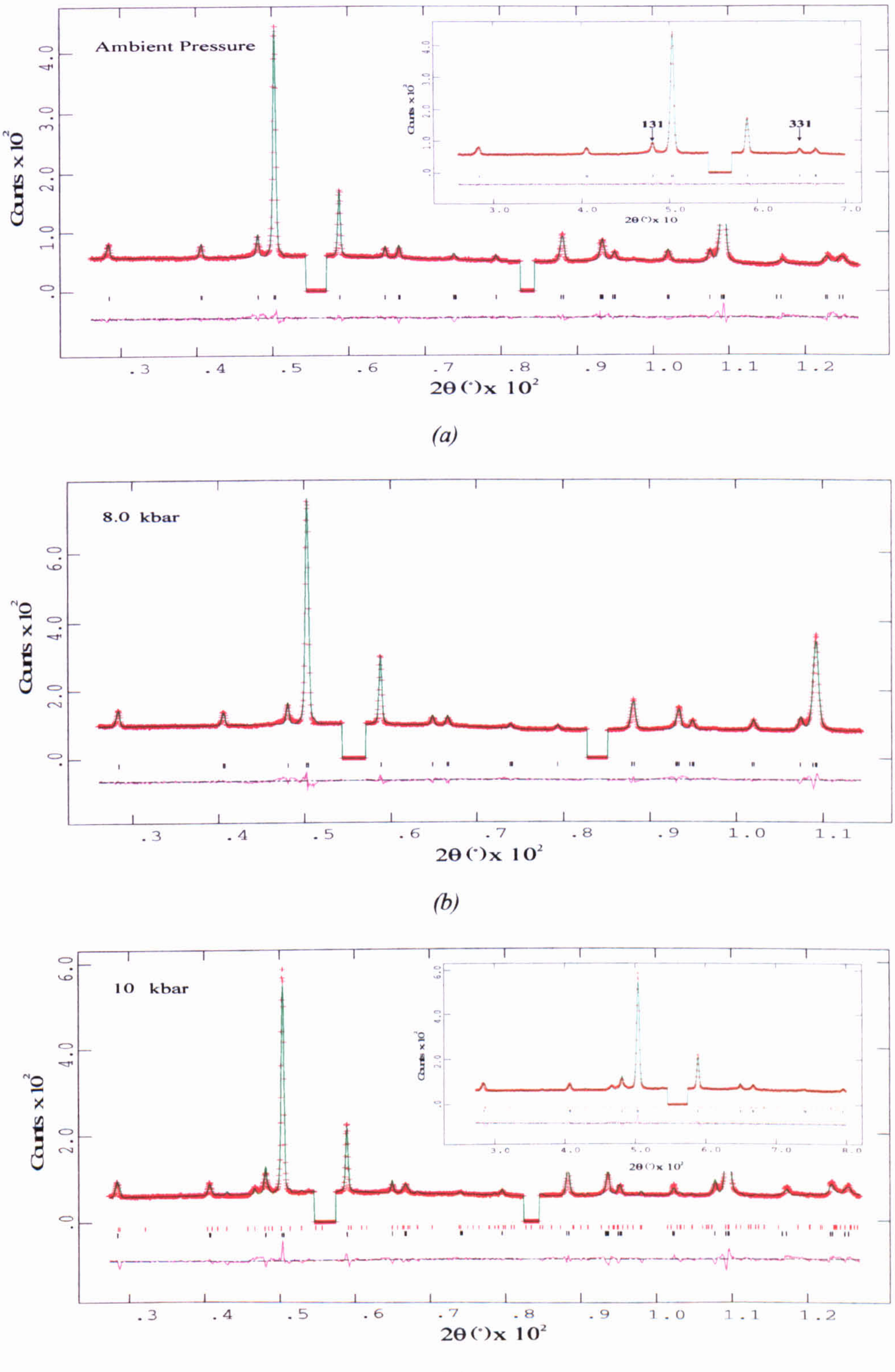

Figure 4.11. *The observed, calculated, and difference curves from the Rietveld refinement of $Na_{0.5}Bi_{0.5}TiO_3$ at 273 K. (a) refinement in R3c, ambient pressure, the mid-angle data ($25<2\theta<70°$), showing the first two superstructure peaks are magnified in the insert. (b) refinement in R3c at 8 kbar pressure, (c) refinement in R3c and Pnma coexistence phases, at 10 kbar pressure, the mid-angle data ($25<2\theta<80°$), is magnified in the insert. The black and red marks indicate the positions of the rhombohedral and orthorhombic reflections respectively. Two diffraction peaks originating from the pressure cell housing were excluded in the refinement process.*

4.4 Discussion

Synchrotron and neutron powder diffraction experiments as a function of pressure have been undertaken for NBT for the first time. In the following discussion the crystal structure and phase transitions as a function of pressure are reported. The new pressure-induced orthorhombic phase is presented with structural modifications being reported as a function of pressure.

4.4.1 Lattice Parameters and Phase Transitions

Lattice parameters obtained from final refinements of data for the orthorhombic and rhombohedral phases have been plotted as a function of pressure in Figures 4.12 (a), (b) and 4.13 (a), (b) respectively. Looking first at the orthorhombic phase, the cell parameters: a_o, b_o and c_o decrease steadily with increasing pressure, as expected. By calculating fits to the data the gradients da_o/dP, db_o/dP and dc_o/dP were found to be $-1.07\ (5) \times 10^{-3}$, $-1.44\ (5) \times 10^{-3}$ and $-1.5\ (1) \times 10^{-3}$ Å kbar^{-1} respectively. Therefore in terms of the rate of decrease in the lattice parameter as a function of pressure, we find that b_o and c_o have very similar values whereas a_o decreases at a slower rate (27 % of the average rate of decrease shown by b_o and c_o). Between 19.4 and 97.5 kbar, a_o, b_o, and c_o are compressed by 0.079, 0.1165 and 0.1198 Å respectively. It can be concluded that in the orthorhombic phase of NBT the cell is more compressible in b_o and c_o. Figure 4.12 (c) shows the variation in unit cell volume as a function of pressure. A steadily decreasing trend is seen due to the pressure-induced contractions in the lattice parameters. There is no indication of any anomalous changes in the crystal volume. Comparing directly the values between 19.4 and 97.5 kbar the orthorhombic unit cell contracts by 11.6 (2) Å^3 or 5.05 (8) %.

The unit cell dimensions of the rhombohedral phase determined via neutron powder diffraction, at ambient pressure (room temperature) were in good agreement with those determined previously (section 3.2.5) to within 0.0015 (2) and 0.0147 (2) Å for a_H and c_H respectively. The values were also in good agreement with those obtained using synchrotron radiation (sample housed in pressure cell) to within 0.0023 (2) and 0.0099 (4) Å for a_H and c_H respectively. In the pressure range between 8 and 10 kbar there is a discontinuous jump in a_H, c_H and cell volume. This is possibly related to the occurrence of the first-order phase transition between the rhombohedral and orthorhombic phases. Figure 4.13 (c) shows the variation in rhombohedral unit cell volume as a function of

pressure. The trend mirrors that of the unit cell parameters with a clear volume change at the phase transition $\Delta V = -3.27\ (5)\ Å^3$ being observed.

The pure rhombohedral structure of NBT persists up to 8 kbar, between 10-19.4 kbar a rhombohedral/orthorhombic coexistence region is observed and above 26.2 kbar the purely orthorhombic phase is seen. From refinement calculations, an 83 % rhombohedral phase volume is observed at 10 kbar and 26 % at 19.4 kbar. Therefore over a 2 kbar pressure region (between 8-10 kbar) the rhombohedral phase diminishes by 17 %, and over 9.4 kbar (between 19.4-10 kbar) the phase diminishes by 57 %.

4.4.2 Octahedral Tilting and Cation Displacements

The rhombohedral phase (polar space group R3c) and the $a^-a^-a^-$ antiphase tilt system have been discussed previously (section 3.3.4) and a representation of the structure can be seen in Figure 3.16. Figures 4.14 (a) and (b) show the variation of the Na/Bi (*s*) and Ti (*t*) cation shifts as a function of pressure. The overall displacements of cations calculated in the Rietveld refinements are from the centres of their co-ordination polyhedra. An overall decreasing trend in *s* and *t* is observed with increasing pressure. The ambient pressure displacements are in good agreement with values taken on diffractometer D2B discussed in section 3.3.5.1. Examination of the Na/Bi shifts show a sharp (34 %) reduction occurring at 10 kbar. This occurrence is directly related to the large changes observed in the lattice parameters at this pressure.

The pressure dependence of the experimentally determined rhombohedral phase tilt angles, ω, are summarised in Figure 4.14 (c). As the pressure is increased the unit cell is compressed and one would normally expect the degree of tilting to increase. The tilt angle variation determined in this case however shows a small gradual overall decrease, with the change in tilt angle between 1-19.4 kbar being 0.27 (4)°. The ambient pressure tilt angle is comparable in magnitude with that determined previously (section 3.3.5.3) to within 0.12 (4)°.

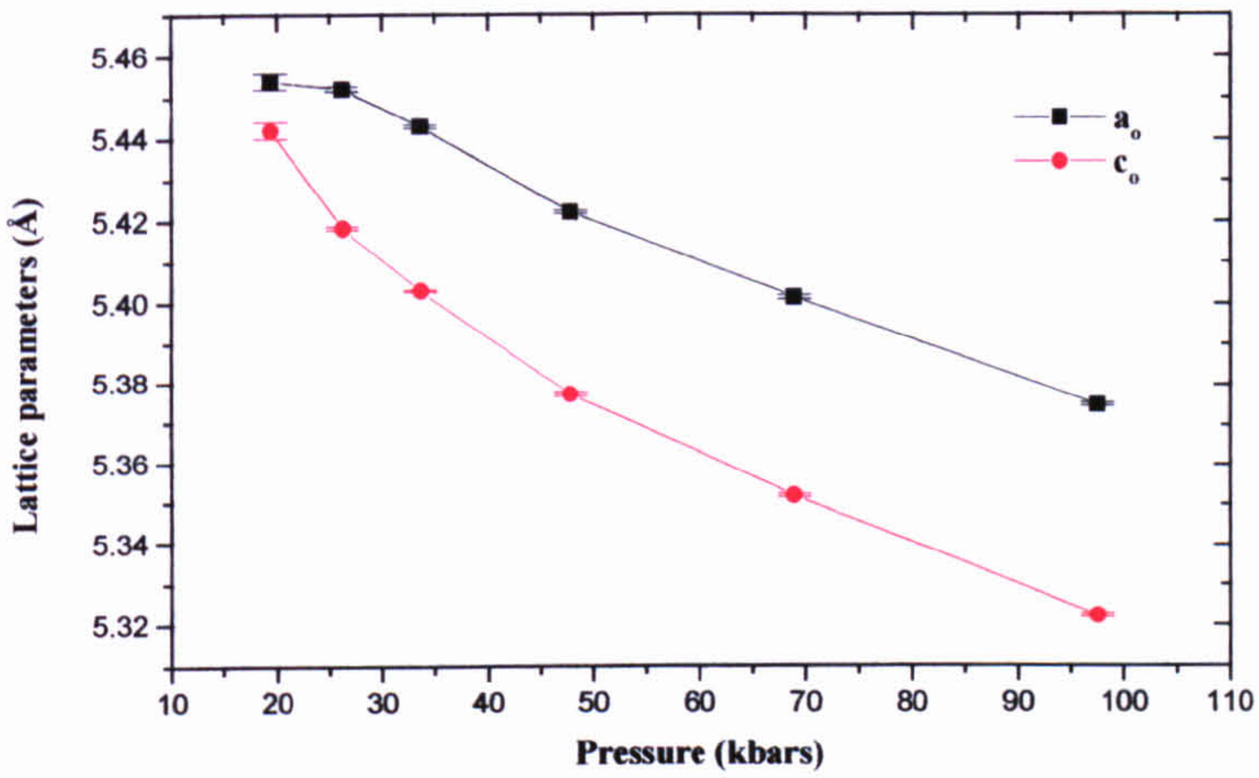

(a)

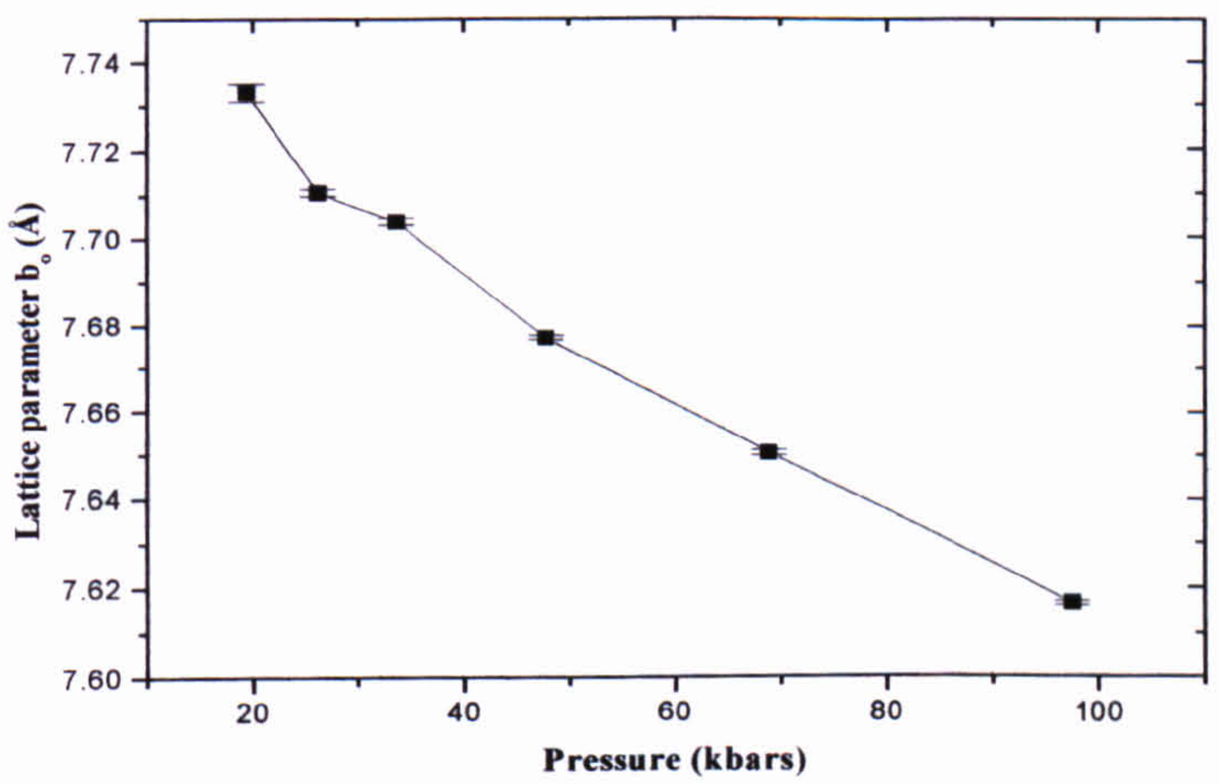

(b)

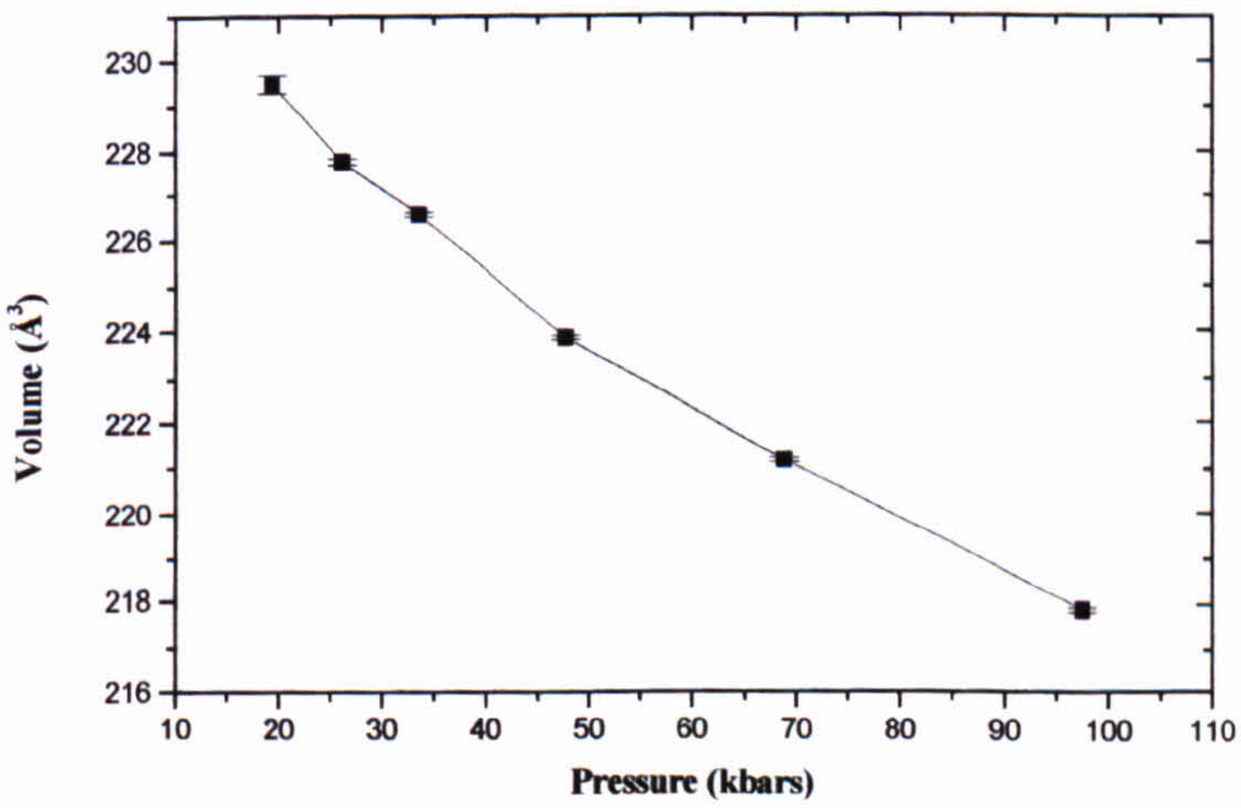

(c)

Figure 4.12. *Pressure dependence of the experimentally determined lattice parameters and unit cell volume of the orthorhombic phase (Pnma) of $Na_{0.5}Bi_{0.5}TiO_3$.*

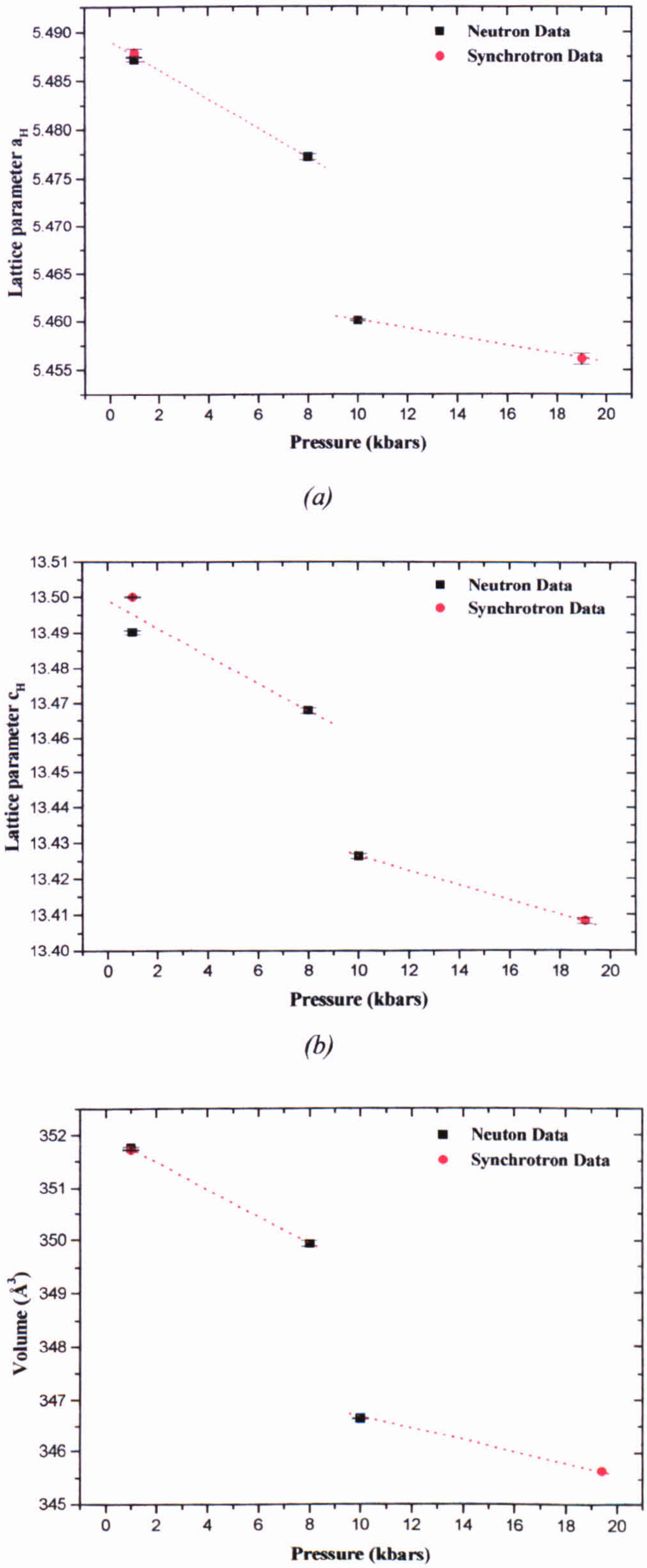

Figure 4.13. *Experimentally determined rhombohedral lattice parameters and unit cell volume as a function of pressure calculated from neutron and synchrotron Rietveld refinements. The dotted lines (linear fits) are guides for the eye.*

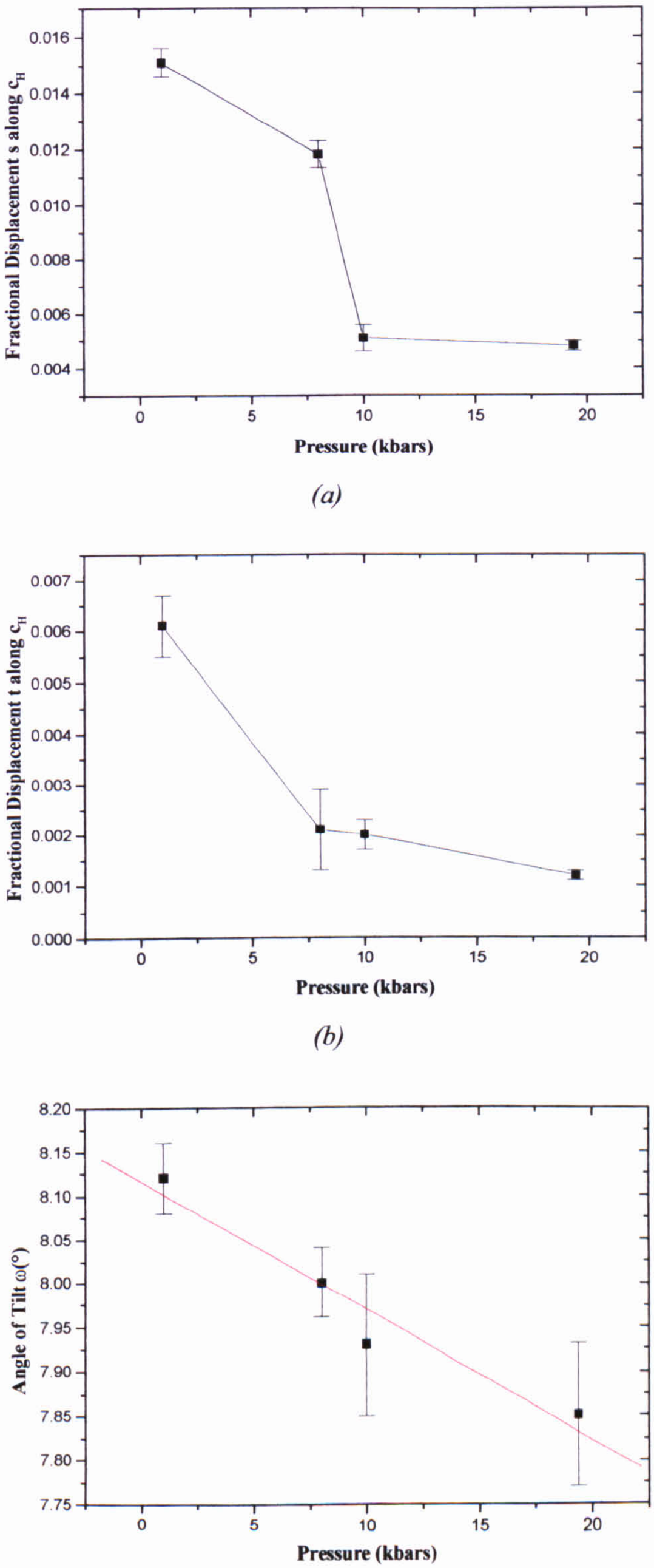

Figure 4.14. *The experimentally determined variation of (a) Na/Bi cation shifts and (b) Ti cation shifts (expressed in fractions of c_H) with pressure. (c) The experimentally determined variation of the octahedron tilt angle ω(°) with pressure (the red line indicates linear fit to data).*

A phase transition is observed to have occurred by 19.4 kbar, causing a deformation of the rhombohedral cell to one of orthorhombic symmetry. This is associated with the disappearance of the oxygen octahedra tilting about the three-fold pseudo-cubic axes and the appearance of spontaneous x- and y-tilting about the pseudo-cubic axes. The pressure-induced orthorhombic structure has Pnma symmetry with the $a^-b^+a^-$ tilt system of oxygen octahedra and antiparallel A-cation ordering along [010]. This tilt system is described by antiphase tilts of equal magnitude about [100] and [001], coupled with in-phase tilts about [010]. Schematic representations of the distortions within the structure viewed down [010] and [001] are shown in Figures 4.15 (a) and (b) respectively.

The centrosymmetric site symmetry of the B-cation, prohibits off-centre displacements of the B-cations but the space group permits A-cation displacements. Therefore in NBT the Ti cations are not displaced (as they lie on centres of symmetry) whereas the Na/Bi cations are antiferroelectrically ordered along [010]. The off-centre displacements of the A-cations within the AO_{12} polyhedron act as a stabilising mechanism in order to achieve closer co-ordination by oxygen ions. This allows the TiO_6 framework to collapse further[15]. If we consider the orthorhombic structure as a deformation from the prototypic cubic perovskite structure, then displacements (u, v, w) from the ideal cubic positions in the space group Pnma, calculated from refinements can be determined. Table 4.06 exemplifies this procedure for the refined data taken at 97.5 kbar (which shows the greatest distortion).

Atomic Species	Position	x	y	z	u	v	w
Na/Bi	4(c)	u	¼	w	0.0321(4)	0	-0.0043(4)
Ti	4(b)	½	0	0	0	0	0
O(4)	8(d)	$¾ + u_{(O4)}$	$v_{(O4)}$	$¼ + w_{(O4)}$	0.017(3)	-0.022(2)	0.063(3)
O(5)	4(c)	$u_{(O5)}$	¼	$½ + w_{(O5)}$	-0.054(5)	0	-0.149(3)

Table 4.06. Restrictions on atomic displacements corresponding to the orthorhombic space group Pnma.

The rotation of whole octahedra is a direct consequence of the oxygen atom displacements. From these displacements the tilt amplitudes may be calculated. Using the visual crystal structure programme Diamond[16], tilt angle magnitudes were calculated by measuring the deviations of neighbouring oxygen octahedra from their ideal, zero-

distortion positions. Clockwise tilt angles about [010] were derived from the bond angles represented by ψ in the figures, between O(4) atoms residing on the 8d sites and Ti atoms residing on the 4c sites. Anti-clockwise tilt angles about [100]/[001] were derived from bond angles represented by ϕ between O(5) atoms residing on the 4c sites and Ti atoms residing on the 4b sites. Figure 4.15 (c) shows the variation of the orthorhombic tilt angles about [010] and [100]/[001] as a function of pressure. The distortions about [010] rise gradually with increasing pressure. Over the pressure range 19.4-97.5 kbar there is an overall increase in the tilting angle of 1.52°. This is in marked contrast to the tilting around [100]/[001], which shows a significant increase. Over the same pressure interval the tilting around [100]/[001] increases by 12.6°, (an 83 % relative increase). The pressure dependence of the tilt angles should be directly related to the bond compressibility of the Na/Bi and Ti cations within the structure. It is the relative strength of the Na(Bi)-O and Ti-O bonds which will determine any deformations that are brought about by pressure changes. We intuitively expect that the compressibility of the Na(Bi)-O bonds is higher than the Ti-O bonds, therefore, as a function of increasing pressure as the unit cell is compressed to a greater extent (thereby forcing neighbouring octahedra closer together) tilt amplitudes will increase. Looking at the A-site substituted perovskite $(Ca_2NdAg)Ti_4O_{12}$[10] the tilts are estimated to be 7.4 (1)° clockwise for the antiphase tilts about [100]/[001] and 7.7 (2)° anti-clockwise for the in-phase tilts about [010], calculated at ambient pressure. In NBT the antiphase and in-phase tilting are of similar magnitudes at 19.4 kbar (but with the antiphase tilting being larger). As a function of increasing pressure the antiphase tilting is significantly more dominant in NBT. In Figures 4.16 and 4.17 the structure of NBT (from final refinements) at 33.6 and 97.5 kbar projected down [010] and [001] is represented. From these, the distortions caused by the tilted octahedra are clearly visible. Figure 4.17 represents the highest-pressure (97.5 kbar) refined structure, whilst this is the best model to fit our current data, the extent of the distortions tolerated seem unusually large. It would be beneficial to collect higher-quality data at higher resolution to confirm this highly distorted structural variant.

4.4.3 Valency Calculations

For the majority of compounds the sum of bond valances around an atom is equal (or nearly equal) to its oxidation state. In practice however this is not always strictly adhered too due to uncertainties in the bond lengths that are actually measured. The

difference between the determined bond valence sum and the atomic valence is usually small however, unless strain causes excessive stretching or compression of the bonds. Crystal structures with very large deficiencies are generally found to be either incorrect or refined in a space group with too high symmetry. Using the program VaList, bond valence calculations for the orthorhombic phase of NBT were performed. The calculated bond valence sums for Na^{1+} and Ti^{4+} show a 2 % and 5 % difference, respectively, from their ideal values. The bond valence sum calculated for Bi^{3+} shows a 34 % difference from its ideal value of 3.0. The Bi^{3+} cations in the orthorhombic structure of NBT show a relatively large difference whereas the bond valences of both Na^{1+} and Ti^{4+} cations are closer to their formal oxidation state values. A similar trend has been previously observed in the rhombohedral (R3c, $a^-a^-a^-$) and tetragonal (P4bm, $a^0a^0c^+$) phases of NBT (section 3.3.5.4) with Bi^{3+} showing a 22 % and 32 % deficiency respectively. Valence deficiency has also been seen in the orthorhombic phase of $Ag_{0.5}Bi_{0.5}TiO_3$[17] (Ibam, $a^0a^0c^-$) with Ag^{1+}, Ti^{4+} and Bi^{3+} cations showing 2 %, 1 % and 26 % deficiencies, respectively, from their ideal values. A further example can be seen in the orthorhombic perovskite $(Ca_2NdAg)Ti_4O_{12}$[10] (Pnma, $a^-b^+a^-$) were Ag^{1+}, Nd^{3+}, Ca^{2+} and Ti^{4+} show 16 %, 10 %, 9 % and 1.5 % differences respectively. Structural distortions, such as octahedral tilting (which are largely governed by the A-cation size) play an important role in reducing bond valence differences and achieving an optimal minimal energy configuration. Considering the size of ionic radii within these compounds, one would expect that the bond valence deficiencies in the NBT analogue $Ag_{0.5}Bi_{0.5}TiO_3$ to be greater than in NBT due to the larger A-cation size and smaller octahedral distortions. This is not the case however, which may be due to the fact that the orthorhombic structure of NBT is a pressure-induced highly distorted variant of the perovskite structure, in which the cations are forced into non-ideal bonding environments. Even though the Bi-cations are displaced, again it seems that it is unable to reach a perfect match to its valency.

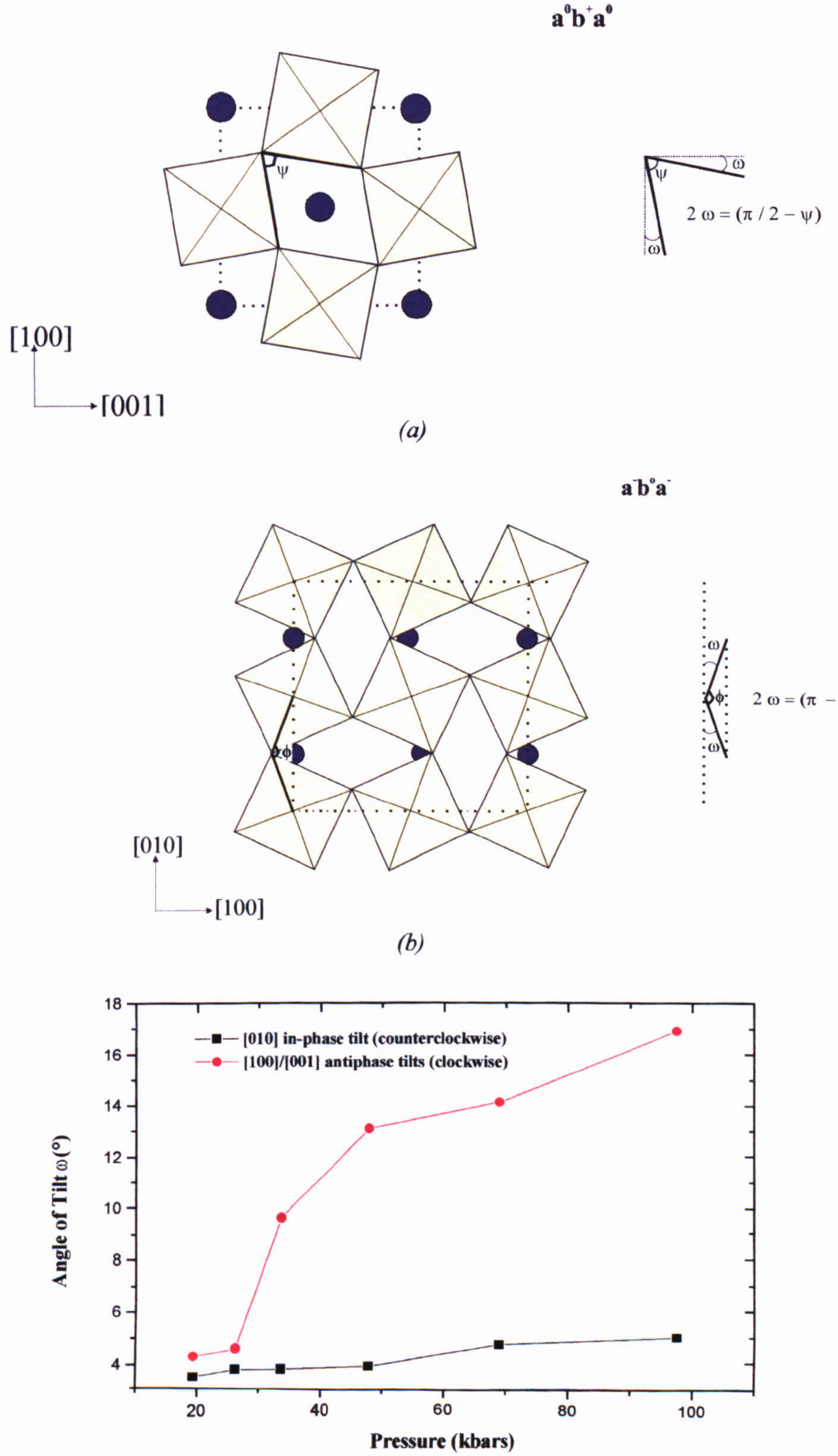

Figure 4.15. *Schematic representation of the distorted (Pnma, $a^-b^+a^-$) perovskite structure viewed down (a) [010] and (b) [001], ψ and ϕ represent the measured bond angles used in the determination of the tilt angles ω, clockwise about [010] and anti-clockwise about [100]/[001] respectively. (c) The experimentally determined variation in the octahedron tilt angles about [010] and [100]/[001] with pressure.*

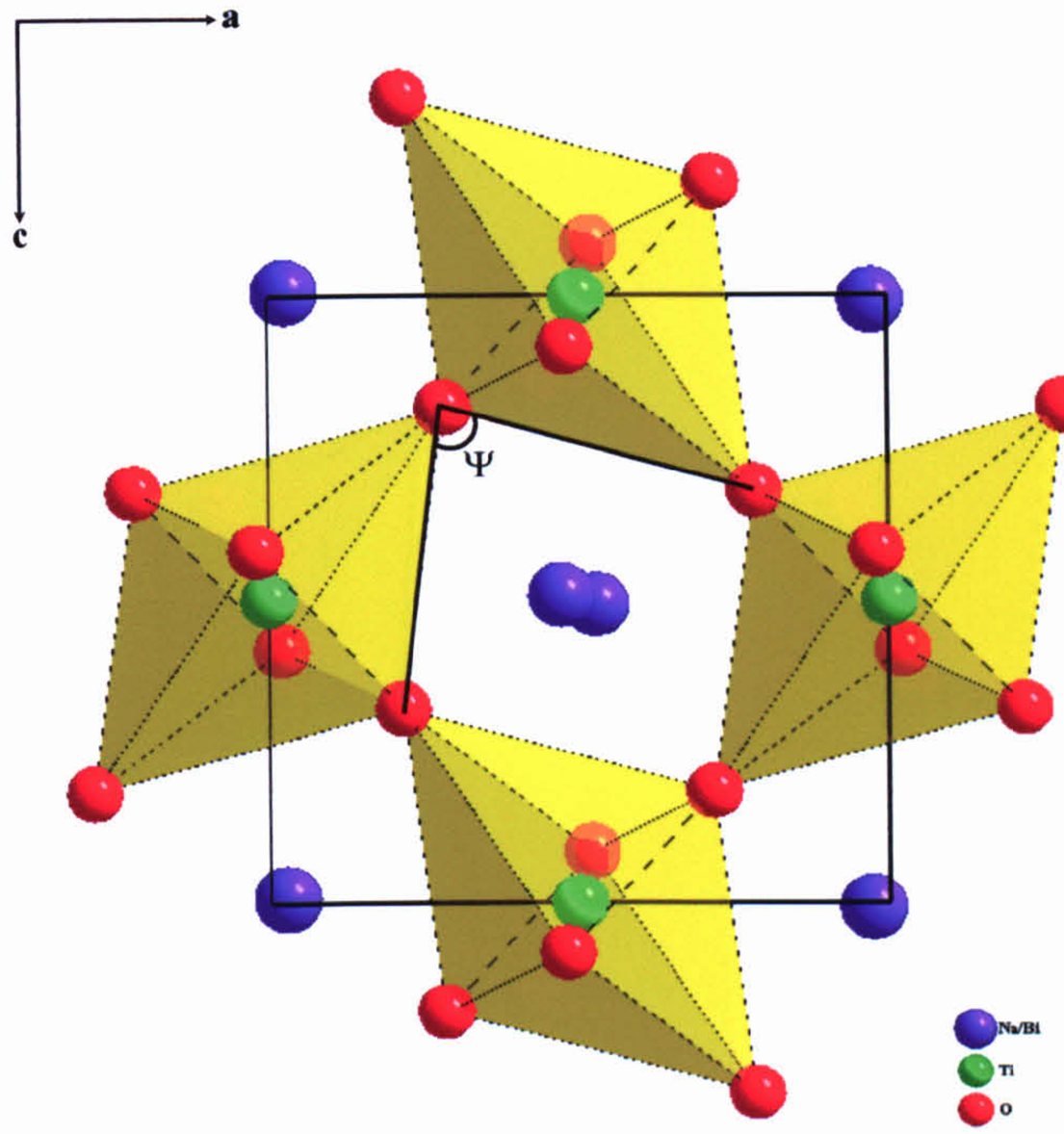

(a)

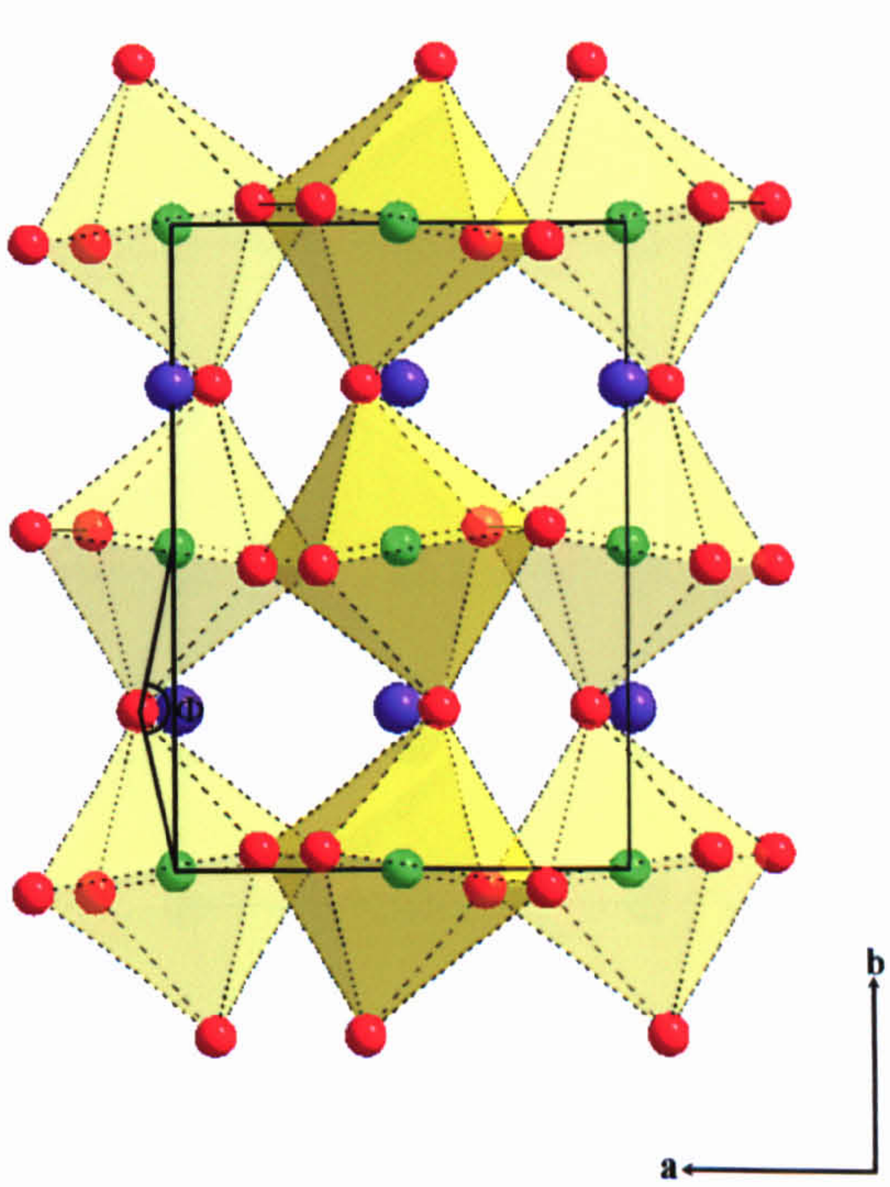

(b)

Figure 4.16. *The structure of $Na_{0.5}Bi_{0.5}TiO_3$ at 33.6 kbar, (Pnma, $a^-b^+a^-$) looking down (a) [010] and (b) [001]. Ψ and Φ represent the octahedral tilt angles clockwise about [010] and anti-clockwise about [100]/[001] respectively.*

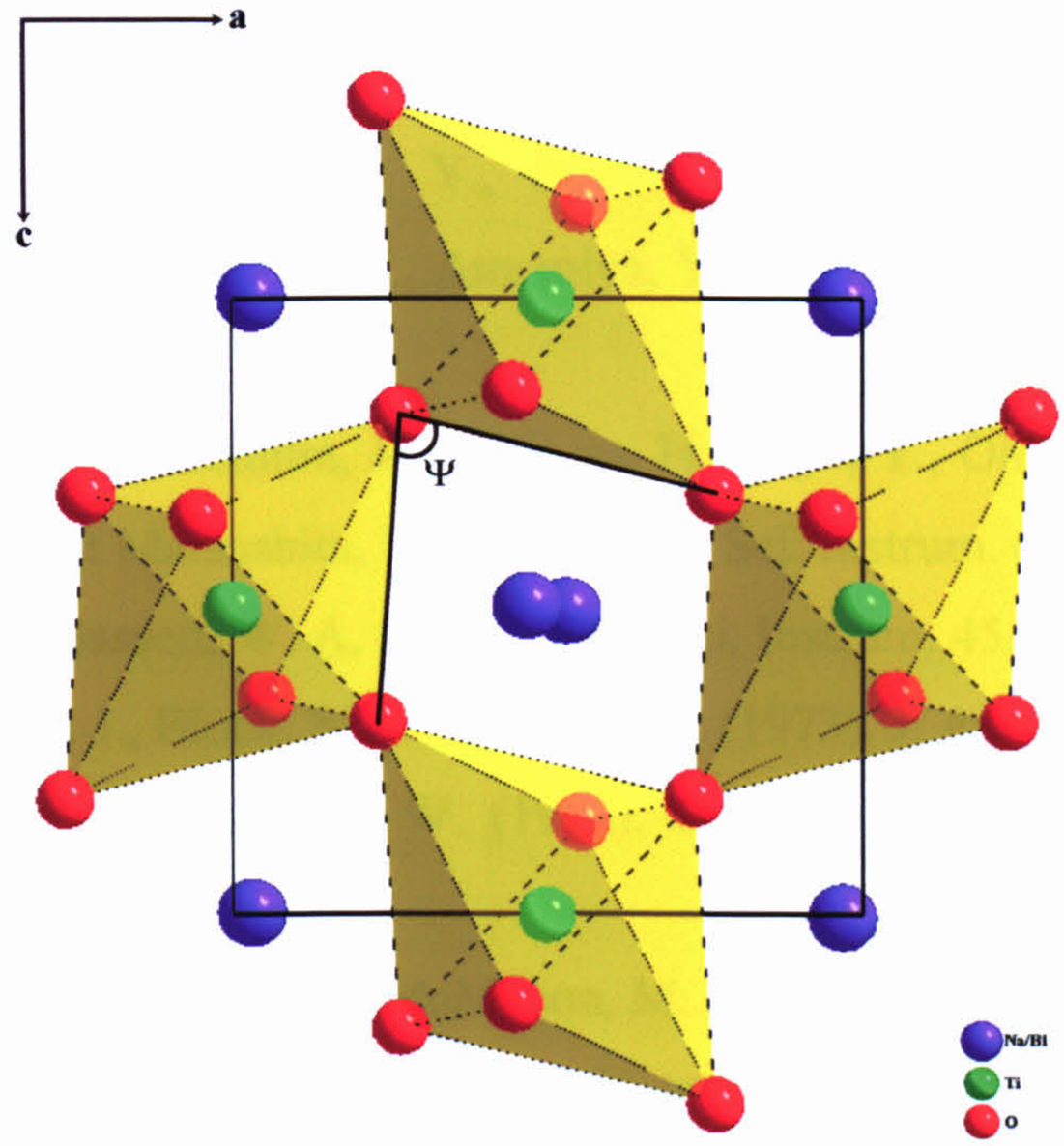

(a)

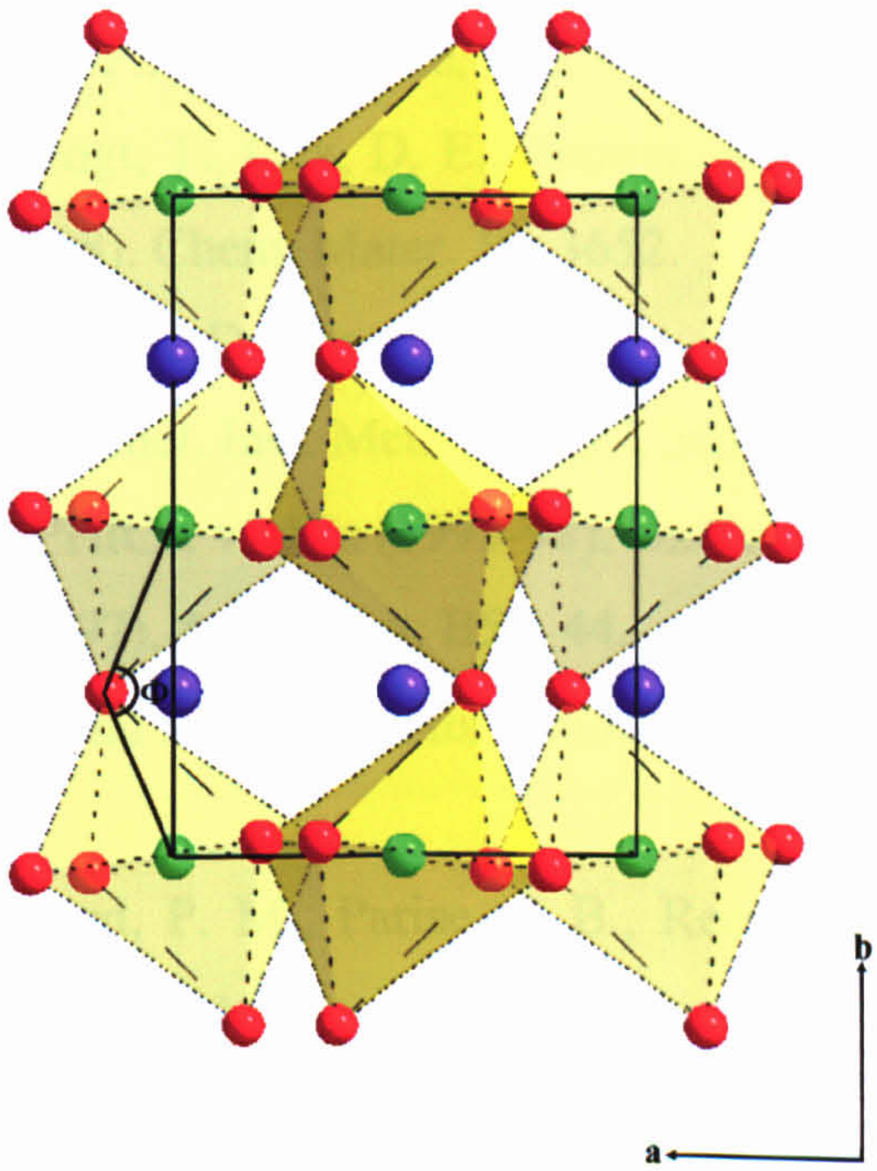

(b)

Figure 4.17. *The structure of $Na_{0.5}Bi_{0.5}TiO_3$ at 97.5 kbar, (Pnma, $a^-b^+a^-$) looking down (a) [010] and (b) [001]. Ψ and Φ represent the octahedral tilt angles clockwise about [010] and anti-clockwise about [100]/[001] respectively.*

References

[1] Fujii, Y., Hose, K.,Ohishi, Y., Fujihisa, H., Hamaya, N., Takemura, K., Shimomura, O., Kikegawa, T., Amemiya, Y. & Matsushita, T. (1989). Phys. Rev. Lett. 63, 536.

[2] Shimomura, O., Takemura, K., Fujihisa, H., Fujii, Y., Ohishi, Y., Kikegawa, T., Amemiya, Y. & Matsushita, T. (1992). Rev. Sci. Instrum. 63, 967.

[3] Merrill, L. & Bassett, W. A. (1974). Rev. Sci. Instrum. 45, 290.

[4] Piermariini, G. J., Block, S. & Barnett, J. D. (1973). J. Appl. Phys. 44, 5377.

[5] Hazen, R. M & Finger, L. W. (1982). Comparative Crystal Chemistry (New York: Wiley), p37.

[6] Nelmes, J. R., Hatton, P. D., McMahon, M. I., Piltz, R. O., Crain, J., Cernik., R. J. & Bushnell-Wye, G. (1992). Rev. Sci. Instrum. 63 (1), 1039.

[7] Piltz, R. O., McMahon, M. I., Crain, J., Hatton, P. D. & Nelmes, R. J. (1992). Rev. Sci. Instrum. 63 (1), 700.

[8] Nelmes, J. R. & McMahon, M. I. (1994). J. Synch. Rad. 1, 69.

[9] Kay, H. F. and Bailey, P. C. (1957). Acta Cryst. 10, 219.

[10] Park, J-H, Woodward, P., M. & Parise, J. B. (1998). Chem. Mater. 10, 3092.

[11] Woodward, P. M., Vogt, T., Cox, D. E., Arulraj, A., Rao, C. N. R., Karen, P. & Cheetham, A. K. (1998). Chem. Mater. 10, 3652.

[12] Inorganic Crystal Structure Database. (1990).

[13] Hewat, A. W. (1975). Nucl. Inst. Methods. 127, 36170.

[14] CRYSTALLOGRAPHICA v1.50a (1995-98). Oxford Cryosystems, Oxon.

[15] Woodward, P. M. (1997). Acta Cryst. B53, 44.

[16] Diamond, Visual Crystal Structure Information System, v2.0e. (1996-98). Crystal Impact GbR.

[17] Park, J. H., Woodward, P. M., Parise, J. B., Reeder, R. J., Lubomirsky, I. & Stafsudd, O. (1999). Chem. Mater. 11, 177.

Chapter 5

$(Na_{1-x}K_x)_{0.5}Bi_{0.5}TiO_3$ – Structural Study as a Function of Substitution (x) and Temperature.

5.1 Introduction

This chapter examines the structural variations across the $(Na_{1-x}K_x)_{0.5}Bi_{0.5}TiO_3$ series ($x = 0, 0.2, 0.4, 0.5, 0.6, 0.8, 1.0$) solid solution series as a function of temperature. From an applications point of view, the diverse range of structural variations and physical properties seen in solid solutions especially at compositions close to a structural phase transition may be ultimately of some industrial use. One of the best known examples is the technologically important $Pb(Zr_xTi_{1-x})O_3$ (PZT) near the morphotropic phase boundary[1] between R3c → R3m ($x \approx 0.48$). As the amount of potassium doping is increased across the series, fundamental changes in the structure are observed. The proportions of potassium cations that are incorporated into the NBT structure have effects on the unit cell dimensions, the perovskite tilting mechanisms and the phase transition temperatures. From x-ray and neutron powder diffraction data collected between $293 \leq T \leq 993$ K structures have been determined and characterised. The study follows the temperature and doping level dependence of the octahedral deformation and cation shifts through the sequence of phase transitions.

The room temperature structural variation across the series ranging from the rhombohedral (tilted) R3c structure at the $x = 0$ end to the intermediate (zero-tilt) rhombohedral R3m structure and finishing with the tetragonal P4mm structure at $x = 1$ end is reported for the first time. The temperature induced phase transitions for the series (revealing the unusual tetragonal structure with space group P4bm for $x = 0.2$) are reported and structural modifications are discussed. Experimental techniques, data collections and refinement procedures are also described.

5.2 Neutron Powder Diffraction

Accurate structural determinations of these materials by single crystal x-ray diffraction have been inhibited by the difficulty in preparing/selecting good quality single-domain crystals (and in the case of KBT, any crystals at all). As previously

remarked in section 3.3 neutron powder diffraction is a powerful tool for investigations of tilted perovskites especially in relation to octahedral deformations. The technique prevents erroneous data arising from unobserved twins while allowing precision to be achieved in the determination of the oxygen fractional co-ordinates. The high-resolution two-axis diffractometer D1A[2] housed at the Institut Laue-Langevin (ILL) was used in diffraction experiments. Details of the research facility and instrument can be found in sections 3.3.1 and 4.3.1, respectively.

5.2.1 Sample Preparation and Environment

The majority of crystals in all the solid solution range were surrounded with trace amounts of flux. As much flux, as possible was removed to keep any contamination down to a minimum. Fragments of flux grown crystals were chosen and finely ground into powder. All powders were sieved to obtain particles with approximate diameters < 38 μm and compacted into 60 × 5 mm, thin walled vanadium canisters. A schematic diagram of the canister can be seen in Figure 3.02. As in previous neutron diffraction experiments Polaroid photographs were taken to confirm the correct geometry had been attained.

5.2.2 Data collections and Treatment

Data sets were taken from the solid solution series for x = 0.2, 0.4, 0.5, 0.6. Canisters were mounted inside a high-temperature furnace under vacuum and data sets collected from room temperature to 993 K on heating. A furnace similar to the one used in the collection of data for NBT and outlined in section 3.3.3 was used. For all data sets, complete diffraction profiles were made up from sections by counting at each 2θ position until a predetermined number of monitor counts was achieved. The complete angular range between $0 < 2\theta < 160°$ was covered in 120 steps of 0.05°. This operation was repeated a number of times and the subsequent profiles averaged. A room temperature data collection for KBT (x = 1.0) was also taken on diffractometer D2B[3] using a high-temperature furnace. Details of the diffractometer and the instruments used have been previously described in section 3.3.1.

As only a finite period of time had been allocated to carry out the experiments in full, the number of averaged scans taken and individual count times per scan were varied according to the judged quality of profile data. All individual data runs were merged and

converted into a GSAS-compatible format. Table 5.01 lists the details of the data collections carried out.

$(Na_{1-x}K_x)_{0.5}Bi_{0.5}TiO_3$ *(x)*	Temperature (K)	Individual Scans	Total scan time (hours)
0.2	293 393, 493, 593, 693, 993	six, 60 min scans five, 48 min scans	6 4
0.4	293 393 493, 593, 693, 993	five, 52 min scans five, 75 min scans five, 93 min scans	4.3 6.3 7.8
0.5	293, 393, 493, 593, 693, 993	four, 60 min scans	4
0.6	293, 393, 493, 593, 693, 993	four, 60 min scans	4
1.0	293 on D2B	five, 75 min scans	6.3

Table 5.01. Neutron data collections on diffractometers D1A/D2B.

5.2.3 Rietveld Structural Refinements

The Rietveld method (section 3.2.1) was employed in order to refine the crystallographic structures as a function of increasing K^{1+} content across the solid solution series, and also for individual compounds as a function of temperature. All data sets were analysed with the Rietveld refinement software package GSAS.

5.2.3.1 $(Na_{0.8}K_{0.2})_{0.5}Bi_{0.5}TiO_3$ *(x = 0.2)*

Rhombohedral Phase – The refinement of these data sets were based on the rhombohedral unit cell, since broadening of the *h*, *k*, *l* reflections where $h = k = l$, was observed. In the room temperature powder pattern, reflections of the type *h* odd, *k* odd, *l* odd were observed. These superstructure reflections were also evident (but with reduced intensity) at 393 K and 493 K (Figure 5.01). As discussed in section 3.3.4, these peaks result from the oxygen octahedra tilting about the three-fold pseudo-cubic axes, and are consistent with the $a^-a^-a^-$ tilt system seen in rhombohedral perovskites. The tilt system is characterised by antiphase rotations of octahedra along each axis, which results in cell doubling of all three pseudo-cubic axes. Initial refinements for the room-temperature phase were based on the final refinements of the room-temperature neutron diffraction data for NBT, as outlined in section 3.3.4. The final room-temperature structural model

was then used as a starting model for the corresponding higher temperature structures. Structural refinements were carried out with reference to hexagonal axes. The structure was refined in the space group R3c. The background was based on a linear interpolation function with 8 coefficients and peak shapes described by pseudo-Voigt profiles. Anisotropic Lorentzian terms representing strain broadening used in the determination of the peak shape functions, were also refined but their effects were never significant. A 2θ angular range between 21.51-134.51° was used in the refinements, which included 95 reflections. The $O_{(Z)}$ position was fixed to 1/12 during refinements, refer to Table 3.04. Isotropic temperature factors were initially refined followed by anisotropic parameters, in the later stages of refinement. Na, K and Bi atoms with site occupation factors 0.4, 0.1 and 0.5 respectively were constrained to be at the same positional co-ordinates during refinements. As a check on stoichiometry, the occupancies of Na, K and Bi (given the constraint that total occupancy should be 1) were refined. This resulted in site occupation factors for Na, K and Bi of 0.37 (2), 0.12 (2) and 0.51 (1) respectively showing that the deviation from the ideal composition was small. The occupancies were subsequently fixed to their expected values, since refinement of these parameters did not improve the fit.

A first examination of the room temperature pattern suggested that the first superstructure peak (131) was split (Figure 5.01). Closer examination of the pattern revealed other low intensity peaks that could not be explained by any perovskite tilting model. These unexplained peaks persisted as the temperature was increased suggesting that an impurity phase, possibly originating from the crystal flux also was present. The high temperature (993 K) data also shows these extra peaks indicating that this phase is stable at high temperatures. Using the program CRYSTALLOGRAPHICA[4] powder pattern simulations (for neutron radiation, λ = 1.91 Å) were calculated for the initial products of the compound namely: Bi_2O_3[5] (collection code 38436), K_2CO_3[6] (collection code 10191), Na_2CO_3[7] (collection code 80985) and TiO_2[8] (collection code 9852) using data taken from the ICSD[9]. From these simulations it was evident that the profile data for $(Na_{0.8}K_{0.2})_{0.5}Bi_{0.5}TiO_3$ (x = 0.2) and $(Na_{0.4}K_{0.2})_{0.5}Bi_{0.5}TiO_3$ (x = 0.6) contained small amounts of a TiO_2 anatase phase. The TiO_2 structure taken from the ICSD, was incorporated into the refinements with lattice parameters, isotropic temperature factors and fractional phase contributions being refined. The fractional volume of the TiO_2 phase refined to values of 4 and 8 % for $(Na_{0.8}K_{0.2})_{0.5}Bi_{0.5}TiO_3$ and $(Na_{0.4}K_{0.6})_{0.5}Bi_{0.5}TiO_3$

respectively. These fractional percentages were subsequently fixed and employed in higher temperature refinements. An attempt to refine the data in the non-polar space group $R\bar{3}c$ was also made, however this was unstable, as none of the free structural parameters could be refined.

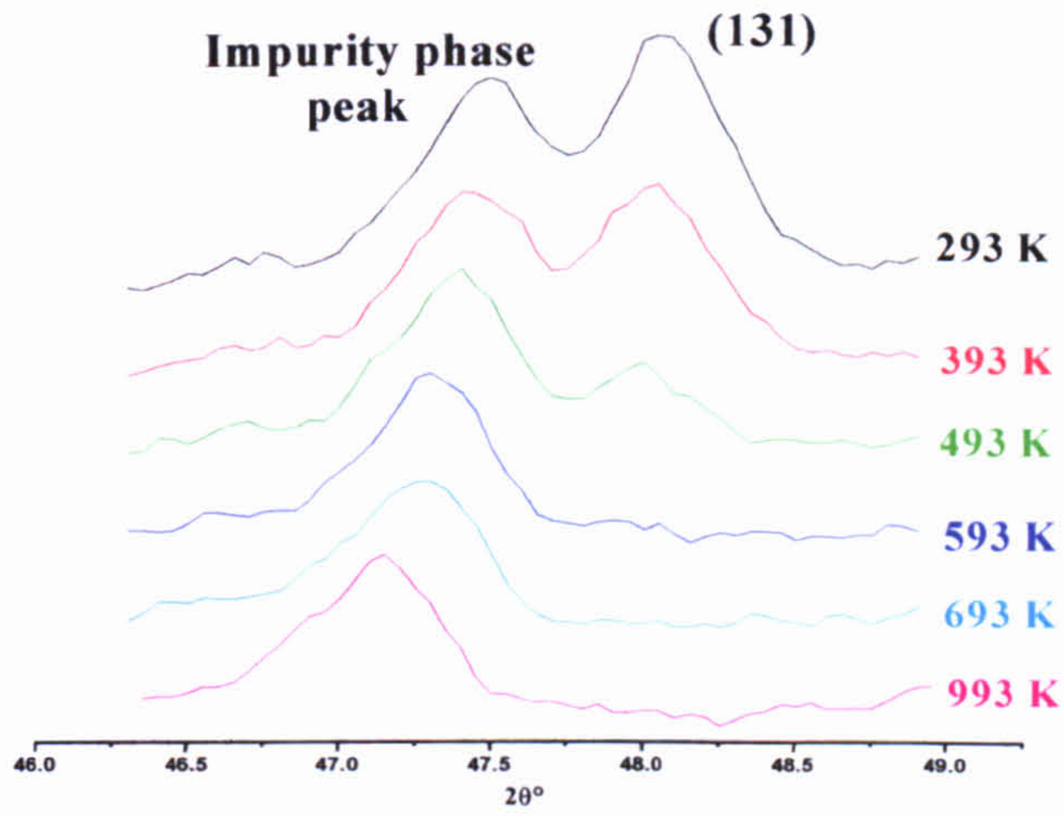

Figure 5.01. *$(Na_{0.8}K_{0.2})_{0.5}Bi_{0.5}TiO_3$- at various temperatures showing the (311) superstructure peak and peak from TiO_2 contamination.*

Tetragonal Phase – Data set refinements were based on the tetragonal unit cell, since splitting/broadening of certain reflections were observed, refer to Table 3.03. As previously seen in NBT, compared with the pseudo-cubic powder pattern referred to the $2a \times 2b \times 2c$ ($8 \times 8 \times 8$ Å^3) unit cell, superstructure reflections of the type *h* odd, *k* odd, *l* even were observed at temperatures 493, 593 and 693 K. These reflections are consistent with the $a^0a^0c^+$ tilt system and the tetragonal unit cell $\sqrt{2}a \times \sqrt{2}b \times c$. In this system the tilting causes cell doubling in the [100] and [010] directions only. Initial refinements for this phase were based on the P4bm tetragonal phase (698 K) of NBT. A 2θ angular range between 21.51-134.51° was used in the refinements. There were 86 reflections within this range. The background was based on a linear interpolation function with 8 coefficients and peak shape parameters based on earlier refinements. During structural refinements the $Ti_{(Z)}$ position was fixed at zero. Isotropic temperature factors were initially refined followed by anisotropic parameters, in the later stages of refinement. Na, K and Bi atoms with site occupation factors 0.4, 0.1 and 0.5 respectively were constrained to be at the same positional coordinates during refinements. Coexistence of rhombohedral (77 %) and tetragonal phases (19 %) (and TiO_2 (4 %)) at 493 K, as indicated by the presence of both types of superstructure reflections (*h* odd, *k* odd, *l* odd and *h* odd, *k* odd, *l* even), were based on the nearest subsequent refinement model and

refined together. A 2θ angular range between 21.51-134.51° was used in the refinements, which included 150 reflections.

Cubic Phase – The high temperature, paraelectric form of $(Na_{0.8}K_{0.2})_{0.5}Bi_{0.5}TiO_3$, space group $Pm\bar{3}m$ possessing no tilts or cation displacements was seen at 993 K. Initial refinements were based on the previous tetragonal phase profile parameters. The same angular range was used as before and included 56 reflections.

All refinements were stable and converged readily. The crystallographic data for the three phases between 293-993 K are presented in Table 5.02 (a) and (b). The observed, calculated and difference profiles from the final Rietveld refinements for all phases are shown in Figure 5.02. Figures 5.03 (a) and (b) show the rhombohedral (293 K) and tetragonal (593 K) structures, from final refinements.

Rhombohedral (R3c) Phase (293 K)

Atom	x	y	z	U11	U22	U33	U12	U13	U23
Na	0.0	0.0	0.2594(5)	0.020(8)	0.020(8)	0.004(1)	0.010(6)	0.0	0.0
K	0.0	0.0	0.2594(5)	0.037(4)	0.037(4)	0.036(7)	0.018(2)	0.0	0.0
Bi	0.0	0.0	0.2594(5)	0.054(4)	0.054(4)	0.048(7)	0.027(2)	0.0	0.0
Ti	0.0	0.0	0.0024(8)	0.033(3)	0.033(3)	-0.020(3)	0.017(1)	0.0	0.0
O	0.1295(6)	0.326(1)	0.0833	0.024(1)	0.024(1)	0.056(2)	-0.013(1)	0.001(3)	-0.001(3)

Tetragonal (P4bm) Phase (593 K)

Atom	x	y	z	U11	U22	U33	U12	U13	U23
Na	0.0	½	0.549(2)	0.032(5)	0.032(5)	0.042(1)	-0.005(2)	0.0	0.0
K	0.0	½	0.549(2)	0.034(4)	0.034(4)	0.039(2)	0.001(1)	0.0	0.0
Bi	0.0	½	0.549(2)	0.050(9)	0.050(9)	0.09(2)	0.016(7)	0.0	0.0
Ti	0.0	0.0	0.0	0.039(5)	0.035(5)	-0.013(6)	0.0	0.0	0.0
O(I)	0.0	0.0	0.526(3)	0.048(3)	0.048(3)	0.008(3)	0.0	0.0	0.0
O(II)	0.2642(5)	0.2357(5)	0.0181(1)	0.037(3)	0.037(3)	0.040(1)	-0.015(2)	-0.002(1)	0.002(1)

Cubic ($Pm\bar{3}m$) Phase (993 K)

Atom	x	y	z	U11	U22	U33	U12	U13	U23
Na	0.0	0.0	0.0	0.079(4)	0.079(4)	0.079(4)	0.0	0.0	0.0
K	0.0	0.0	0.0	0.037(4)	0.037(4)	0.037(4)	0.0	0.0	0.0
Bi	0.0	0.0	0.0	0.083(2)	0.083(2)	0.083(2)	0.0	0.0	0.0
Ti	½	½	½	0.020(1)	0.020(1)	0.020(1)	0.0	0.0	0.0
O	½	½	0.0	0.055(1)	0.055(1)	0.055(1)	0.0	0.0	0.0

Table 5.02 (a). Fractional co-ordinates and equivalent anisotropic displacement parameters ($Å^2$) for $(Na_{0.8}K_{0.2})_{0.5}Bi_{0.5}TiO_3$.

Chemical formula	**$(Na_{0.8}K_{0.2})_{0.5}Bi_{0.5}TiO_3$ (x = 0.2)**
Chemical formula weight	213.49
Specimen Shape	Random powder
Specimen preparation	Crystal growth from flux, Powder prepared from ground crystals
Specimen Pressure	Ambient
Colour	Pale Yellow
Radiation Type	Neutron
Wavelength	1.91 Å

Crystal System	**Rhombohedral**	**Tetragonal**	**Cubic**
Temperature (K)	293	593	993
Space Group	R3c	P4bm	$Pm\bar{3}m$
a_H (Å)	5.4960 (9)	-	-
c_H (Å)	13.5063 (6)	-	-
a_p (Å)	-	5.5154 (4)	3.91905 (3)
c_p (Å)	-	3.8999 (4)	-
α,β,γ (°)	90, 90, 120	90, 90, 90	90, 90, 90
Volume (Å^3)	353.33 (1)	118.66 (4)	60.193 (1)
Z	6	2	1
D_x (Mg.m^{-3})	6.020	5.975	5.89
s	0.0094 (7)	0.023 (1)	0.0
t	0.0024 (1)	-0.018 (1)	0.0
d	-0.0002 (3)	-	-
e	0.0168 (6)	-	-
Tilt System	$a^-a^-a^-$ (three tilt system, anti-phase)	$a^0a^0c^+$ (one tilt system, in-phase)	$a^0a^0a^0$ (zero-tilt system)
Displacements	Parallel along $[111]_p$	Anti-parallel along [001]	None
ω (°)	6.6 (2)	1.1 (4)	0.0
$\zeta \times 10^2$	-0.387 (5)	-	-
Nº of refined parameters	47	48	39
Profile R-factors			
R_p	0.089	0.091	0.074
wR_p	0.123	0.125	0.117
χ^2	0.445	0.436	0.387

Table 5.02 (b). Summary of experimental details, data collection and refinement for the three phases of $(Na_{0.8}K_{0.2})_{0.5}Bi_{0.5}TiO_3$.

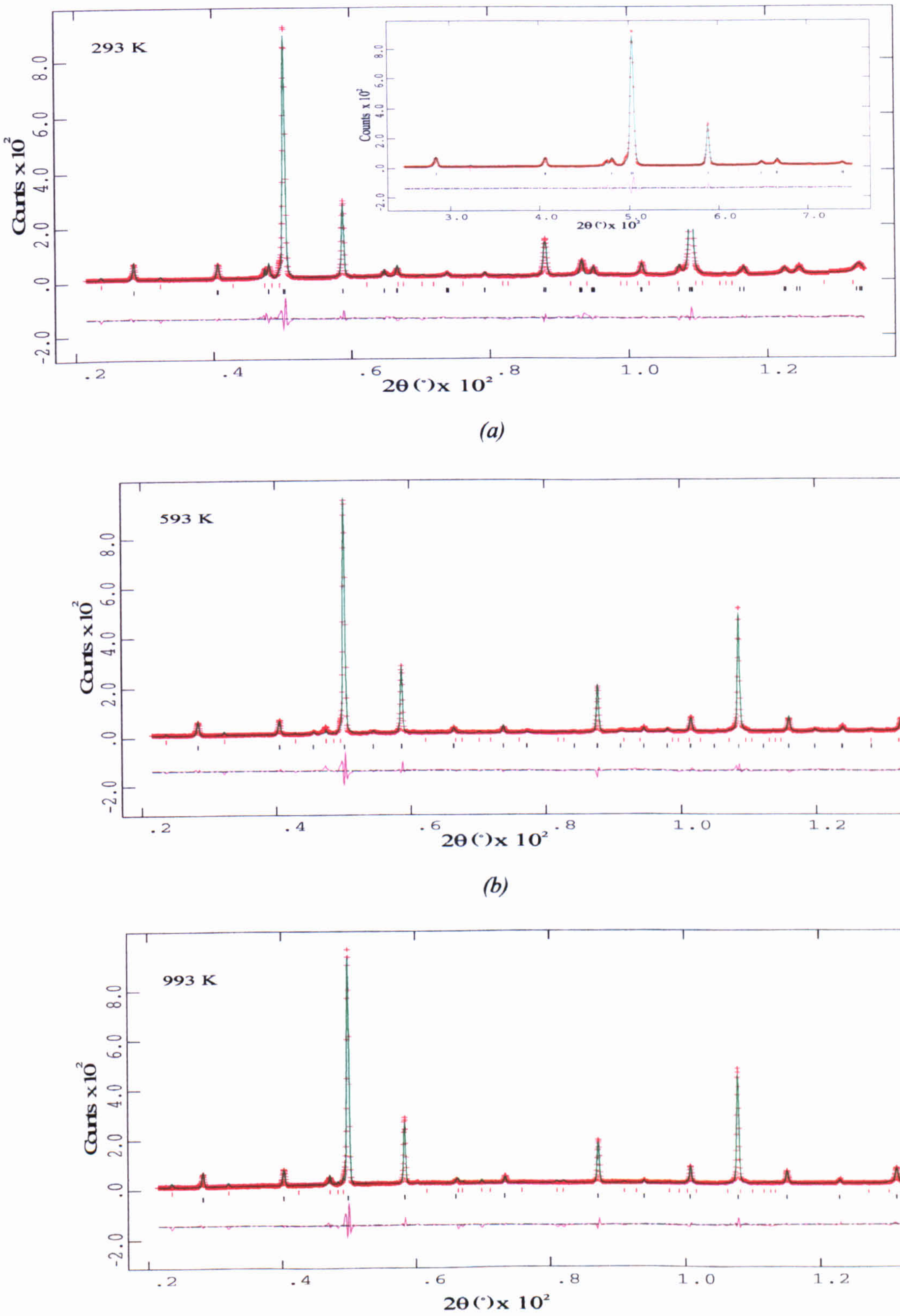

(a)

(b)

(c)

Figure 5.02. *The observed, calculated and difference curves from the final Rietveld refinements of $(Na_{0.8}K_{0.2})_{0.5}Bi_{0.5}TiO_3$ ($x = 0.2$). (a) refinement in R3c, at 293 K, the black and red marks indicate the position of the $(Na_{0.8}K_{0.2})_{0.5}Bi_{0.5}TiO_3$ and TiO_2 reflections respectively. The low angle data ($25 < 2\theta < 75°$) are magnified in the insert. (b) refinement in P4bm, at 593 K. (c) refinement in $Pm\bar{3}m$, at 993 K.*

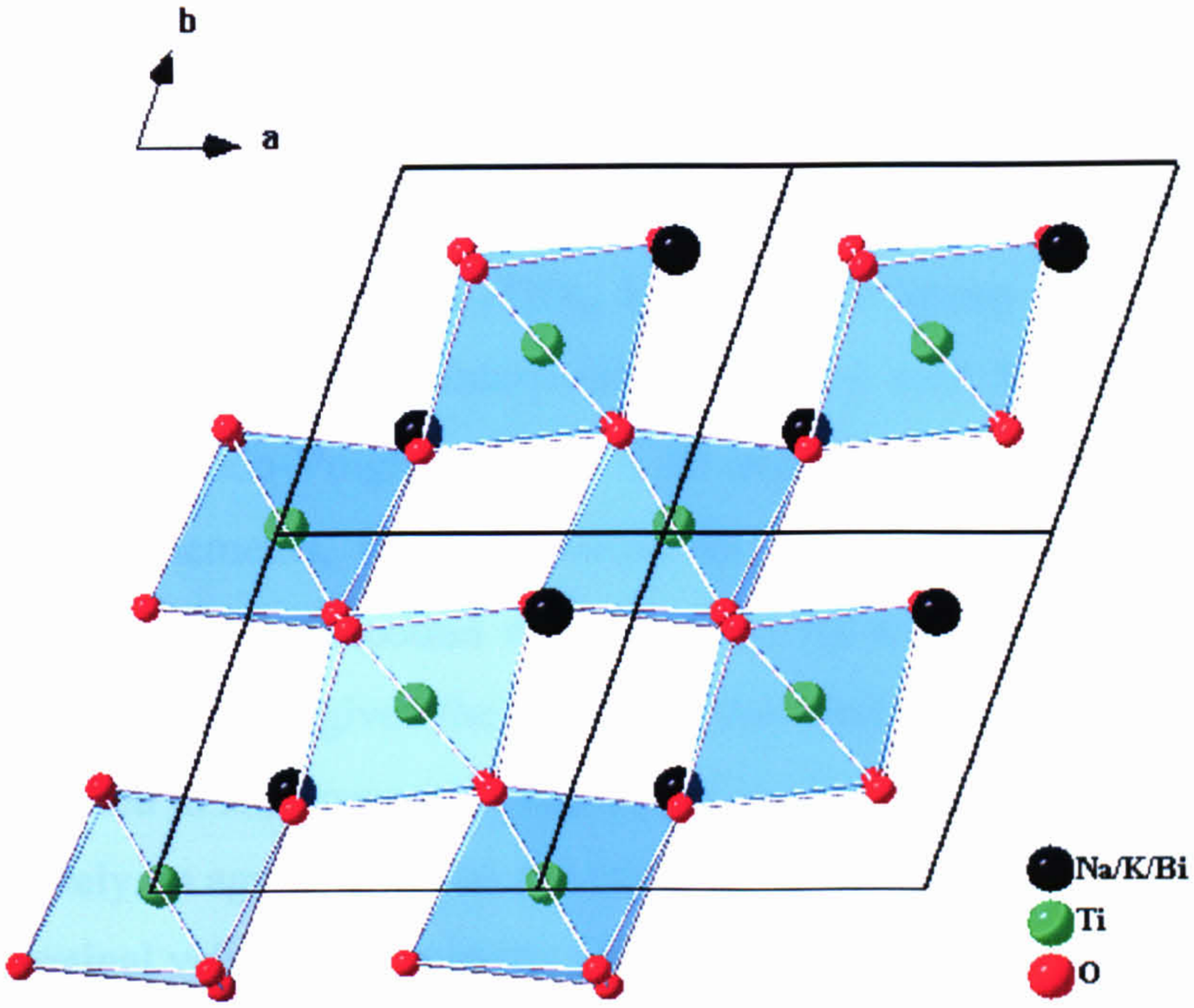

(a)

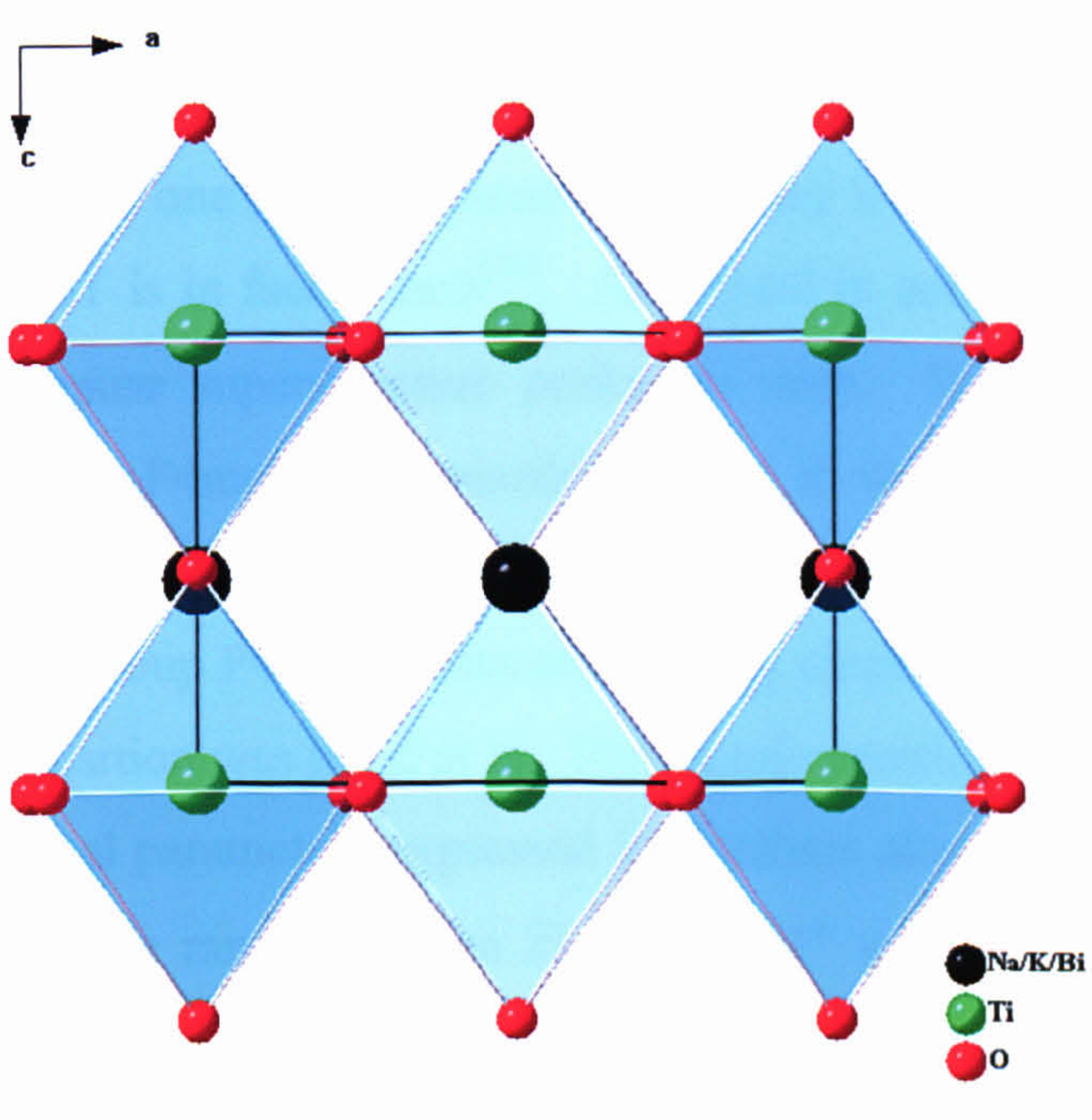

(b)

Figure 5.03. *The structure of $(Na_{0.8}K_{0.2})_{0.5}Bi_{0.5}TiO_3$ (a) rhombohedral structure at 293 K, looking down [001], (b) tetragonal structures at 593 K, looking down [010].*

5.2.3.2 $(Na_{0.6}K_{0.4})_{0.5}Bi_{0.5}TiO_3$ ($x = 0.4$)

Rhombohedral Phase – As for the $x = 0.2$ compound, reflections of the type h odd, k odd, l odd were observed. Initial refinements were based on the room temperature final refinement of $(Na_{0.8}K_{0.2})_{0.5}Bi_{0.5}TiO_3$, in the space group R3c. As before the background was based on a linear interpolation function with 8 coefficients and peak shapes described by pseudo-Voigt profiles. A 2θ angular range between 21.51-134.51° was used in the refinements, which included 65 reflections. The same refinement strategy as for the $x = 0.2$ compound was adopted. As a check on stoichiometry, the occupancies of Na, K and Bi (given the constraint that total occupancy should be 1) were refined. This resulted in site occupation factors for Na, K and Bi of 0.28 (2), 0.21 (2) and 0.51 (1) respectively, in agreement with the expected composition; these parameters were fixed to their nominal values. No impurity phase was present in this sample.

Tetragonal Phase – No superstructure peaks associated with oxygen octahedral tilting were observed in this phase. Tetragonal distortions as shown by the splitting/broadening of certain reflections were clearly evident. Table 3.03 lists some of the reflections that were used to determine the presence of rhombohedral and tetragonal symmetries. From an x-ray powder diffraction experiment (which is less sensitive to the superstructure peaks than one using neutron diffraction) it has been reported that the tetragonal phase of NBT is in fact P4mm[10]. As argued in section 3.3.4 this cannot be the case for NBT because superstructure peaks are seen. However for the $x = 0.2$ compound, space group P4mm is a possibility and it was therefore tried. Initial refinements were based on the reported structure of $PbTiO_3$[11]. The non-centrosymmetric space group P4mm allows an arbitrary choice of origin, so in structural refinements the $Ti_{(Z)}$ position was fixed at ½. The atomic positions can then be described in terms of the positional parameters expressed in fractions along the c-axis as shown in Table 5.03. A 2θ angular range between 21.51-134.51° was used in the refinements, which included 30 reflections. Coexisting rhombohedral (74 %) and tetragonal phases (26 %) at 493 K, were refined using the nearest related structural model. A 2θ angular range between 21.51-134.51° was refinements, which included 95 reflections. It should be noted that an attempt to refine the data in the non-polar space group P4/mmm was unstable, as none of the free structural parameters could be refined.

Atomic Species	Position/ Symmetry	x	y	z
Na/K/Bi	1(a) 4mm	0	0	$0 + \delta z_A$
Ti	1(b) 4mm	½	½	½
O(5)	1(b) 4mm	½	½	$\delta z_{O(5)}$
O(6)	2(c) 2mm	½	0	$½ + \delta z_{O(6)}$

Table 5.03. Fractional coordinates of atoms corresponding to the tetragonal space group P4mm. δz_A and δz_O represent displacements along [001].

Cubic Phase – The high temperature cubic form, space group $Pm\bar{3}m$ was seen at 993 K. Initial parameters were taken from the tetragonal final refinement. A 2θ angular range between 21.51-134.51° was used in the refinements, which included 26 reflections.

All refinements were stable and converged readily. The crystallographic data for the three phases between 293-993 K are presented in Table 5.04 (a) and (b). The observed, calculated and difference profiles from the final Rietveld refinements for all phases are shown in Figure 5.04.

Rhombohedral (R3c) Phase (293 K).

Atom	x	y	z	U11	U22	U33	U12	U13	U23
Na	0.0	0.0	0.2553(9)	0.038(1)	0.038(1)	-0.019(1)	0.019(6)	0.0	0.0
K	0.0	0.0	0.2553(9)	0.027(2)	0.027(2)	-0.004(2)	0.013(8)	0.0	0.0
Bi	0.0	0.0	0.2553(9)	0.081(6)	0.081(6)	0.048(7)	0.040(3)	0.0	0.0
Ti	0.0	0.0	0.0011(4)	0.041(3)	0.041(3)	-0.038(3)	0.021(1)	0.0	0.0
O	0.1431(2)	0.3385(4)	0.0833	0.017(4)	0.022(6)	0.027(4)	0.026(6)	-0.011(2)	-0.012(1)

Tetragonal (P4mm) Phase (593 K).

Atom	x	y	z	U11	U22	U33	U12	U13	U23
Na	0.0	0.0	-0.006(1)	0.079(2)	0.076(2)	0.048(4)	0.0	0.0	0.0
K	0.0	0.0	-0.006(1)	0.054(3)	0.054(3)	0.044(6)	0.0	0.0	0.0
Bi	0.0	0.0	-0.006(1)	0.081(7)	0.081(7)	0.068(9)	0.0	0.0	0.0
Ti	½	½	½	0.020(4)	0.020(4)	0.029(9)	0.0	0.0	0.0
O(I)	½	½	0.016(5)	0.068(5)	0.068(5)	-0.004(4)	0.0	0.0	0.0
O(II)	½	0.0	0.512(9)	0.019(3)	0.020(5)	0.068(4)	0.0	0.0	0.0

Cubic ($Pm\bar{3}m$) Phase (993 K).

Atom	x	y	z	U11	U22	U33	U12	U13	U23
Na	0.0	0.0	0.0	0.060(6)	0.060(6)	0.060(6)	0.0	0.0	0.0
K	0.0	0.0	0.0	0.052(9)	0.052(9)	0.052(9)	0.0	0.0	0.0
Bi	0.0	0.0	0.0	0.089(2)	0.089(2)	0.089(2)	0.0	0.0	0.0
Ti	½	½	½	0.021(1)	0.021(1)	0.021(1)	0.0	0.0	0.0
O	½	½	0.0	0.054(1)	0.054(1)	0.054(1)	0.0	0.0	0.0

Table 5.04 (a). Fractional co-ordinates and equivalent anisotropic displacement parameters ($Å^2$) for $(Na_{0.6}K_{0.4})_{0.5}Bi_{0.5}TiO_3$.

Chemical formula	**$(Na_{0.6}K_{0.4})_{0.5}Bi_{0.5}TiO_3$ (x = 0.4)**		
Chemical formula weight	215.10		
Specimen Shape	Random powder		
Specimen preparation	Crystal growth from flux, Powder prepared from ground crystals		
Specimen Pressure	Ambient		
Colour	Pale Yellow		
Radiation Type	Neutron		
Wavelength	1.91 Å		
Crystal System	**Rhombohedral**	**Tetragonal**	**Cubic**
Temperature (K)	293	593	993
Space Group	R3c	P4mm	$Pm\bar{3}m$
a_H (Å)	5.5047 (2)	-	-
c_H (Å)	13.5341 (7)	-	-
a_p (Å)	-	3.9032 (1)	3.92154 (4)
c_p (Å)	-	3.9112 (2)	-
α,β,γ (°)	90, 90, 120	90, 90, 90	90, 90, 90
Volume ($Å^3$)	355.17 (2)	59.588 (3)	60.307 (2)
Z	6	1	1
D_x ($Mg.m^{-3}$)	6.034	5.995	5.92
s	0.0053 (5)	0.034 (9)	0.0
t	0.0011 (4)	0.012 (9)	0.0
d	-0.0012 (1)	-	-
e	0.0129 (2)	-	-
Tilt System	$a^-a^-a^-$ (three tilt system, anti-phase)	$a^0a^0a^0$ (zero-tilt system)	$a^0a^0a^0$ (zero-tilt system)
Displacements	Parallel along $[111]_p$	Parallel along [001]	None
ω (°)	5.11 (8)	0.0	0.0
$\zeta \times 10^2$	-0.025 (1)	-	-
Nº of refined parameters	47	48	39
Profile R-factors			
R_p	0.098	0.090	0.076
$_wR_p$	0.123	0.124	0.104
χ^2	0.109	0.181	0.125

Table 5.04 (b). Summary of experimental details, data collection and refinement for the three phases of $(Na_{0.6}K_{0.4})_{0.5}Bi_{0.5}TiO_3$.

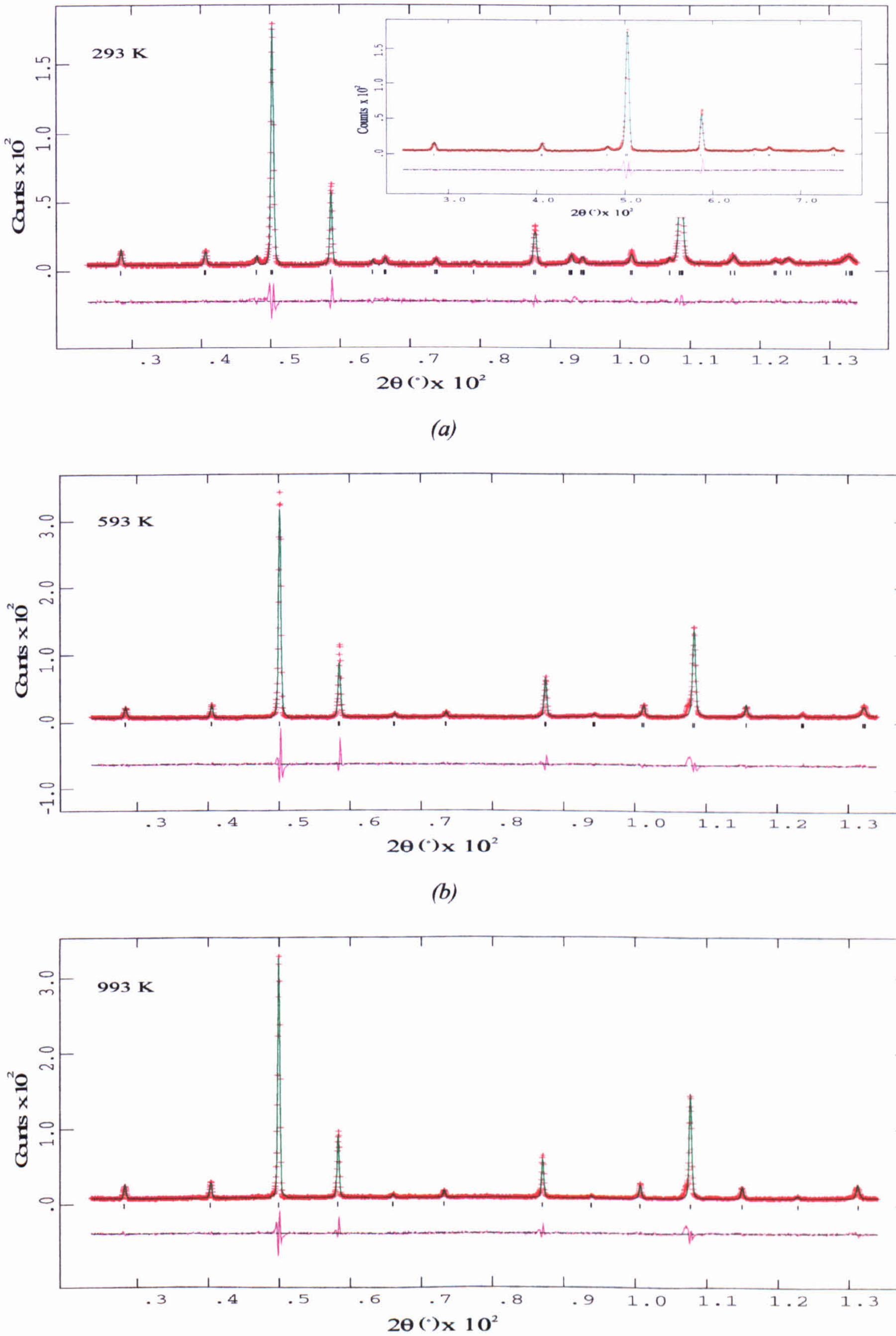

(a)

(b)

(c)

Figure 5.04. *The observed, calculated and difference curves from the final Rietveld refinements of $(Na_{0.6}K_{0.4})_{0.5}Bi_{0.5}TiO_3$ (x = 0.4). (a) refinement in R3c, at 293 K, the black marks indicate the position of the reflections. The low angle data ($25 < 2\theta < 75^{\circ}$) are magnified in the insert. (b) refinement in P4mm, at 593 K. (c) refinement in $Pm\bar{3}m$, at 993 K.*

5.2.3.3 $(Na_{0.5}K_{0.5})_{0.5}Bi_{0.5}TiO_3$ ($x = 0.5$)

Rhombohedral Phase – The room temperature powder pattern for this compound revealed no superstructure peaks associated with oxygen octahedral tilting. The diffraction pattern did however show rhombohedral broadening/splitting of the *h*, *k*, *l* reflections where $h = k = l$. The known rhombohedral perovskites are restricted to structures with space groups R3m, $R\bar{3}m$, $R\bar{3}c$ and R3c. Of these, R3m is a non-centrosymmetric space group that allows cation displacements along $[111]_p$ but does not support any tilt systems. The lack of tilts ($a^0a^0a^0$) leads to the primitive unit cell ($a_p \times a_p \times a_p$) and the structural description is normally performed with lattice parameters $a_H \approx 5.5$ and $c_H \approx 7.2$ Å. However in order to compare the rhombohedral phases (R3c and R3m) and have a common geometrical representation across the solid solution range, it is easiest to keep the structural model in the doubled hexagonal cell. The structural description developed by Megaw and Darlington[12] and presented in Table 3.06 was used. As there is no octahedral tilting in R3m, the parameter *e* is set to zero. Table 5.05 lists the set of atomic fractional co-ordinates for this space group.

Atomic Species	x	y	z
Na/K/Bi	0	0	$s + 0.25$
Ti	0	0	t
O	$1/6 - 2d$	$1/3 - 4d$	1/12

Table 5.05. Fractional co-ordinates for hexagonal setting of R3m, in terms of independent refinable parameters.

The symmetry operators of space group R3c were used, but a restriction was inserted for the oxygen positions by constraining $\Delta y_O = 2\Delta x_O$. This restriction artificially introduces into the unit cell, mirror planes (not given by the space group) containing the threefold axis and each oxygen atom [Figure 5.05 (a) and (b)]. The condition thereby allows the parameter *d* to refine whilst restricting *e* to zero.

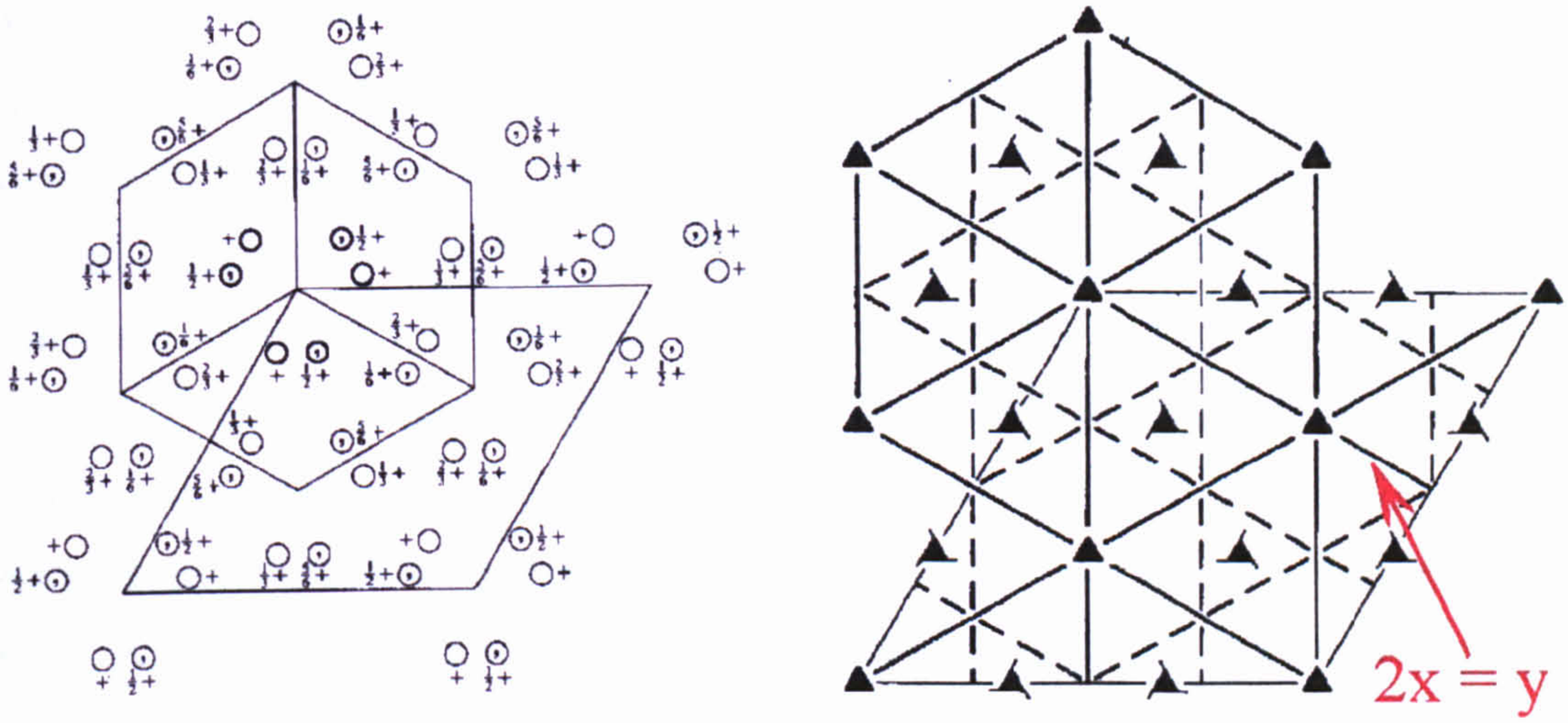

(a)

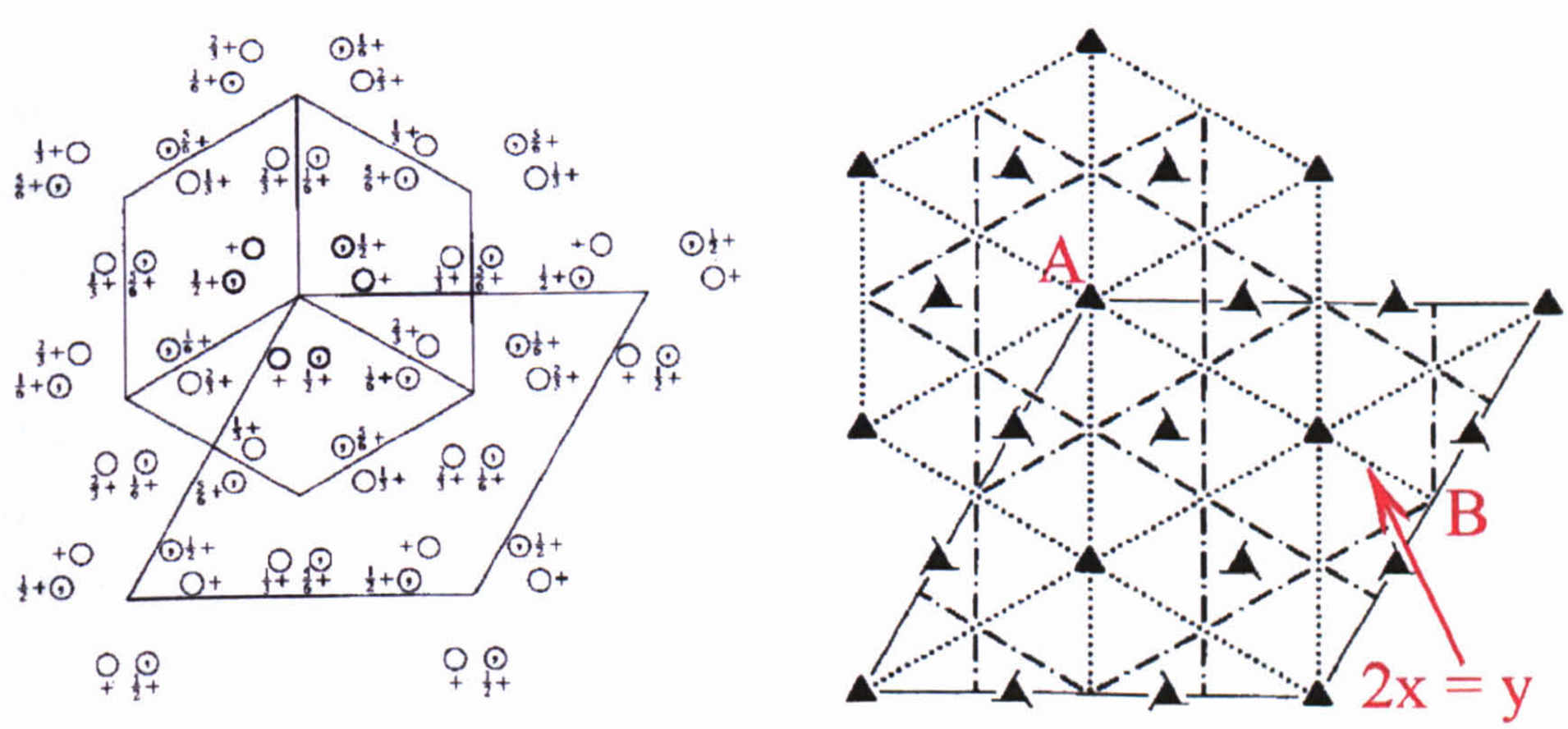

(b)

Figure 5.05. *(a) Space group R3m, (origin on 3m); (b) Space group R3c (origin on 3c), projected down [111]. When oxygen atoms are placed on the glide plane AB, it turns transforms into a mirror plane.*

Refinements for the room temperature phase were based on the final refinements of the room temperature data for $(Na_{0.6}K_{0.4})_{0.5}Bi_{0.5}TiO_3$ in the doubled unit cell with space group R3c. Preliminary refinements in the space group R3c (without restrictions) were made to converge with some difficulty and as expected, the magnitude of the tilts refined to zero, to within error. With the constraint imposed however, the refinement continued without further problems. The same refinement strategy was adopted as before for a 2θ angular range between 22.51-136.51°, which included 65 reflections. The refined shared site occupation factors for Na, K and Bi (0.23 (5), 0.25 (5) and 0.52 (4) respectively) were in agreement with the expected values and these were subsequently fixed. No impurity phase was present in this sample. It should be noted that an attempt to refine the data in the non-polar space group $R\bar{3}m$ was unstable, resulting in negative temperature factors and a much worse fit ($\chi^2 = 2.501$).

Tetragonal Phase – Initial refinements were based on the tetragonal structure of $(Na_{0.6}K_{0.4})_{0.5}Bi_{0.5}TiO_3$. The space group P4mm was used and the same refinement procedure followed. A 2θ angular range between 22.51-136.51° was used in the refinements, which included 30 reflections. Coexisting rhombohedral (72 %) and tetragonal phases (28 %) at 493 K, were based on the nearest related models and refined together. A 2θ angular range between 22.51-136.51° was used in these refinements, which included 96 reflections.

Cubic Phase – The high temperature, paraelectric form of $(Na_{0.5}K_{0.5})_{0.5}Bi_{0.5}TiO_3$, space group $Pm\bar{3}m$ was observed at 993 K. Initial refinements were based on the previous tetragonal phase. A 2θ angular range between 22.51-136.51° was used in the refinements, which included 26 reflections.

All refinements were stable and converged readily. The crystallographic data for the three phases between 293-993 K are presented in Table 5.06 (a) and (b). The observed, calculated and difference profiles from the final Rietveld refinements for all phases are shown in Figure 5.06.

Rombohedral (R3m†) Phase (293 K).

Atom	x	y	z	U11	U22	U33	U12	U13	U23
Na	0.0	0.0	0.2543(2)	0.024(8)	0.024(8)	-0.018(7)	0.012(4)	0.0	0.0
K	0.0	0.0	0.2543(2)	0.017(8)	0.017(8)	-0.004(1)	0.009(3)	0.0	0.0
Bi	0.0	0.0	0.2543(2)	0.058(7)	0.058(7)	0.043(1)	0.029(3)	0.0	0.0
Ti	0.0	0.0	0.0010(4)	0.021(1)	0.021(1)	-0.021(8)	0.011(1)	0.0	0.0
O	0.1671(1)	0.3342(1)	0.0833	0.022(6)	0.022(6)	0.027(4)	0.026(6)	-0.009(5)	-0.011(1)

† Refined in R3c – refer to text

Tetragonal (P4mm) Phase (593 K).

Atom	x	y	z	U11	U22	U33	U12	U13	U23
Na	0.0	0.0	-0.046(2)	0.051(2)	0.051(2)	0.055(4)	0.0	0.0	0.0
K	0.0	0.0	-0.046(2)	0.046(2)	0.046(2)	0.047(2)	0.0	0.0	0.0
Bi	0.0	0.0	-0.046(2)	0.059(5)	0.059(5)	0.082(1)	0.0	0.0	0.0
Ti	½	½	½	0.029(4)	0.029(4)	-0.005(4)	0.0	0.0	0.0
O(I)	½	½	0.007(3)	0.040(3)	0.040(3)	0.015(4)	0.0	0.0	0.0
O(II)	½	0.0	0.520(2)	0.021(3)	0.034(3)	0.021(4)	0.0	0.0	0.0

Cubic (Pm $\bar{3}$ m) Phase (993 K).

Atom	x	y	z	U11	U22	U33	U12	U13	U23
Na	0.0	0.0	0.0	0.068(6)	0.068(6)	0.068(6)	0.0	0.0	0.0
K	0.0	0.0	0.0	0.061(9)	0.061(9)	0.061(9)	0.0	0.0	0.0
Bi	0.0	0.0	0.0	0.089(2)	0.089(2)	0.089(2)	0.0	0.0	0.0
Ti	½	½	½	0.021(1)	0.021(1)	0.021(1)	0.0	0.0	0.0
O	½	½	0.0	0.043(1)	0.043(1)	-0.006(1)	0.0	0.0	0.0

Table 5.06 (a). Fractional co-ordinates and equivalent anisotropic displacement parameters ($Å^2$) for $(Na_{0.5}K_{0.5})_{0.5}Bi_{0.5}TiO_3$.

Chemical formula	**$(Na_{0.5}K_{0.5})_{0.5}Bi_{0.5}TiO_3$ (x = 0.5)**
Chemical formula weight	215.91
Specimen Shape	Random powder
Specimen preparation	Crystal growth from flux, Powder prepared from ground crystals
Specimen Pressure	Ambient
Colour	Pale Yellow
Radiation Type	Neutron
Wavelength	1.91 Å

Crystal System	**Rhombohedral**	**Tetragonal**	**Cubic**
Temperature (K)	293	593	993
Space Group	R3m (refined in R3c)†	P4mm	$Pm\bar{3}m$
a_H (Å)	5.5207 (3)	-	-
c_H (Å)	13.567 (2)	-	-
a_p (Å)	-	3.9136 (2)	3.93009 (7)
c_p (Å)	-	3.9289 (3)	-
α,β,γ (°)	90, 90, 120	90, 90, 90	90, 90, 90
Volume (Å^3)	358.12 (3)	60.174 (4)	60.702 (3)
Z	6	1	1
D_x (Mg.m^{-3})	6.007	5.957	5.91
s	0.0043 (2)	0.053 (5)	0.0
t	0.0010 (4)	0.020 (2)	0.0
d	-0.0002 (1)	-	-
e	0.0	-	-
Tilt System	$a^0a^0a^0$ (zero-tilt system)	$a^0a^0a^0$ (zero-tilt system)	$a^0a^0a^0$ (zero-tilt system)
Displacements	Parallel along $[111]_p$	Parallel along [001]	None
ω (°)	0.0	0.0	0.0
$\zeta \times 10^2$	-	-	-
N^o of refined parameters	46	48	39
Profile R-factors			
R_p	0.098	0.102	0.081
wR_p	0.133	0.138	0.113
χ^2	0.442	0.476	0.340

Table 5.06 (b). Summary of experimental details, data collection and refinement for the three phases of $(Na_{0.5}K_{0.5})_{0.5}Bi_{0.5}TiO_3$ (†refer to text).

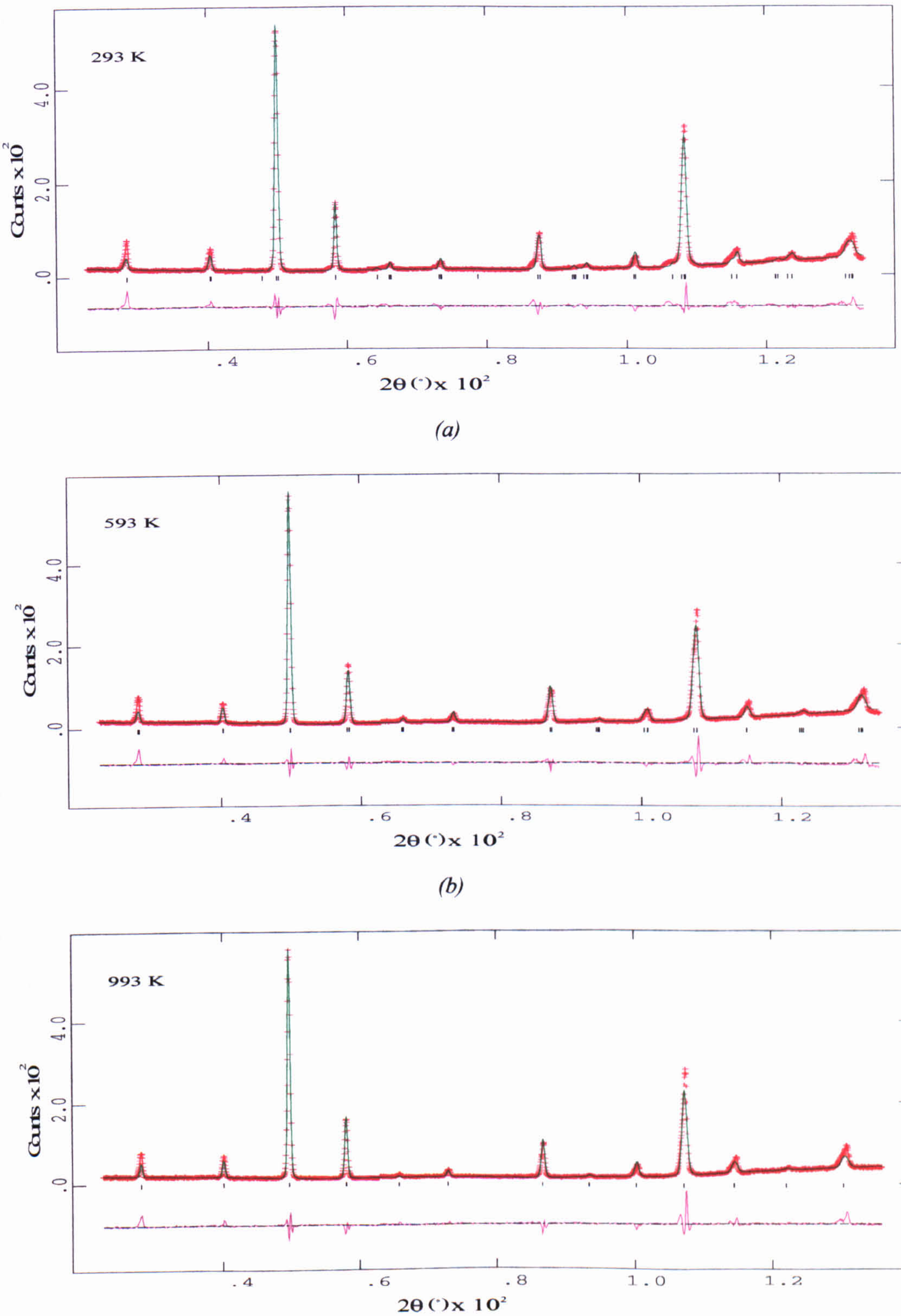

(a)

(b)

(c)

Figure 5.06. *The observed, calculated and difference curves from the final Rietveld refinements of $(Na_{0.5}K_{0.5})_{0.5}Bi_{0.5}TiO_3$ (x = 0.5). (a) R3m († refer to text) refinement in R3c, at 293 K, the black marks indicate the position of reflections. (b) refinement in P4mm, at 593 K. (c) refinement in $Pm\bar{3}m$, at 993 K.*

5.2.3.4 $(Na_{0.4}K_{0.6})_{0.5}Bi_{0.5}TiO_3$ ($x = 0.6$)

Rhombohedral Phase – The room temperature powder pattern for this compound showed rhombohedral broadening of lines but possessed no superstructure peaks. Refinements for the room temperature phase were based on the final refinements of the room temperature data for $(Na_{0.5}K_{0.5})_{0.5}Bi_{0.5}TiO_3$, as described before. A 2θ angular range between 23.51-139.51° was used in the refinements, which included 95 reflections. The refined shared-site occupation factors for Na, K and Bi were 0.15 (3), 0.34 (2) and 0.51 (2) respectively.

A TiO_2 impurity phase was also found to be present with this compound. Its abundancy was estimated to be 8 % from the room-temperature profile and this was fixed in the subsequent refinements.

Tetragonal Phase – Initial refinements were based on the tetragonal structure of $(Na_{0.5}K_{0.5})_{0.5}Bi_{0.5}TiO_3$. The space group P4mm was used and the same refinement procedure followed. A 2θ angular range between 23.51-139.51° was used in the refinements, which included 86 reflections. Coexisting rhombohedral (71 %), tetragonal phases (21 %) and TiO_2 (8 %) at 443 K, were based on the nearest related structural models and refined together. A 2θ angular range between 23.51-138.01° was used in the refinements, which included 131 reflections.

Cubic Phase – The high temperature, paraelectric form of $(Na_{0.4}K_{0.6})_{0.5}Bi_{0.5}TiO_3$, space group $Pm\bar{3}m$ was observed at 993 K. Initial refinements were based on the previous tetragonal phase. A 2θ angular range between 23.51-139.51° was used in the refinements, which included 56 reflections.

All refinements were stable and converged readily. The crystallographic data for the three phases between 293-993 K are presented in Table 5.07 (a) and (b). The observed, calculated and difference profiles from the final Rietveld refinements for all phases are shown in Figure 5.07.

Rombohedral (R3m†) Phase (293 K).

Atom	x	y	z	U11	U22	U33	U12	U13	U23
Na	0.0	0.0	0.2540(4)	0.014(5)	0.014(5)	0.023(6)	0.007(3)	0.0	0.0
K	0.0	0.0	0.2540(4)	0.024(6)	0.024(6)	0.034(1)	0.012(3)	0.0	0.0
Bi	0.0	0.0	0.2540(4)	0.064(5)	0.064(5)	0.068(9)	0.032(2)	0.0	0.0
Ti	0.0	0.0	0.0012(4)	0.015(6)	0.015(6)	0.002(1)	0.007(3)	0.0	0.0
O	0.1608(3)	0.321(6)	0.0833	0.031(3)	0.006(3)	0.027(1)	0.012(1)	-0.004(1)	-0.011(1)

† *Refined in R3c – refer to text*

Tetragonal (P4mm) Phase (593 K).

Atom	x	y	z	U11	U22	U33	U12	U13	U23
Na	0.0	0.0	-0.033(4)	0.031(4)	0.031(4)	0.035(2)	0.0	0.0	0.0
K	0.0	0.0	-0.033(4)	0.032(4)	0.032(4)	0.039(2)	0.0	0.0	0.0
Bi	0.0	0.0	-0.033(4)	0.074(8)	0.074(8)	0.09(2)	0.0	0.0	0.0
Ti	½	½	½	0.004(3)	0.004(3)	0.009(7)	0.0	0.0	0.0
O(I)	½	½	0.032(4)	0.052(3)	0.052(3)	0.007(3)	0.0	0.0	0.0
O(II)	½	0.0	0.528(3)	0.013(2)	0.019(4)	0.046(4)	0.0	0.0	0.0

Cubic (Pm $\bar{3}$ m) Phase (993 K).

Atom	x	y	z	U11	U22	U33	U12	U13	U23
Na	0.0	0.0	0.0	0.074(1)	0.074(1)	0.074(1)	0.0	0.0	0.0
K	0.0	0.0	0.0	0.058(6)	0.058(6)	0.058(6)	0.0	0.0	0.0
Bi	0.0	0.0	0.0	0.084(2)	0.084(2)	0.084(2)	0.0	0.0	0.0
Ti	½	½	½	0.020(1)	0.020(1)	0.020(1)	0.0	0.0	0.0
O	½	½	0.0	0.049(1)	0.049(1)	0.013(1)	0.0	0.0	0.0

Table 5.07 (a). Fractional co-ordinates and equivalent anisotropic displacement parameters ($Å^2$) for $(Na_{0.4}K_{0.6})_{0.5}Bi_{0.5}TiO_3$.

Chemical formula	**$(Na_{0.4}K_{0.6})_{0.5}Bi_{0.5}TiO_3$ (x = 0.6)**
Chemical formula weight	216.72
Specimen Shape	Random powder
Specimen preparation	Crystal growth from flux, Powder prepared from ground crystals
Specimen Pressure	Ambient
Colour	Pale Yellow
Radiation Type	Neutron
Wavelength	1.91 Å

Crystal System	**Rhombohedral**	**Tetragonal**	**Cubic**
Temperature (K)	293	593	993
Space Group	R3m (refined in R3c)†	P4mm	$Pm\bar{3}m$
a_H (Å)	5.5257 (6)	-	-
c_H (Å)	13.580 (1)	-	-
a_p (Å)	-	3.9130 (1)	3.9312 (1)
c_p (Å)	-	3.9215 (2)	-
α,β,γ (°)	90, 90, 120	90, 90, 90	90, 90, 90
Volume (Å^3)	359.1 (1)	60.0442 (3)	60.752 (5)
Z	6	1	1
D_x (Mg.m^{-3})	6.035	5.994	5.924
s	0.0040 (4)	0.065 (8)	0.0
t	0.0012 (4)	0.028 (3)	0.0
d	-0.003 (1)	-	-
e	0.0	-	-
Tilt System	$a^0a^0a^0$ (zero-tilt system)	$a^0a^0a^0$ (zero-tilt system)	$a^0a^0a^0$ (zero-tilt system)
Displacements	Parallel along $[111]_p$	Parallel along [001]	None
ω (°)	0.0	0.0	0.0
$\zeta \times 10^2$	-	-	-
N° of refined parameters	46	48	39
Profile R-factors			
R_p	0.115	0.089	0.069
$_wR_p$	0.148	0.122	0.100
χ^2	0.534	0.346	0.231

Table 5.07 (b). Summary of experimental details, data collection and refinement for the three phases of $(Na_{0.4}K_{0.6})_{0.5}Bi_{0.5}TiO_3$ (†refer to text).

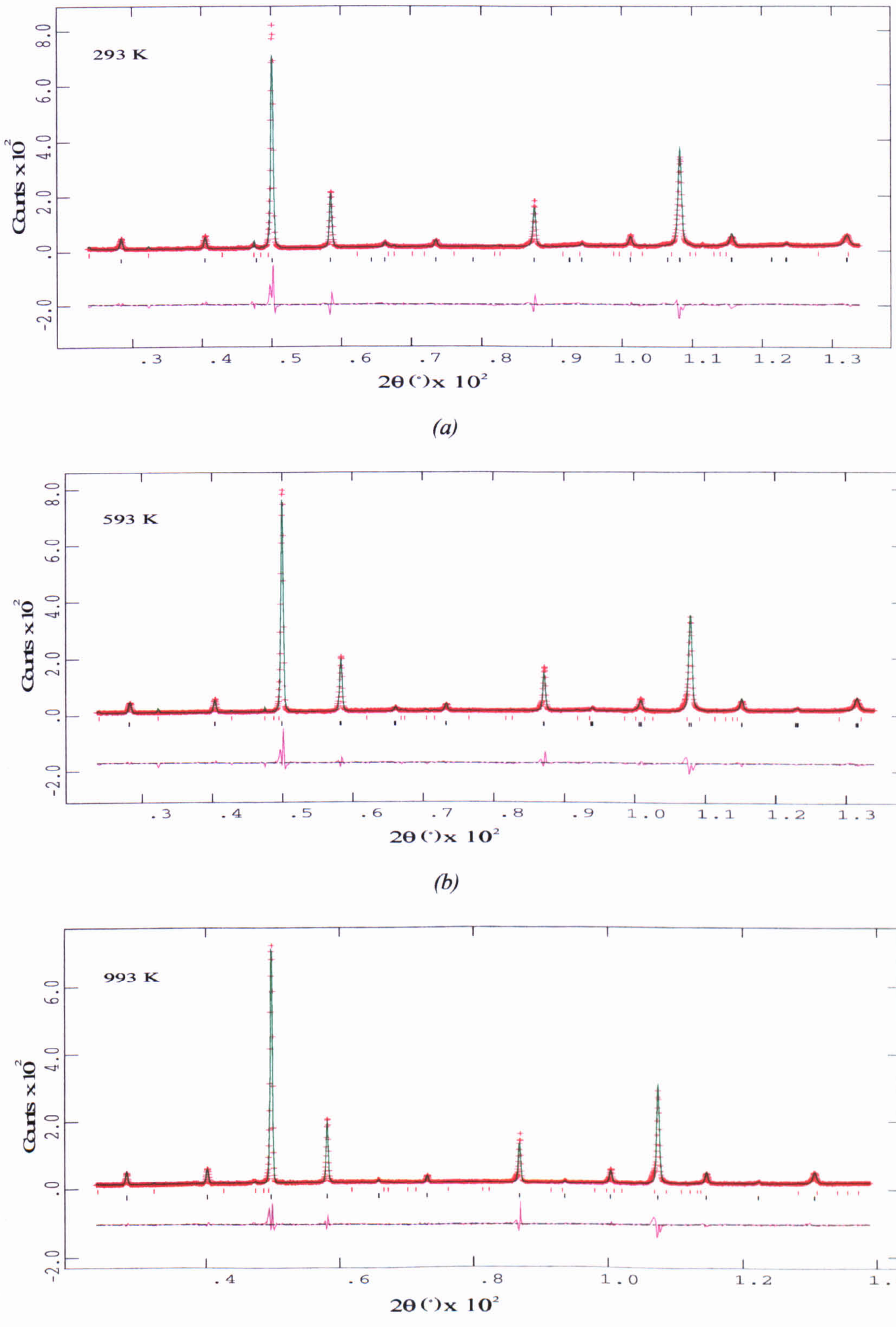

Figure 5.07. *The observed, calculated and difference curves from the final Rietveld refinements of $(Na_{0.4}K_{0.6})_{0.5}Bi_{0.5}TiO_3$ (x = 0.6). (a) R3m (†refer to text) refinement in R3c, at 293 K, the black and red marks indicate the position of the $(Na_{0.4}K_{0.6})_{0.5}Bi_{0.5}TiO_3$ and TiO_2 reflections respectively. (b) refinement in P4mm, at 593 K. (c) refinement in $Pm\bar{3}m$, at 993 K.*

5.2.3.5 $K_{0.5}Bi_{0.5}TiO_3$ ($x = 1.0$)

Tetragonal Phase –Tetragonal distortions as shown by the splitting/broadening of certain reflections were clearly evident in the room temperature diffraction pattern. Initial refinements were based on the tetragonal structure of $(Na_{0.4}K_{0.6})_{0.5}Bi_{0.5}TiO_3$. The space group P4mm was used and the same refinement procedure followed. A 2θ angular range between 21.01-132.00° was used in the refinements, which included 30 reflections. Data collections were also taken as a function of temperature however due to inadequate scanning times, the data were of insufficient quality to allow structural refinement. The crystallographic data for the room temperature tetragonal structure is presented in Table 5.08 (a) and (b). The observed, calculated and difference profiles from the final Rietveld refinements are shown in Figure 5.08.

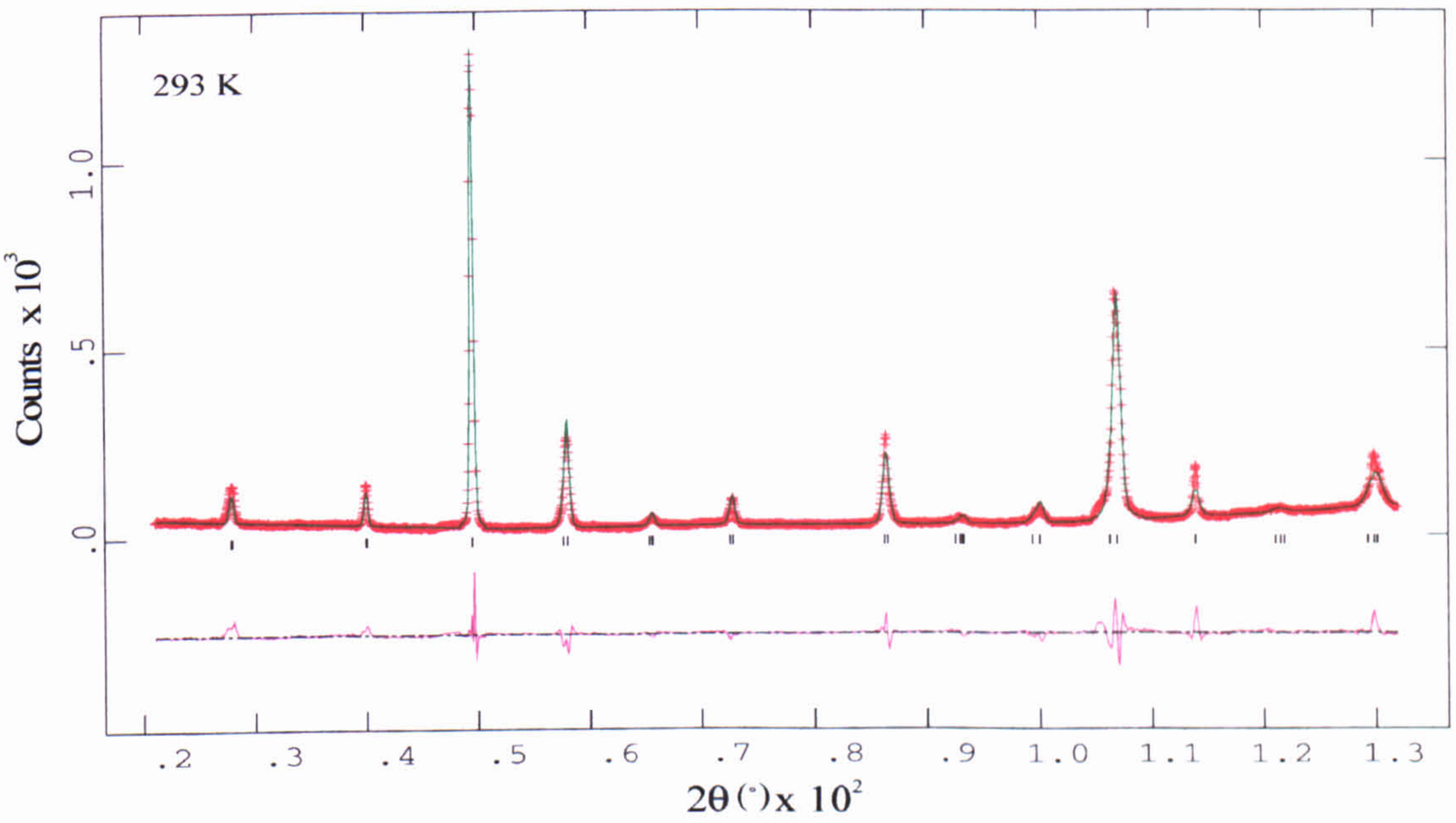

Figure 5.08. *The observed, calculated and difference curves from the final Rietveld refinements of $K_{0.5}Bi_{0.5}TiO_3$. The marks indicate the position of reflections. Refinement in P4mm, at 293 K.*

Tetragonal (P4mm) Phase (293 K).

Atom	x	y	z	U11	U22	U33	U12	U13	U23
K	0.0	0.0	-0.0444(1)	0.032(4)	0.032(4)	0.052(9)	0.0	0.0	0.0
Bi	0.0	0.0	-0.0444(1)	0.050(8)	0.050(8)	0.068(7)	0.0	0.0	0.0
Ti	½	½	½	0.015(4)	0.015(4)	0.012(9)	0.0	0.0	0.0
O(I)	½	½	0.0015(1)	0.010(2)	0.010(2)	0.021(3)	0.0	0.0	0.0
O(II)	½	0.0	0.527(2)	0.009(3)	-0.012(5)	0.045(4)	0.0	0.0	0.0

Table 5.08 (a). *Fractional co-ordinates and equivalent anisotropic displacement parameters ($Å^2$) for $K_{0.5}Bi_{0.5}TiO_3$.*

Chemical formula	**$K_{0.5}Bi_{0.5}TiO_3$**
Chemical formula weight	219.94
Specimen Shape	Random powder
Specimen preparation	Fabrication from flux
Specimen Pressure	Ambient
Colour	Pale Yellow
Radiation Type	Neutron
Wavelength	1.91 Å
Crystal System	**Tetragonal**
Temperature (K)	293
Space Group	P4mm
Unit Cell	**a × b × c**
a_T (Å)	3.9388 (2)
c_T (Å)	3.9613 (4)
c_T / a_T	1.00571(5)
α,β,γ (°)	90, 90, 90
Volume (Å^3)	61.457 (8)
Z	1
D_x (Mg.m^{-3})	5.943
s	0.0459 (2)
t	0.027 (2)
Tilt System	$a^0a^0a^0$ (zero-tilt system)
Displacements	Parallel along [001]
Nº of refined parameters	48
Profile R-factors	
R_p	0.856
$_wR_p$	0.115
χ^2	0.722

Table 5.08 (b). Summary of experimental details, data collection and refinement for $K_{0.5}Bi_{0.5}TiO_3$.

5.3 Discussion

Within the literature certain NBT related solid solutions for example $(Na_{0.5}Bi_{0.5})_{1-x}Pb_xTiO_3$[13-17] or $(Na_{0.5}Bi_{0.5})_{1-x}Sr_xTiO_3$[18-20] have attracted much attention due mainly to potentially interesting electromechanical properties at the structural phase boundary between the two end members. However very few studies[21-24] (x-ray diffraction and dielectric/piezoelectric measurements) have been conducted on the $(Na_{1-x}K_x)_{0.5}Bi_{0.5}TiO_3$, NKBT solid solution series. The limited results from these studies disagree, the main discrepancy being in relation to the nature of the NBT (rhombohedral) to KBT (tetragonal) phase transitions. No mention of possible space groups, tilting or cation displacements are given. The following discussion will address these

discrepancies and a detailed systematic structural investigation with varying composition and temperature will be presented.

5.3.1 Lattice parameters and phase transitions

Lattice parameters obtained from the final refinements of each compound as a function of temperature have been plotted in Figures 5.09(a)–(d). Looking at the rhombohedral phases (plotted with reference to rhombohedral crystallographic axes) the cell parameter a_R increases steadily as expected with increasing temperature. Figure 5.10 (a)-(c) shows the room temperature lattice parameters and volume (between $0.0 < x < 0.6$) obtained as a function of composition across the solid solution series. Across the series the magnitudes of a_H, c_H and volume (V), all increase as the proportion of K^{1+} doping is increased. Considering the ionic radii of the various atoms in the unit cell this trend is to be expected. Table 5.09 lists the average ionic radii $<r_A>$ of the A-site cations and the tolerance factor t, for the solid solution compounds. The average ionic radii $<r_A>$, has been calculated using values obtained from Shannon[25] that have co-ordination closest to the expected co-ordination. In calculating the tolerance factor t, the $Na^{1+}/K^{1+}/Bi^{3+}$ ions are assumed to be randomly distributed and act as a single virtual ion with a single averaged radius $<r_A>$. At the same temperature as the value of $<r_A>$ increases the unit cell increases in order to accommodate the larger virtual ions. It is interesting to consider further the non-equivalence of the ionic radii in these compounds. If the ions are considered as hard spheres of individual sizes, (which is the model that ionic radii are based on) and distributed randomly on the A-sites throughout the structure, then the lattice would contract until contact was made with the larger K^{1+} ions. This would essentially leave the smaller Na^{1+}/Bi^{3+} ions to move within the cuboctahedral cage. In such a model, the distortion would be influenced by the larger ion only. Ions are not rigid spheres however as indicated by the steady increase in volume with increasing K^{1+} doping (and therefore increasing $<r_A>$). However the pronounced non-linearity of the volume increase (within errors) illustrates that the behaviour does not approximate to that associated with randomly distributed ions with an average ionic radius. In terms of cation percentages resident at the A-site, NBT is made up of a 50:50 Na:Bi ratio. Comparing the compound $(Na_{0.8}K_{0.2})_{0.5}Bi_{0.5}TiO_3$ with NBT we see that replacing 10 % of the Na atoms with the larger ionic radii K^{1+} atoms has the effect of increasing the cell dimensions and thus volume (further structural effects occur and will

be discussed in the following sections). At room temperature there is a volume increase of 0.4 % ($\Delta V = 1.00\ (2)\ Å^3$).

Composition (x) $(Na_{1-x}K_x)_{0.5}Bi_{0.5}TiO_3$	Average Ionic radii $\langle r_A \rangle$ (Å)	*Tolerance factor*, t $t = (\langle r_A \rangle + r_X)/\sqrt{2}(r_B + r_X)$
0.0	1.315	0.850
0.2	1.348	0.860
0.4	1.381	0.871
0.5	1.398	0.877
0.6	1.414	0.882
0.8	1.447	0.893
1.0	1.480	0.904

Table 5.09. *Average Ionic radii and tolerance factors for NKBT solid solution series. Calculated from individual radii of ions[25] Na^{1+}=1.32, Bi^{3+}=1.31, K^{1+}=1.65, Ti^{4+}=0.88, O^{2-}=1.28Å.*

It is known that the location of a phase boundary depends upon the degree of lattice distortion of the end member of the solid solution[1]. It terms of the small tetragonal lattice distortion of KBT ($c/a \approx 1.006$) it would be reasonable to expect that for small K^{1+} doping proportions, NKBT would maintain the NBT rhombohedral structure and for larger proportions move towards the KBT tetragonal structure. Previous published work relating to NKBT report a room temperature phase boundary for x close to 0.2[21-23]. Figure 5.11 shows the phase boundary limits from the literature and results from this study.

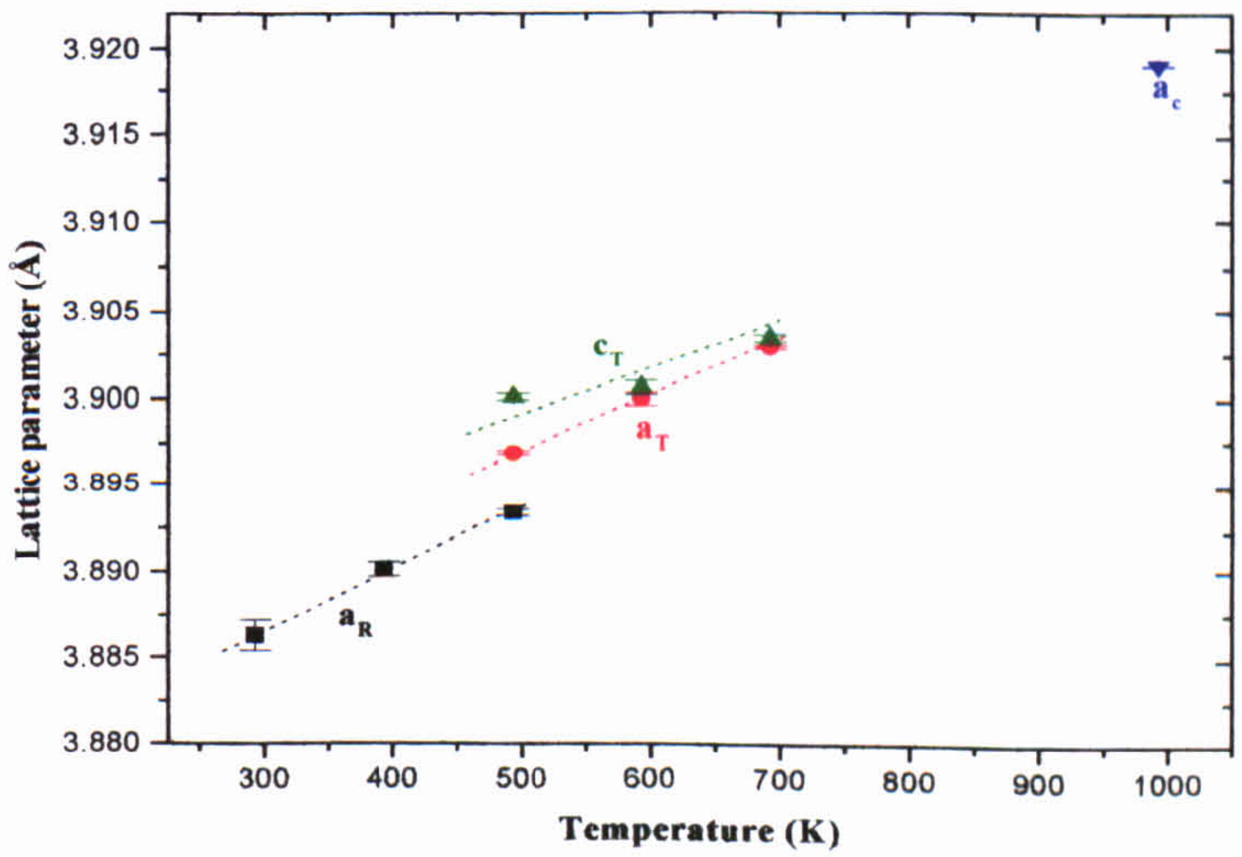

(a)

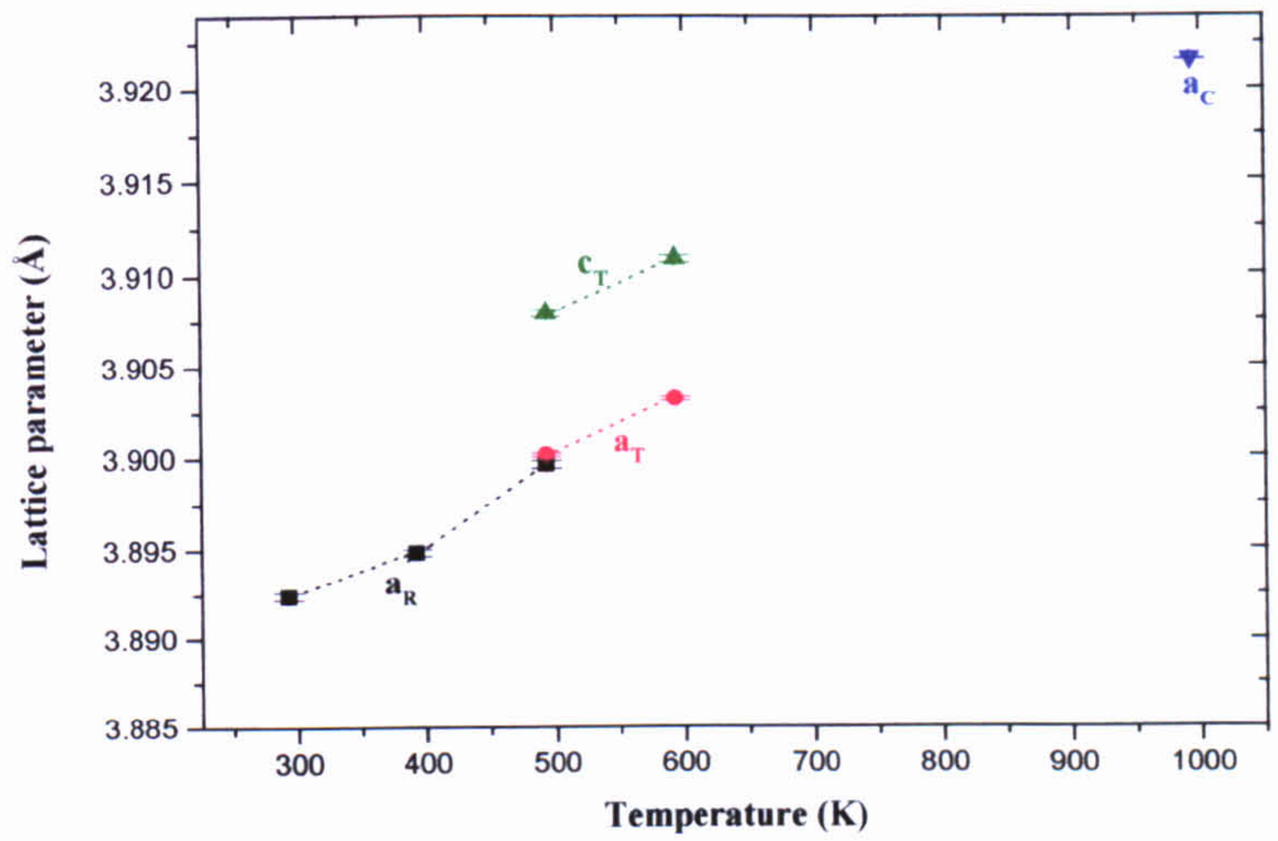

(b)

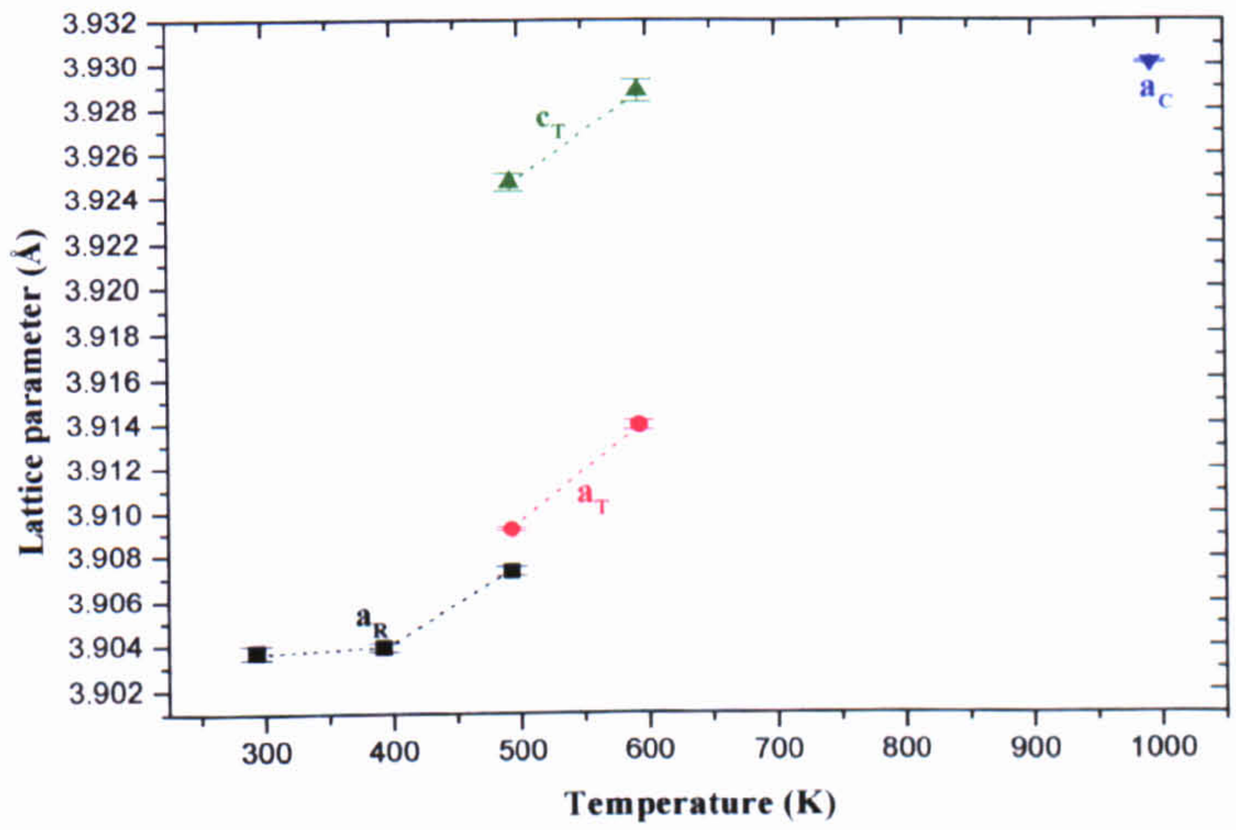

(c)

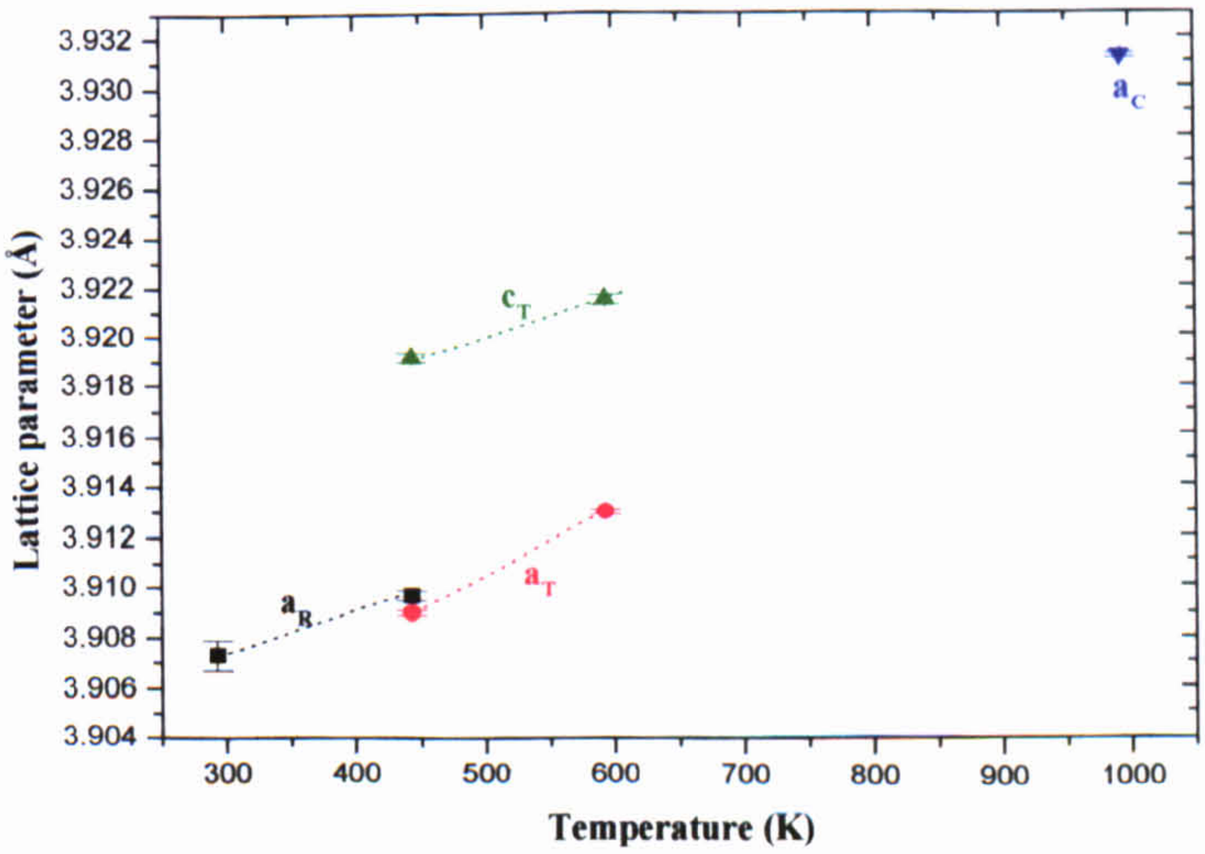

(d)

Figure 5.09. *Lattice parameter evolution as a function of temperature for (a) $(Na_{0.8}K_{0.2})_{0.5}Bi_{0.5}TiO_3$ $(x = 0.2)$ (b) $(Na_{0.6}K_{0.4})_{0.5}Bi_{0.5}TiO_3$ $(x = 0.4)$ (c) $(Na_{0.5}K_{0.5})_{0.5}Bi_{0.5}TiO_3$ $(x = 0.5)$ (d) $(Na_{0.4}K_{0.6})_{0.5}Bi_{0.5}TiO_3$ $(x = 0.6)$.*

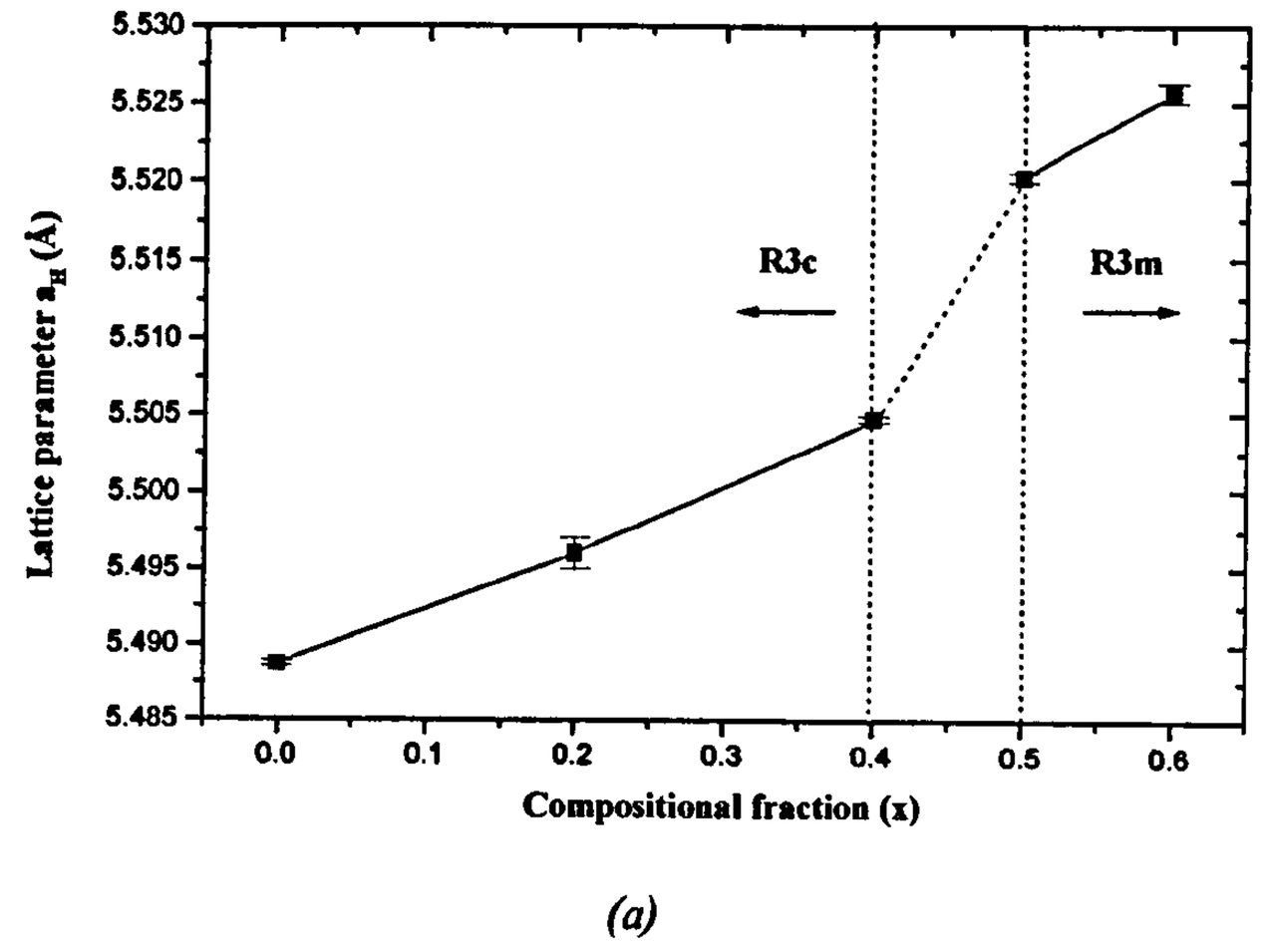

(a)

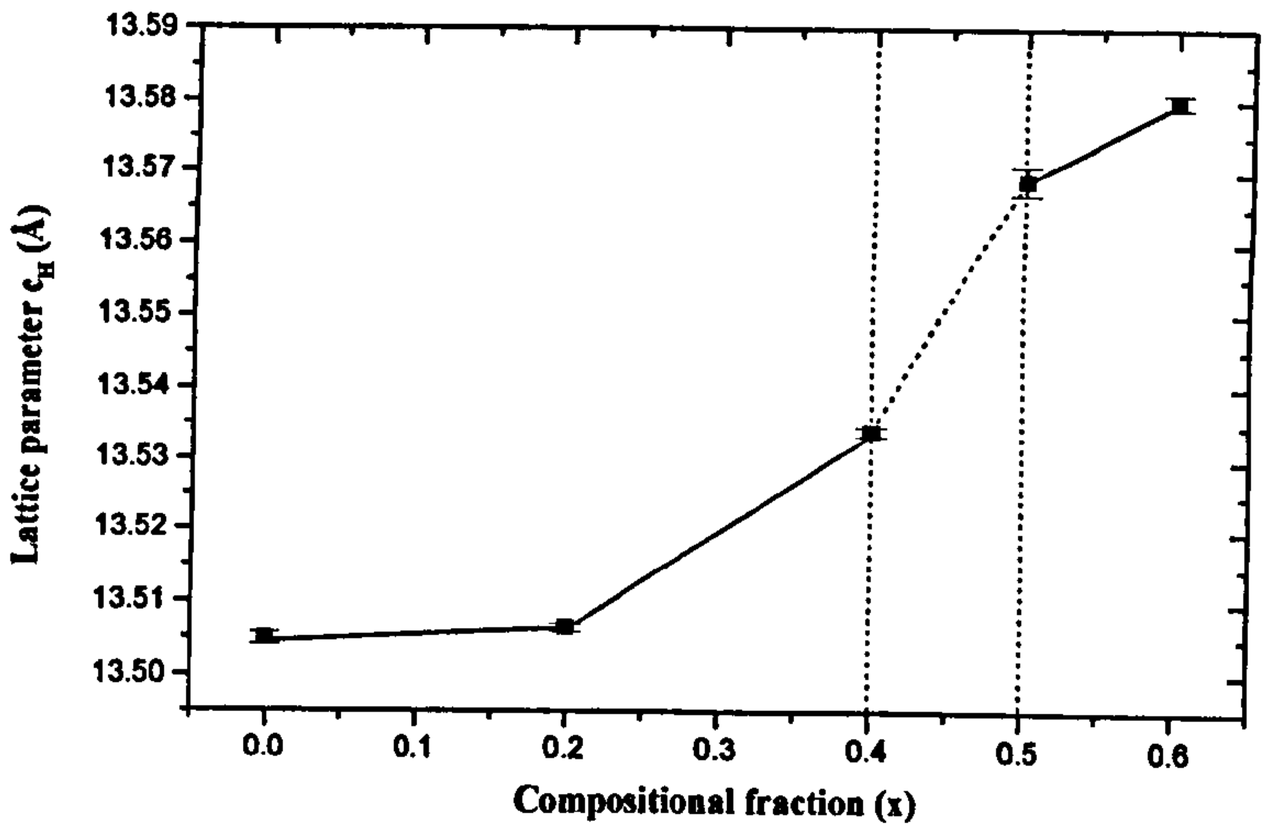

(b)

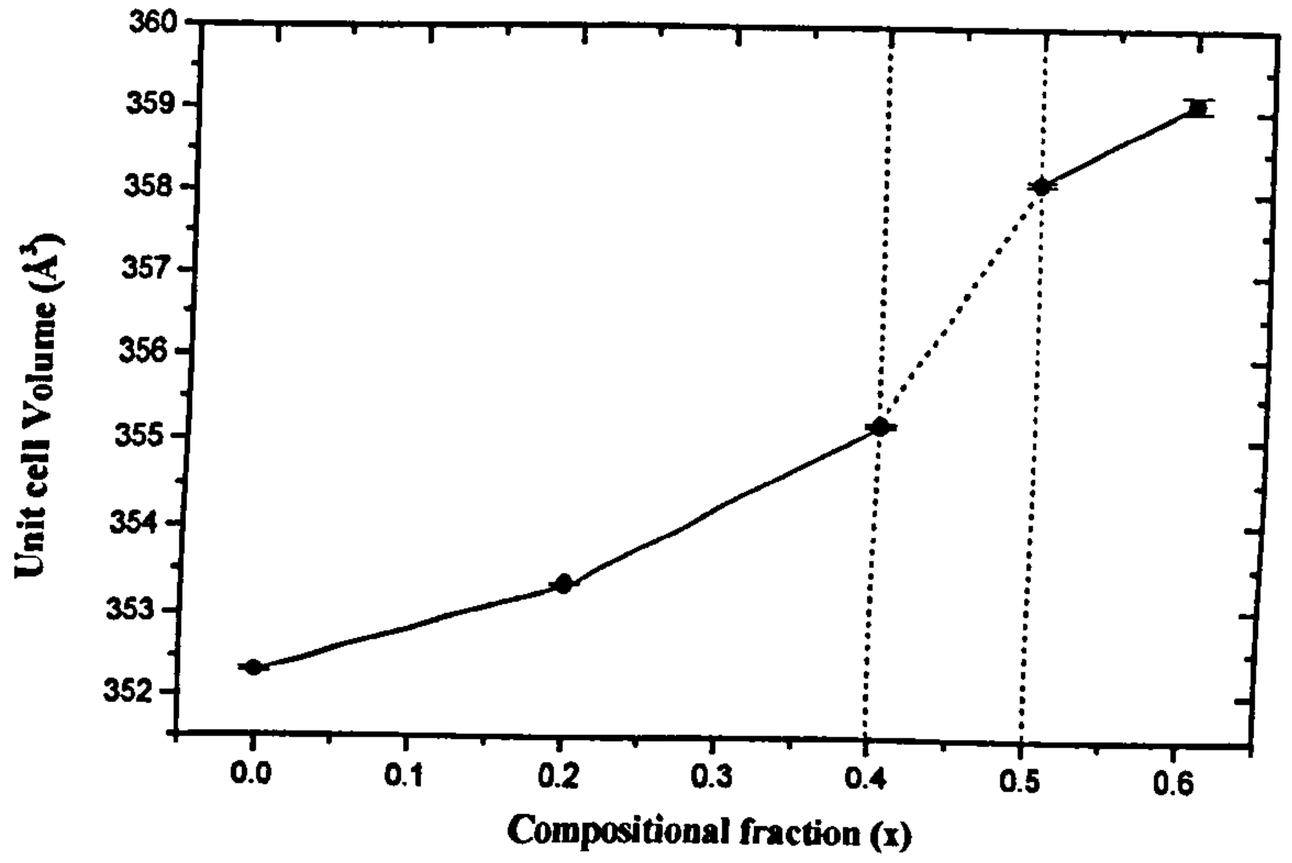

(c)

Figure 5.10. *The room temperature lattice parameters (a) a_H, (b) c_H and, (c) unit cell volume, of the rhombohedral phases (R3c and R3m) across solid solution range NBT (x = 0) – $(Na_{0.4}K_{0.6})_{0.5}Bi_{0.5}TiO_3$ (x = 0.6).*

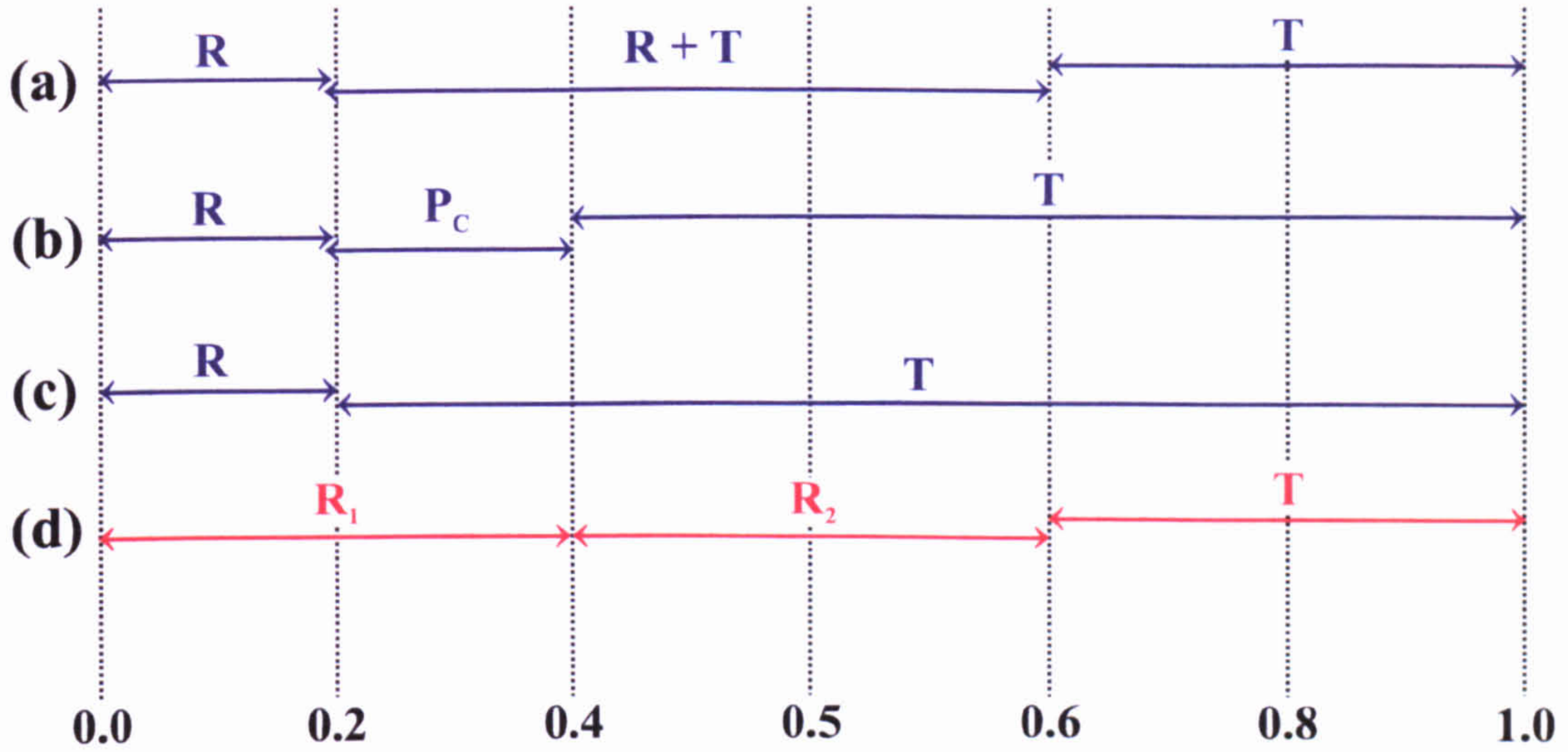

Figure 5.11. *$(Na_{1-x}K_x)_{0.5}Bi_{0.5}TiO_3$ crystal structures (R: rhombohedral, (R_1=R3c, R_2=R3m) T: tetragonal, P_C: pseudo-cubic) as reported in the literature; (a) [22], (b) [21], (c) [23], (d) this study.*

With reference to Figure 5.11, we see that the only agreement of phases is at the end members. The controversy of the phase boundaries lie in the region $0.2 < x < 0.6$, with a coexistence of rhombohedral/tetragonal[(a)], pseudo-cubic and tetragonal phases[(b)] and purely tetragonal phases[(c)] being reported. The results from this study[(d)] were obtained via neutron powder diffraction, this method is more sensitive in relation to tilting than with the x-ray methods used in the other studies. As superstructure peaks associated with the $a^-a^-a^-$ tilt system were clearly observed up to $x = 0.2$ we are confident that the rhombohedral space group R3c which we have assigned is correct. Apart from the splitting/broadening of certain lines (which in many cases can be difficult to differentiate between) there can be little apparent difference between the rhombohedral R3m and tetragonal P4mm powder diffraction profiles of these compounds. In order to complement neutron results x-ray powder data were taken on the solid solution range. X-ray powder diffraction data on NKBT were recorded with a Stoë STADI 2P automatic powder diffractometer working in transmission mode and fitted with a curved position-sensitive detector (each NKBT powder was scanned through a 2θ-range of 20-80° with step size 0.01° using CuK_α radiation). The lattice parameters were calculated using Si as an internal standard. Figure 5.12 shows the x-ray powder diffraction pattern for the NKBT solid solution range.

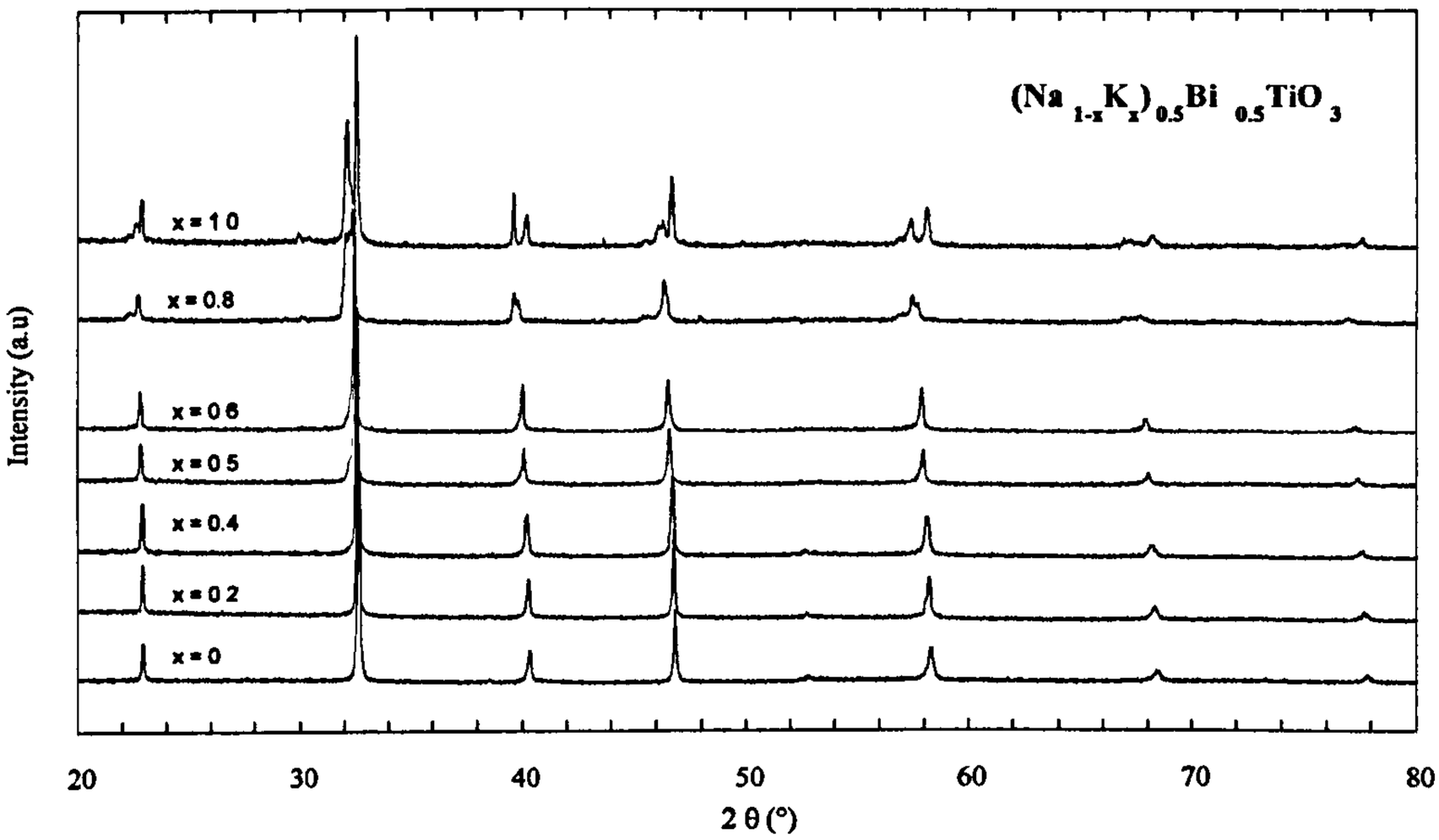

Figure 5.12. X-ray powder diffraction profiles for $(Na_{1-x}K_x)_{0.5}Bi_{0.5}TiO_3$.

As shown in Figure 5.12, the x-ray powder diffraction profiles do not show a significant change between $0.0 < x < 0.6$. For example looking at the region $45 < 2\theta < 48°$ as shown in Figure 5.13, between $0.0 < x < 0.6$ the single (200) remains essentially the same only shifting slightly to lower angles as the unit cell size increases. However a splitting of the (200) reflection is prominent for $x \geq 0.8$. The splitting of this peak strongly suggests tetragonal symmetry (Table 3.03) although it should be noted that generally the occurrence of a split reflection alone does not constitute sufficient evidence. This is because in tetragonal structures, where the lattice distortion is very small, a resolvable splitting may not be distinguished. However, the change in diffraction profile pattern between $0.6 < x < 0.8$ is so large that a crystal structural change in this region of the composition is strongly suggested from these results alone.

The findings of the x-ray phase boundary investigations carried out here are in agreement with the results obtained through neutron refinements. The lattice parameter values obtained from both methods are in good agreement. In relation to the lattice parameters it is interesting to examine the $0.0 \leq x \leq 0.6$ region more closely. Figures 5.10 (a) and (b) show the plots of the lattice parameters a_H and c_H across the NKBT series obtained from neutron refinements. Figures 5.14. show the rhombohedral lattice parameters a_R and distortion α_R obtained from the x-ray data. In both sets of Figures it can clearly be seen that the gradient changes quite dramatically between $0.4 \leq x \leq 0.5$. This corresponds to the second structural change from R3c to R3m as established from the neutron refinements.

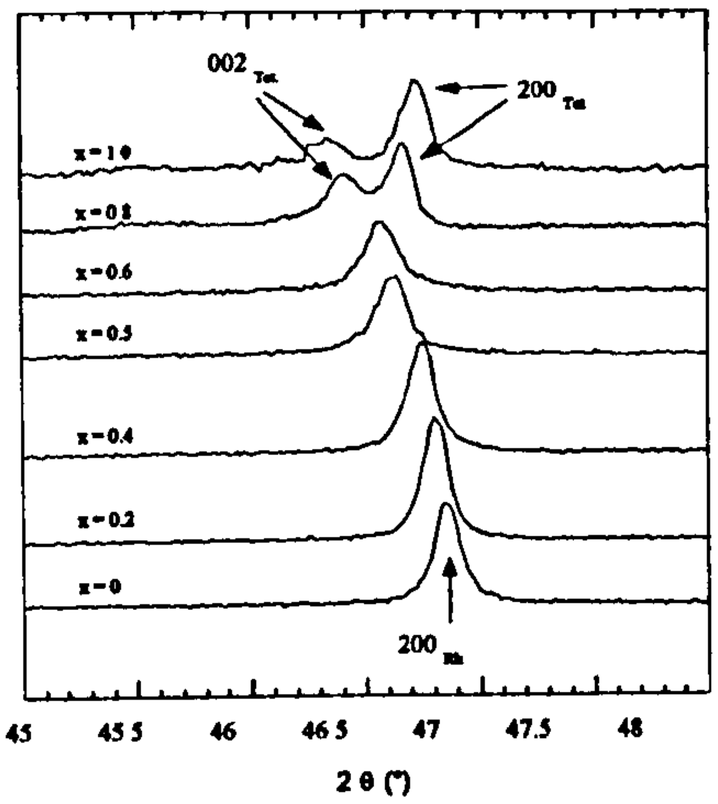

Figure 5.13. Detailed scan of x-ray reflections for $(Na_{1-x}K_x)_{0.5}Bi_{0.5}TiO_3$ between $45 < 2\theta < 48°$.

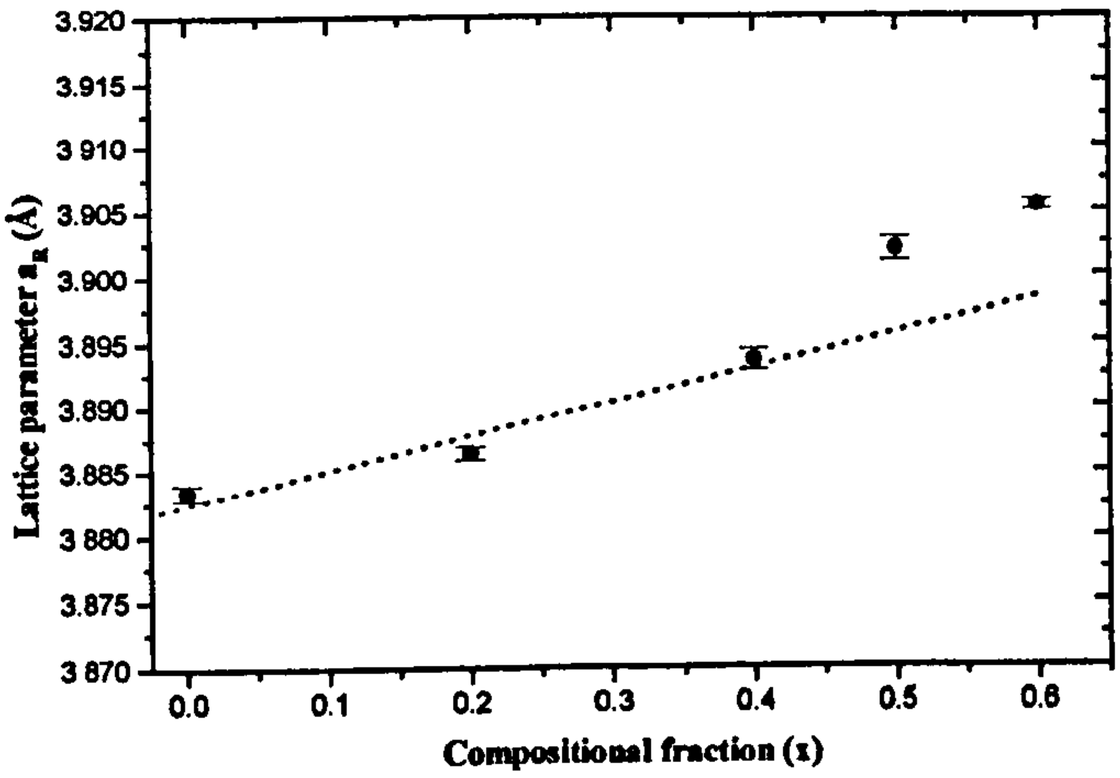

(a)

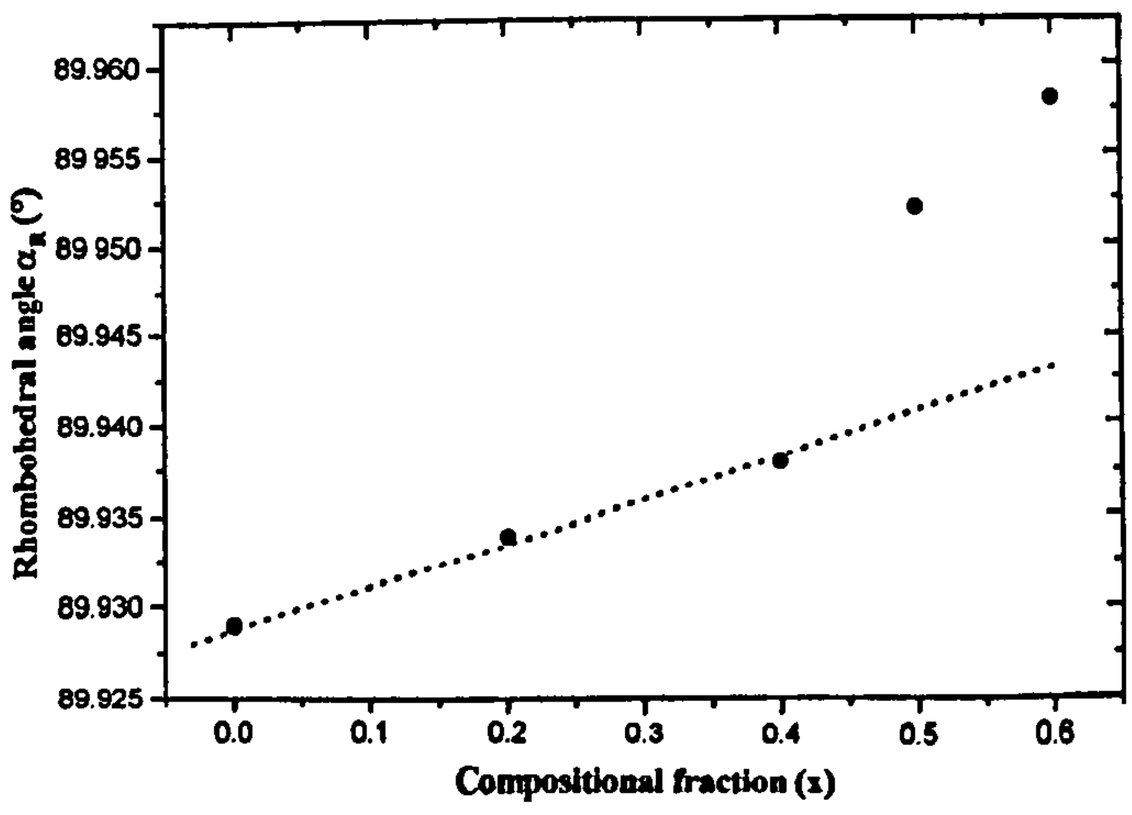

(b)

Figure 5.14. Evolution of the (a) lattice parameters a_R, (b) and rhombohedral lattice distortion α_R for $(Na_{1-x}K_x)_{0.5}Bi_{0.5}TiO_3$ for $x \leq 0.8$, from x-ray powder diffraction.

It is worth comparing the neutron/x-ray data obtained here with published results. As shown schematically in Figure 5.11, a rhombohedral/tetragonal coexistence region between $0.18 \leq x \leq 0.6$[22] or a pseudo-cubic phase between $0.17 \leq x \leq 0.4$[21], have been reported. The results from both x-ray and neutron data in this study, give no evidence for a coexistence of rhombohedral/tetragonal phases; the results reported by Elkechai *et al.*[22] could be explained as resulting from different preparation conditions. From high-resolution neutron diffraction results conducted here, the presence of a pseudo-cubic phase reported by Pronin *et al.*[21] can also be excluded.

A basic phase diagram for the NBKT solid solution series constructed from these powder diffraction results is shown in Figure 5.15. This representation is at best only a general guide outlining the phase boundaries across the solid solution range and with increasing temperature. The general nature of this phase diagram reflects the limited number of diffraction patterns that could be obtained within the allotted time periods.

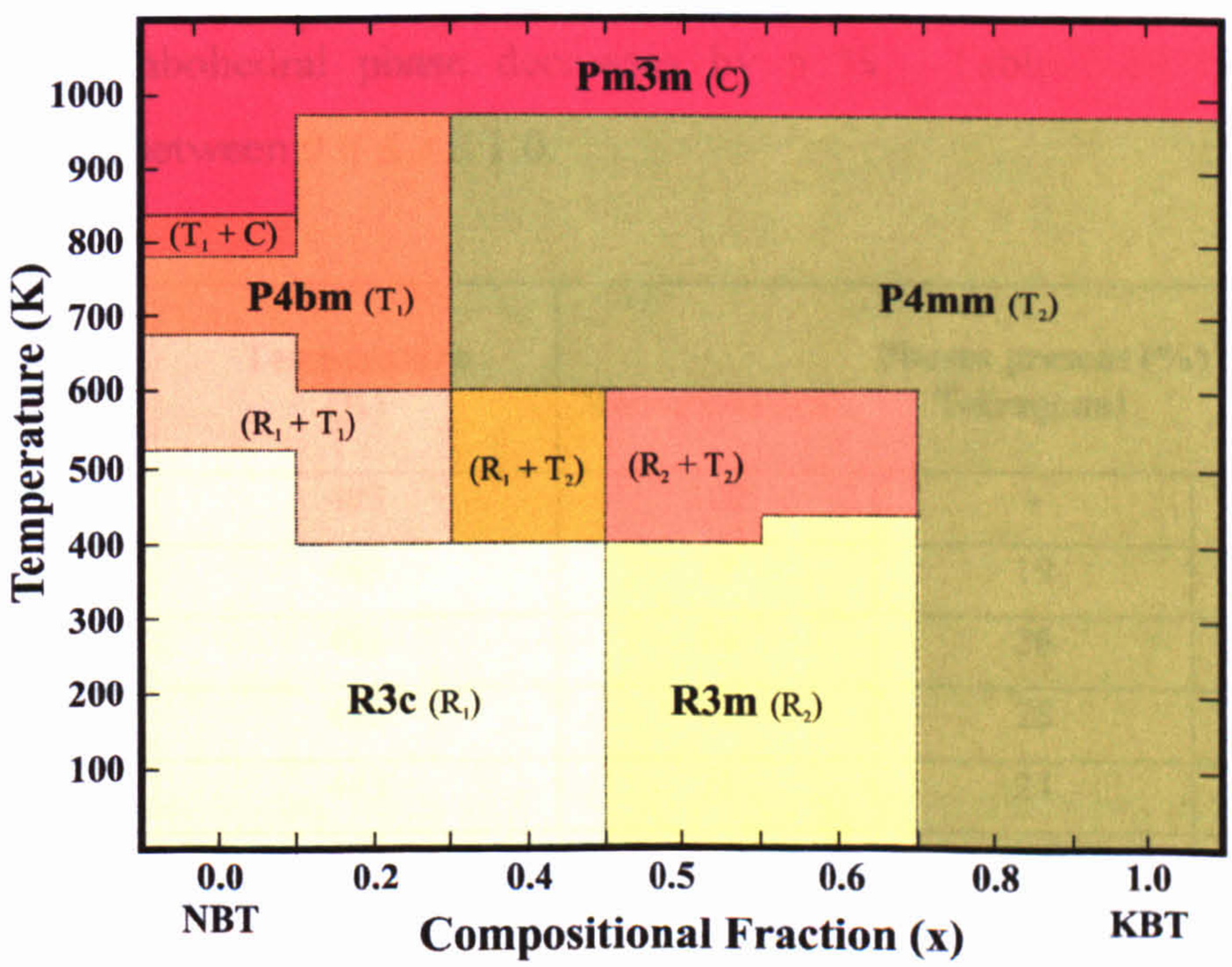

Figure 5.15. Basic phase diagram of the $(Na_{1-x}K_x)_{0.5}Bi_{0.5}TiO_3$ solid solution series.

The solid solution series NKBT displays an intricate phase diagram as shown in Figure 5.15. Although at high temperatures these compounds exhibit a high-symmetry primitive cubic structure, at lower temperatures a variety of octahedral tilts (section 5.3.3), cation shifts (section 5.3.4) and deformations occur leading to a number of different structures. At room temperature for instance these include the rhombohedral R3c ($a^-a^-a^-$) phase

exhibiting both cation displacements along $[111]_P$ and octahedral tilts about $[111]_P$. With increasing K^{1+} content, a new ferroelectric rhombohedral phase R3m ($a^0a^0a^0$) is observed in which the tilts disappear but cations remain displaced in parallel along $[111]_P$, continuing to the tetragonal P4mm ($a^0a^0a^0$) end phase. Looking at individual compounds as a function of temperature, we see that the general phase trend of rhombohedral → tetragonal → cubic (as already seen in NBT) is repeated between $0.0 \leq x \leq 0.6$. The unusual tetragonal symmetry P4bm seen for NBT is also observed for $(Na_{0.8}K_{0.2})_{0.5}Bi_{0.5}TiO_3$ with in-phase tilts being present as well as cation displacements. The phase transition boundaries are based on the data available. It is thought for example, that the phase transition to the cubic phase of compounds between $0.2 \leq x \leq 1.0$ occurs somewhat below 993 K. Another interesting feature displayed in the phase diagram is the temperature range over which the coexistence of tetragonal/rhombohedral region first occurs. It is seen to develop at lower temperatures than in NBT. From structural refinements of the data at 493 K we see that between $0.2 \leq x \leq 0.5$ the percentage of rhombohedral phase decreases by 5 %. Table 5.10 lists the phase percentage present between $0.0 \leq x \leq 1.0$.

Concentration (x) $(Na_{1-x}K_x)_{0.5}Bi_{0.5}TiO_3$	Temperature (K)	Phases present (%) Rhombohedral	Tetragonal	TiO_2
0.0	493	100	-	-
0.2	493	77	19	4
0.4	493	74	26	-
0.5	493	72	28	-
0.6	443	71	21	8
1.0	493	-	100	-

Table 5.10. Refined phase contributions in coexistence region for $(Na_{1-x}K_x)_{0.5}Bi_{0.5}TiO_3$.

In comparison with the onset of the coexistence region in NBT (which is first seen at 573 K (section 3.3.5.1) these results show that as the amount of K^{1+} doping is increased the rhombohedral/tetragonal phase transition onset occurs at lower temperatures (it would not be unreasonable to assume this happens across the series). The refined values for $x = 0.6$ appears to be out of sequence. However this data was collected at 443 K and the others listed in Table 5.10 at 493 K.

5.3.2 Cation Ordering

As previously stated in section 3.3.5.2, cation ordering is known to be favoured in complex B-site substituted perovskites, where there is sufficiently large differences between ion size and charge. These compounds are driven towards ordering by electrostatic forces, whereas materials with closely matched cation size are nearly always disordered. The chemical nature of the NKBT series raises the question of a possible ordering scheme of the A-cations. As concluded in section 3.3.5.2 no long range ordering was evident in NBT (but there remained the possibility that short range order exists, section 2.3.4). Table 5.11 lists some known A-site substituted perovskite compounds in which the percentage differences in ionic radii for the A-cations have been calculated.

A-site Substituted Perovskite Compound	A-site cation (size Å)	Percentage differences in ionic radii	Cation Ordering
$Na_{0.5}Bi_{0.5}TiO_3$† (Rhombohedral, R3c)	Na^{1+} (1.32), Bi^{3+} (1.31)	Na:Bi 0%	No
$Ag_{0.5}Bi_{0.5}TiO_3$[26] (Orthorhombic, Ibam)	Ag^{1+} (1.42), Bi^{3+} (1.31)	Ag:Bi 8%	No
$Nd_{0.5}Ag_{0.5}TiO_3$[27] (Tetragonal, P4/nbm)	Nd^{1+} (1.25), Ag^{1+} (1.42)	Nd:Ag 14%	Yes
$K_{0.5}Bi_{0.5}TiO_3$ (Tetragonal, P4mm)	K^{1+} (1.65), Bi^{3+} (1.31)	K:Bi 21%	No

Table 5.11. Table of various A-site substituted perovskites listing the ionic radii of A-cation and the calculated percentage difference in ionic size. † refer to section 3.3.5.2.

No superstructure peaks associated with cation ordering were observed in KBT or any of the solid solution compounds. This observation is not totally as expected. Continuing on ionic size difference arguments from section 3.3.5.2, no ordering in NBT was seen nor in its analogue $Ag_{0.5}Bi_{0.5}TiO_3$[26], however cation ordering has been observed in $Nd_{0.5}Ag_{0.5}TiO_3$ where there is a 14 % difference in the A-cation sizes. Since there is an even larger difference in KBT (21 %), one might expect ordering to be present. There remains the possibility that the signal-to-noise of the data is not sufficient to determine these peaks.

5.3.3 Octahedral Tilting

For the solid solution member $(Na_{0.8}K_{0.2})_{0.5}Bi_{0.5}TiO_3$ ($x = 0.2$) as temperature is decreased, the prototypic cubic perovskite structure distorts by octahedral tilting. Superstructure reflections associated with tetragonal symmetry are seen to emerge, then diminish, with rhombohedral superstructure reflections appearing with further reductions in temperature. The oxygen octahedral tilting sequence observed in this compound is comparable to that seen in NBT, the only real difference being the phase transition temperatures (section 5.3.1). In section 3.3.5.3, the idea of cation size and tilting was broached. The impetus for octahedral tilting is associated with the need to optimize the anion co-ordination about the A-cation, and since Bi^{3+} and Na^{1+} are relatively small cations (1.31 and 1.32 Å respectively) on the A-site, it was concluded that the presence of octahedral tilts in NBT is expected. Replacing 20 % of Na^{1+} with K^{1+} in $(Na_{0.8}K_{0.2})_{0.5}Bi_{0.5}TiO_3$, increases the average ionic radii by only ≈ 2½ % (Table 5.10) so following similar arguments, tilting in this compound would also not be unexpected. Like NBT, the tetragonal structure of $(Na_{0.8}K_{0.2})_{0.5}Bi_{0.5}TiO_3$ is distorted from cubic by in-phase rotations of the TiO_6 octahedra about the *c*-axis ($a^0a^0c^+$ tilt system), combined with antiparallel displacement of the cations along the polar *c*-axis. The rhombohedral phase of $(Na_{0.8}K_{0.2})_{0.5}Bi_{0.5}TiO_3$ is also analogous to that of NBT, it is described by the polar space group R3c, and characterized by antiphase ($a^-a^-a^-$) rotations of the TiO_6 octahedra about the pseudo-cubic axes combined with parallel A- and B-cations displacements along $[111]_p$. Representations of the $a^0a^0c^+$ and $a^-a^-a^-$ tilt systems are shown in Figures 3.13 (a), (b) and 3.15 respectively. The inclusion in NBT of such a small amount of K^{1+} and the associated average ionic radii increase of around 2½ % has little effect on the absolute structures, but undoubtedly has subtle effects on other parameters such as cation displacements (section 5.3.4) and valency considerations (section 5.3.5).

Turning next to the compound $(Na_{0.6}K_{0.4})_{0.5}Bi_{0.5}TiO_3$ ($x = 0.4$), as temperature is decreased, a phase transition from the ideal cubic structure to tetragonal structure is seen. No tetragonal superstructure reflections are observed; therefore no tilting of the octahedra occurs. With further reductions in temperature, rhombohedral superstructure reflections appear associated with the $a^-a^-a^-$ antiphase tilt system. Compared to NBT, replacing 40 % of Na^{1+} with K^{1+} in $(Na_{0.6}K_{0.4})_{0.5}Bi_{0.5}TiO_3$, increases the average ionic radii by 5 %. This increase leaves the rhombohedral tilt system essentially the same but has the effect of annihilating tetragonal tilts all together. The question of why the tilts in the tetragonal phase are now restricted, but tilts in the rhombohedral phase are still present, must relate

to the initial octahedral distortion levels and will be addressed later in reference to tilt magnitudes across the series.

The next compound in the series is $(Na_{0.5}K_{0.5})_{0.5}Bi_{0.5}TiO_3$ (x = 0.5). As temperature is decreased, a phase transition sequence from cubic to tetragonal to rhombohedral symmetry is observed. No superstructure peaks are seen in any phase. This indicates that a compositionally driven transition between the x = 0.4 and x = 0.5 compounds has transpired. Again, compared to NBT replacing 50 % of Na^{1+} with K^{1+} in $(Na_{0.5}K_{0.5})_{0.5}Bi_{0.5}TiO_3$, increases the average ionic radii by 6.3 %. This increase results in the total suppression of all tilts in the compound.

The phase symmetry and transition progression in $(Na_{0.4}K_{0.6})_{0.5}Bi_{0.5}TiO_3$ (x = 0.6), is analogous with x = 0.5. A high temperature cubic to tetragonal transition followed by a room-temperature rhombohedral phase is observed.

For the end member KBT, we see as temperature in reduced a phase transition from cubic to tetragonal symmetry. As no neutron diffraction data were collected for the $(Na_{0.2}K_{0.8})_{0.5}Bi_{0.5}TiO_3$ (x = 0.8) compound, then similar temperature comparisons cannot be made. However with reference to the tetragonal distortions seen in this compound and KBT (Figures 5.12 and 5.13) it would not be unreasonable to assume a similar phase transition behaviour as KBT is adopted.

Figure 5.16 shows the variation in the experimentally determined room-temperature tilt, ω, angle with composition.

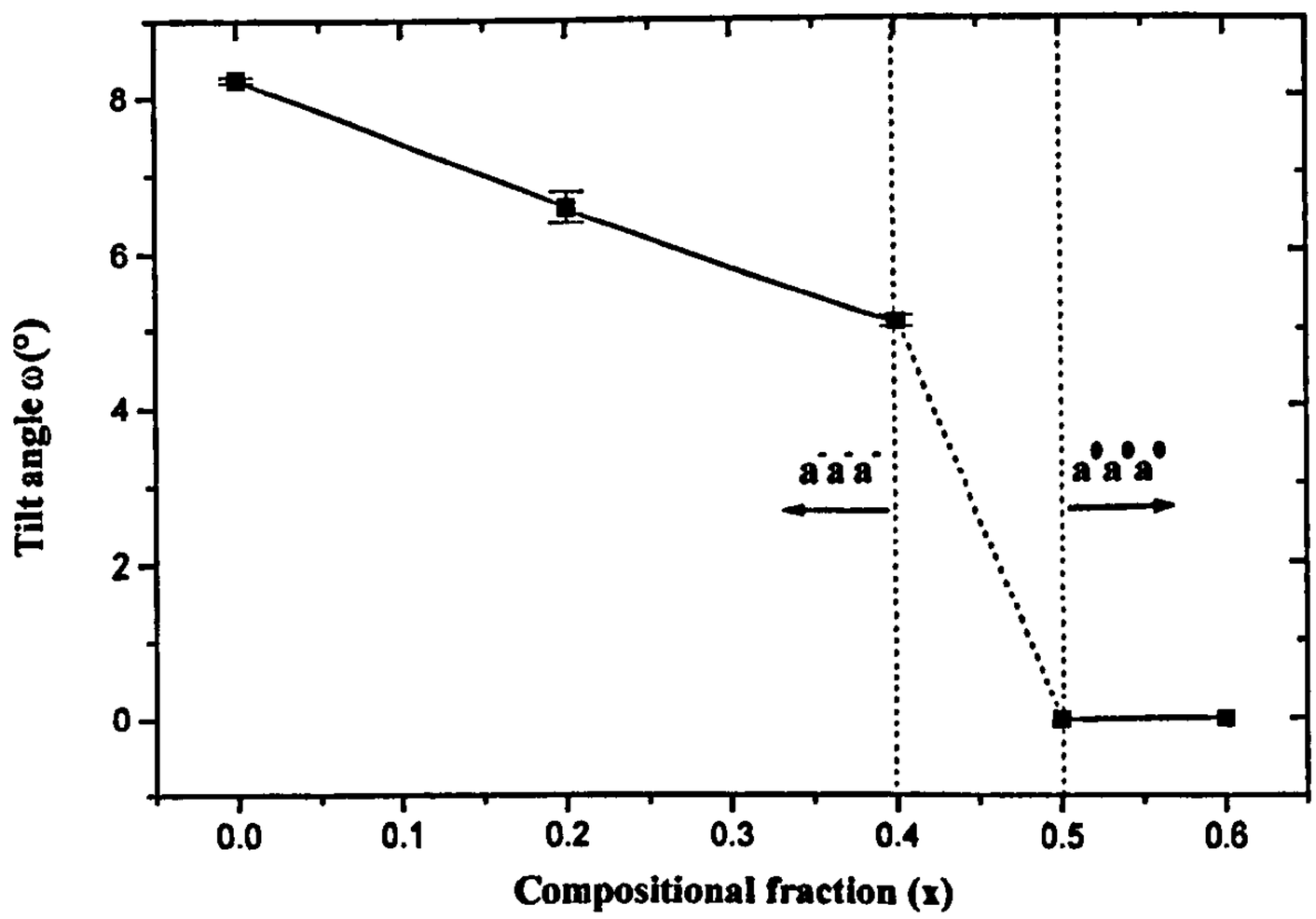

Figure 5.16. The variation of octahedral tilt angle ω(°), with composition (x).

The tilt angle shows a decrease with increasing K^{1+} content until the R3c → R3m phase boundary is reached, representing a transition from the $a^-a^-a^-$ → $a^0a^0a^0$ tilt systems. The tilt magnitudes decrease linearly between $0.0 < x < 0.4$. Between NBT ($x = 0.0$) and $(Na_{0.6}K_{0.4})_{0.5}Bi_{0.5}TiO_3$ ($x = 0.4$) the tilt angle is reduced from 8.24 (4)° to 5.11 (8)°. Over the phase boundary the tilt is reducing from 5.11 (8) ° to zero. It is instructive to re-plot the tilt angle data shown in Figure 5.16 against tolerance factors as shown in Figure 5.17.

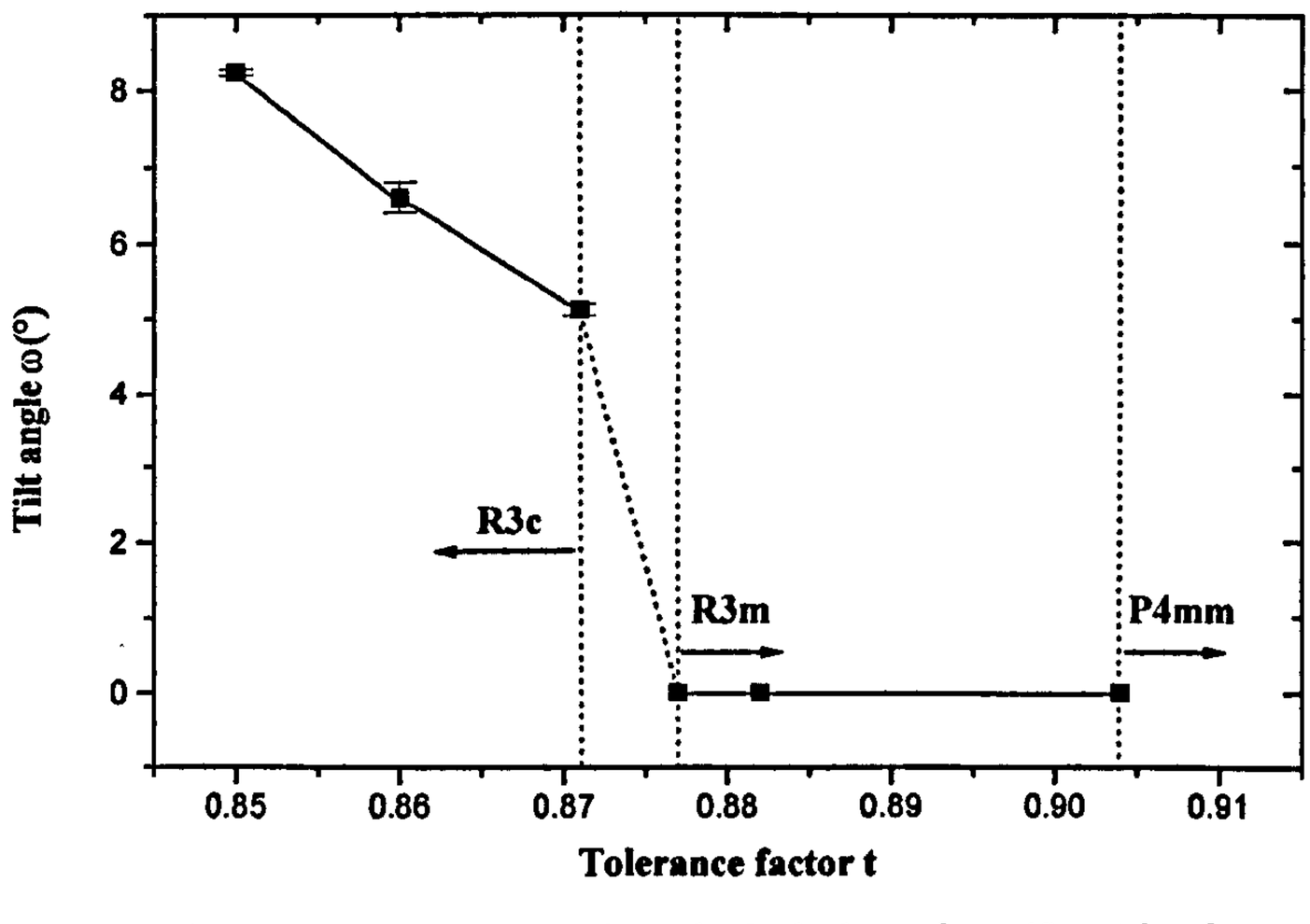

Figure 5.17. The variation of octahedral tilt angle ω (°), with tolerance factor t.

From this figure we can gauge the subtle effects that the changes in the average ionic radii have on the structure in these compounds. The tilt angle depends primarily on packing around the A-cation, and hence the size of A (or the average size of the virtual A-cation in complex perovskites), therefore larger cations (compounds with larger tolerance factors) give rise to smaller tilts. As shown in Figure 5.17 there is an upper limit between 0.871-0.877 were the effect is large enough to terminate tilting altogether. At this point it is no longer energetically favourable to undergo such distortions in order to optimize A-O interactions in these compounds.

The question of why the tilts in the tetragonal phase for $x = 0.4$ are zero but tilts in the rhombohedral phase are still present, can be explained in terms of the initial tilt magnitudes. We have observed that the magnitude of tetragonal tilts are always lower than the tilts in the rhombohedral phases; for example, the largest rhombohedral tilt angle in NBT was found to be 9.5° and the largest tetragonal tilt angle 3.2° (section 3.2.5). Also, we observe that the tilt magnitudes are decreasing as the average A-cation size is increasing (and tolerance factor). So in this compound the size effect is enough to

eliminate the smaller tetragonal tilts but in the rhombohedral structure only reduces the magnitude.

The compounds under study here are A-site substituted complex perovskites i.e. $(A'_xA''_{1-x})BX_3$. It is informative to compare tilting effects as a function of ionic radii in the more common B-site substituted complex perovskites i.e. $A(B'_xB''_{1-x})X_3$ (section 1.1). Much work has been carried out on the perovskite $Pb(Zr_xTi_{1-x})O_3$, PZT, (for its interesting technological properties) and this will be the subject of the comparison. The phase diagram (Figure 5.18) of the system was established by a number of researchers[28-32]. The phase diagram shows there is an almost vertical boundary between a tetragonal ferroelectric phase and a rhombohedral ferroelectric phase. This boundary is approximately temperature independent and is termed the morphotropic phase boundary (MPB)[1]. The transition behaviour shown in PZT as a function of increasing Ti content is similar to the NKBT series (with increasing K content). At room temperature there is a R3c → R3m → P4mm phase transition sequence. Even the transitions as a function of temperature are similar.

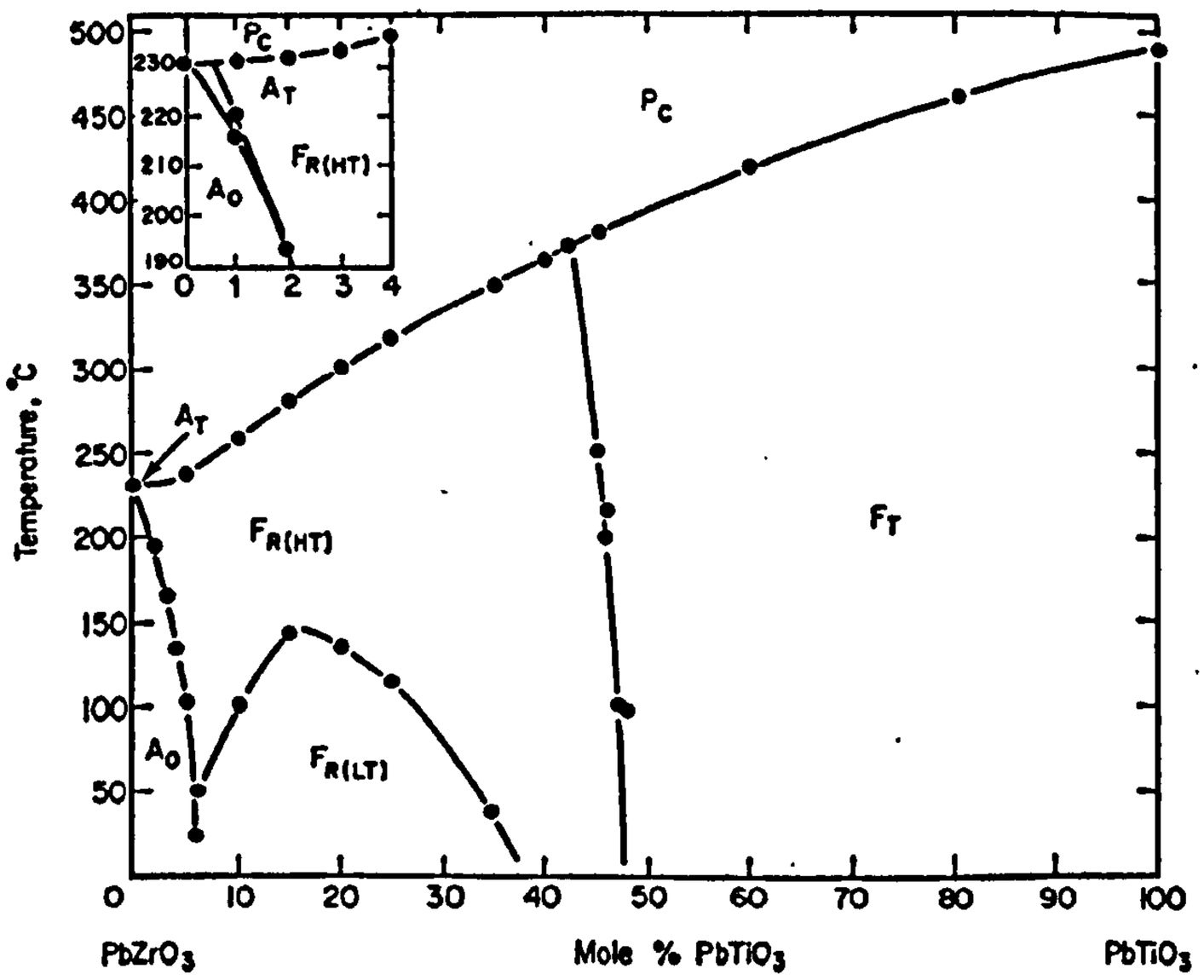

Figure 5.18. *The phase diagram of lead zirconate titanate (PZT) system[1] where; A_O represents an orthorhombic phase, $F_{R(LT)}$ and $F_{R(HT)}$ represent rhombohedral low-temperature (R3c) and high-temperature (R3m) forms, F_T represents a tetragonal (P4mm) and P_C a high-temperature cubic (Pm-3m) form. The MPB is located around $x \approx 0.48$.*

In both of these solid solutions an ionic radii mismatch is present. Looking at the ionic radii of the B-site cations in PZT we see that Zr^{4+} is around 11 % bigger than Ti^{4+} in

comparison K^{1+} is around 25 % bigger than $<Na^{1+}/Bi^{3+}>$. Within the literature[33-34] we see that increasing the Ti content (i.e. replacing a larger cation with a smaller cation on the B-site) has the effect of reducing the tilt magnitude until the R3c → R3m phase boundary is reached. In NKBT replacing a smaller cation with a larger cation on the A-site has the same effect. From the point of view of cations within the structure trying to attain their preferred co-ordination these effects are analogous and demonstrates the dramatic effect varying the composition on complex perovskites can have. The complex perovskites PZT and NKBT have many similarities and potentially a MPB may exist in NKBT, although this remains to be established.

5.3.4 Cation Displacements

With the exception of the high-temperature paraelectric cubic, $Pm\bar{3}m$ phase all other phases across the solid solution range namely R3c, R3m P4bm and P4mm are non-centrosymmetric and permit cation displacements.

The tetragonal P4bm phase of $(Na_{0.8}K_{0.2})_{0.5}Bi_{0.5}TiO_3$ was also observed in NBT. As discussed (section 3.3.5.3), from a geometrical point of view there is no obvious incentive for cation displacement in a tilt system of this nature. However the verdict was reached that the displacements resulted from the need to accommodate the stereo-active lone pair on the Bi^{3+} ions. Na/K/Bi-cation, *s*, and Ti-cation displacements, *t*, (calculated in Rietveld refinements from the centre of their co-ordination polyhedra) were found (like NBT) to be in opposite directions, along the polar *c*-axis. The tetragonal phases of the remaining solid solution range ($0.4 < x < 1.0$) showed no octahedral tilting. Rietveld refinements suggested the P4mm space group. The displacements of the A- (*s*) and B-cations (*t*), along the polar [001] axes show an overall decrease with increasing temperature. This proceeded until the phase transition into the cubic perovskite structure was reached (as only between 2 diffraction data profiles were taken in the tetragonal phases in each compound, the displacement magnitudes as a function of temperature have not been plotted).

In the rhombohedral structures of the solid solution series A- and B-cation displacements are parallel to each other, along $[111]_p$. Figures 5.19 (a) and (b) show the A- and B-cation refined fractional displacements along c_H plotted as a function of temperature. The overall displacements of the cations calculated in the Rietveld refinements are from the centres of their co-ordination polyhedra. With reference to A-

cation displacements (Figure 5.19 (a)), within the errors the overall trend is a decrease of displacement with increasing temperature. This trend is to be expected and is brought about by the contraction of the c_H axes and elongation of the a_H axes with increasing temperature (consequently the *c/a* ratio decreases giving rise to decreases in cation displacements relative to the oxygen octahedra). Looking at the B-cation displacements (Figure 5.18 (b)) within experimental errors the displacements decrease with increasing temperature, although for $x = 0.2$ and $x = 0.4$ a slight increase between $393 < T < 493$ K is observed.

Figure 5.19 (c) shows the variation of A- and B-cations refined displacements as a function of compositional fraction across the solid solution series (for the rhombohedral phase). The trend for *s* and *t* are very similar with only the initial magnitudes being different. The displacement for both cations decreases linearly between $0.0 < x < 0.4$ (corresponding to the R3c rhombohedral phases) and then levels with a much lower rate of change (corresponding to the R3m phases). The plot indicates the effect that increasing the average ionic radii has on the displacements. It can be observed that as the average ionic radii is increased the initial displacements diminish (relatively) linearly until the R3c → R3m phase boundary is reached whereupon its influence on displacement magnitudes appears much less. Off-centre displacements result from cations trying to fulfil their bonding requirements and so act as stabilising (energy minimisation) mechanisms. Larger A-cations will adopt larger AO_{12} polyhedra, which have the energetic advantage of reducing the oxygen-ion repulsive energy. As the average ionic radii increases within the AO_{12} polyhedron its co-ordination is better matched thereby reducing the need for larger displacements. This can be illustrated with reference to the ternary iron oxide perovskites for example. Amongst these compounds $LuFeO_3$ has the largest displacements (0.430 Å) and $LaFeO_3$ the smallest (0.18843 Å). This directly reflects the fact that Lu^{3+} has the smallest ionic radii (0.861 Å)[25] amongst these compounds and La^{3+} the highest (1.031 Å)[25], showing that smaller ions require larger displacements in order to optimise their co-ordination by oxygen ions. The similarity of the *s* and *t* displacement trends is not unexpected, as the tilting and *s* decrease with increasing ionic size, there is a reduction in A-B repulsion forces and hence *t* will also diminish. As a function of compositional fraction the displacements found in the Rietveld refinements (Figure 5.19 (c)) show a similar trend to ω (Figure 5.16).

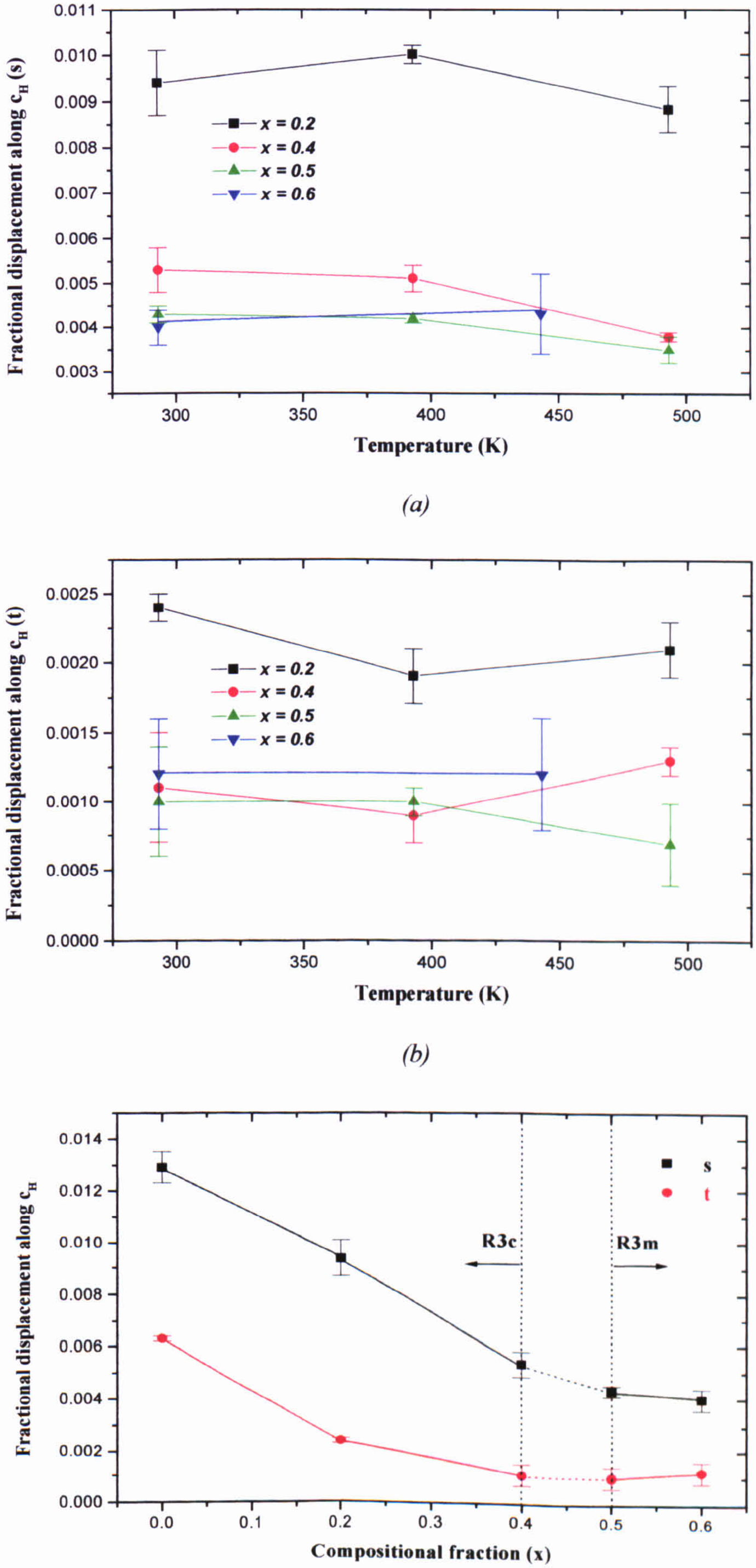

Figure 5.19. *The variation of (a) Na/K/Bi, (b) Ti cation shifts (expressed in fractions along c_H with temperature in the solid solution $(Na_{1-x}K_{0x})_{0.5}Bi_{0.5}TiO_3$. (c) The variation of cation shifts (expressed in fraction along c_H) as a function of compositional fraction (x).*

5.3.5 Valency Calculations

As previously pointed out (section 3.3.5.4) a valency deficiency gives rise to a displacement of certain cations. The cation will move off-centre in order to achieve a valency closer to its ideal value. Bond valence calculations (Table 5.12) for the room-temperature rhombohedral phases across the NKBT series were performed using the program VaList.

Composition (x) $(Na_{1-x}K_x)_{0.5}Bi_{0.5}TiO_3$	Valency Deficiency (%) (Rhombohedral phase)				Average A-cation valency deficiency $< V_A >$ (%)
	Na^{1+}	K^{1+}	Bi^{3+}	Ti^{4+}	
0.0	6	-	22	2	14.0
0.2	2	6	28	3	12.0
0.4	5	3	30	3	12.6
0.5	11	3	34	3	16.0
0.6	11	3	34	4	16.0
1.0	12	3	33	3	16.0

Table 5.12. Calculated valency deficiencies (%) of cations in the rhombohedral phases across the $(Na_{1-x}K_x)_{0.5}Bi_{0.5}TiO_3$ series. The A-cation valences for the NKBT compositions are contained in 3 columns, this reflects the statistical occupation of A-sites by Na^{1+}, K^{1+} and Bi^{3+} ions. The final column lists the averaged percentage valency deficiency $< V_A >$ of the A-cations.

The overall trends observed in the NKBT solid solutions are the same as that seen for NBT. Looking at the compound $x = 0.2$, for example we see that the values for Na^{1+}, K^{1+} and Ti^{4+} show deficiencies of only 2, 6 and 3 % respectively, from their ideal values. However, the bond valence sum calculated for Bi^{3+} shows a 28 % deficiency. A similar conclusion therefore must be reached that even though Bi^{3+} moves off centre in order to satisfy its own stereo-chemical preferences it seems that it is unable to achieve a perfect match to its valency. Moving across the NKBT series we observe an increase in the valency deficiencies for Na^{1+} and Bi^{3+}. However the valency deficiency of K^{1+} shows an initial decrease then levels at 3 %. As the concentration of the larger K^{1+} cation increase its valency is better matched, however it becomes more difficult to achieve a valency match for the other A-cations. As an average structure the K^{1+} cations seem to have a dominating effect, this is reflected by the fact that cation displacements are decreasing across the series as K^{1+} co-ordination is better matched. The conclusion that across the

series an average structure becomes less and less suited to the shared-site cations is therefore reached.

In conclusion a systematic study of structural trends as a function of the average radii of Na/K/Bi and temperature has been carried out in the NKBT system. For the first time the structural variation and space group assignments have been reported. General trends of cation displacements and various deviations of the octahedral network from the ideal cubic perovskite model have been established.

References

[1] Jaffe, B., Cook, W. R. & Jaffe, H. (1971). *Piezoelectric Ceramics (London: Academic Press)*.

[2] Hewat, A. W. (1975). Nucl. Inst. Methods. 127, 36170.

[3] Hewat, A. W. (1986). Mat. Sci. Forum. 9, 69.

[4] CRYSTALLOGRAPHICA v1.50a (1995-98). Oxford Cryosystems, Oxon.

[5] Battle, P. D., Catlow, C. R. A., Drennan, J. & Murray, A. D. (1983). Journal of Physics C 16, 561.

[6] Gatehouse, B. M & Lloyd D. J. (1973). Journal of the Chemical Society. Dalton Transactions, Inorganic Chemistry, 70.

[7] Swainson, I. P., Dove, M. T. & Harris, M. J. (1995). Journal of Physics: Condensed Matter 7, 4395.

[8] Horn, M., Schwerdtfeger, C. F. & Meagher, E. P. (1970). Journal of the American Ceramic Society 53, 124-126.

[9] Inorganic Crystal Structure Database (1990).

[10] Zvirgzds, J. A., Kapostins, P. P., Zvirgzde J. V. & Kruzina, T. V. (1982). Ferroelectrics 40, 75.

[11] Glazer, A. M. & Mabud, S. A. (1977). Acta Cryst. B34, 1065.

[12] Megaw, H. D. & Darlington, C. N. (1975). Acta Cryst. A31, 161.

[13] Hong, K. S. & Park, S. E. (1996). J. Appl. Phys. 79, 388.

[14] Park, S. E. & Hong, K. S. (1996). J. Appl. Phys. 79, 383.

[15] Isupov, V. A, Strlets, P. L., Serova, I. A., Yataenko, N. D. & Shirobokikh, T. M. (1964). Sov. Phys. Solid State 6, 615.

[16] Sakata, K., Takenaka, T. & Naitou, Y. (1992). Ferroelectrics 131, 219.

[17] Elkechai, O., Marchet, P., Thomas, P., Manier, M. & Mercurio, J-P. (1997). J. Mater. Chem. 7, 91.

[18] Park, S. E. & Hong, K. S. (1997). J. Mater. Res. 12, 2152.

[19] Sakata, K. & Masuda, Y. (1974). Ferroelectrics 7, 347.

[20] Emelyanov, S. M., Raevskii, I. P. & Prokopalo, O. I. (1983). Sov. Phys. Solid State 25, 889.

[21] Pronin, I., Parfenova, N. N., Zaitseva, N. V. & Smolenskii, G. A. (1982). Sov. Phys. Solis State 24, 1060.

[22] Elkechai, O., Mainer, M. & Mercurio, J. P. (1996). Phys. Status Solidi A 157, 499.

[23] Yamada, Y., Akutsu, T., Asada, H., Nozawa, K., Hachachiga, S., Kurosaki, T., Fujiki, H., Hozumi, K., Kawamura, T., Amakawa, T., Hirota, K. & Ikeda, T. (1995). Japan. J. Appl. Phys. 34, 5462.

[24] Gadzhiev, M. S., Abiev, A. K., Isupov, V. A. & Ismailzade, I. G. (1985). Sov. Phys. Solid State 27 (8), 1502.

[25] Shannon, R. D. (1976). Acta Cryst. A32, 751.

[26] Park, J. H., Woodward, P. M. & Parise, J. B. (1998). Chem. Mater. 10, 3092.

[27] Park, J. H., Woodward, P. M., Parise, J. B., Reeder, R. J., Lubomirsky, I. & Stafsudd, O. (1999). Chem. Mater. 11, 177.

[28] Shirane, G. & Takeda, A. (1952). J. Phys. Soc. Japan 1, 5.

[29] Shirane, G. & Suzuki K. (1952). J. Phys. Soc. Japan 7, 333.

[30] Shirane, G. Suzuki, K. & Takeda, A. (1952). J. Phys. Soc. Japan 1, 12.

[31] Sawaguchi, E. (1953). J. Phys. Soc. Japan 8, 615.

[32] Barnett, H. M. (1962). J. Appl. Phys. 33, 1606.

[33] Glazer, A. M. & Mabud, S. A. (1978). Acta Cryst. B34, 1060.

[34] Corker, D. L. Glazer, A. M. Whatmore, R. W., Stallard, A. & Fauth, F. (1998). J. Phys.: Condens. Matter. 10, 6251.

Chapter 6

Optical and Raman Measurements

6.1 Introduction

The crystal structures and phase transitions in NBT, induced by variations in temperature, pressure and composition have been studied using diffraction techniques outlined in chapters 3, 4 and 5 respectively. In this chapter alternative experimental techniques are used to complement these studies. Room temperature second harmonic generation measurements as a function of particle size for the NKBT solid solution range and as a function of temperature for NBT are reported. Birefringence imaging of phase transitions for a number of compounds is also reported, as well as a substitutional and pressure study of NBT using Raman spectroscopy. The principal objective of this chapter is through the use of alternative techniques to, ascertain supplementary information on these compounds and to obtain further evidence in support of the conclusions previously reached.

6.2 Linear and Non-linear Optics

Materials may be grouped, optically into two main categories, isotropic and anisotropic (birefringent) depending on their optical responses. When an electric field, E, is applied to an isotropic material, an induced polarization, P, parallel to the applied electric field occurs. This is related by a scale factor, which is independent of the direction of the field:

$$P = \varepsilon_o \chi_e E \tag{6.01}$$

In anisotropic materials however, the induced polarization is dependent on both the magnitude and direction of the applied field.

$$P_i = \varepsilon_o \chi_{ij} E_j \tag{6.02}$$

where χ_{ij} is the dielectric susceptibility 2nd-rank tensor. The dielectric response of the crystal can also be described by using the electric permittivity tensor ε_{ij}, defined by:

$$D_i = \varepsilon_{ij} E_i \tag{6.03}$$

where D is the dielectric displacement. When this is substituted into equation 6.04,

$$D = \varepsilon_o E + P \tag{6.04}$$

the dielectric constants of the material are given:

$$\varepsilon_{ij} = \varepsilon_o \left(1 + \chi_{ij}\right) \tag{6.05}$$

A consequence of dielectric anisotropy is birefringence. The phase velocity of the propagating beam is dependent on the direction of polarization of the E-field. In an isotropic medium the induced polarization is independent of the field direction, χ_e and hence ε_o are independent, and since the phase velocity $c = \sqrt{\mu\varepsilon}$ it therefore means that it is also independent of the direction. In an anisotropic material however, the phase velocity depends on the direction of polarization. If a wave propagates along z for example, it is linearly polarised along x and y, but the anisotropy of the material means that as the wave moves through the medium the x and y components become out of phase resulting in the wave being elliptically polarised. This variation in polarization results in the medium having different refractive indices along each axis. The optical refractive index of an anisotropic material is given by:

$$\eta_{ij} = \varepsilon_{ij}^{1/2} \tag{6.06}$$

The variation of the refractive index in the different directions can be represented by an ellipsoid called the optical indicatrix, represented by:

$$\frac{X_1^2}{n_1^2} + \frac{X_2^2}{n_2^2} + \frac{X_3^2}{n_3^2} = 1 \tag{6.07}$$

where X_i represent the principal axes of the dielectric constant tensor and n_i are the refractive indices for the respective axes[1].

The electric polarization resulting from the propagation of electromagnetic radiation in a linear medium is proportional to the electric field. In non-centrosymmetric materials however, the induced polarization is not directly proportional to the field. As well as the linear response a non-linear effect may be present, which is proportional to higher powers of the optical field amplitude, E_j. The non-linear response is much smaller in magnitude than the linear effect and in most cases is negligible in comparison.

However, lasers are light sources of sufficient intensity that the non-linear characteristics of these materials can be exploited.

In order to include non-linear effects, the polarization described by equation 6.02, is expanded as a Taylor series in E to obtain the following expression:

$$P_i = P_o + \varepsilon_o \chi_{ij}^{(1)} E_j + 2\varepsilon_o \chi_{ijk}^{2} E_j E_k + 4\varepsilon_o \chi_{ijkl}^{3} E_j E_k E_l + \ldots \qquad (6.08)$$

where P_o is the static polarization of the sample, $\chi^{(1)}$ is the linear susceptibility tensor, $\chi^{(2)}$ and $\chi^{(3)}$ are the second and third non-linear susceptibility tensors respectively and ε_o the vacuum permittivity. As can be seen from 6.08, the second-order term causes the polarization to be dependent on E^2. It is the crystal symmetry that dictates the form of the tensors χ_{ijk} and χ_{ijkl}. In particular, symmetry conditions dictate that all the coefficients of χ_{ijk} must be zero for centrosymmetric crystals. For a material to exhibit a non-linear optical response it must therefore be described by one of the 21 non-centrosymmetric point groups. Only the second order non-linear optical effect of second harmonic generation (SHG) will be considered here. SHG is characterised by the term $2\chi_{ijk}^{(2)} E_j E_k$ in equation 6.08. If a non-linear optical crystal is illuminated with light at two frequencies ω_1 and ω_2, then $\chi_{ijk}^{(2)}$ will give rise to polarizations at $\omega_3 = \omega_1 + \omega_2$ and $\omega_4 = \omega_1 - \omega_2$. If we allow $\omega_1 = \omega_2 = \omega$, the frequency generated is 2ω, twice the fundamental frequency. High-laser intensities are not always necessary for the observation of non-linear optical effects. Provided that the assembly of dipoles oscillate coherently, (with a definite phase relationship), the field that they radiate individually can in certain circumstances add together constructively to produce a much larger total intensity. This process is termed phase-matching.

Phase-matching facilitates the energy transfer from fundamental to the harmonic wave. For this transfer to occur the waves must travel through the crystal in phase. The fundamental wave has a phase velocity of ω/k_ω, where ω is the frequency and k_ω is the wave vector, whilst the second harmonic wave has a phase velocity of $2\omega/k_{2\omega}$. The phase-matching condition $\Delta k = 2k_\omega - k_{2\omega} = 0$ occurs when these two-phase velocities are equal. The fundamental wave and second harmonic wave at 2ω are then in phase synchronism. If however, $\Delta k \neq 0$ then the fundamental and harmonic wave become out

of phase by 180° after a distance $L_c = |\pi/\Delta k|$, known as the coherence length. In general due to dispersion effects $\Delta k \neq 0$, and therefore $I_{2\omega}$ increases in the first distance L_c, then decreases to zero over the next L_c, while the intensity is transferred back to I_ω and so on. In the case when the process is phase-matched ($\Delta k = 0$, $L_c \rightarrow \infty$), $I_{2\omega}$ and the conversion efficiency is maximised.

6.2.1 Second Harmonic Generation

In the following sections, room temperature SHG as a function of particle sizes is described for the NKBT solid solution range. SHG measurements as a function of temperature for NBT are also described. The measurement provides a sensitive test for non-centrosymmetry, demonstrating whether the crystal symmetry contains a centre of inversion or not and so can be used to resolve certain space group ambiguities. Using the experimental set-up and apparatus similar to that described by Kurtz and Perry[2], the SHG signals for the materials were detected and measured.

6.2.1.1 Kurtz and Perry Technique

Depending on the sample, the growth of large, optical-quality crystals required for accurate optical experiments, can be difficult. In order to allow the easier study of new materials the Kurtz and Perry technique has been devised, that enables SHG measurements to be made from polycrystalline samples. Using this method it is possible to find the optical response of a material and by heating the sample, phase transitions may be distinguished through signal changes. A schematic representation of the experimental set-up used for SHG measurements, based on the Kurtz and Perry technique, is shown in Figure 6.01. Powdered samples mounted within glass cells (section 6.2.1.2) were placed in an intense 100mJ, 100ms pulse beam (attenuated using a neutral density filter) from a Q-switched Nd:YAG laser (λ = 1064 nm). In order to remove traces of the fundamental beam, the scattered radiation was filtered using a 25.4 mm diameter 8.6 nm FWHM bandwidth interference filter and a 50.8 × 50.8 × 2 mm^3 (Schott BG20) green filter. The second harmonic signal (λ = 532 nm) was then detected using a photomultiplier. This was then displayed as a signal verses time pattern on a M221 100MHz digital oscilloscope using SCOPE Software[3]. A beam splitter and photodiode were employed to monitor the fundamental beam, so any corrections could be

made for variations in laser output. The entire experimental set-up was enclosed in a lightproof box.

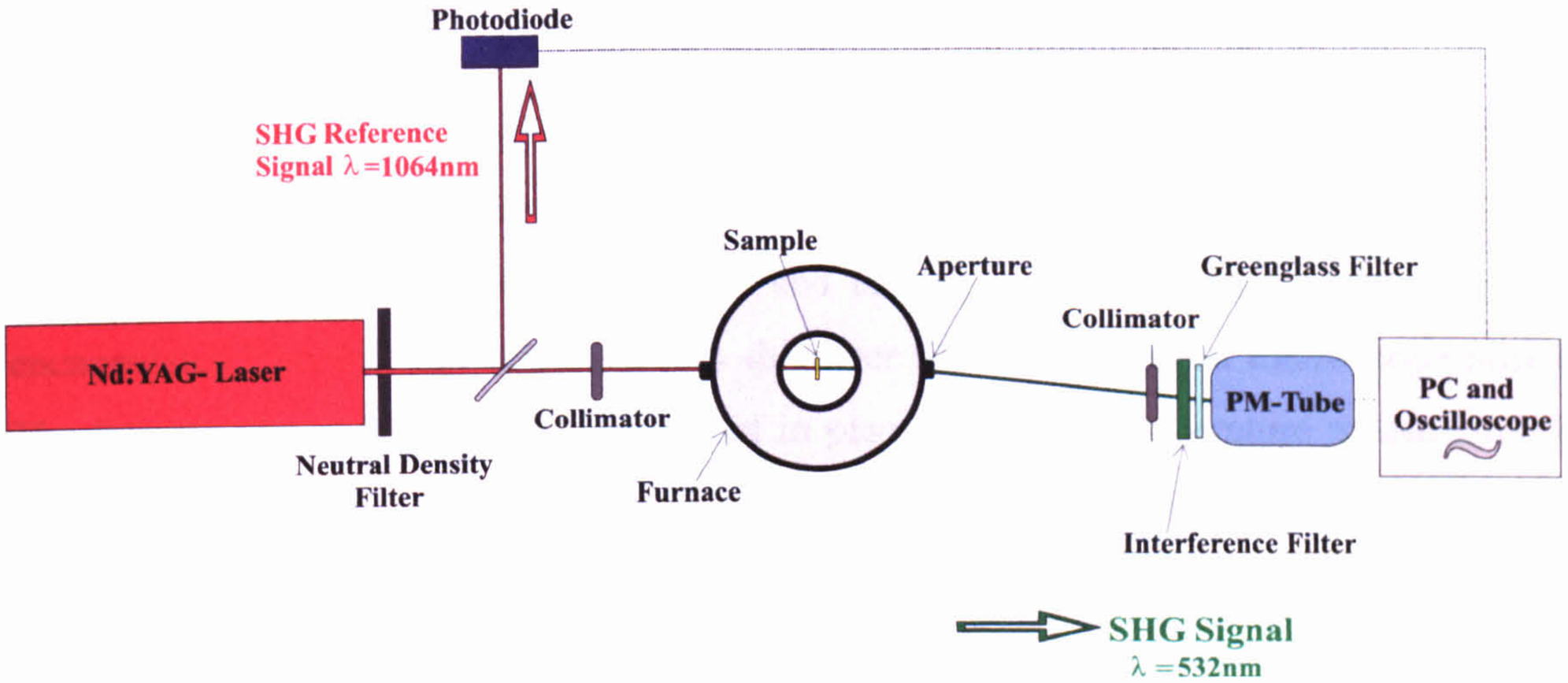

Figure 6.01. *Schematic representation of the experimental set-up for powder SHG measurement as a function of temperature.*

Before the sample materials were tested, a check was performed with a standard sample, crystalline quartz (α-SiO_2). The sample produced a distinct harmonic signal as shown in Figure 6.02 (a). Once a positive signal was established, a null check was performed. The centrosymmetric compound Al_2O_3 was investigated for this purpose. Figure 6.02 (b) shows the null signal given by Al_2O_3, taken at the oscilloscopes highest sensitivity.

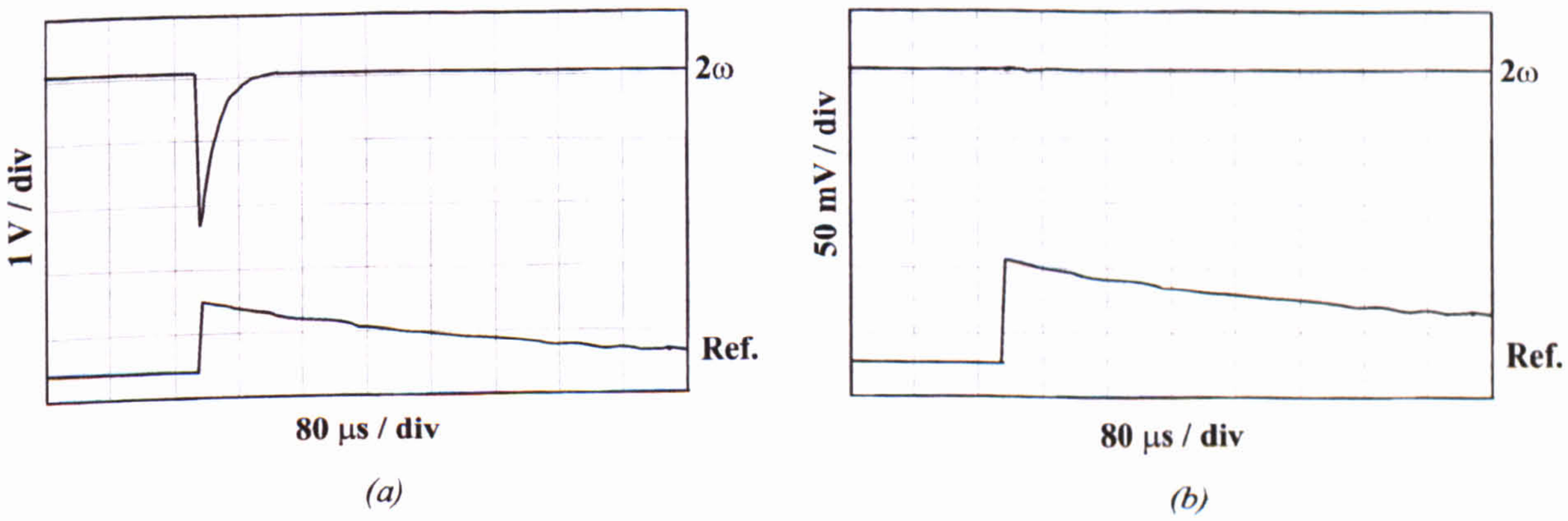

Figure 6.02. *Oscilloscope measurement of the SHG signal for (a) quartz sample (b) Al_2O_3.*

Initial measurements were carried out at room temperature for the NKBT series. NBT was also investigated as a function of increasing temperature over a range between 293-993 K.

6.2.1.2 Sample Preparation and Environment

For room-temperature studies of $(Na_{1-x}K_x)_{0.5}Bi_{0.5}TiO_3$ (x = 0.2, 0.4, 0.5, 0.6, 0.8, 1.0), polycrystalline samples were sieved to give a known particle size range and encapsulated into 0.5 mm thick, 16 mm diameter rings mounted on microscope slides. The furnace shown in Figure 6.01 was not in place for room-temperature measurements of the NKBT series. NBT samples were encapsulated in glass cells suitable for high-temperature studies. These cells were made from two 6 mm diameter, (0.08-0.12 mm thick) glass cover slips separated by ≈ 0.3 mm. Typically crystalline powder sample masses of approximately 15 mg were used. A schematic of the NBT cell design on the alumina mounting rod is shown in Figure 6.03. Due to the high sensitivity of the technique, cleanliness during sample preparation was extremely important, as small amounts of dust or trace amounts of contamination (of truly non-centrosymmetric materials) can result in misleading signals.

For the study of phase transitions in NBT, the samples were heated in a nitrogen-cooled cylindrical (5 cm diameter, 5cm height) furnace capable of heating between 293-1293 K. The furnace was lowered over the aligned sample, which was mounted above an alumina rod. The furnace apertures lay normal to the sample orientation so the optical alignment was not disturbed. The separation between the furnace and sample mounting isolated the sample from any heating coil vibrations within the furnace. The furnace consisted of a pyrophilite core, with resistance thermocouple wire wound around the outside. These wires were insulated by an 1 cm thick alumina wool layer and a copper tube was wound around the assembly to provide nitrogen cooling. This tubing itself was encased in a copper jacket. Brass baffles are fitted onto the furnace base and beam windows in order to limit airflow and force the air to enter from the base, producing a slow stable flow. The pyrophilite top stops thermal buffeting of the sample by preventing the air rising past the hot walls and falling on the sample. The furnace design is shown in Figure 6.03.

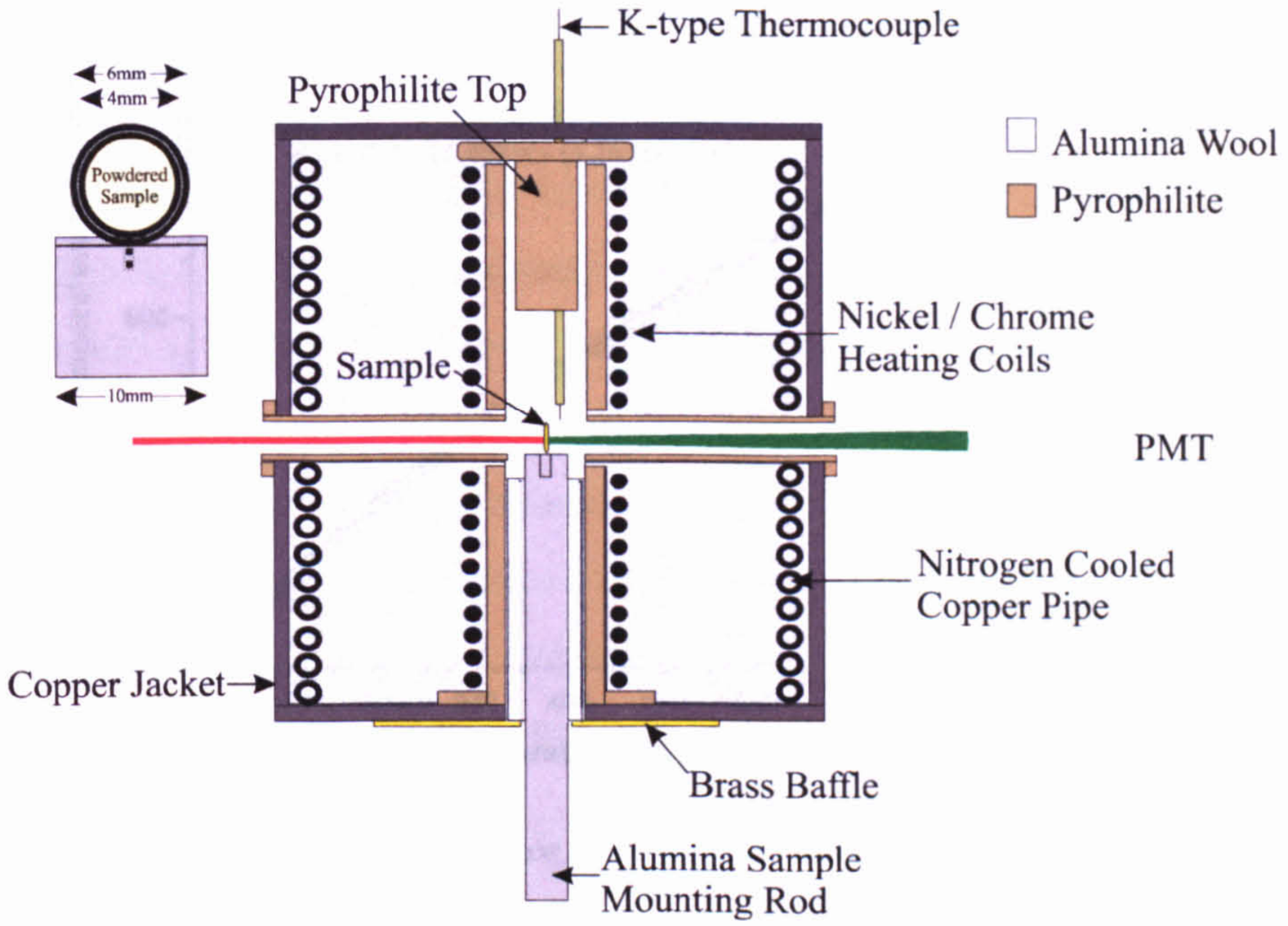

Figure 6.03. Furnace design and glass sample cell used in powder SHG measurements.

6.2.1.3 Temperature Calibration of Furnace

The furnace should provide a uniform stable temperature environment for the sample. However, calibration of the absolute temperature was needed for accurate determination of the phase transition temperatures. The furnace temperature was measured by a K-type thermocouple mounted through the pyrophilite top. This guaranteed repeatable positioning between runs. The thermocouple was situated approximately 3 mm away from the sample within the flow of hot air (Figure 6.03). This ensured a fast response of the thermocouple, but measured a higher temperature than the sample actually experiences. To correct for temperature variations a K-type thermocouple was placed in the sample position on *blank* calibration runs. The temperature measured by a Comark 6400 (calibrated digital thermometer), was used to determine the actual temperature profile experienced by the sample. Figure 6.04, shows the calibration curve obtained and the fitted polynomial curve to the data.

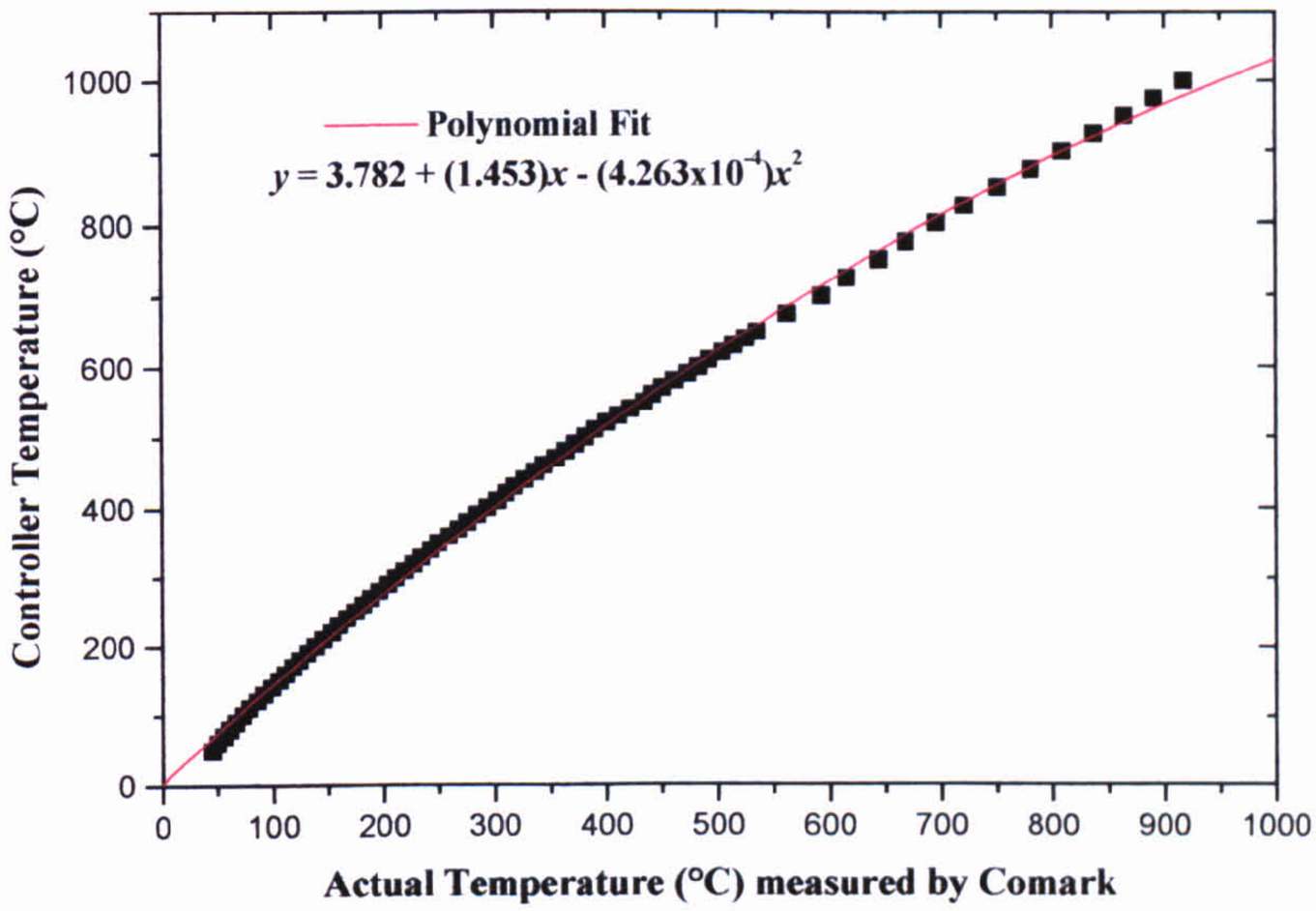

Figure 6.04. *Calibration curve of furnace used in SHG measurements, the red line indicates the polynomial fit to the data.*

6.2.2 Discussion

Room temperature tests gave a clearly positive SHG response on all samples. It was found that a degree of laser damage was caused in all the samples investigated. This was indicated by the very slight graying of the surface layer of powder where the laser beam was incident. This damage did not affect the signal. The room-temperature normalised particle-size dependencies of second-harmonic intensity for $(Na_{1-x}K_x)_{0.5}Bi_{0.5}TiO_3$ (for x = 0.2, 0.4, 0.5, 0.6, 0.8, 1.0) and NBT are shown in Figures 6.05 (a)-(f) and 6.06 (a) respectively. Signals have been corrected for variations in fundamental power input and normalised to the highest intensity of signal. The SHG signal varies characteristically with the dimensions of the particles. From the graphs, the non-phase-matched[2,4] nature of these powders is clearly evident. The room temperature SHG evidence together with the refinements of the NKBT structures (section 5.2.3) strongly suggests that the correct polar space groups R3c, R3m and P4mm across the series at room temperature have been assigned.

Figure 6.06 (b) shows the SHG signal as a function of temperature for NBT. The dotted line marked by R represents the upper limit where the pure rhombohedral phase exists obtained from neutron diffraction data. Lines marked by T and C represent the beginning of the pure tetragonal and cubic phases respectively. The plot indicates that changes occur in the regions associated with phase transition regions obtained from neutron data. The cubic phase indicated by zero output appears at 893 K, which is higher

than the temperature determined from neutron diffraction by 80 K. Signal intensity variations show a gradual decrease from room temperature to around 500 K. Within errors the intensity stays essentially level between 500-575 K, then shows a further decrease until 650 K. The signal intensity increases slightly to a maximum at 725 K and decreases to zero at 893 K. The signal intensity variations suggest transitions are taking place. As the cubic phase transition occurs at a higher temperature in comparison to the neutron data results, the direct comparison of the onset of phases shown in Figure 6.08 as indicated by the dotted lines may also show some shift. The fact that there is a clear signal over the tetragonal phase region supports the proposition that the non-centrosymmetric space group (P4bm) assignment is accurate (section 3.3.4).

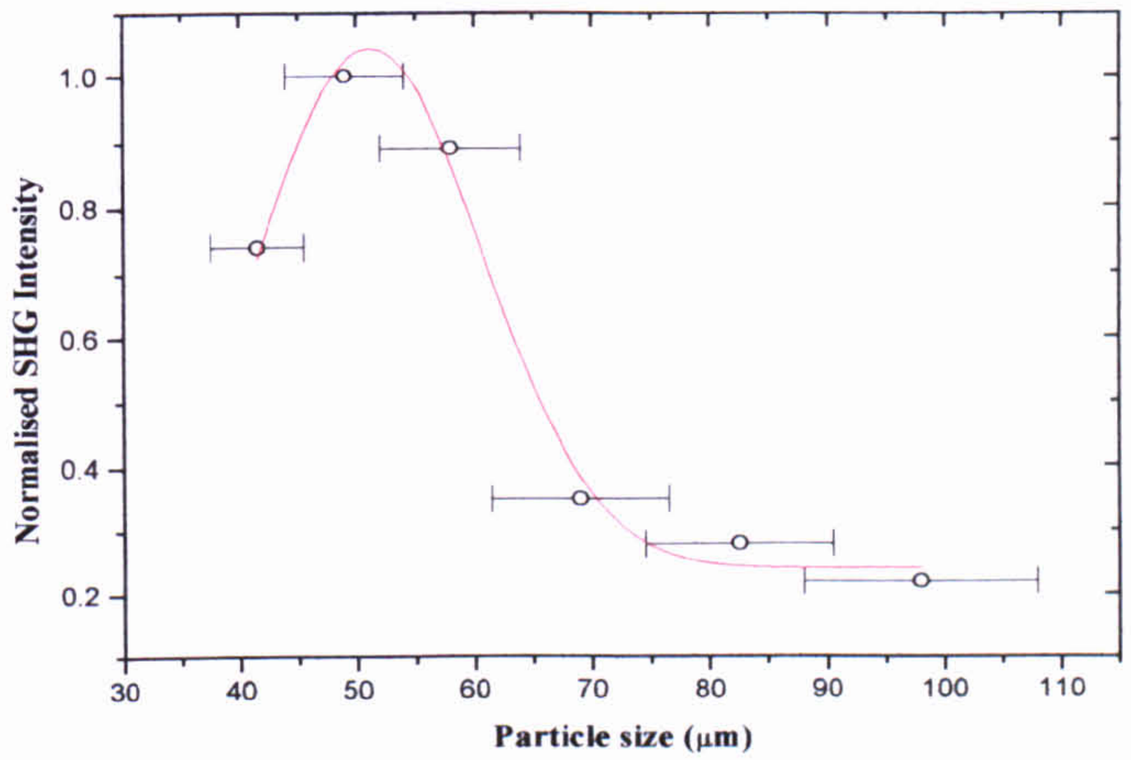

(a)

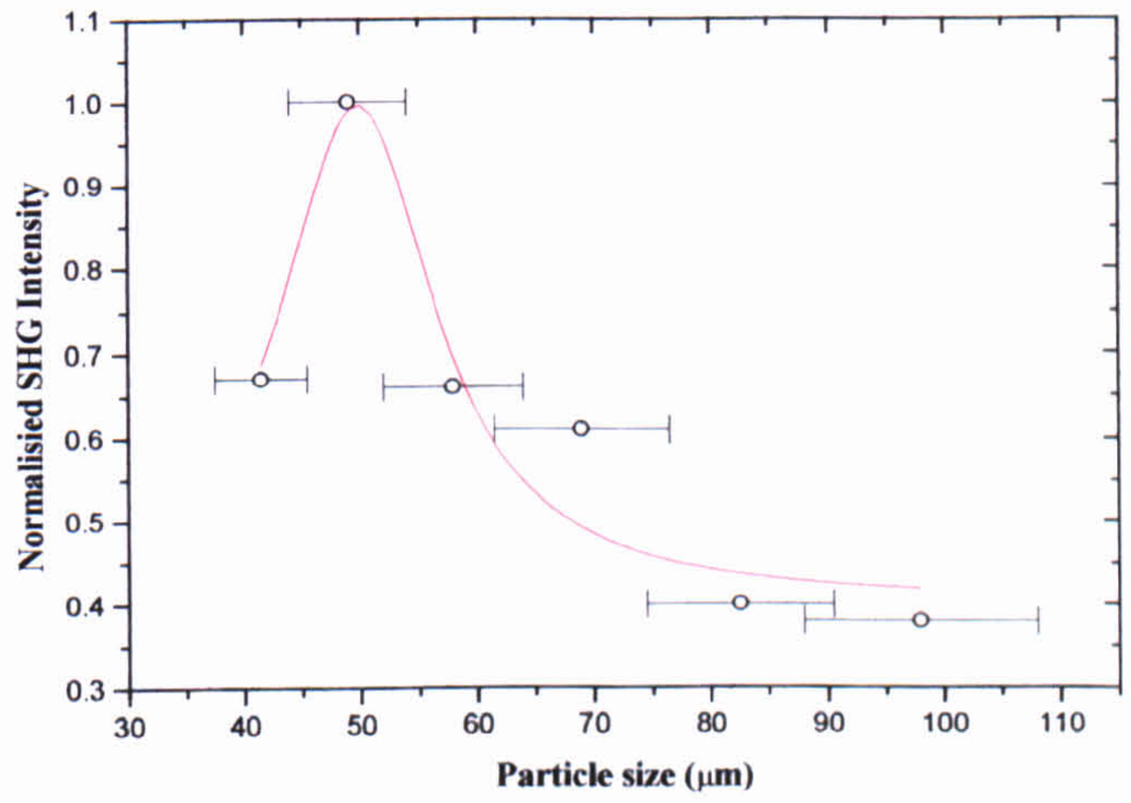

(b)

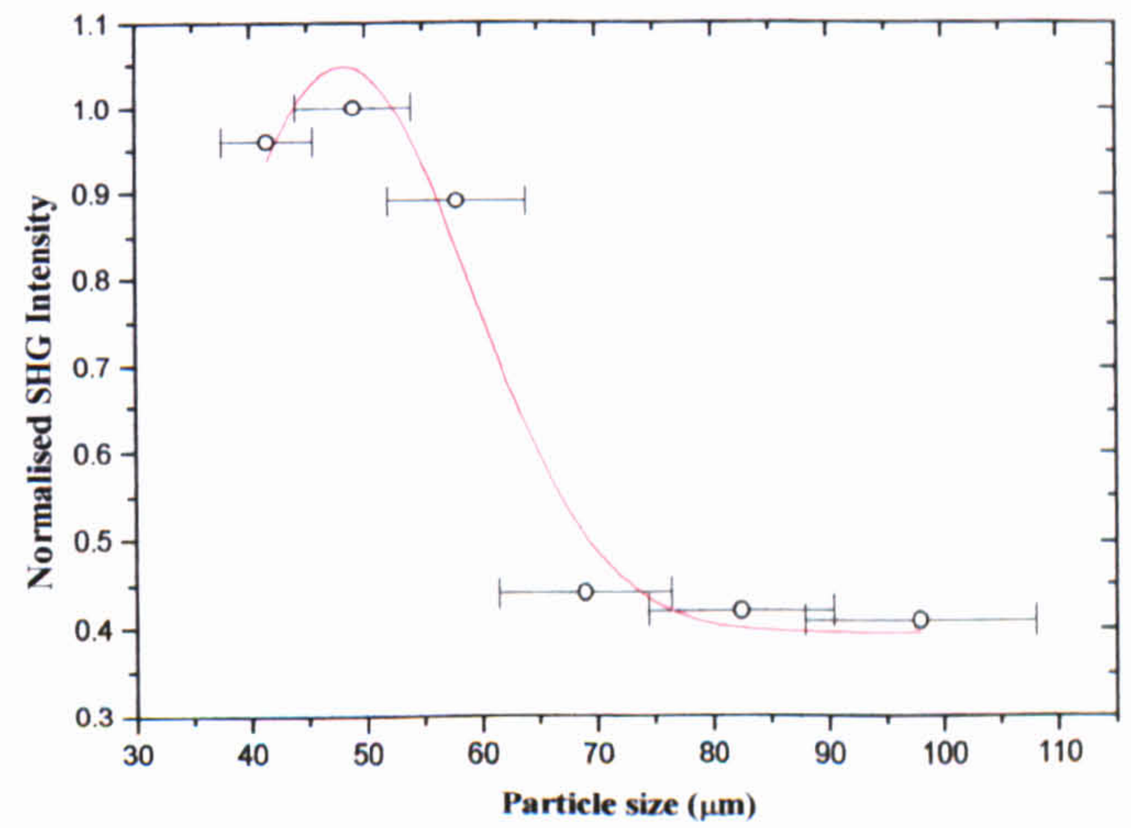

(c)

Figure 6.05. ***Normalised particle size dependence of second harmonic intensity. Non-phased matched (a) $(Na_{0.8}K_{0.2})_{0.5}Bi_{0.5}TiO_3$ ($x = 0.2$), (b) $(Na_{0.6}K_{0.4})_{0.5}Bi_{0.5}TiO_3$ ($x = 0.4$), (c) $(Na_{0.5}K_{0.5})_{0.5}Bi_{0.5}TiO_3$ ($x = 0.5$). Red lines represent Voight fits to data and are included as a guide for the eyes.***

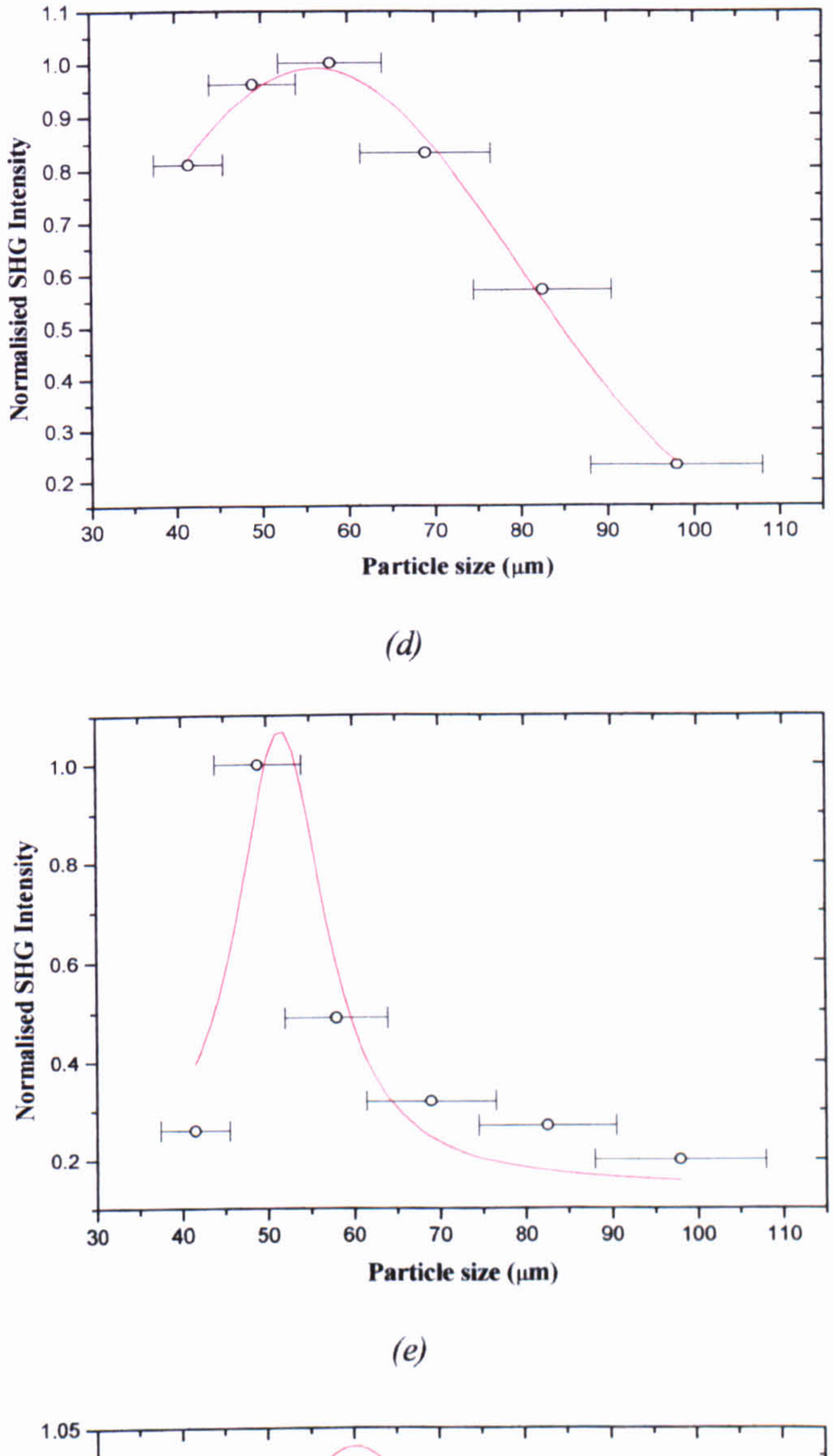

Figure 6.05. *Normalised particle size dependence of second harmonic intensity. Non-phased matched (d) $(Na_{0.4}K_{0.6})_{0.5}Bi_{0.5}TiO_3$ ($x = 0.6$), (e) $(Na_{0.2}K_{0.8})_{0.5}Bi_{0.5}TiO_3$ ($x = 0.8$), (f) $K_{0.5}Bi_{0.5}TiO_3$ ($x = 1.0$). The SHG data have been normalised to the laser power output. Red lines represent Voight fits to data and are included as a guide for the eyes.*

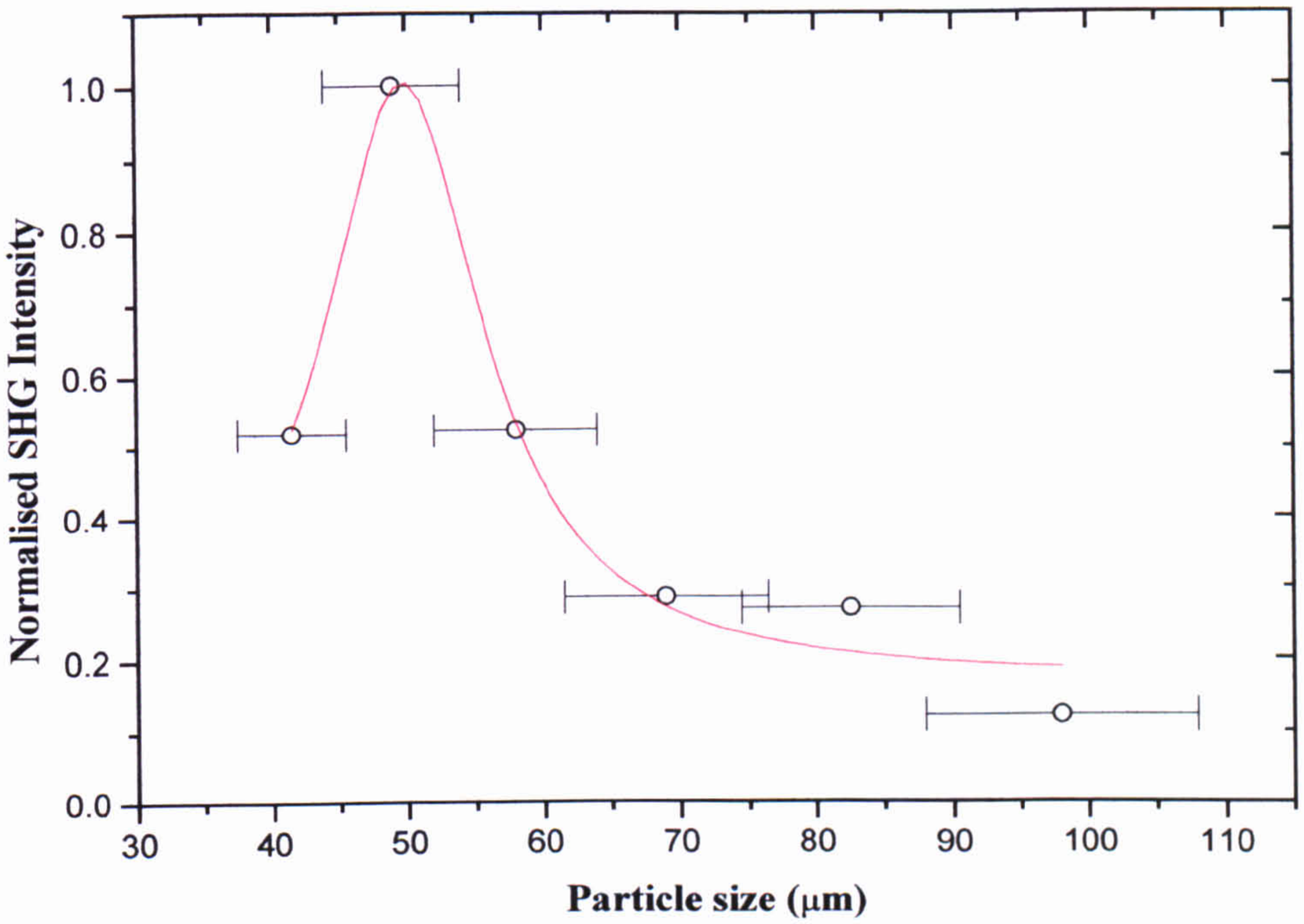

(a)

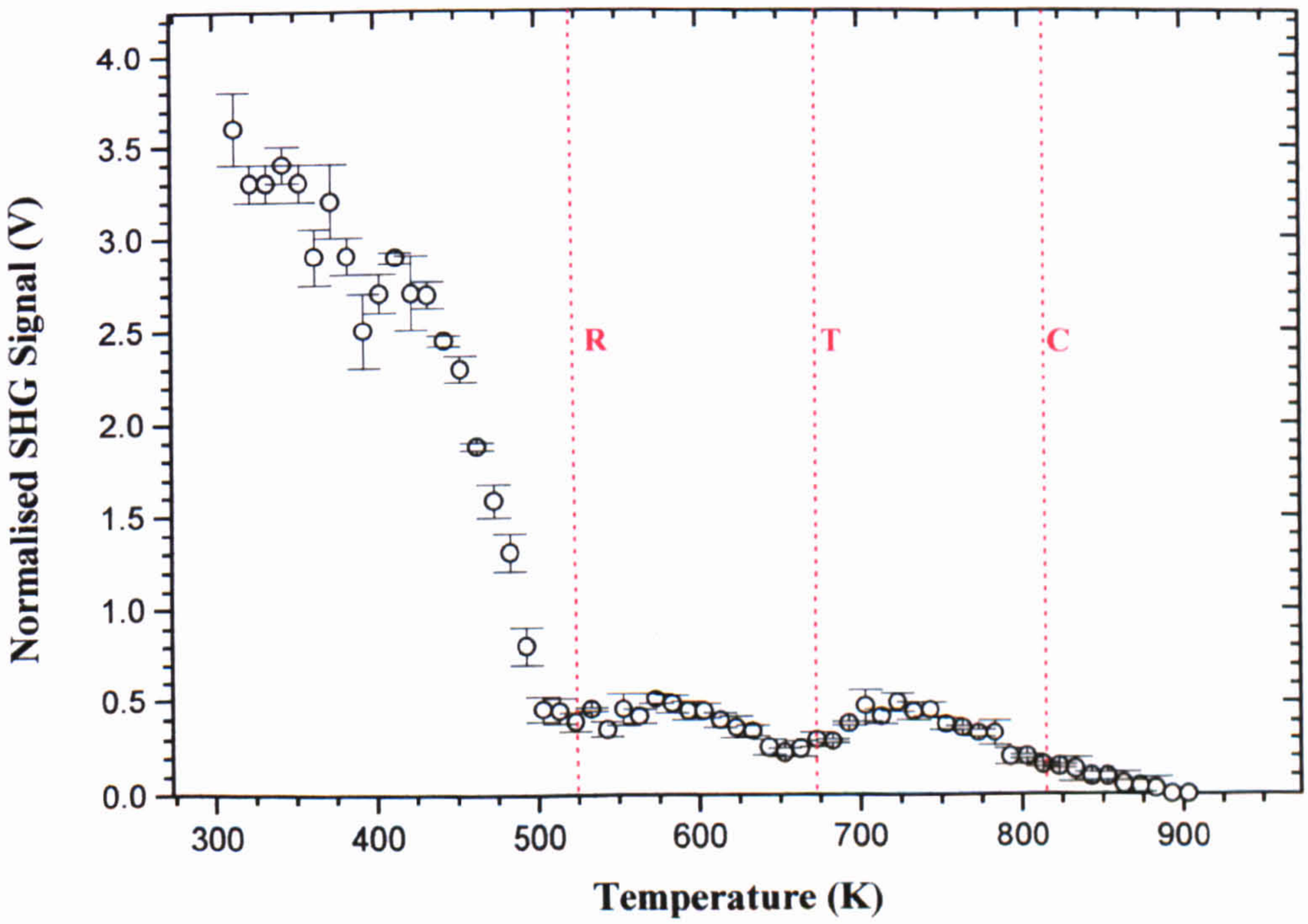

(b)

Figure 6.06. *(a) Normalised particle size dependence of second harmonic intensity, non-phased matched for $Na_{0.5}Bi_{0.5}TiO_3$. The red line represents a Voight fit to the data and is included as a guide for the eyes. (b) Second harmonic signal in $Na_{0.5}Bi_{0.5}TiO_3$ as a function of temperature. The red dotted lines marked R, T and C represent the onset of the rhombohedral, tetragonal and cubic regions obtained by neutron diffraction refinements. The SHG data have been normalised to the laser power output.*

6.2.3 Birefringence Imaging of Phase Transitions

Optical linear birefringence results from anisotropy within a crystal, this leads to a variation of the refractive index, n, as a function of the polarisation of the incident light. This variation can be represented by the optical indicatrix (section 6.2, equation 6.07) which is described by three principal refractive indices. For any given incident light direction, the perpendicular cross-section of the indicatrix will have the general form of an ellipse. The difference in the lengths of the axes of the ellipse, together with the inclination, φ, of the indicatrix relative to some reference co-ordinate system, describe the optical retardation within the crystal for the particular direction of light.

The difference in the refractive index implies that two different polarisations will emerge from the sample, with a phase difference:

$$\delta = \Delta n L 2\pi/\lambda \tag{6.09}$$

where Δn is the difference in the refractive indices of the two beams, L is the sample thickness and λ is the wavelength of the light. Thus, on passing through the birefringent sample, a beam of linearly polarised light will, in general become elliptically polarised with a phase difference δ, and a difference in amplitude depending on the inclination φ, between the incoming electric field and the ellipse axes.

An imaging version of the rotating-polariser method has been used in order to study the phase transitions in NKBT crystals, for x = 0.0, 0.2 and 0.4. The imaging system is capable of determining the variation of $|sin\delta|$, the transmittance, I_o and the orientation of the transmitted polarisations, φ, throughout the crystal. False-coloured images representing these parameters are created and, when combined with a heating stage, provide images of orientation and the magnitude of optical anisotropy as a function of temperature[5,6].

6.2.3.1 Imaging System and Data Collections

The imaging system consisted of a polarising microscope fitted with a computer-controlled rotating polariser and a circular analyser combined with a highly accurate heating stage (LINKAM TP93), capable of controlling the temperature to within ± 0.1 K and CCD camera. Details of the set-up can be found elsewhere[5,6]. Birefringence imaging as a function of temperature was performed on transparent NKBT crystals (for x = 0.0, 0.2 and 0.4) grown by flux-techniques (sections 2.2.2 and 2.2.4). Collaborators[7]

(M. Geday *et al.*) at Oxford University performed the measurements. Crystal were cut perpendicular to one of the pseudo-cubic axes and polished to a thickness of 0.1 mm. Before each experiment was started, the crystals were heated to 873 K (the maximum temperature that the heating stage is capable of reaching) and left for several hours in order to release strain introduced in the non-cubic phases. Each run was carried out with a constant change in temperature, and images of the birefringence were taken at constant time intervals on cooling at 3 K min^{-1}. By the selection of a particular region in the image and averaging the values of φ and $|\sin\delta|$, plots of the temperature development were obtained.

6.3.4 Discussion

Selected images of φ and $|sin\delta|$ as a function of temperature are shown in Figures 6.07 and 6.08 respectively, Figure 6.09 shows the typical temperature development of these parameters in NKBT crystals for $x = 0.0, 0.2, 0.4$.

For the NBT crystal a number of cooling and heating experiments were performed[7], at a constant temperature gradient of ± 5 $Kmin^{-1}$. Phase transition temperatures given are averaged values obtained from several individual heating and cooling experiments. The different phases of NBT ($x = 0.0$) are clearly shown.

Cubic Phase – At high temperature the $|\sin\delta|$ image shows a very low birefringence, and the nearly randomly distributed orientation φ, confirms that there is very little strain within the crystal. The crystal structure is optically isotropic as expected for the cubic phase. On cooling, a purely cubic phase is seen above 823 K and completely disappears at 803 K. On heating, the cubic phase starts to appear at 803 K and disappears at 833 K, which indicates a noticeable hysteresis effect of 20 K. The results are in close agreement with neutron diffraction data (section 3.3.1) where the pure cubic phase was seen to appear on heating at 813 K.

Cubic-tetragonal phase transition – With reference to birefringence measurements, a phase transition to the tetragonal phase was clearly observed. There is a short temperature interval, between 823-803 K on cooling and 803-833 K on heating, in which a coexistence of cubic/tetragonal phases is present. From the neutron diffraction results, a cubic/tetragonal coexistence phase was found on heating at 793 K. The maximum temperature range over which the coexistence region could extend was found to be between 779-813 K. In comparison Suchanicz and Kwapulinski[8] who carried out

single crystal x-ray measurements on cooling, found this coexistence region to be between 779-813 K.

Tetragonal phase – The phase is characterised by the presence of three ferroelastic orientation states. Two of the twins can easily be distinguished, as orange and white blocks in the orientation image, and the other is observed as a light-blue background. The range over which the pure tetragonal phase exists was found to be between 493-803 K on cooling and 573-803 K on heating. An upper limit of between 593-793 K was found for the purely tetragonal phase from neutron results.

Tetragonal-rhombohedral phase transition – From repeated experiments, it was found that the rhombohedral/tetragonal coexistence region was located, on average, between 493-413 K on cooling and 463-573 K on heating. This gives coexistence ranges of 80 and 110 K on cooling and heating, respectively. It was concluded from neutron results that an upper limit of 145 K was associated with this coexistence region.

Rhombohedral phase – The room-temperature rhombohedral phase is characterised by a large number of areas with different orientations. The complex nature of the pattern results from twinning coupled with induced strain.

Isotropic region – In Figure 6.09 it can be seen that between the rhombohedral and tetragonal phases, $|sin\delta|$ drops to very low values over a large temperature range with a minimum at approximately 573 K. At the same time, the orientation angle φ changes smoothly. An isotropic region has previously been reported[9] to occur at 538 K. The origin of the isotropization is not precisely clear. Park *et al.*[9] proposed a mixture of tetragonal and rhombohedral regions smaller than the resolution of the microscope as a possible explanation. Other possibilities include; (i) it is a glassy or amorphous phase between the rhombohedral and tetragonal phases, (ii) it is an example of a re-entrant cubic phase, (iii) that the rhombohedral phase becomes optically isotropic close to or at the temperature of the phase transition. Cases (i) and (ii) could be considered attractive since the change in rhombohedral to tetragonal structures is great and a cubic or amorphous intermediate phase would make the transition more energetically plausible. The cubic intermediate phase is a supergroup of the rhombohedral and tetragonal phases, so that one could pass easily from the rhombohedral to the tetragonal structure (or vice versa) by raising the symmetry group to the cubic intermediate and then reducing it back again to form the desired phase. It is possible however, that the room-temperature rhombohedral phase is undergoing, but not necessarily completing, a second-order phase transition towards the cubic phase, when at a critical point the tetragonal phase suddenly

becomes more stable and forces the first-order rhombohedral to tetragonal phase transition. Another possibility is, as suggested by Kruzina *et al.*[10], that the sign of the birefringence accidentally changes within the rhombohedral phase (the rotating polarizer gives relative changes in optical retardation and without extra information is unable to determine the sign of the birefringence). In this case there is a smooth development in birefringence. Neutron diffraction results in this temperature range do not show the existence of an isotropic region. Diffraction patterns at 573 K (where, $|sin\delta|$ reaches a minimum) clearly show rhombohedral and tetragonal tilt peaks. Phase volumes of 44 % rhombohedral and 56 % tetragonal are obtained from refinements here. Tilt angles of 4.2 (2)° and 2.9 (1)° are obtained from refinements for the rhombohedral and tetragonal phases respectively. The results suggest that the proposal by Park *et al.*[9] of a mixture of tetragonal and rhombohedral regions that are smaller than the resolution of the microscope may, therefore, be the best explanation.

The different phases of $(Na_{0.8}K_{0.2})_{0.5}Bi_{0.5}TiO_3$ ($x = 0.2$) and $(Na_{0.6}K_{0.4})_{0.5}Bi_{0.5}TiO_3$ ($x = 0.4$) are also evident by observing the change in twin patterns and the variation in birefringence. Similar results are obtained and conclusions reached for these crystals as have already been discussed in detail for NBT, with the following differences. In both cases the cubic phases are not reached by the maximum temperature of 873 K. The width in temperature of the tetragonal phase region increase, with the tetragonal/rhombohedral coexistence phases moving to lower temperatures in comparison with NBT. This is consistent with the trends observed in neutron refinements (section 5.3.1). Large isotropic regions (coloured red in the $|sin\delta|$ images of Figures 6.08) are observed even at room temperature. As with NBT, neutron diffraction patterns do not show any indication of a crystallographic isotropic phase in the vicinity of the optical isotropization point.

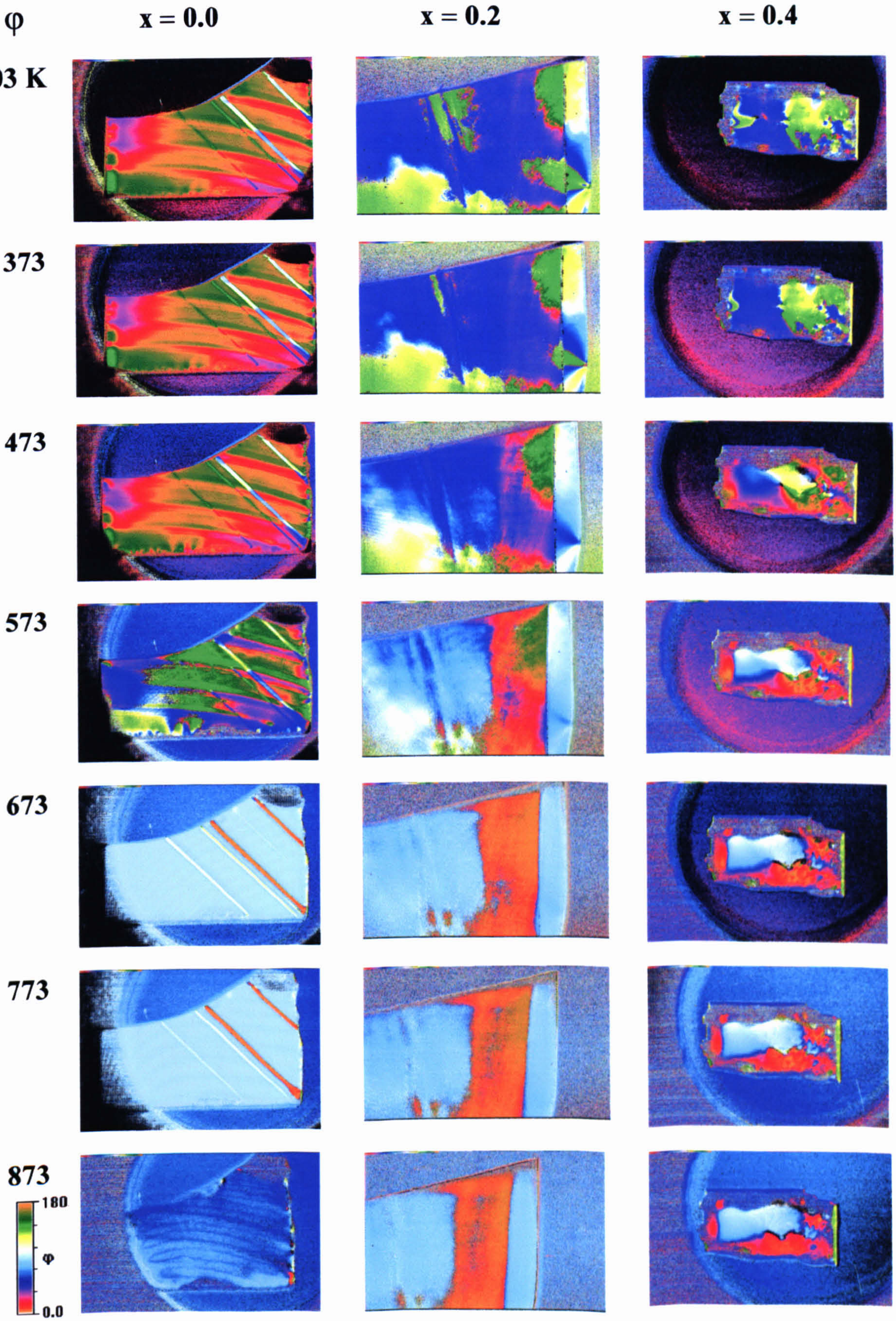

Figure 6.07. Selected orientation, φ, images as a function of temperature for NBT (x = 0.0), $(Na_{0.8}K_{0.2})_{0.5}Bi_{0.5}TiO_3$ (x = 0.2) and $(Na_{0.6}K_{0.4})_{0.5}Bi_{0.5}TiO_3$ (x = 0.4).

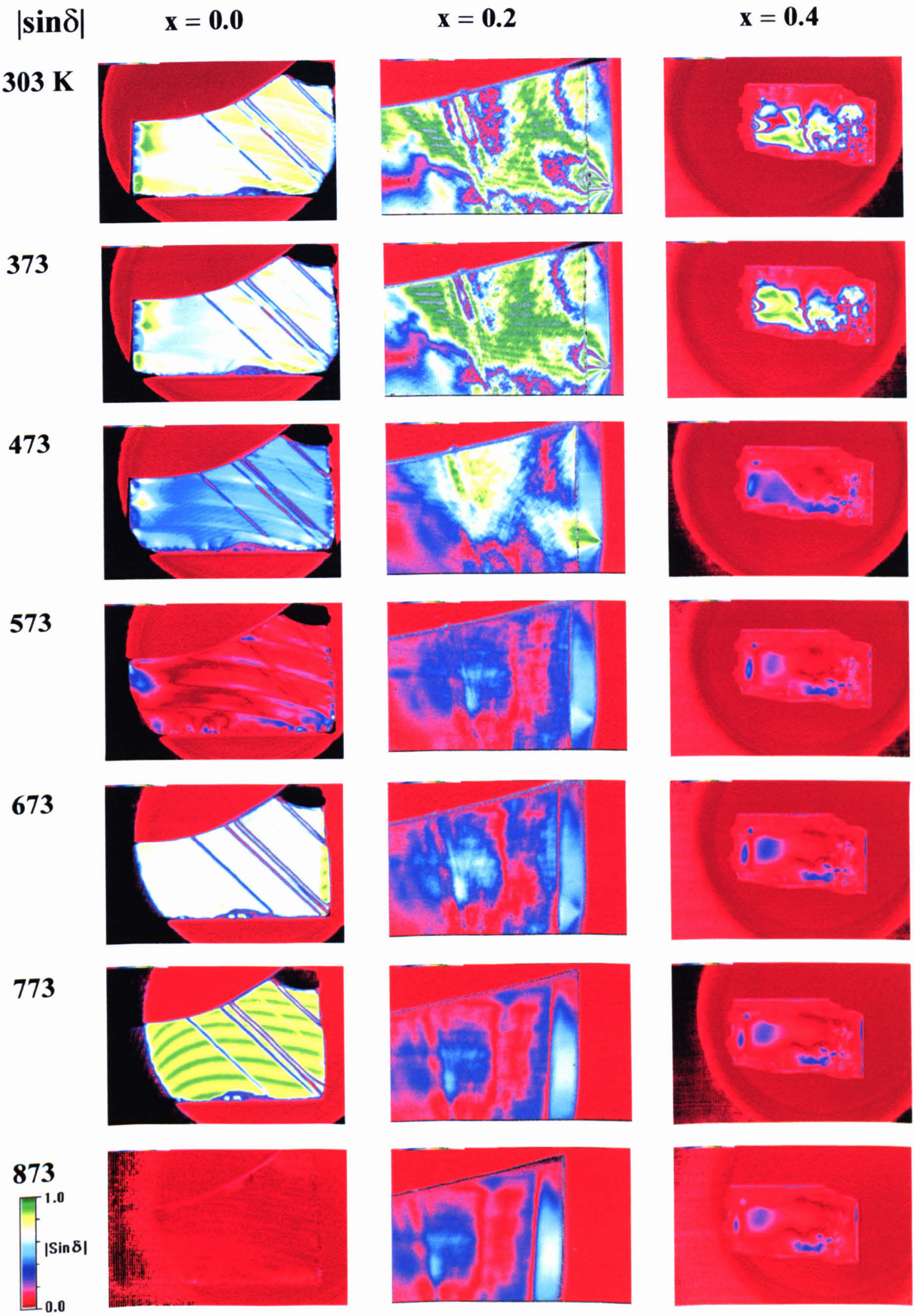

Figure 6.08. Selected $|\sin\delta|$ images as a function of temperature for NBT (x = 0.0), $(Na_{0.8}K_{0.2})_{0.5}Bi_{0.5}TiO_3$ (x = 0.2) and $(Na_{0.6}K_{0.4})_{0.5}Bi_{0.5}TiO_3$ (x = 0.4).

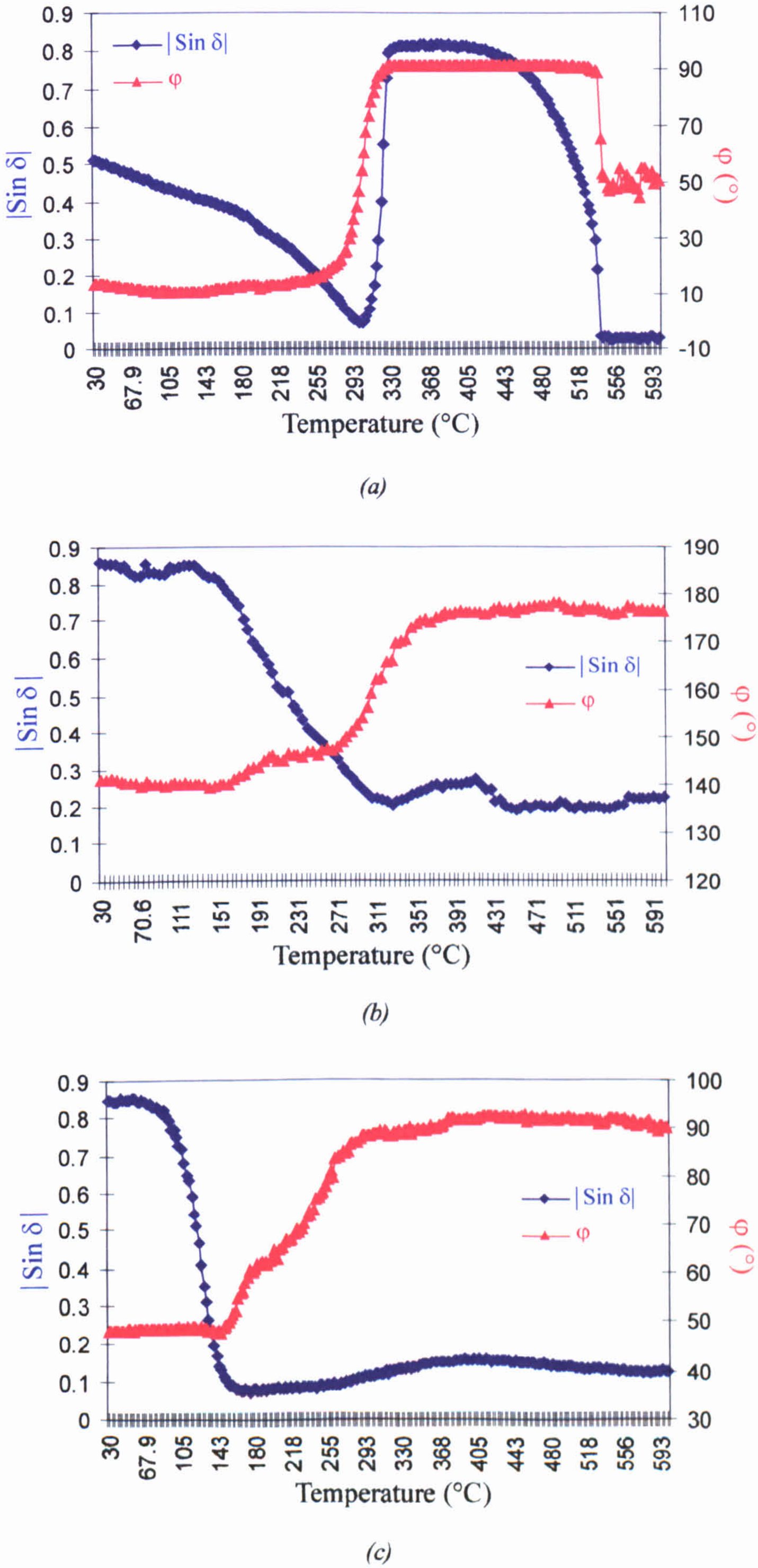

Figure 6.09. *Typical temperature development of |sin δ| and φ for (a) $Na_{0.5}Bi_{0.5}TiO_3$ (x = 0.0), (b) $(Na_{0.8}K_{0.2})Bi_{0.5}TiO_3$ (x = 0.2) and (c) $(Na_{0.6}K_{0.4})Bi_{0.5}TiO_3$ (x = 0.4). The graphs are generated by averaging over a region of 20 × 20 pixels.*

6.3 Raman Spectroscopy

When a sample is irradiated with monochromatic light, the incident radiation may be absorbed, may stimulate emission or may be scattered. A part of the scattered radiation is referred to as the Raman spectrum. It is found that some photons lose energy in scattering from a molecule in the sample and emerge with a lower frequency; these photons produce what are referred to as Stokes lines in the spectrum of scattered radiation. A smaller fraction of the scattered photons gains energy in striking a molecule in the sample and emerge with a higher frequency; these photons produce what are referred to as anti-Stokes lines. The interpretation of Raman spectra is based on the conservation of energy, which requires that when a photon of frequency ν is scattered by a molecule in a quantum state with energy E_i and the outgoing photon has a frequency ν', the molecule ends up in quantum state f with energy E_f.

$$h\nu + E_i = h\nu' + E_f \tag{6.10}$$

or

$$h(\nu' - \nu) = E_i - E_f = h\Delta\nu_R = hc\Delta\tilde{\nu}_R \tag{6.11}$$

where the shift in frequency is $\Delta\nu_R$ and the shift in wavenumber is $\Delta\tilde{\nu}_R$.

The frequency shifts seen in Raman experiments correspond to vibrational or rotational energy differences, so this kind of spectroscopy gives us information relating to the vibrational and rotational states of molecules. The Raman effect arises from the induced polarization of scattering molecules that is caused by the electric vector of the electromagnetic radiation. Considering an isotropic molecule, classically, a dipole moment μ is induced by an electric field E:

$$\mu = \alpha E \tag{6.12}$$

where α is the polarizability. For an isotropic molecule the vectors μ and E point in the same direction, and the polarizability α is scalar. The polarizability α of a molecule that is rotating or vibrating is not constant, but varies with some frequency ν_k (for example, a vibration or rotation frequency) according to:

$$\alpha = \alpha_o + (\Delta\alpha)\cos 2\pi\nu_k t \tag{6.13}$$

where α_o is the equilibrium polarizability and $\Delta\alpha$ is its maximum variation. Since the electric field of the impinging electromagnetic radiation varies with time according to:

$$E = E_o \cos 2\pi \nu_o t \tag{6.14}$$

the induced dipole moment of the molecule is given by:

$$\mu = [\alpha_o + (\Delta\alpha)\cos 2\pi \nu_k t] E_o \cos 2\pi \nu_o t \tag{6.15}$$

$$\Rightarrow \mu = \alpha_o E_o \cos 2\pi \nu_o t + 1/2\,(\Delta\alpha) E_o [\cos 2\pi(\nu_o + \nu_k)t + \cos 2\pi(\nu_o - \nu_k)t] \tag{6.16}$$

The three terms in equation 6.16, provide the classical explanation for Rayleigh scattering (ν_o), anti-Stokes lines ($\nu_o+\nu_k$), and Stokes lines ($\nu_o-\nu_k$), respectively. The classical treatment incorrectly implies that the Stokes and anti-Stokes lines will occur with equal intensity. The anti-Stokes lines are however weaker because they depend on the population of excited levels.

In order for a molecular motion to be Raman active, the polarizability must change when that motion occurs. In order for a vibrational mode to be Raman active, the polarizability must change during the vibration, and for a rotation to be Raman active, the polarizability must change as the molecule rotates in an electric field. The polarizability of both homonuclear and heteronuclear diatomic molecules changes as the distance between nuclei changes because this alters the electronic structure. The polarizability of an atom does not change in a rotation, thus atoms do not have rotational Raman effects. All other molecules are anisotropically polarizable (i.e. the polarization is dependent on the orientation of the molecule in the electric field). When a molecule is anisotropic, the application of an electric field E in a particular direction induces a moment μ in a different direction. In this case α is a tensor, and the induced dipole moment is given by:

$$\mu = \alpha E \tag{6.17}$$

In matrix form this is written as:

$$\begin{bmatrix} \mu_x \\ \mu_y \\ \mu_z \end{bmatrix} = \begin{bmatrix} \alpha_{xx} & \alpha_{xy} & \alpha_{xz} \\ \alpha_{yx} & \alpha_{yy} & \alpha_{yz} \\ \alpha_{zx} & \alpha_{zy} & \alpha_{zz} \end{bmatrix} \begin{bmatrix} E_x \\ E_y \\ E_z \end{bmatrix} \tag{6.18}$$

This is equivalent to the following set of algebraic equations:

$$\mu_x = \alpha_{xx} E_x + \alpha_{xy} E_y + \alpha_{xz} E_z \tag{6.19}$$

$$\mu_y = \alpha_{yx}E_x + \alpha_{yy}E_y + \alpha_{yz}E_z \quad (6.20)$$

$$\mu_z = \alpha_{zx}E_x + \alpha_{zy}E_y + \alpha_{zz}E_z \quad (6.21)$$

Thus each component (μ_x, μ_y, μ_z) of the induced dipole moment μ can depend on each component (E_x, E_y, E_z) of the electric field E. Only six of the nine coefficients of the polarizability are independent, since it can be shown that $\alpha_{xy} = \alpha_{yx}$, $\alpha_{xz} = \alpha_{zx}$, and $\alpha_{yz} = \alpha_{zy}$[11]. In diatomic molecules, the vibration occurs only along the chemical bond connecting the nuclei. In polyatomic molecules, the situation is more complicated because all the nuclei perform their own harmonic oscillations. However, it can be shown that any of these complicated vibrations of a molecule can be expressed as a superposition of a number of normal vibrations that are completely independent of each other. To determine whether a vibration is active, the selection rules must be applied to each normal mode. The specific selection rules for rotation Raman transitions are as follows for linear and symmetric top molecules:

Linear molecules $\Delta J = 0, \pm 2$

Symmetric topmolecules $\Delta J = 0, \pm 2, \Delta K = 0$ when $K = 0$ and $\Delta J = 0, \pm 1, \pm 2, \Delta K = 0$ when $K \neq 0$

where K is the component of the angular momentum J along the principal symmetry axis. The $\Delta J = 0$ applies in vibration-rotation transitions. The $\Delta K = 0$ is a result of the fact that the dipole of a symmetric top molecule is along the principal axis, and so there cannot be a component of the dipole moment perpendicular to this axis.

If we now turn to the case of Raman scattering from a crystal, the energy in a lattice vibration or elastic wave is quantized. The quantum of energy in such an elastic wave is called a phonon. The incident electromagnetic field couples with the phonon field through an induced dipole moment. This is accomplished by the variation of the electronic polarizability tensor with the lattice configuration during a normal vibration. In a crystal, the photon is scattered inelastically with the creation (Stokes) or annihilation (anti-Stokes) of a phonon. Similarly to the case for molecules, in crystals there exists wavevector selection rules for allowed transitions between quantum states[12].

6.3.1 NKBT– Raman spectra as a Function of Substitution

The phases in NBT and its solid solutions have been studied by x-ray and neutron diffraction (chapters 3, 4 and 5), which gives information about long-range order. Raman spectroscopy, on the other hand, is known to be an appropriate technique for the

investigation of the short-range order[13-16] and phase transitions in perovskites[15-18]. A group theory treatment of NBT and KBT leads to 13 and 15 Raman active modes respectively, details of which can be found elsewhere[19]. Compared with the atomic mass of bismuth (208.98), the atomic mass of sodium (22.99) and potassium (39.10) are similar and thus a mass effect can be considered to be negligible for most of the modes (except for those involving mainly bismuth cations). On the other hand their ionic radii are quite different (Na^{1+} = 1.32, K^{1+} = 1.65, Bi^{3+} = 1.31 Å). The increase of the ionic radii, when going from Na^{1+} to K^{1+}, leads naturally to a distortion of the structural framework (sections 5.3.1 and 5.3.3), and polyhedral distortion in oxides is known to result in a high-frequency shift[20-23]. Any change in the crystal structure or physical properties will, in principle, lead to a variation in the phonon behaviour. Therefore an analysis of the frequency, intensity and linewidth evolution of the whole spectra across the NKBT solid solution series is expected to give an insight into the phase changes present. This section describes the structural variations across the NKBT solid solution range as determined by Raman spectroscopy.

6.3.1.1 Data Collections

Raman spectra of NKBT powders were recorded from 70 to 700 cm^{-1} with a microscope-equipped Dilor XY multichannel spectrometer. The 514.5 nm line of an Ar-ion laser was used as an excitation line. Experiments were conducted in a micro-Raman back scattering configuration with the laser focused to a 1 μm^2 spot. The instrument resolution was 2.8 ±0.2 cm^{-1}. It was verified that laser powers up to 20 mW did not produce significant heating or damage to the sample[19]. Experiments were then carried out using incident powers of approximately 5 mW. Measurements were performed under a microscope and recorded in a back scattering geometry. The band positions in the Raman spectra for each substitution *(x)*, were determined with JANDEL Peakfit software. Measurements were taken by collaborators[24] (J. Kreisel *et al.*) at the Laboratoire d'Electrochimie et de Physicochimie des Matériaux et des Interfaces, Grenoble, France.

6.3.2 Discussion of Raman Spectra

Figure 6.10 (a) shows the room temperature Raman spectra of NBT and KBT, together with their spectral deconvolution into Lorentzian-shape peaks. As can be seen

in the figure, the Raman bands for both these compounds are relatively broad. This is mainly due to the disorder on the A-site, but also results from overlapping Raman modes. The Raman spectrum observed for NBT is similar to data already reported[25-27]. As expected from the crystal structure, the KBT Raman spectrum shows a different spectral profile compared with NBT. As a consequence of the spectral difference between the two end member compounds, the evolution of the phonon behaviour in the NKBT series can be followed.

Raman spectra of the NKBT (x = 0.0, 0.2, 0.4, 0.5, 0.6, 0.8 and 1.0), recorded at room temperature are shown in Figure 6.10 (b). Several qualitative features in the series can be observed with increasing K^{1+} content:

- With the exception of certain peaks (especially around 135 cm^{-1}), there is a general upward shift of the Raman frequencies.
- The broad band centred around 260 cm^{-1} is first split into two and then into three components.
- The overlapping bands at 400-650 cm^{-1} are split.

The 135 cm^{-1} peak is the only band showing a clear low frequency shift. However the shift is relatively weak (14 cm^{-1} for x = 0.40). Since the band position changes with substitution rate, this band should be assigned to vibrations involving the A-site (because vibrations involving the B-site are expected to be unaffected by substitution). Low frequency modes of this nature are known to be dominated by cation displacement[19] along a crystallographic axis; consequently, the downward shift should be mainly attributed to the increasing mass on the A-site. In the harmonic oscillator approximation with negligible force constant changes, the masses and frequencies are related by the following:

$$\left(\nu_{x=0}/\nu_{x=0.4}\right)^2 \approx \left(M_{x=0.4}/M_{x=0}\right) \tag{6.22}$$

where $\nu_{x=0}/\nu_{x=0.4} \approx 1.11$. The main difficulty in a mass effect study is the vibrational picture that needs to be taken in order to describe the three different species that are present on the A-site. Two situations are useful to consider:

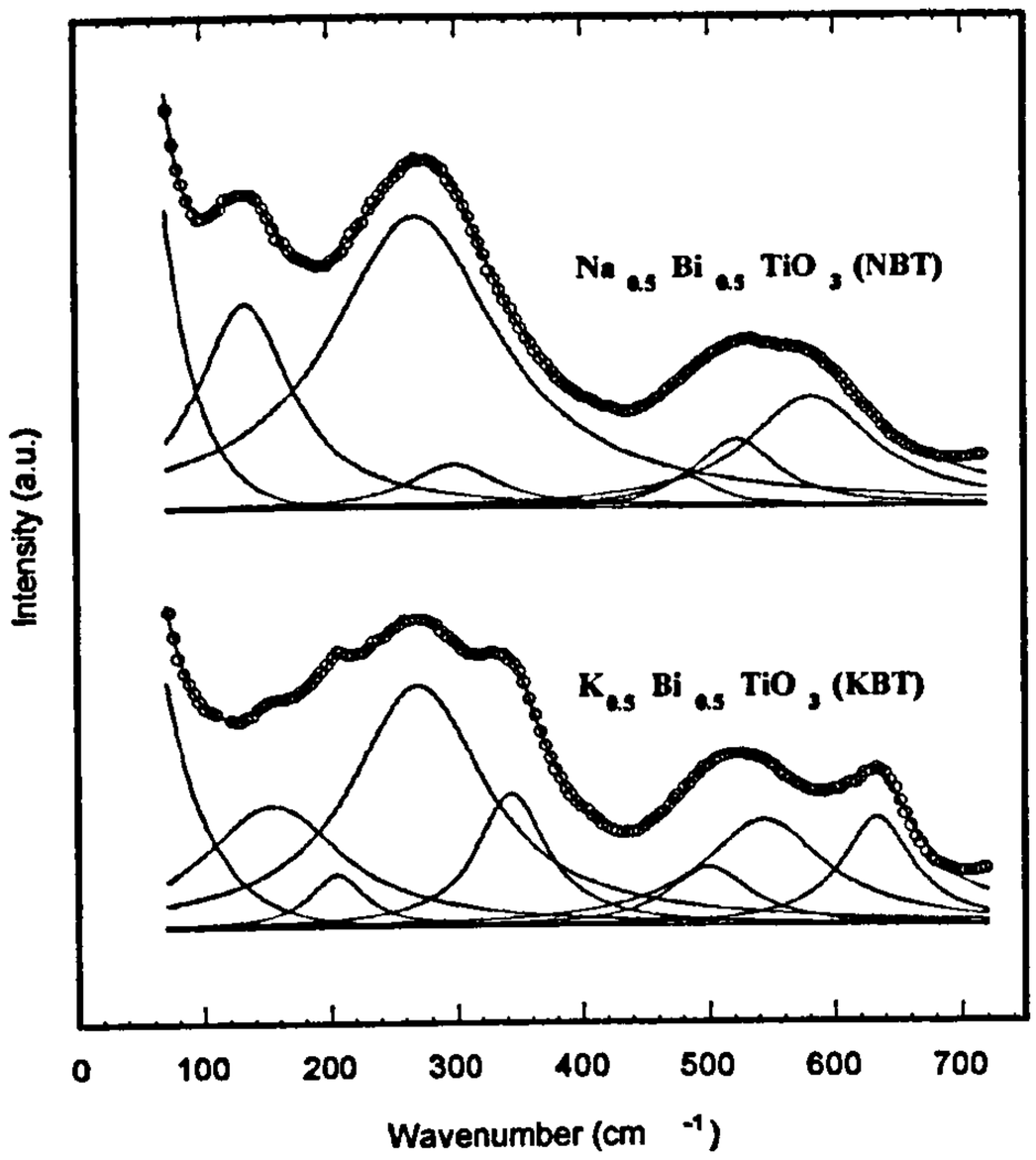

(a)

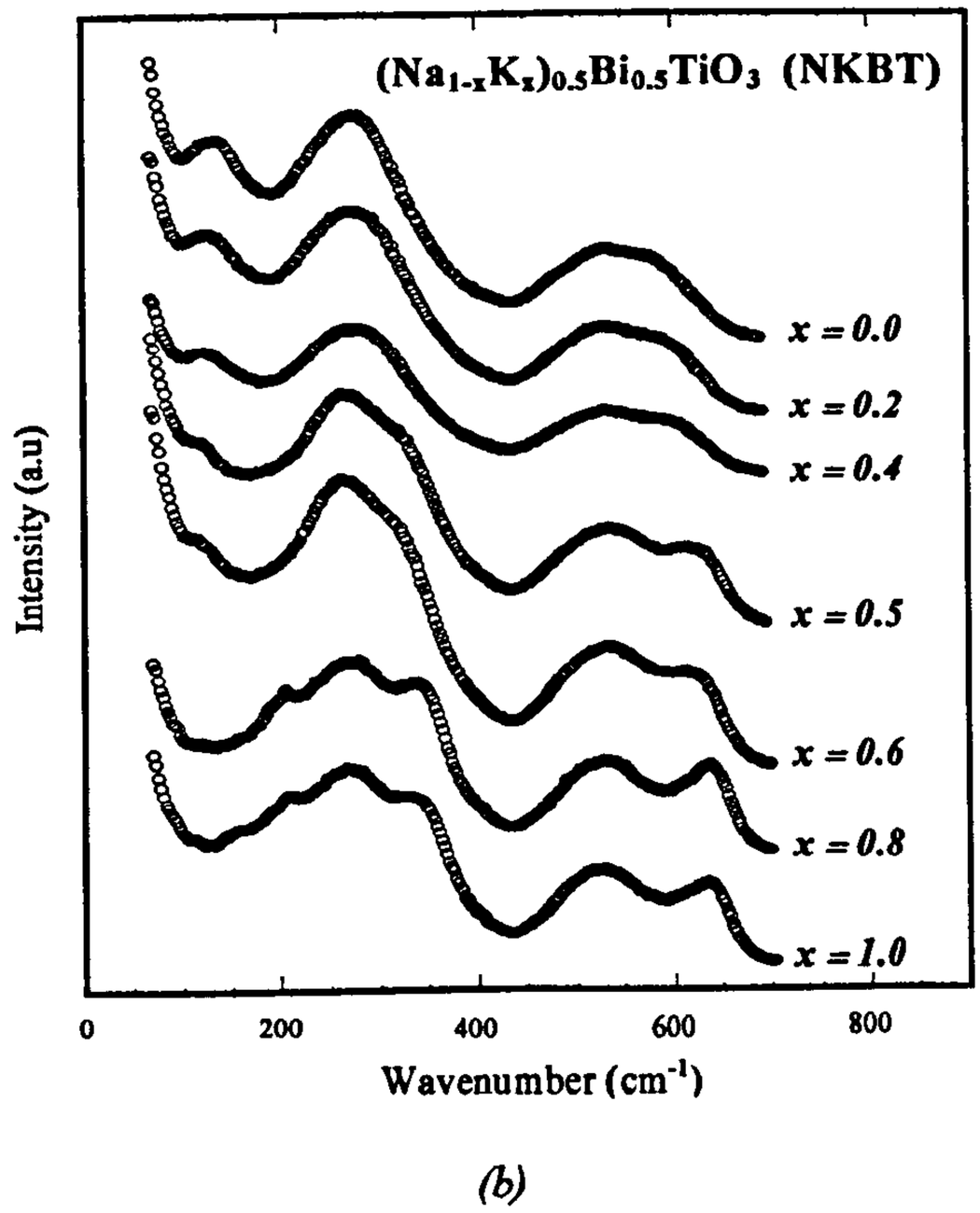

(b)

Figure 6.10. *(a) Room temperature Raman spectra of $Na_{0.5}Bi_{0.5}TiO_3$ (NBT) and $K_{0.5}Bi_{0.5}TiO_3$ (KBT). The open circles are plotted for every fifth point of the experimental data and the solid lines display the spectral deconvolution. (b) Room-temperature Raman spectra for $(Na_{1-x}K_x)_{0.5}Bi_{0.5}TiO_3$ (NKBT). The shifts and splitting of the phonon bands are due to structural phase transitions between the end members of NBT and KBT.*

(a) *The virtual ion model*, where the virtual ion can be seen as an ion with average properties of the cations on the A-site (section 5.3.1). Generally the concept is an effective approximation when mass and force constant differences small. This is not the case for NKBT, since the mass of the Na and K cations are ≈ 11 % and 19 % the mass of the Bi cation, respectively. Bi is therefore expected to vibrate at significantly lower frequencies than the Na/K cations. Also, the Na/K-O and Bi-O bondings are not expected to be similar, as a result of the behaviour of the stereo-active lone pair of Bi^{3+} (section 3.3.5.3). As a consequence, the virtual ion model is unlikely to represent the physical actuality.

(b) *Multiple mode behaviour*, here the compound may be viewed as an alternation of zones richer in one constituent than the other. As these zones are of the order of nanometres, phase separation cannot be revealed by diffraction. For NBT this would lead to separate Bi-O and Na-O bands. In NKBT, with Na and K having relatively similar masses, one could expect this to lead to separate Bi-O and Na_{1-x}/K_x bands. In fact, the experimental value of $\nu_{x=0}/\nu_{x=0.4} \approx 1.11$ corresponds well with $((0.6 \times m_{Na} + 0.4 \times m_K)/m_{Na})^{1/2} \approx 1.12$. This supports the outline of a two-mode behaviour for NBT, where one of the bands shifts for NKBT with the substitution rate to lower frequency according to the virtual ion model. The Raman spectra taken do not show the Bi-O bands. However, this is not unexpected, as they would be located at very low frequencies (resulting from the large mass), as observed for example in α-Bi_2O_3[28] and would, therefore, fall under the central peak. Assuming that the 135 cm^{-1} band is a Na/K-O band, its presence implies that at least nanometre-size domains exist, because otherwise the phonon lifetime would have been too short to result in a defined Raman peak. Such nanodomains should be seen as local *clusters* of Bi- and Na/K-containing unit cells. In principle such domains are undetectable by x-ray diffraction with its coherence length of around 20 unit cells (≈ 8 nm). The presence of diffuse scattering in NBT crystals (section 2.3.4) supports this idea. Furthermore, a preliminary transmission electron microscopy (TEM) investigation, which can be an efficient probe for the study of local structure on an atomic level, suggested the existence of local one-dimensional chains over several unit cells in NBT.

In the 200-300 cm^{-1} frequency region the most obvious spectral changes (Figure 6.11) are observed.

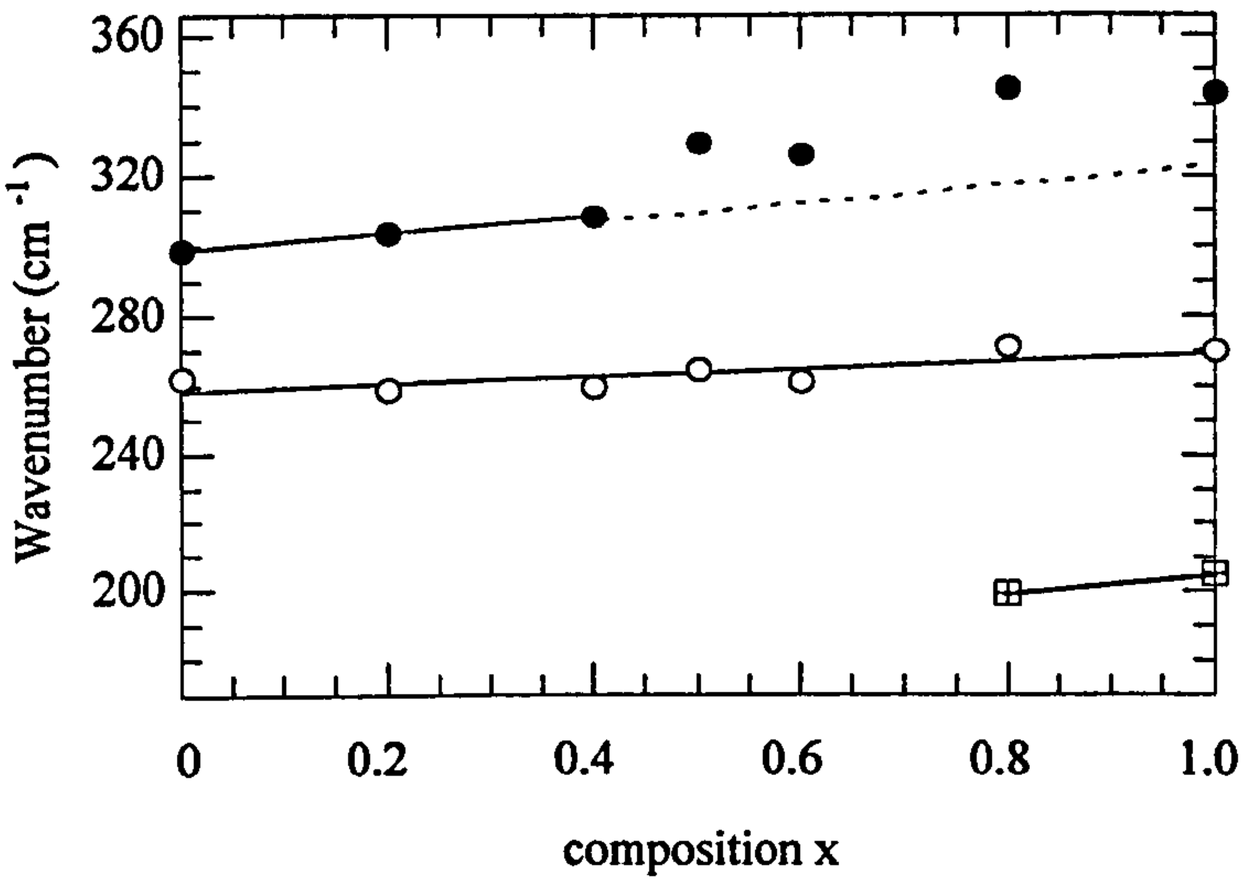

Figure 6.11. Band position change in the Raman spectra of $(Na_{1-x}K_x)_{0.5}Bi_{0.5}TiO_3$ as a function of composition for the broad feature at 200-300 cm^{-1}. The lines are guides for the eyes to emphasize spectral changes.

The first obvious change for the broad feature is observed for x = 0.5, where the underlying component appears as a clear shoulder on the high frequency side of the 280 cm^{-1} peak, departing from the linear evolution given for lower substitution rates. The appearance of this shoulder might be seen as the rise of an underlying component, but the gradient change in frequency is more likely to be interpreted as a structural change. This agrees well with structural changes observed from neutron diffraction studies (chapter 5). Between $0.0 < x < 0.5$ a room temperature phase transition is observed from the tilted rhombohedral system with space group R3c to a zero tilt rhombohedral phase, space group R3m (section 5.3.1). The second more pronounced spectral change occurs for $x = 0.8$. The sudden appearance of the peak at ≈ 200 cm^{-1} can be seen as the most sensitive indication in the NKBT Raman spectra for the presence of the tetragonal phase as indicated by the tetragonal splitting of the peaks in Figures 5.11 and 5.12 and refinements outlined in section 5.2.3. In general, it is one of the advantages of Raman spectroscopy, over diffraction methods, that phonon signals from local parts of a sample are simply superimposed so that the macroscopically measured spectrum contains all local information. Raman spectroscopy is sensitive even to very small phase fractions, and the fact that the peak at ≈ 200 cm^{-1} has not been observed for lower substitution rates allows us to rule out both (i) a tetragonal/rhombohedral two-phase region, as reported by

Elkechai *et al.*[29], and (ii) that the tetragonal phase extends to $x = 0.4$[30] or $x = 0.2$[31] (as reported by other researches and outlined in section 5.3.1). The Raman results reported here fully support the conclusions reached in the diffraction study of chapter 5.

The 400-700 cm^{-1} region is composed of three bands, two dominant and one smaller underlying band. Since this region does not show obvious drastic spectral changes like the one at 200-300 cm^{-1}, it is useful to plot the substitution-dependent evolution of the frequency, the FWHM and the intensity for each of the three lines (Figure 6.12). The overall feature in Figure 6.12, which is most visible in the intensity, is that the phonon characteristics in NKBT show a pronounced change between $0.4 < x < 0.5$, which is evidence of a phase change and therefore, strengthens the interpretation above for the high-frequency part of the 200-300 cm^{-1} region.

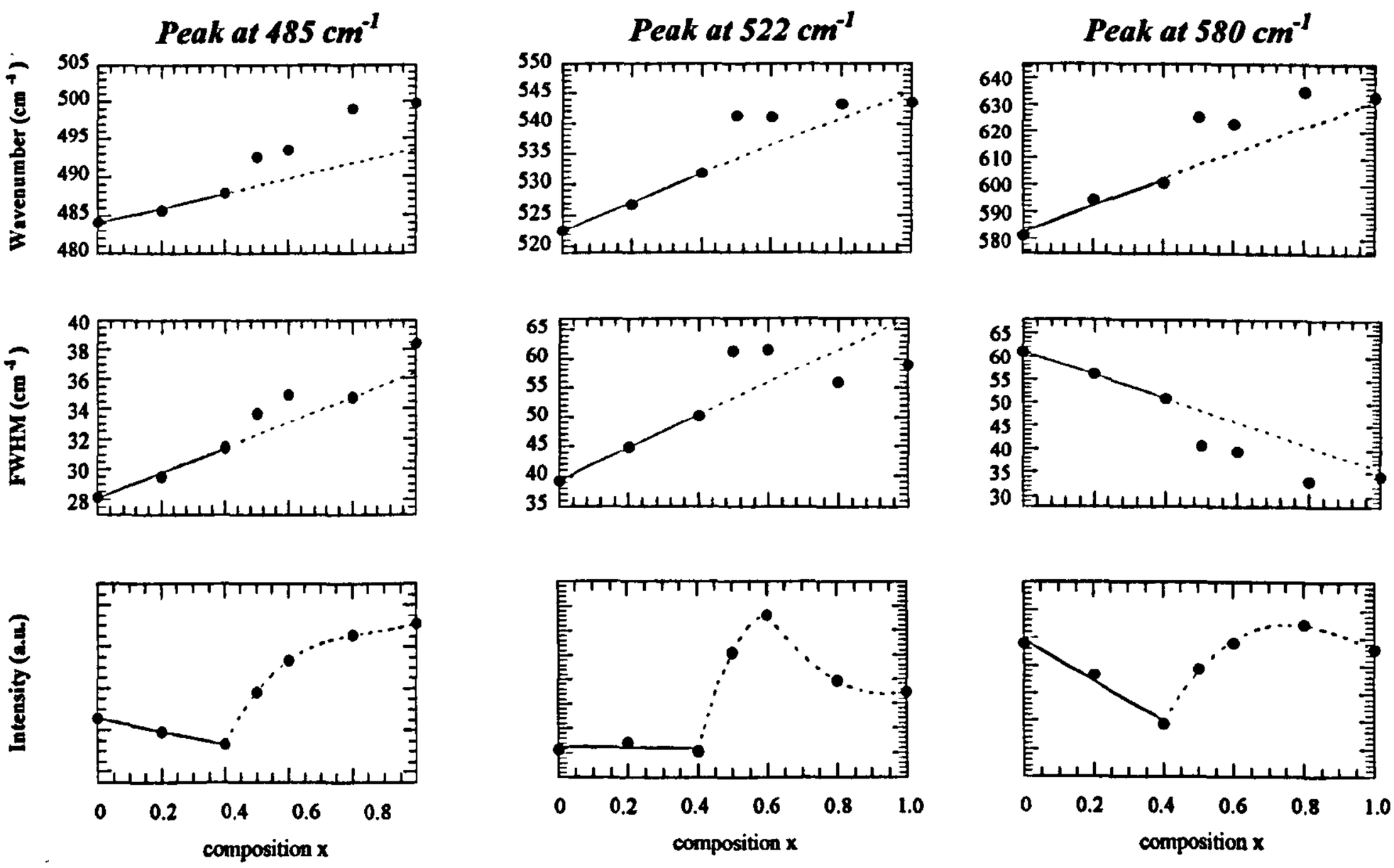

Figure 6.12. Band positions, FWHM and intensity change in the Raman spectra of $(Na_{1-x}K_x)_{0.5}Bi_{0.5}TiO_3$ as a function of composition for the broad feature at 450-650 cm^{-1}. The lines are guides for the eyes to emphasize spectral changes.

6.3.3 NBT – High-pressure Raman Study

Raman spectroscopy is known to be a useful diagnostic tool for the study of pressure induced phase transitions. This has been shown for various perovskite-type titanates (e.g. $BaTiO_3$[32-33], $PbTiO_3$[34-35], $SrTiO_3$[36], $CaTiO_3$[37]). Information relating to the intermolecular interactions, phase transitions and structural changes are obtainable. The long-range order of NBT has been studied as a function of pressure using

synchrotron and neutron diffraction (chapter 4). In this section a room-temperature pressure dependent investigation of NBT between 4.2-190 kbar, which explores the short-range order, is presented.

6.3.3.1 Data Collections

Raman spectra of NBT powders were recorded in back-scattering geometry with a Dilor XY multichannel spectrometer equipped with a microscope. The 514.5 nm line of an Ar-ion laser was used as a excitation line. High-pressure experiments were performed in a diamond anvil cell. A 16:4:1 mixture of methanol-ethanol-water was used as the high-pressure transmitting medium. Powder samples were placed in a chamber 250 μm in diameter and 50 μm thick. Pressure calibration was accomplished by monitoring the shift of fluorescence bands[38] of Cr^{3+} ions in a small ruby crystal placed in the vicinity of the sample[39]. NBT was studied between 4.2-190 kbar. The Raman spectra were decomposed into individual Lorentzian components using JANDEL Peakfit software. Measurements were taken by collaborators[40] (J. Kreisel *et al.*) at the Laboratoire d'Electrochimie et de Physicochimie des Matériaux et des Interfaces, Grenoble, France.

6.3.4 Discussion of Raman Spectra

Before discussing the phonon characteristics of NBT at different hydrostatic pressures it is useful to compare the Raman data for the highest and lowest pressures measured. Raman spectra at 4.2 and 190 kbar are shown in Figure 6.13 (a), together with their spectral deconvolution into Lorentzian-shape peaks. The Raman spectrum at 4.2 kbar can be deconvoluted in the 100-700 cm^{-1} range into 5 peaks[41] located at approximately 135, 275, 490, 530 and 580 cm^{-1}. The Raman spectrum at 190 kbar is dominated by a band at 600 cm^{-1}. At lower frequencies, it can be deconvoluted into 6 bands at roughly 165, 255, 300, 345, 400 and 445 cm^{-1}. The obvious differences displayed in Figure 6.13 (a), point to a structural re-arrangement with applied pressure.

Figure 6.13 (b) represents the Raman spectra as a function of applied hydrostatic pressure from 4.2-190 kbar. Figure 6.13 (c), shows the pressure-dependent evolution of the band frequencies obtained from spectra deconvolution. Several features in the Raman spectra can be seen as a function of increasing pressure in NBT:

- At approximately 135 cm^{-1}, there is a low frequency shift from 4.2 up to 27 kbar. When the pressure is further increased a gradient change is seen and the band starts to shift at a rate ≈ 3.2 cm^{-1}/kbar to higher frequencies. This anomaly seems to be accompanied by a splitting into two overlapping components *A*/*A*', mainly observed through the increasing peak-width.
- The broad band *B* centred on 275 cm^{-1} shows a negative frequency-shift from 4.2 up to 50 kbar, where a discontinuity is observed, after which it shifts by ≈ 1.7 cm^{-1}/kbar to higher frequencies.
- A number of new bands are seen to appear in the middle-frequency region at pressures higher than 50 kbar.
- The overlapping, *C*, *C'* and *C''* high-frequency bands, observed around 500-600 cm^{-1} at 4.2 kbar, merge into a single band at 50 kbar. The single band then shifts ≈ 5 cm^{-1}/kbar to higher frequencies.
- The high-frequency feature around 600 cm^{-1} (bands *C*, *C'* and *C''*) behaves differently in comparison with the low- and middle-frequency regions. Once bands *C*, *C'* and *C''* have merged, the single band remains almost unchanged in its shape and intensity with increasing pressure, while the features at lower frequencies decrease dramatically in intensity.

Each of the points mentioned above, describing a discontinuous or distinct change in the Raman spectral features, indicate a pressure-induced structural phase transition has occurred in NBT in the 27-50 kbar region.

From the pressure-induced structural study of NBT conducted via powder diffraction techniques (chapter 4), it was revealed that the ambient pressure rhombohedral structure persists up to 8 kbar, between 10-19.4 kbar a rhombohedral/orthorhombic coexistence region is observed and above 26.2 kbar the purely orthorhombic phase is observed. The new high-pressure phase of NBT (section 4.2.3) is isomorphic to the orthorhombic structure of $CaTiO_3$ (space group Pnma, with tilt system $a^-b^+a^-$). In the following, the different characteristic spectral changes will be discussed in relation to the rhombohedral (R3c) → orthorhombic (Pnma) phase transition.

At 4.2 kbar, the 80-200 cm^{-1} region is dominated by an intense band at 135 cm^{-1}, which has been associated with Na-O vibrations (section 6.3.2). In the rhombohedral

structure the A-site sodium atoms are displaced along $[111]_p$ from the centre of a dodecahedral co-ordination of the oxygen atoms in the ideal perovskite structure. A vibrational mode associated with this cation is expected to be sensitive towards phase transitions when the site symmetry is changed. As a consequence, the gradient change in the pressure dependent frequency evolution of band *A* in NBT (Figure 6.13 (c)) gives evidence for a structural change, which is associated with a symmetry change of the Na-site, i.e. to another type of cation displacement. In the orthorhombic Pnma, structure the Na-cations are displaced in the [100] direction and are antiferroelectrically ordered along $[010]_p$. As a consequence the 135 cm^{-1} band may be interpreted as a pressure-induced change in the cation displacements.

The intense broad band *B* centred on 275 cm^{-1} and assigned to TiO_6 octahedra[41] is the dominating feature in the 4.2 kbar spectrum. In discussing this band it is useful to consider Raman studies on materials having a similar crystal structure, like $ATiO_3$ (A = Ba, Pb) titanates, where the tetragonal → cubic structure is obtained by cation-anion displacements without octahedral tilting. In the Raman spectra of these titanates pressure-induced negative frequency-shifts have been observed for the 260, 350 and 300 cm^{-1} bands in $BaTiO_3$[42], $PbTiO_3$[43] and $Ba_{0.78}Pb_{0.22}TiO_3$[44] respectively. This negative frequency shift has been interpreted in terms of a soft-mode behaviour describing a pressure-induced tetragonal → cubic phase transition, i.e. the reduction of the anion-cation displacement towards totally symmetric anion-cation octahedra in the ideal perovskite structure. However, other studies of isostructural materials seem to indicate a correlation between the vibrational frequency and structural distortion. For example in the orthorhombically distorted perovskites, $RTiO_3$ (R = La, Ce, Pr, Nd, Sm, Gd), a band decrease from 385-287 cm^{-1} with decreasing orthorhombic distortion is observed[41]. The negative frequency shift seen in NBT Raman spectra therefore suggests this particular phonon may be directly involved in the structural phase transition. The proposed high-pressure orthorhombic structure for NBT has no Ti-cation displacements but is characterised by an $a^-b^+a^-$ tilt system. In this context the downward shift of this band is probably related to a structural rearrangement that is conditioned by both, the restoring of the Ti-cation to the centre of symmetry ($[111]_p \rightarrow [000]$) and a change in the tilt system ($a^-a^-a^- \rightarrow a^-b^+a^-$).

The 300-500 cm^{-1} region is first dominated by the large tail of the *B* band (Figure 6.13 (b)), and then develops new bands as a function of increasing pressure. This

suggests a transition to a crystal symmetry, whose irreducible representations are characterised by a higher number of Raman active bands. This observation is in agreement with a phase transition from R3c (13 Raman-active modes) to Pnma (24 Raman-active modes)[41].

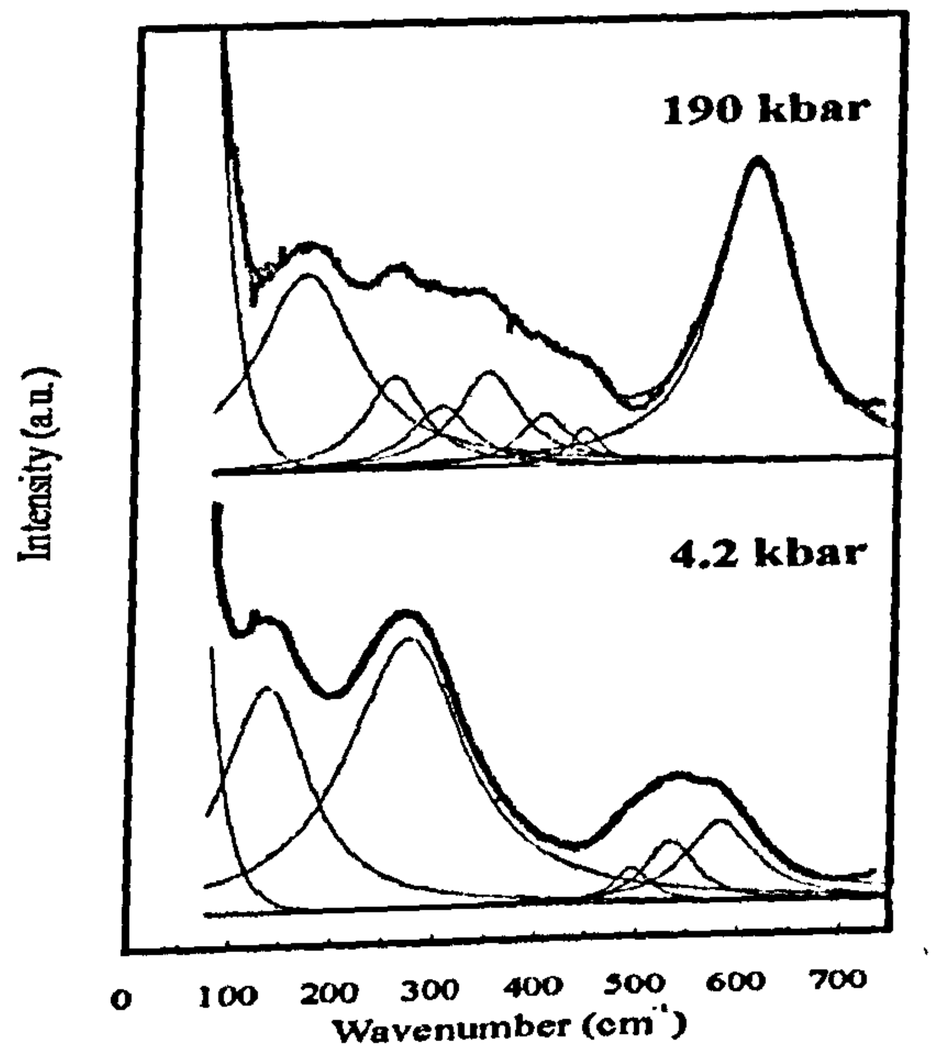

(a)

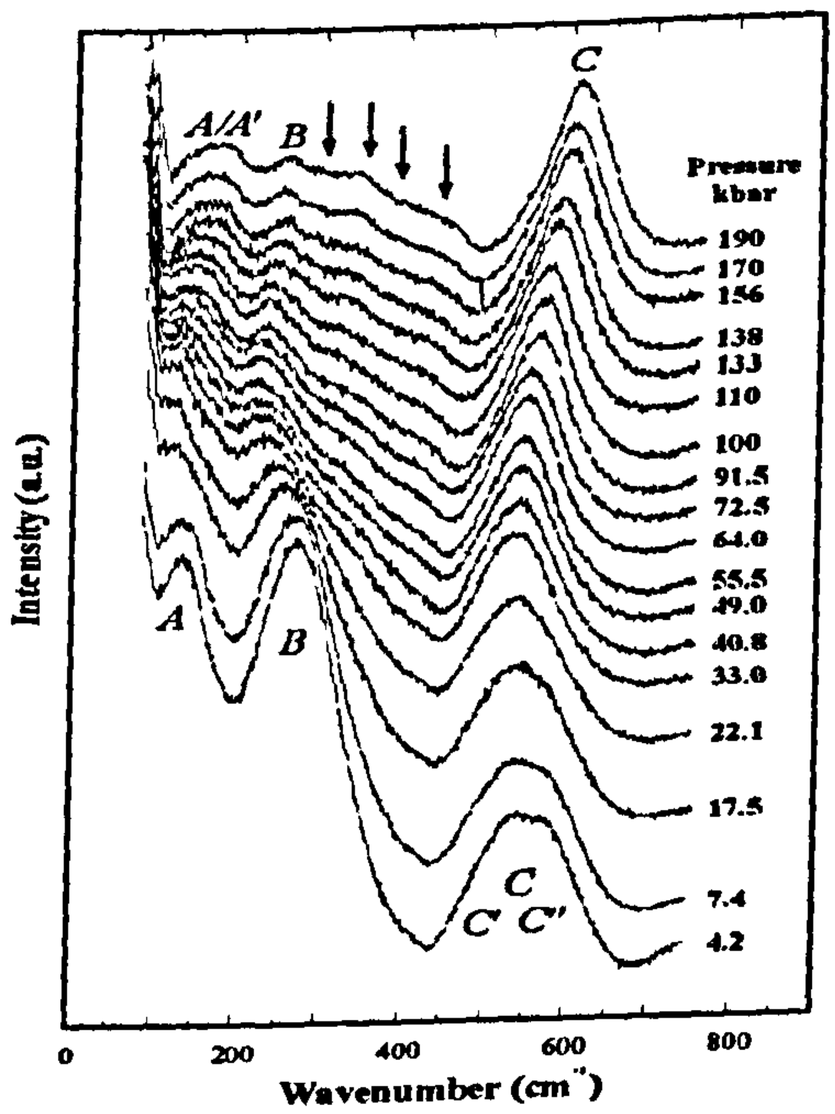

(b)

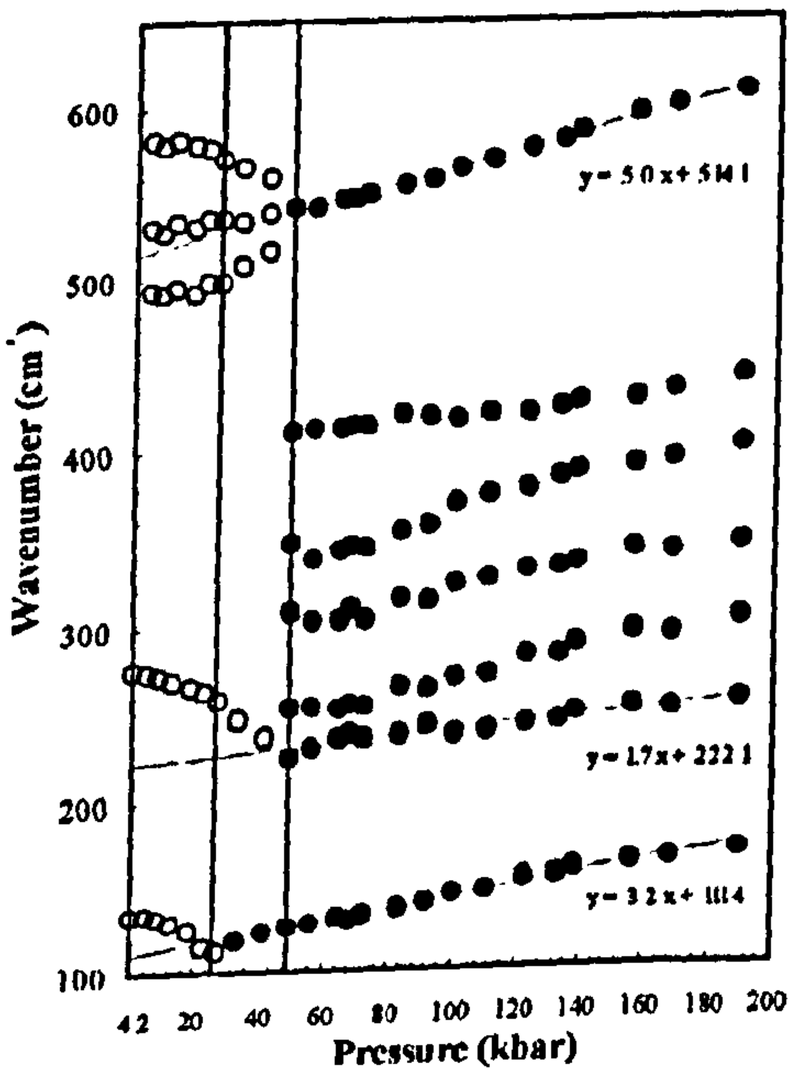

(c)

Figure 6.13. *(a) Raman spectra for NBT at 4.2 and 190 kbar respectively. The gray continuous lines represent the experimental data, the solid thin lines display the spectral deconvolution, (b) Pressure-dependent Raman spectra for NBT, (c) Band position change as a function of pressure in the Raman spectra of NBT. The lines are guides for the eyes to emphasize spectral changes and equations are relative to a linear fit in the 50-190 kbar range.*

High-frequency bands in oxides are dominated by vibrations involving mainly oxygen displacements and can often be interpreted in terms of polyhedra vibrations[20,23]. In NBT the high-frequency bands *C*, *C'* and *C''* have been assigned to vibrations of TiO_6 octahedra[19]. These three bands merge into a single band at 50 kbar (Figures 6.13 (b) and (c)), indicating a structural phase transition has occurred.

In summary, through discontinuous or distinct changes in the Raman spectra, structural changes can be inferred to occur in NBT. At 27 kbar the structural variation is manifested by the frequency change in band *A* (Figure 6.13 (b)), which is related to the Na-O vibrations and has been interpreted as associated with pressure-induced cation displacement changes. At 50 kbar, the structural variations are manifested by the evolution of bands *B* and *C* (Figure 6.13 (b)): these are related to vibrations of TiO_6 octahedra and therefore associated with octahedral tilting. Whether the spectral features observed at 27 and 50 kbar indicate that the transition does not occur in a single step, but goes through an intermediate phase needs to be considered. The results of neutron and synchrotron diffraction studies (chapter 4) show no indication of an intermediate phase in this pressure region. In comparison, results show that the rhombohedral → orthorhombic phase transition appears earlier than that found through Raman studies. According to neutron results at 10 kbar an 83:17 coexistence of rhombohedral/orthorhombic phase exists. From synchrotron results a 26:74 coexistence of rhombohedral/orthorhombic phase exists at 19.4 kbar, with the pure orthorhombic phase being observed at 26.2 kbar. There is no indication from the Raman spectra of the coexistence of the two structures, but it cannot be excluded as the low-frequency features associated with the orthorhombic phase could effectively be masked by the broad and intense bands of the rhombohedral structure. In order to explain the possible origins of structural changes at 27 and 50 kbar from Raman spectra, cation displacements and tilting trends obtained through Rietveld refinements of the synchrotron/neutron data must be considered. In the rhombohedral phase the Na/Bi displacements are seen to plunge to almost zero at 10 kbar (Figure 4.14 (a)). This is accompanied by a abrupt decrease (≈1 %, or 3.27(5) $Å^3$) in the cell volume (Figure 4.13 (c), brought about by the rapid decrease in both the a_H and c_H lattice parameters (Figures 4.13 (a) and (b)) of the rhombohedral cell. Raman spectra confirm the drastic change in displacements, but sees the onset at a higher pressure, starting at 27 kbar. A possible explanation for this disparity could be due the fact that cation shifts to the octahedra centres at 10 kbar occurs, as seen through diffraction techniques, but gives

way to a dynamical disorder around the centre. In this case, for diffraction the cation is in average in the plane, while with Raman, displacements are still observed. If we consider octahedral tilting, from synchrotron studies at 26.2 kbar, cation ordering peaks and antiphase tilt peaks are observed, increasing in intensity as a function of pressure. The tilt angles are seen to increase rapidly after 26.2 kbar (Figure 4.15 (c)), which could correspond to what the Raman sees as the first sign of a single transition. At around 50 kbar we see that the rate of increase of the tilt angle slows sharply. This may correspond to the second set of features in the Raman spectra around 50 kbar. Both techniques agree about the fact that the orthorhombic phase is completely well established by 50 kbar. This pressure may represent a final stabilization for the orthorhombic phase in NBT.

References

[1] Hartshorne, N., H. & Stuart, A. (1970). *Crystals and the Polarising Microscope*. London, Arnold Press.

[2] Kurtz, S. K. & Perry, T. T. (1968). J. Appl. Phys. 39 (8), 3798.

[3] SCOPE Software, ETC Ltd. (1996). 01008 Zilina, Slovak Republic.

[4] Graja, A. (1968). Phys. Stat. Sol. 27, K93-97.

[5] Geday, M., Kreisel, J., Glazer, A. M. & Roleder, K. (2000). J. Appl. Cryst. 33, 909.

[6] Glazer, A. M., Lewis, J. G. & Kaminsky, W. (1996). Proc. R. Soc. London Ser. A. 452, 2751.

[7] Geday, M., Kreisel, J. & Glazer, A. M. Physics Department, Clarendon Laboratory, University of Oxford, Parks Road, Oxford. OX1 3PU.

[8] Suchanicz, J. & Kwapulinski, J. (1995). Ferroelectrics 165, 249.

[9] Park, S.-E., Chung, S.-J., Kim, I.-T. & Hong, K. S. (1994). J. Am. Ceram. Soc. 77, 2641.

[10] Krunzina, T. V., Gene, V. V., Isupov, V. A. and Sinyakov, E. V. (1981). Sov. Phys. Crystallography 26, 852.

[11] Alberty, R. A. & Silbey, R. J. (1997). Physical Chemistry, John Wiley & Sons, Inc.

[12] Nudelman, S. & Mitra, S. S. (1969). *Optical Properties of Solids*. New York, Plenum Pess.

[13] Salje, E. K. H. & Bismayer, U. (1997). Phase transitions 63, 1.

[14] Bismayer, U., Devarajan, V. & Groves, P. (1989). J. Phys.: Condens. Matter 1, 6977.

[15] Frantti, J., Lantto, V. & Lapplalainen, J. (1996). J. Appl. Phys. 79, 1065.

[16] Frantti, J. & Lantto, V. (1997). Phys. Rev. B56, 221.

[17] Zhang, H., Leppävuori, S. & Karjalainen, P. (1995). J. Appl. Phys. 77, 2691.

[18] Meng, J., Zou, G, Ma, Y., Wang, X. & Zhao, M. (1994). J. Phys.: Condens. Matter 6, 6549.

[19] Kreisel, J., Glazer, A. M., Jones, G. O., Thomas, P. A., Abello, L, & Lucazeau, G. (2000). J. Phys.: Condens. Matter. 12, 3267.

[20] Kreisel, J., Lucazeau, G. & Vincent, H. (1998). J. Solid State Chem. 137, 127.

[21] Kreisel, J., Vincent, H. & Lucazeau, G. (1999). J. Raman Spectroscopy 30, 115.

[22] Tarte, P. (1967). Spectrochim. Acta A23, 2127.

[23] Tarte, P., Rulmont, A., Liégeois-Duycckaerts, M., Cahay, R. & Winand, J. M. (1990). Solid State Ion. 42, 177.

[24] †Kreisel, J., ‡Abello, L, & ‡Lucazeau, G. †Physics Department, Clarendon Laboratory, University of Oxford, Parks Road, Oxford. OX1 3PU. ‡Laboratoire d'Electrochimie et de Physicochimie des Matériaux et des Interfaces, ENSEEG, BP 75, 38402 St Martin d' Hères Cédex, Grenoble, France.

[25] Siny, I. G., Smirnova, T. A & Kruzina, T. V. (1991). Ferroelectrics 124, 207.

[26] Siny, I. G., Smirnova, T. A & Kruzina, T. V. (1991). Sov. Phys. Solid State 33, 61.

[27] Zhang, M. S. & Scott, J. F. (1986). Ferroelectric Letters 6,147.

[28] Denisov, V. N., Ivlev, A. N., Lipin, A. S., Mavrin, B. N. & Orlov, V. G. (1997). J. Phys. Condens. Matter 9, 4967.

[29] Elkechai, O., Mainer, M. & Mercurio, J. P. (1996). Phys. Status Solidi A 157, 499.

[30] Pronin, I., Parfenova, N. N., Zaitseva, N. V. & Smolenskii, G. A. (1982)Sov. Phys. Solis State 24, 1060.

[31] Yamada, Y., Akutsu, T., Asada, H., Nozawa, K., Hachachiga, S., Kurosaki, T., Fujiki, H., Hozumi, K., Kawamura, T., Amakawa, T., Hirota, K. & Ikeda, T. (1995). Japan. J. Appl. Phys. 34, 5462.

[32] Sood, A. K., Chandrabas, N., Muthu, D. V. S. & Jayaraman, A. (1995). Phys. Rev. B51, 8892.

[33] Venkateswaran, U. D., Naik, V. M & Naik, R. (1998). Phys. Rev. B58, 14256.

[34] Sanjurjo, J. A., Lopez-Cruz, E, & Burns, G. (1983). Phys Rev. B28, 7260.

[35] Cerdeira, F., Holzapfel, W. B. & Bauerle, D. (1975). Phys. Rev. B11, 1188.

[36] Grzechnik, A., Wolf, G. H. & McMillan, P. F. (1997). J. Raman Spectroscopy 28, 885.

[37] Gillet, P. Guyot, F., Price, G. D., Tournerie, B. & Cleach, A. L. (1993). Phys. Chem. Minerals 20, 159.

[38] Kreisel, J., Glazer, A. M., Bouvier, P. & Lucazeau, G. (2000). Phys. Rev. B (submitted).

[39] Pieramini, G. J., Block, S., Barnett, J. D. & Forman, R. A. (1975). J. Appl. Phys. 46, 2774.

[40] †Kreisel, J., ‡Bouvier, P. and ‡Lucazeau, G. †Physics Department, Clarendon Laboratory, University of Oxford, Parks Road, Oxford. OX1 3PU. ‡Laboratoire d'Electrochimie et de Physicochimie des Matériaux et des Interfaces, ENSEEG, BP 75, 38402 St Martin d' Hères Cédex, Grenoble, France.

[41] Kreisel, J., Glazer, A. M., Bouvier, P. and Lucazeau, G. (2001). Phys. Rev. B, (submitted).

[42] Venkateswaran, U. D., Naik, V. M. and Naik, R. (1998). Phys. Rev. B58, 14256.

[43] Sanjurjo, J. A., Lopez-Cruz, E. and Burns, G. (1983). Phys Rev. B28, 7260.

[44] Burns, G., Sanjurjo, J. A. and Lopez-Cruz, E. (1984). Phys Rev. B30, 7170.

Chapter 7

Conclusions and Future Work

7.1 Introduction

Sodium Bismuth Titanate is an A-site substituted complex, distorted perovskite. The rare feature of this material is the formation of a compound through substitution at the A-site. The formation of this perovskite has offered the opportunity to investigate the structural influence of the A-site as the primary determiner of the resulting crystal structures and phase transitions, and not simply as a spacer required for filling the framework and to charge balance. This study has presented a different perspective on the perovskite structure.

At the outset of this work, there remained wide debate concerning phase transition temperatures, the development of regions of coexistence of rhombohedral/tetragonal phases and tetragonal/cubic phases and their electric order in NBT. The symmetry and structure of these phases also, had not unambiguously been established. Using a variety of experimental techniques and drawing together results, controversies within the literature have been resolved. The symmetry and structures of known phases have been unambiguously determined and new structural phases have been established and are reported for the first time. A summary of the phase transitions, induced by temperature, pressure and variations in composition as well as conclusions reached is presented in the following section. Suggestions for future work, carrying on from this study are also given.

7.2 Summary of Results

Optimum fabrication routes for the production of powders and single crystals of the NKBT solid solution series were investigated and successfully established. Characterisation of these materials has been carried out and the morphology and properties reported. Details of the stages involved and sintering times used for the successful production of ceramics have also been presented. Subsequent ceramic density measurements are given for the first time.

An extensive study of the crystal structure and phase transitions in NBT was carried out. The fundamental sequence of phase transitions from the high-temperature

prototypic cubic to one of tetragonal and then rhombohedral structure, with coexistence phases of tetragonal/cubic and rhombohedral/tetragonal has been observed. The pure rhombohedral phase persists from 5-528 K, between 573-593 K, a coexistence region was seen and from 673-773 the pure tetragonal phase was seen to occur. The tetragonal/cubic coexistence region lies within 773-813 K, with the pure cubic phase occurring at 813 K. The rhombohedral/tetragonal coexistence range was found to be around 145 K (this figure indicates a maximum temperature limit).

The results of powder profile refinements revealed the rhombohedral phase, space group R3c, exhibits an antiphase, $a^-a^-a^-$, oxygen octahedra tilt system, resulting in a doubled unit cell, with parallel cation displacements. The tilting arises from oxygen octahedra tilting about the three-fold pseudo-cubic axes, and is characterised by opposite rotations of adjacent octahedra along each axis. With increasing temperature, the Na/Bi and Ti cation displacements were seen to decrease as expected. There was also a continual decrease in the octahedron tilting with increasing temperature.

As the temperature was increased from room temperature, rhombohedral superstructure reflections of the type odd-odd-odd with $k \neq l$, disappeared and tetragonal superstructure reflections of the type odd-odd-even appeared. The tetragonal phase, space group P4bm, possesses an unusual combination of in-phase oxygen octahedra tilts described by $a^0a^0c^+$ and antiparallel cation ordering along the polar axis. The rotation of the octahedra associated with this system, results in cell doubling in the [100] and [010] directions, but as successive octahedra are rotated in the same direction about [001], there is no doubling in this direction. Na/Bi displacements were seen to follow a gradual rise followed by a rapid drop and then a moderate displacement decrease as a function of temperature. Ti displacements are antiparallel to Na/Bi displacements and showed a relatively constant progression with increasing temperature. The tilt angle in the tetragonal phase varied modestly at first then dropped to zero when the transition to the cubic phase occurred. Since A-cation displacements along [001] are not driven by the octahedral tilts, it was proposed that they result from the need to accommodate the stereo-active lone pair on Bi^{3+}. Although tetragonal perovskites of symmetry P4bm have the capability of showing ferroelectric properties through cation displacements, until now no system has been found that exploits this ability. This structure-type is unprecedented amongst the perovskites, and results in a completely new variant of the perovskite structure being detected.

A further increase in temperature diminished the tetragonal superstructure reflections until the final phase transition to the cubic perovskite, space group $Pm\bar{3}m$, possessing no tilts or cation displacements occurred.

All indications are that there is no long-range ordering in NBT. Therefore, the evidence is that the rule governing B-site ordering (section 3.3.5.2) also holds for A-site ordering. However, as indicated by diffuse scattering experiments and preliminary TEM experiments, short-range ordering is sometimes present. Single crystal x-ray diffraction experiments showing additional scattering in between the Bragg peaks, in the form of streaks gave further evidence in support of this idea.

Valency calculations on NBT revealed that in all phases, the Bi^{3+} shows a relatively large valency deficiency from its ideal value. The opinion is reached that, even though Bi^{3+} moves off-centre in order to satisfy its own stereo-chemical preferences, on the A-site of the perovskite structures in the polar rhombohedral and tetragonal phases it is unable to achieve a perfect match to its valency.

For the first time NBT has been characterised as a function of pressure. The ambient pressure rhombohedral structure undergoes a phase transition to an orthorhombic structure. Superstructure reflections of the type odd-odd-odd and odd-even-odd associated with the octahedra tilting and even-even-odd, associated with cation displacements were observed. The orthorhombic distortion was seen to increase as a function of applied pressure. The newly detected orthorhombic structure of NBT has Pnma symmetry with the $a^-b^+a^-$ tilt system of oxygen octahedra and antiparallel A-cation ordering along [010]. The pure rhombohedral structure was seen to persist up to 8 kbar, between 10-19.4 kbar a rhombohedral/orthorhombic coexistence region was observed and above 26.2 kbar the purely orthorhombic phase was seen. The tilt angle distortions about [010] were seen to rise gradually with increasing pressure, whereas the tilts around [100]/[001] were more dominant and showed significant increases with pressure.

Similar bond-valency characteristics as were seen for the rhombohedral and tetragonal phases were observed for the orthorhombic phase of NBT. Again the conclusion that even though the Bi-cations are displaced, there is an imperfect match to its valency was reached.

A detailed systematic structural investigation across the $(Na_{1-x}K_x)_{0.5}Bi_{0.5}TiO_3$ solid solution series with varying composition and temperature has been presented. The

discrepancies concerning the relation of the nature of the NBT to KBT phase transitions have been fully resolved. The room temperature structural variation across the series ranging from the tilted rhombohedral (space group, R3c) structure at the $x = 0$ end to the intermediate (zero-tilt) rhombohedral (space group, R3m) structure, finishing with the tetragonal (space group, P4mm) structure at $x = 1$ end, has been established. The series of phase transitions including space group assignment, tilting systems and cation displacements has been reported for the first time on these materials. A basic phase diagram for the NKBT solid solution series has been constructed: phase boundaries are outlined across the solid solution range and as a function of temperature.

In order to complement the diffraction work, optical and Raman studies were conducted on the NKBT series. SHG measurements, conducted as a function of particle sizes for the NKBT solid solution range and as a function of temperature for NBT have been reported for the first time. The non-phase-matched nature of these powders was clearly observed. Results supported the assignment of polar space groups to rhombohedral and tetragonal phases of these compounds. The measurement of SHG signal as a function of temperature in NBT has shown the usefulness of this method in determining phase transitions in materials of this nature.

Birefringence imaging as a function of temperature was used to study phase transitions in selected NKBT crystals. Results showed that all crystals possessed large amounts of twinning coupled with strain. Phase transition temperatures found for NBT were in close agreement with results obtained through diffraction studies and revealed that a thermal hysteresis for the rhombohedral/tetragonal coexistence phase exists. Similar results were obtained for $(Na_{0.8}K_{0.2})_{0.5}Bi_{0.5}TiO_3$ and $(Na_{0.6}K_{0.4})_{0.5}Bi_{0.5}TiO_3$. However, the cubic phase was seen to move to higher temperatures and the width in temperature of the tetragonal phase region increased with the tetragonal/rhombohedral coexistence phases moving to lower temperatures in comparison to NBT. The results also revealed the existence of isotropic regions between the rhombohedral and tetragonal phases within the crystals studied.

Raman spectra have been taken as a function of substitution across the NKBT series. All bands showed high-frequency shifts with increasing substitution rate. The only exception was the band at 135 cm^{-1}, being assigned to a Na/K-O vibration, which suggests the existence of local clusters of Bi- and Na/K-containing unit cells. Phase transition results across the series fully support the conclusions reached in the diffraction

studies. The pressure-dependent Raman spectra of NBT also has been studied for the first time. Through changes in the Raman spectra phase transitions have been analyzed in terms of a rhombohedral (R3c) → orthorhombic (Pnma) phase transition.

7.3 Future Work

There still remains scope for further research of NBT and the solid solution range. Firstly, it could be informative to investigate the width over which the tetragonal region extends, to study the role of the crystal preparation route taken. Alternative preparative routes to those discussed for example in chapter 2, such as thin-film synthesis could be used. The possibility that the occurrence of the tetragonal phase may in fact be associated with growth imperfections and strain within the crystal structure could be investigated. The possibility of a direct rhombohedral to cubic phase transition, which structurally would be more favourable, could be investigated.

If improved single-crystals could be produced, then sterochemical studies to complement those already undertaken could be undertaken. These could include further valency studies as a function of temperature and pressure to see if a specific phase interval exists in which the Bi^{3+} cation in particular, reaches a perfect (or very close) match to its ideal valency, *i.e.*, where it is neither over- or under-bonded. Studies of this nature could reveal important information about the nature of the stabilizing mechanisms involved in these types of compounds. Continuing on from the initial electron diffraction and diffuse scattering studies carried out here, improved single-crystals would also be of great benefit in the study of the short-range ordering in these compounds. To complement these studies, other techniques such as Extended X-ray Absorption Fine Structure (EXAFS) and Nuclear Magnetic Resonance (NMR) could be used in order to obtain information on the local environment of the cations. NMR experiments are currently being undertaken at the University of Warwick.

The initial high-pressure high-temperature fabrication routes could be more fully investigated in order to produce single crystals of KBT and possibly other new isostructural compounds i.e. doped with cations such as barium, strontium etc. In order to facilitate a more complete phase diagram across the NKBT series, further compounds between the NBT and KBT end members could be made and similar structural characterisation work as a function of temperature conducted. This would also facilitate

the completion of the phase-transition composition phase diagram and reveal whether a morphotropic phase boundary exists in this system.

Computational modeling studies, such as those being conducted using *ab initio* and pair-potential codes at the University of Warwick, may give an insight into areas such as short-range ordering and details of phase transitions. Also, the possible electronic causes of the structural distortions in the non-cubic phases observed in these perovskites could be investigated. Substitution by alternative dopants and non-stoichiometric effects in the compounds under study here could also be conducted. These methods could also be extended as a predictive tool to evaluate the stability of new hypothetical complex perovskite compositions.